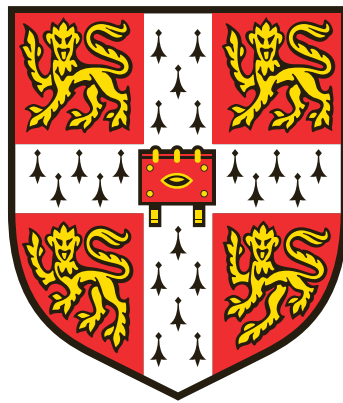


# HIGH FIDELITY OPEN ROTOR NOISE PREDICTION



**Paul Huw Thomas**

King's College  
University of Cambridge

December 2017

*This dissertation is submitted for the degree of  
Doctor of Philosophy*

*“I did know once, only I’ve sort of forgotten.”* - A. A. Milne, Winnie-the-Pooh

O you dimbo, battle’s over. At last! (5,6,4)

# Declaration

This dissertation is the result of my own work and includes nothing which is the outcome of work done in collaboration except as declared in the Preface and specified in the text. It is not substantially the same as any that I have submitted, or, is being concurrently submitted for a degree or diploma or other qualification at the University of Cambridge or any other University or similar institution except as declared in the Preface and specified in the text. I further state that no substantial part of my dissertation has already been submitted, or, is being concurrently submitted for any such degree, diploma or other qualification at the University of Cambridge or any other University or similar institution except as declared in the Preface and specified in the text. This thesis consists of fewer than 54,000 words and 110 figures.

Paul Thomas



# Preface

When I began this PhD (a time now lost in hallowed antiquity), the chance to do something difficult and new that was entirely my own work was, rather arrogantly, very exciting. However, I have come to realise over the last \*cough\* \*splutter\* years that a PhD is far from being something you undertake by yourself. I have had a huge amount of support and there is no way that I would be sitting here writing this without that help.

My first thanks have to go to my supervisor, Cesare Hall, who has been absolutely fantastic throughout my studies. Given that just about everyone I know has finished their PhD before me, even people who were not at university when I started mine, I know exactly how lucky I am to have a supervisor who has supported me whilst also trusting and enabling me to find my own way. The fact that he has continued to believe in me despite the many mistakes I have made is something I am eternally grateful for. My advisor, Tom Hynes, has also been hugely helpful.

Alongside Chez, I have to thank Rolls-Royce plc and the Engineering and Physical Sciences Research Council for funding my PhD. More than just the money, the enthusiasm with which so many people at Rolls-Royce engaged with me and the technical expertise they provided was absolutely invaluable. In particular, Tony Parry was a constant help and I am only sorry that he has had to wait so long for

my results! I also have to thank my employers, McLaren Applied Technologies, for being so understanding and for allowing me to continue my PhD while working for them.

Back at the Whittle Lab in Cambridge, there is an entire community of people that were such a wonderful mix of fun, inspiration and eccentricity that I fear I won't get a chance to experience something like it again. In particular, I owe a great debt of thanks to Nishad Sohoni for being my knight in shining armour when things got tough, I am eternally grateful. There are so many others I would love to thank, but I know the most effective means of communication is cake, so I'll leave it there.

All of the above people have been vital in supporting the technical side of my PhD, but there has also been a huge burden on my personal life. Hence I have just as many people to thank not for helping with my research but for making sure I come out the other side of it without a straitjacket on. In particular, my sanity has been greatly aided by knowing there is someone out there who is more stressed about my PhD than I am. This is, of course, my mum. Her "encouragement" and "enthusiasm" were a great motivation, as well as the little things like raising me to be the person I am today and setting the example I try to live by. To the rest of my family, Rachel and Fred, I thank you for keeping Mum at bay as best you can. To all my friends, I thank you for your constant ridicule and merciless pessimism, it made it so much easier to ignore you all so badly for the last few years.

Finally, there is one person above all who sacrificed for me above and beyond anything I had a right to expect. Tinikins, I am so, so lucky to have had you with me through this. You were kind when I was struggling, fun when I needed distraction and strict when I needed discipline. I could not have done this without you and I cannot wait to spend the rest of our lives making it up to you by loading the dishwasher once in a while.

# Contents

<b>List of Figures</b>	<b>x</b>
<b>List of Tables</b>	<b>xvii</b>
<b>Nomenclature</b>	<b>xxi</b>
<b>1 Introduction</b>	<b>1</b>
1.1 Context and Motivation . . . . .	1
1.2 Research Objectives . . . . .	6
1.3 Thesis Structure . . . . .	8
<b>2 Literature Review</b>	<b>11</b>
2.1 Aeroacoustic Analogies . . . . .	13
2.2 Surface Introduction . . . . .	20
2.3 Formulations of Solution . . . . .	33
2.3.1 The Fundamental Convolution . . . . .	33
2.3.2 Collapsing Sphere Formulations . . . . .	37
2.3.3 Emission Time Formulations . . . . .	38
2.4 Solver Methodologies . . . . .	45
2.4.1 Observer Dominant Methodologies . . . . .	46

2.4.2	Source Dominant Methodologies . . . . .	47
2.4.3	Frequency Domain Methodologies . . . . .	49
2.5	Verification and Validation . . . . .	52
2.6	Open Rotors . . . . .	60
2.6.1	Rotor Alone Effects . . . . .	61
2.6.2	Interaction Effects . . . . .	66
2.6.3	Installation Effects . . . . .	72
2.6.4	Modern Research . . . . .	73
2.6.5	Z-08 Test Case . . . . .	79
2.7	Summary . . . . .	82
<b>3</b>	<b>Numerical Methods</b>	<b>85</b>
3.1	Key Concepts . . . . .	86
3.1.1	Periodicity . . . . .	86
3.1.2	Panel Averaging . . . . .	86
3.1.3	Propagation Time Calculation . . . . .	87
3.1.4	Surface Files . . . . .	90
3.1.5	Flow Files . . . . .	90
3.2	Codes . . . . .	91
3.2.1	Acoustic Monopole Input . . . . .	91
3.2.2	Turbostream Input . . . . .	95
3.2.3	Surface Interpolation . . . . .	99
3.2.4	Source Term Construction . . . . .	102
3.2.5	Frequency Domain Conversion . . . . .	102
3.2.6	Solvers . . . . .	106
3.3	Summary . . . . .	109

<b>4</b>	<b>Discretisation Errors</b>	<b>119</b>
4.1	Basic Principles . . . . .	120
4.1.1	Geometric Resolution . . . . .	121
4.1.2	Observer Resolution . . . . .	123
4.1.3	Flow Resolution . . . . .	126
4.1.4	Surface Motion . . . . .	128
4.2	Error Study Framework . . . . .	130
4.3	Analytical Test Case . . . . .	133
4.3.1	Description . . . . .	134
4.3.2	Dimensional Analysis . . . . .	140
4.4	Method Study . . . . .	142
4.4.1	Initial Methodology . . . . .	143
4.4.2	Panel Averaging . . . . .	144
4.4.3	Observer and Source Dominant Propagation . . . . .	147
4.4.4	Flow Solution Domain . . . . .	148
4.4.5	Frequency Domain Propagation . . . . .	150
4.4.6	Surface Rotation . . . . .	151
4.5	Summary . . . . .	153
<b>5</b>	<b>Neglection Errors</b>	<b>159</b>
5.1	Generic Aeroacoustic Analogy . . . . .	160
5.2	New Surface Discontinuity Method . . . . .	165
5.2.1	Derivation . . . . .	166
5.2.2	Comparison with FW-H and Kirchhoff Methods . . . . .	170
5.3	Semi-Analytical Test Case . . . . .	177
5.4	Summary . . . . .	188

<b>6</b>	<b>Demonstration On Realistic Test Case</b>	<b>191</b>
6.1	Test Case . . . . .	192
6.2	Periodicity Problem . . . . .	200
6.3	Surface Interpolation . . . . .	206
6.4	Initial Results . . . . .	207
6.5	Discretisation Errors . . . . .	212
6.6	Neglection Errors . . . . .	214
6.7	Summary . . . . .	218
<b>7</b>	<b>Conclusions and Further Work</b>	<b>221</b>
7.1	Discretisation Errors . . . . .	221
7.1.1	Conclusions . . . . .	221
7.1.2	Future Work . . . . .	223
7.2	Neglection Errors . . . . .	224
7.2.1	Conclusions . . . . .	224
7.2.2	Future Work . . . . .	227
	<b>Bibliography</b>	<b>228</b>

# List of Figures

- 1.1 Rolls-Royce open rotor design concept from Zachariadis [87]. . . . . 2
- 1.2 Comparison of turboprop, turbofan and open rotor efficiencies from Zachariadis [87]. . . . . 3
- 1.3 Frequency spectrum for a counter-rotating open rotor from Czech [20]. 4
  
- 2.1 Illustration of FW-H surface discontinuity concept. . . . . 22
- 2.2 FW-H surface naming convention from Brentner and Farassat [8]. . . 30
- 2.3 Noise results for a) Kirchhoff and b) FW-H methods from Brentner and Farassat [8]. . . . . 30
- 2.4 FW-H surface naming convention from Spalart and Shur [78]. . . . . 31
- 2.5 Noise results for a) adjusted FW-H b) traditional FW-H and c) Kirchhoff source terms from Spalart and Shur [78]. . . . . 32
- 2.6 Illustration of sifting of  $\delta(g(x_i, t))$  term. . . . . 34
- 2.7 Illustration of sifting of  $\delta(g(r_i, t - \tau))$  term. . . . . 36
- 2.8 Illustration of analytical test case from Casalino [12]. . . . . 58
- 2.9 Calculated time signal for the test case from Casalino [12]. . . . . 58
- 2.10 Plot of RMS error vs. step size from Casalino [12]. . . . . 59

2.11 Representation of a propeller blade as a stack of airfoils from Gutin [42]. . . . .	62
2.12 Calculated variation of noise with directivity from Gutin [42]. . . . .	63
2.13 Experimental variation of noise with directivity from Gutin [42]. . . . .	64
2.14 Predicted variation of noise with axial location from Rohrbach et al [69]. . . . .	65
2.15 Experimental variation of sound with axial location from Rohrbach et al [69]. . . . .	66
2.16 Experimental set up from Woodward [86]. . . . .	68
2.17 Typical open rotor frequency content from Woodward [86]. . . . .	68
2.18 Directivity of rotor alone and interaction tones from Woodward [86]. . . . .	69
2.19 Blade row rotations for an 8/6 bladed open rotor in the a) rotating and b) absolute frames. . . . .	71
2.20 Pressure frequency content on a rear blade for a) zero and b) 12° angle of attack from Sohoni et al [77]. . . . .	74
2.21 Experimental and calculated data for the (1,1) interaction tone from Colin et al [15]. . . . .	75
2.22 Experimental and calculated results for different mesh densities from Colin et al [14]. . . . .	76
2.23 Illustration of refraction concept from Colin et al [16]. . . . .	78
2.24 Open and closed surface placements from Colin et al [16]. . . . .	78
2.25 Experimental and calculated data for different surface placements from Colin et al [16]. . . . .	79
2.26 Experimental setup for an installed Z-08 case from Paquet et al [64]. . . . .	81
2.27 Experimental data for the (2,1) and (2,2) interaction tones for the Z-08 test case from Paquet et al [64]. . . . .	81

2.28	Meshing strategy and boundary conditions for Z-08 test case from Sohoni et al [77]. . . . .	83
3.1	Illustration of the Garrick triangle. . . . .	88
3.2	Basic schematic of <code>fwh_input</code> functionality. . . . .	92
3.3	Pressure field, surface intersection (black line) and comparison point (red cross) for a rotating monopole. . . . .	93
3.4	Comparison of $p'$ and $c^2\rho'$ for a rotating monopole. . . . .	94
3.5	Mass conservation for a rotating monopole. . . . .	94
3.6	Momentum conservation for a rotating monopole. . . . .	95
3.7	Basic schematic of <code>fwh_ts2fwh</code> functionality. . . . .	97
3.8	Unstructured cut taken from Turbostream. . . . .	98
3.9	Structured cut output by mesh conversion algorithm. . . . .	98
3.10	Pressure and density variation in output of <code>fwh_ts2fwh</code> . . . . .	99
3.11	Velocity variation in output of <code>fwh_ts2fwh</code> . . . . .	100
3.12	Basic schematic of <code>fwh_interp</code> functionality. . . . .	110
3.13	Illustration of <code>fwh_interp</code> overlap algorithm. . . . .	111
3.14	Pressure signals for rotating, non-rotating and interpolated surfaces. . . . .	111
3.15	Time domain comparison for FFTs using different sample periods. . . . .	112
3.16	Frequency domain comparison for FFTs using different sample periods. . . . .	112
3.17	Frequency components calculated by a) FFT and periodic sample, b) FFT and non-periodic sample, c) LSSA with periodic sample and all tones, d) LSSA with non-periodic sample set and all tones, and e) LSSA with non-periodic sample set and the 1 Hz tones. . . . .	113

3.18	Results of LSSA method refinement, showing a) original FFT, b) LSSA using one tone, c) FFT of the corresponding residual, d) LSSA using both tones, and e) FFT of the corresponding residual. . . . .	114
3.19	Basic schematic of FW-H solver functionality. . . . .	115
3.20	Time domain validation results for <code>fw_h_ret</code> . . . . .	116
3.21	Time domain validation results for <code>fw_h_adv</code> . . . . .	116
3.22	Frequency domain validation results for all codes. . . . .	117
4.1	Illustration of simple acoustic monopole test case. . . . .	122
4.2	Variation of $\epsilon_{RMS}$ with $N_P$ . . . . .	124
4.3	Variation of $\epsilon_{RMS}$ with $N_L$ . . . . .	125
4.4	Variation of $\epsilon_{RMS}$ with $N_\lambda$ and $N_T$ , and contour for $\epsilon_{RMS} = 0.1$ . . . .	127
4.5	Illustration of influence surface distortion for $M_X = 0.5$ and $M_\Omega = 0.5$ . . . .	129
4.6	Variation of $\epsilon_{RMS}$ with $M_X$ and $M_\Omega$ . . . . .	130
4.7	Illustration of analytical open rotor test case kinematics. . . . .	137
4.8	Instantaneous pressure perturbation for datum test case on the $x = 0$ plane. . . . .	137
4.9	Time domain variation of pressure fluctuation and LSSA residual for the datum test case. . . . .	138
4.10	FFT, LSSA and residual FFT of pressure fluctuation for datum test case. . . . .	138
4.11	Variation of the (1,0), (0,1) and (1,1) tones with directivity for the datum case. . . . .	139
4.12	Instantaneous pressure perturbation on datum test case integration surface. . . . .	144
4.13	Calculated and exact observer signals for datum test case. . . . .	145

4.14	FFT, LSSA and residual FFT for calculated and exact datum test cases.	145
4.15	Variation of RMS error with directivity for datum test case. . . . .	146
4.16	Comparison of frequency content for $N_\lambda = 40$ and $N_\lambda = 50$ . . . . .	149
4.17	Comparison of frequency content for methodologies C and D at $N_\lambda =$ 40 and $\theta = \pi/2$ . . . . .	150
4.18	Comparison of methodologies A and G for datum test case. . . . .	153
4.19	Variation of discretisation error with resolution parameters for differ- ent solver methodologies. . . . .	155
5.1	Magnitude of $\alpha_p$ for semi-analytical test case. . . . .	180
5.2	Variation of $\phi$ with directivity for $X_D = 6$ . . . . .	183
5.3	Variation of $\phi$ with directivity for $X_D = 1$ . . . . .	184
5.4	Comparison of different analogies and surface methods for an up- stream observer location. . . . .	185
5.5	Comparison of different analogies and surface methods for a perpen- dicular observer location. . . . .	185
5.6	Comparison of different analogies and surface methods for a down- stream observer location. . . . .	186
5.7	Variation of $\phi$ for different surface methods and source constructions vs. directivity and downstream integration limit. . . . .	187
6.1	Illustration of CFD domain reproduced from Sohoni [77], showing slid- ing planes and boundary conditions. . . . .	193
6.2	Entropy contours across inter-row sliding plane and wake comparison locations, reproduced from Sohoni [77]. . . . .	194
6.3	Plot of wake harmonic propagation quality across the inter-row sliding plane for two different mesh resolutions, reproduced from Sohoni [77].	195

6.4	Plot of cut plane locations and names, as well as Z-08 geometry notation.	196
6.5	Contour plot of pressure perturbation on D1 cut plane, as well as mesh line and point sample locations. . . . .	197
6.6	Contour plot of entropy on D1 cut plane, as well as mesh line and point sample locations. . . . .	197
6.7	Contour plot of $Q$ on D1 cut plane, as well as mesh line and point sample locations. . . . .	198
6.8	Contour plot of $F$ on D1 cut plane, as well as mesh line and point sample locations. . . . .	198
6.9	Radial plot of stagnation pressure on U1 and D1 cut planes. . . . .	199
6.10	Radial plot of $p' - c^2\rho'$ on U1 and D1 cut planes. . . . .	200
6.11	Plot of $Q$ for points A and B on the D1 cut. . . . .	201
6.12	Plot of $\dot{Q}$ for points A and B on the D1 cut. . . . .	202
6.13	Plot of $Q$ for point B compared to the results of the two filtering methods. . . . .	203
6.14	Plot of $\dot{Q}$ for point B compared to the results of the two filtering methods. . . . .	203
6.15	Frequency domain comparison of the original signal to the two filtering methods. . . . .	205
6.16	Comparison of the residual signals for the two filtering methods. . . . .	205
6.17	$Q$ on D1 downstream cut in original flow solution at $t = 0.25T_0$ . . . . .	208
6.18	$Q$ on D1 downstream cut in interpolated flow solution at $t = 2.25T_0$ . . . . .	208
6.19	$Q$ on D1 downstream cut in the original and interpolated flow solutions.	209
6.20	Time domain plot of initial results for the (U1,R1,D1) surface. . . . .	210
6.21	Frequency domain plot of initial results for the (U1,R1,D1) surface. . . . .	210

6.22	Directivity plot of initial results for the (U1,R1,D1) surface and industry standard methodology. . . . .	211
6.23	Directivity plot of initial results for the (U1,R1,D1) surface and best case methodology. . . . .	212
6.24	Variation of the (1,0) interaction tone for different solver methodologies and time steps. . . . .	213
6.25	Variation of the (3,3) interaction tone for different solver methodologies and time steps. . . . .	214
6.26	Variation of the (1,2) interaction tone for different source constructions at a) $\theta = \pi/10$ , b) $\theta = \pi/2$ and c) $\theta = 9\pi/10$ . . . . .	216



# List of Tables

2.1	Key characteristics of Z-08 test case, reproduced from Sohoni et al [76, 77]. . . . .	82
3.1	Description of FW-H solver codes. . . . .	86
4.1	Parameters for geometric resolution test case. . . . .	122
4.2	Variables and datum values for solver methodology test case. . . . .	136
4.3	Values of non-dimensional groups for datum test case. . . . .	141
4.4	Definition of solver methodology options. . . . .	143
6.1	Key characteristics of Z-08 test case. . . . .	192
6.2	Cut plane locations for Z-08 test case. . . . .	194
6.3	Resolution parameters based on different tones. . . . .	207



# Nomenclature

## Roman

$A_0$	Magnitude of constant component of analytical open rotor source strength fluctuation
$A_1$	Magnitude of fluctuating component of analytical open rotor source strength fluctuation
$c$	Wave speed
$e$	Specific total internal and kinetic energy of fluid
$e_{ij}$	Viscous stress tensor
$f$	Arbitrary function where $f = 0$ defines the integration surface
$F_i$	A momentum-like acoustic source term
$G$	Free space Green function for the linear wave equation
$g$	Function where $g = 0$ corresponds to a valid propagation of a wave from source to observer
$H$	Heaviside step function
$K_M$	A velocity-like term used for ease of notation
$L$	Distance from origin to observer
$M_\Omega$	Rotational Mach number equal to $\Omega R/c$
$M_i$	Mach number of the surface velocity
$m_i$	Generic mass flux/momentum density in a realistic fluid

$N_\lambda$	Flow resolution in space metric equal to characteristic wavelength normalised by $\lambda_P$
$N_F$	Front blade number
$n_i$	Unit outward normal of integration surface
$N_L$	Observer resolution metric equal to minimum distance from surface to observer normalised by $\lambda_P$
$N_P$	Geometric resolution metric equal to the square root of the number of panels
$N_R$	Rear blade number
$N_T$	Flow resolution in time metric equal to characteristic wave period normalised by $\Delta t$
$N_{HCF}$	Highest common factor of front and rear blade numbers
$p$	Pressure
$p_F$	Sound field generated by $F_i$
$p_Q$	Sound field generated by $Q$
$p_T$	Sound field generated by $T_{ij}$
$Q$	A density-like acoustic source term
$Q_M$	Magnitude of acoustic monopole source strength fluctuation
$R$	Radius of integration surface
$r_i$	Radiation vector
$R_S$	Radius of analytical open rotor sources
$S$	The integration surface, defined by $f = 0$
$s$	Entropy
$s_{ij}$	Generic stress field in a realistic fluid
$t$	Time

$T_P$	Period of open rotor flow solution in rotating frame
$T_{ij}$	Lighthill's stress tensor
$u_i$	Fluid velocity
$v_i$	Absolute velocity of integration surface
$X_D$	Downstream integration surface limit
$X_G$	Axial gap between open rotor blade rows
$x_i$	Absolute frame position vector
$Y_i$	Acoustic monopole source location
$y_i$	Dummy integration variable representing source location
<b>Greek</b>	
$\alpha$	Generic mass density deficit between realistic and acoustic fluids
$\beta_{ij}$	Generic stress field deficit between realistic and acoustic fluids
$\Delta t$	Flow solution time step
$\delta$	Dirac delta function
$\delta_{ij}$	Kronecker delta
$\epsilon_\theta$	Maximum value of $\epsilon_{RMS}$ in a directivity sweep
$\epsilon_{RMS}$	RMS error of a prediction normalised by RMS of analytical solution
$\eta_i$	Body fixed source location
$\gamma$	Ratio of specific heats
$\gamma_i$	Generic mass flux/momentum density deficit between realistic and acoustic fluids
$\lambda_P$	Panel length scale equal to the square root of the average panel area
$\mu_i$	Generic mass flux/momentum density in an acoustic fluid

$\omega$	Angular frequency
$\Omega_F$	Front row rotational speed
$\Omega_R$	Rear row rotational speed
$\phi$	Generic wave variable
$\phi_F$	Wave variable calculated using the FW-H method
$\phi_K$	Wave variable calculated using the Kirchhoff method
$\phi_N$	Wave variable calculated using the new method
$\psi$	Arbitrary flow property
$\rho$	Mass density
$\tau$	Dummy integration variable representing source time
$\theta$	Observer directivity

### Notation

$(M, N)$	Tone equal to $M\Omega_F + N\Omega_R$
$\dot{\psi}$	Derivative of $\psi_i$ for a point convected with the integration surface
$\hat{\psi}_i$	Unit vector in same direction as $\psi_i$
$\bar{\psi}$	Discontinuous equivalent of $\psi$ .
$\psi$	When $\psi_i$ is a vector, the magnitude of $\psi_i$
$\psi'$	Perturbation of $\psi$
$\psi_0$	Bulk quantity of $\psi$
$\psi_\rho$	Value of generic source term $\psi$ when using a density analogy
$\psi_c$	Cosine component of $\psi$
$\psi_n$	Normal component of $\psi_i$
$\psi_p$	Value of generic source term $\psi$ when using a pressure analogy

$\psi_R$	Component of $\psi_i$ in radial direction
$\psi_r$	Component of $\psi_i$ in the radiation direction
$\psi_s$	Sine component of $\psi$
$\psi_X$	Component of $\psi_i$ in axial direction

**Abbreviations**

BPF	Blade passing frequency
CFD	Computational fluid dynamics
FFT	Fast Fourier transform
FW-H	Ffowcs Williams-Hawkings
LHS	Left hand side
LSSA	Least squares spectral analysis
RHS	Right hand side
RMS	Root mean squared



# Chapter 1

## Introduction

### 1.1 Context and Motivation

Commercial aviation is a huge global industry that is expected to double in size over the next twenty years [70]. This is despite many challenges faced by the industry, such as volatile oil prices and legislative pressure to make technology more environmentally friendly. For jet engine manufacturers, this ultimately translates into an increased need for quieter and more efficient engines.

The turbofan jet engine has dominated the large passenger aircraft market since the 1960s, with most of the rest of the market represented by turboprop engines. Extracting improved performance from these designs has become increasingly difficult. Hence jet engine manufacturers are looking to novel jet engine technologies to provide a step change in efficiency. A leading concept is the “open rotor” jet engine, which has the potential to combine the efficiency of a turboprop with the flight speed of a turbofan by replacing the fan and nacelle with a set of propellers in the external flow. This allows significantly higher bypass ratios than conventional turbofans and

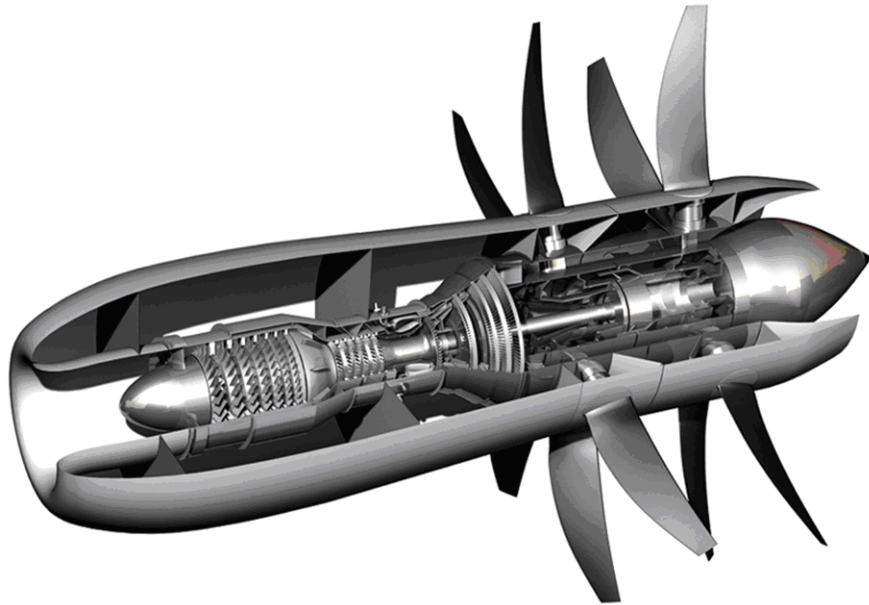


Figure 1.1: Rolls-Royce open rotor design concept from Zachariadis [87].

removes the nacelle drag, which both give significant efficiency improvements.

Early “single rotation” open rotor designs incorporated a single row of blades, leading to large amounts of energy being wasted in downstream swirl [69]. This led to “counter-rotating” designs, such as that illustrated in Figure 1.1, with two rows of counter-rotating blades [67]. The rear row recovers much of the swirl generated by the front row, giving a significant efficiency improvement. A rough comparison of the flight speed and associated installed propulsive efficiency for typical turboprop, turbofan and open rotor designs is given in Figure 1.2. It shows that open rotors have the potential to offer a 10-20% improvement in propulsive efficiency over a turbofan design, while being able to fly at Mach numbers around 0.8. This makes open rotors an extremely attractive technology.

Unfortunately, these benefits come at the cost of noise levels. Because the rotors

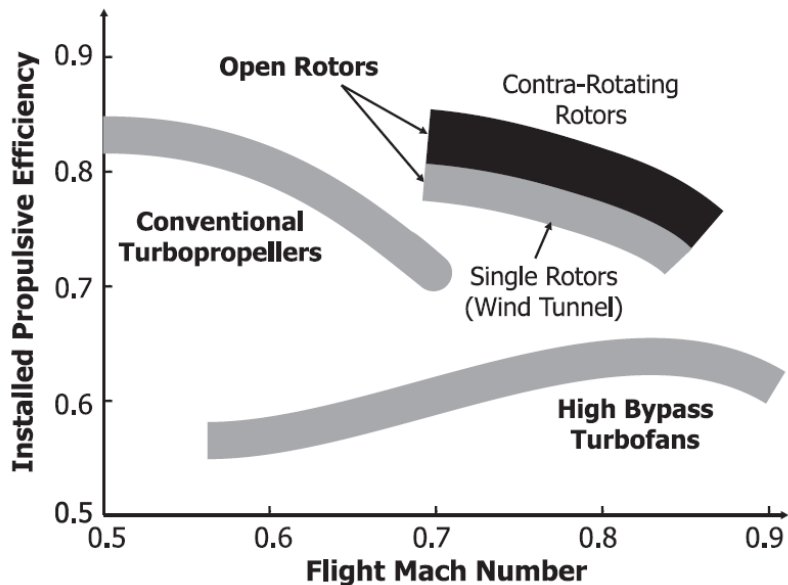


Figure 1.2: Comparison of turboprop, turbofan and open rotor efficiencies from Zachariadis [87].

are exposed to the external flow, rather than being enclosed by a nacelle, they are inherently noisier than modern turbofan designs. The presence of two rotating frames in a counter-rotating open rotor, plus the effect of any non-axisymmetric aspects of the problem such as nearby wings or pylons, means that the generated noise is highly tonal and extremely complex. This is confirmed by Figure 1.3, which shows a typical spectrum at a directivity in the plane of rotation of the open rotors. The accurate prediction of this noise field has proven extremely challenging.

Hence, a critical milestone in the development of open rotor jet engines is their design for low noise, and high fidelity methods for predicting open rotor noise are required. The term “high fidelity” is carefully chosen over “high accuracy”, and it is important to make this distinction clear in the context of the work presented in this thesis. The accuracy of a simulation can only be confirmed by comparing it

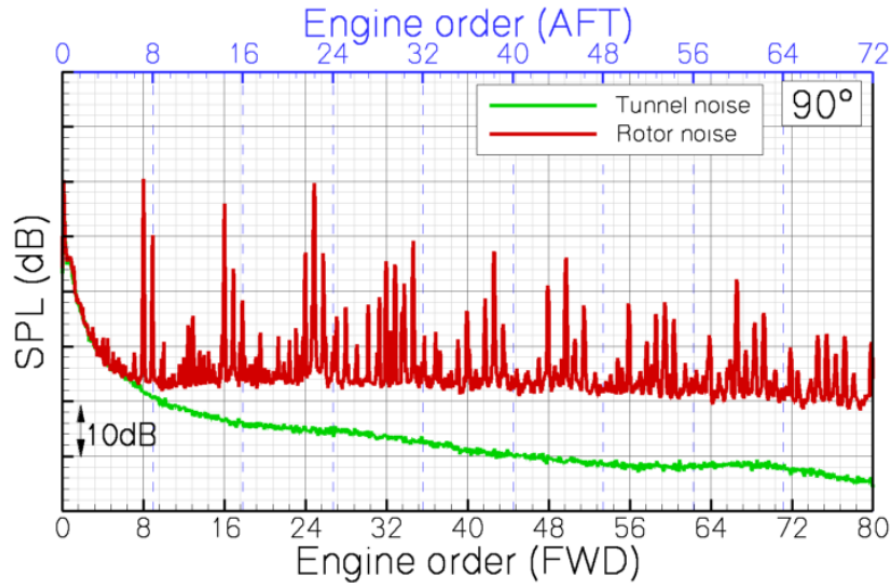


Figure 1.3: Frequency spectrum for a counter-rotating open rotor from Czech [20].

to other existing data, typically experimental. In order to take advantage of this accuracy without having to constantly validate with experimental data and hence defeating the point of simulation, an engineer must be confident that the method accurately represents the physics of the problem, rather than achieving its accuracy via empiricism or “tuning” by the engineer. In other words, a high fidelity method is a combination of high accuracy in the results and deep understanding of and trust in how those results are obtained.

While many methods are available to aeroacousticians, this thesis focuses on one set derived from the so-called Ffowcs Williams-Hawkings (FW-H) equation [84]. The FW-H equation is typically considered to represent the most realistic description of aerodynamic noise generation as it is derived directly from the Navier-Stokes equations without any further assumptions, and hence has the potential to provide extremely high fidelity methods. Methods based on the FW-H equation can be

broken down into five key components:

1. Aeroacoustic analogy - An inhomogeneous wave equation is derived that provides a definition of the source field.
2. Surface discontinuity - A surface discontinuity is introduced into the aeroacoustic analogy to allow for the presence of solid surfaces.
3. Formulation of solution - The wave equation is convolved with a Green function to give a set of integrals that calculate the noise at the observer.
4. Input flow solution - The near field flow solution is calculated using computational fluid dynamics (CFD) to determine the aeroacoustic source field.
5. Solver methodology - The formulation of solution is solved numerically for the given flow solution to calculate the noise at the observer.

As will be discussed in Chapter 2, an aeroacoustic analogy is a theoretically exact rearrangement of the Navier-Stokes equations and the formulation of solution provides a theoretically exact calculation of the external noise. Unfortunately, this theoretical exactness cannot be realised in practice, and the errors generated in a realistic prediction can be split into three types:

1. Discretisation errors - The formulation of solution must be calculated numerically, leading to errors in resolving the integrands.
2. Neglect errors - For practical reasons, the source field external to the surface is almost invariably neglected, meaning the results only account for part of the generated noise.

3. Input errors - A CFD flow solution has its own inaccuracies both due to the CFD itself such as turbulence modelling and complexities of the real flow that are not accounted for such as wind tunnel walls.

It will be shown that there is no clear understanding of the sources of discretisation error, nor a consensus on how best to mitigate them. Neglect errors have been researched in more depth, but current methods for mitigating them lack a clear physical basis. Input errors are the most widely researched of the three types of errors, i.e. they are taken most seriously. This thesis challenges this notion, and seeks to demonstrate that there is no point in spending large amounts of time perfecting a CFD methodology if the FW-H solver it is being coupled with has not been given the same level of attention.

Hence, the key motivation of this thesis is to improve the fidelity of open rotor noise prediction methods based on the FW-H equation by investigating ways of better understanding and mitigating both discretisation and neglect errors.

## 1.2 Research Objectives

This section outlines the specific objectives of the research and why they represent new contributions to the field of high fidelity open rotor noise prediction. The objectives are as follows:

1. Define the sources of discretisation error and the phenomena that affect them.
2. Use dimensional analysis to develop a standard process for isolating and quantifying discretisation errors.

3. Compare a range of solver methodologies and select the current best practice for open rotor noise prediction.
4. Develop new methods of defining aeroacoustic analogies that mitigate neglect errors in a physically meaningful way.
5. Demonstrate the above method improvements using a realistic open rotor test case.

As already discussed, discretisation errors have not been investigated in any real depth by previous research. Several different fundamental approaches have been developed for numerically solving the FW-H equation. It will be shown that these have rarely, if ever, been compared quantitatively. This motivates a full investigation of discretisation errors from basic principles. The sources of discretisation error need to be defined, dimensional analysis needs to be used to provide a process for quantitatively studying discretisation errors, and this process needs to be used to compare a range of solver methodologies in order to select a best practice methodology for use in open rotor noise prediction. It is important to acknowledge that the compared methodologies differed at a very fundamental level, and so only a basic comparison was necessary to demonstrate their relative strengths. Hence, more formal methods of comparison such as order of convergence have been left to future work. The process developed for comparison would remain the same, it would only be the depth of analysis of the differences which would change.

Neglect errors have been the subject of more recent research. Various alternatives to the standard FW-H equation have been examined, with some promising results [8, 59, 78]. Despite these promising results, the methods have struggled to provide a clear physical basis for what the alternatives represent, or how they relate

to the original FW-H equation. This motivates an investigation of new methods for mitigating neglect errors in the source terms of aeroacoustic analogies, with the key requirement that the source terms have a clear physical interpretation.

In undertaking the above work on both discretisation and neglect errors, analytical flow solutions are used to eliminate input errors and allow the other errors to be known precisely. This great strength of analytical flow solutions is also a weakness, as the lack of input errors results from the fact that the solutions are not fully realistic. Hence, it is important that the various method improvements developed in this thesis are also demonstrated on a realistic open rotor flow solution to confirm the significance of discretisation and neglect errors and to show that the method improvements succeed in mitigating them.

### 1.3 Thesis Structure

This section discusses how the thesis has been structured to meet the above objectives and place them into sufficient context. It consists of a literature review in Chapter 2, a description of the numerical methods used in Chapter 3, research pertaining to discretisation errors in Chapter 4, research pertaining to neglect errors in Chapter 5, a demonstration using a realistic open rotor solution in Chapter 6 and a summary of the key conclusions and future work in Chapter 7.

Relevant previous work is discussed in Chapter 2 to clarify the current state of the art and the shortcomings addressed by this thesis. An overview of the FW-H equation and its solution is provided with emphasis on available alternatives and any work relating to discretisation and neglect errors. As the end application is to open rotor noise prediction, an summary of open rotor aeroacoustics is given. Finally, the Rolls Royce Z-08 design is presented as a suitable realistic test case for

the work developed in this thesis.

In order to carry out the work presented in this thesis, a number of numerical codes were written to allow several different solver methodologies to be investigated. Chapter 3 discusses these different codes and presents verification that they work as expected.

Chapter 4 presents the work carried out to investigate and mitigate discretisation errors. The chapter begins with a simple classification of different types of discretisation error and demonstrates each using analytical flow solutions, satisfying the first objective of this thesis. It then applies dimensional analysis to develop a standard process for studying discretisation errors in FW-H solvers, satisfying the second objective of the thesis. Finally, it uses an analytical test case and the above process to compare several different solver methodologies and select a best practice methodology for open rotor noise prediction, hence meeting the third objective of the thesis.

Chapter 5 presents a generic aeroacoustic analogy and uses it to develop a new method of including a surface discontinuity. This new method allows neglection errors to be mitigated while retaining a clear, physical interpretation of what the source terms represent. The new method is compared in a novel fashion with the FW-H and Kirchhoff methods that further emphasises the new method's attractiveness. Finally, a semi-analytical flow solution is used to compare the results of the different methods in terms of their susceptibility to neglection errors. This meets the fourth objective of the thesis.

Chapter 6 presents initial results for the open rotor test case to confirm that they are plausible and hence that the test case is suitable for examining the above method improvements in the context of open rotors. Two short studies are presented that clearly demonstrate that the results of the above work using analytical solutions are

consistent with the realistic test case, confirming the importance of discretisation and neglect errors, the ability of the method improvements to mitigate them and the validity of the novel approaches used to develop these methods. This meets the final objective of the thesis.

Each chapter finishes with a summary of the key points raised by the work presented. These summaries are brought together in Chapter 7 to discuss the extent to which the objectives outlined above have been met, and to highlight important areas for future work.

# Chapter 2

## Literature Review

As discussed in the previous chapter, the fundamental aim of the work presented in this thesis is to understand and mitigate discretisation and neglect errors in FW-H solvers for open rotor noise prediction. Hence, this chapter reviews relevant previous work for both the FW-H equation and open rotor aeroacoustics. The previous chapter split the process for applying the FW-H equation to a realistic problem of interest into five components: an aeroacoustic analogy, a surface discontinuity, a formulation of solution, an input flow solution and a solver methodology.

The research presented in this thesis investigates each of the above components, and hence it is important to give a solid background for all of them. The aeroacoustic analogy derived by Lighthill [52] is the one used by the original FW-H equation and is often considered the foundation of modern aeroacoustics, though alternatives do exist. Section 2.1 gives a derivation of Lighthill's analogy concentrating on the key physical concepts involved as well as a discussion of alternative analogies that have been developed to help mitigate neglect errors.

The FW-H equation represents a method for introducing a surface discontinuity

into Lighthill’s analogy. As with Lighthill’s analogy, there are also alternatives to the FW-H method, most notably the method derived by Kirchhoff [29, 49]. Section 2.2 gives a derivation of the FW-H equation and discusses previous work in comparing it with the Kirchhoff equation. The importance of neglect errors is highlighted, and recent work to adjust the FW-H equation to mitigate this problem is summarised.

Various formulations of solution for solving the FW-H equation are discussed in Section 2.3. These formulations are split into two different types, with the so-called “collapsing sphere” type being discarded in favour of the “emission time” type for investigation in this thesis. In particular, the formulations of Farassat [25, 26] are presented as the industry standard formulations of solution, and his Formulation 1A is selected as the formulation of choice for this thesis.

A formulation of solution provides a set of integrals that need to be solved to calculate the noise at a given observer. Closed form solutions are not available for these integrals and hence they need to be discretised and integrated numerically. This process is described as a “solver methodology”. These solver methodologies are discussed in Section 2.4 and are categorised in terms of how the propagation from source to observer is represented, with the key benefits and limitations of each type discussed.

Section 2.5 presents the acoustic monopole as a useful analytical flow solution for FW-H solvers, outlines how the required flow properties are derived and discusses relevant previous work, showing that it is rare for their use in investigating an FW-H solver to be extended beyond simple verification of the solver. This lack of consensus on which solver methodology is best either in general or for a given problem of interest is highlighted as a key area of research in this thesis, in keeping with the objectives outlined in the previous chapter.

While most of the problems highlighted in the above sections apply to the FW-H

equation in general, this thesis is specifically aimed at their application to open rotors. As such, Section 2.6 discusses the main aerodynamic and aeroacoustic characteristics of open rotors, in order to ensure the work presented in this thesis remains relevant to this end goal. It also presents the Rolls Royce Z-08 design as a suitable realistic test case for demonstrating the work developed in this thesis, including a discussion of the associated CFD provided by Sohoni [76].

## 2.1 Aeroacoustic Analogies

As already discussed, Lighthill’s analogy [52] is usually considered the foundation of modern aeroacoustics. Before his work, the fields of acoustics and aerodynamics had remained relatively separate. Acousticians had understood how sound could propagate through air under the control of a linear wave equation when the perturbations were small, and aerodynamicists had derived the equations for conservation of mass and momentum that govern realistic fluids. It had been shown that these “realistic” equations reduced to the “acoustic” ones under certain assumptions, but what was not understood was how sound could be generated and propagated in regions of a flow where these assumptions were not valid. Lighthill’s analogy successfully answered this question, and hence allowed a fully realistic fluid to be discussed in terms of the acoustic idea of source and propagation.

This section will present a derivation of Lighthill’s analogy that focuses on the physical understanding of what it represents. A more exhaustive derivation, as well as an excellent summary of other aspects of early aeroacoustic research, is given by Goldstein [38]. It is also shown that Lighthill’s analogy is one of a family of “aeroacoustic analogies” that can be derived as a foundation for understanding noise generation in a realistic fluid. One important variation, as given by Morfey [58],

is highlighted as it provides an analogy directly for the pressure, rather than the density. The reasons for this being important are discussed, and are an important motivation for the work presented in Chapter 5.

Lighthill's analogy begins by acknowledging the equations for conservation of mass and momentum in both realistic and acoustic fluids. A realistic fluid is governed by the Navier-Stokes equations, as given below where  $\rho$  is the mass density,  $u_i$  the fluid velocity,  $p$  the pressure,  $e_{ij}$  the viscous stress tensor,  $\delta_{ij}$  the Kronecker delta,  $x_i$  the position and  $t$  the time. Note that gravitational effects are ignored and the Einstein convention for summation of tensors with repeated suffixes is used throughout this thesis. Also, a partial time derivative is assumed to hold the corresponding position constant and vice versa unless explicitly stated.

$$\frac{\partial}{\partial t}(\rho) + \frac{\partial}{\partial x_i}(\rho u_i) = 0 \quad (2.1)$$

$$\frac{\partial}{\partial t}(\rho u_i) + \frac{\partial}{\partial x_j}(p\delta_{ij} + e_{ij} + \rho u_i u_j) = 0 \quad (2.2)$$

An acoustic fluid can have the same mass conservation equation as Equation 2.1, but a different momentum conservation equation is required, as given below where  $c$  is a currently arbitrary constant.

$$\frac{\partial}{\partial t}(\rho u_i) + \frac{\partial}{\partial x_j}(c^2 \rho \delta_{ij}) = 0 \quad (2.3)$$

If the spatial derivative of Equation 2.3 is subtracted from the time derivative of Equation 2.1, a linear wave equation for  $c^2 \rho$  is obtained, as given below.

$$\left( \frac{1}{c^2} \frac{\partial^2}{\partial t^2} - \frac{\partial^2}{\partial x_i^2} \right) (c^2 \rho) = 0 \quad (2.4)$$

The arbitrary constant  $c$  is now clearly defined as the speed of sound in the acoustic fluid. Hence, a realistic fluid can be interpreted as an acoustic fluid if momentum conservation can be sufficiently approximated by Equation 2.3. Previous work had sought to understand the conditions under which this is the case. At this point, it is useful to begin splitting flow properties into their so-called “bulk” and “perturbation” quantities. The bulk component is the value taken by the fluid in its undisturbed state, and is denoted using a suffix 0 throughout this thesis. The perturbation component is the difference between the actual flow property and the bulk component, and is given a dash ( $'$ ). The relationship between actual, bulk and perturbation quantities for a generic flow variable  $\psi$  is given below. Note that bulk components are constant by definition.

$$\psi(x_i, t) = \psi_0 + \psi'(x_i, t) \quad (2.5)$$

It was known that sound (i.e. perturbations) could be incredibly small compared to their bulk quantities, and that these perturbations were capable of propagating great distances from the phenomena that created them, which implies that they propagate very efficiently and do not dissipate energy to the fluid. Hence, it makes physical sense that acoustic perturbations in a realistic fluid would be small and isentropic. By making these assumptions for a perturbation from the bulk condition, the well-known relationship between pressure and density perturbations, and the associated appropriate definition of  $c$  are obtained as given below, where  $\gamma$  is the ratio of specific heats and  $s$  is the entropy of the fluid.

$$\frac{p}{p_0} \Big|_s = \left( \frac{\rho}{\rho_0} \Big|_s \right)^\gamma \quad (2.6)$$

$$\frac{\partial p}{\partial \rho} \Big|_s = \frac{\gamma p}{\rho} \quad (2.7)$$

$$p' = c^2 \rho' \quad (2.8)$$

$$c = \sqrt{\frac{\gamma p_0}{\rho_0}} \quad (2.9)$$

By applying these assumptions to Equation 2.2,  $p$  can be replaced with  $c^2 \rho$  as per Equation 2.8 (it is inside a derivative and hence the bulk component does not matter),  $e_{ij}$  can be neglected as isentropy implies an inviscid flow, and the assumption of small perturbations means  $\rho u_i u_j$  is second order compared to the other terms and can also be neglected. This reduces Equation 2.2 to Equation 2.3, proving that a realistic flow can behave like an acoustic one provided the perturbations are small and isentropic.

This is an important result, as it defines how sound can propagate through a realistic fluid. However, it is only valid when non-linear effects are negligible and does not define how a realistic fluid can generate sound, or how sound propagates through a region of a flow that is non-linear. This is why Lighthill's analogy was so important. Instead of reducing Equation 2.2 to Equation 2.3 via assumptions, Lighthill rearranged it into the form below by moving any terms in the realistic equation that did not occur in the acoustic equation to the right hand side (RHS). Note that perturbation terms are used inside derivatives from now on.

$$\frac{\partial}{\partial t} (\rho u_i) + \frac{\partial}{\partial x_j} (c^2 \rho' \delta_{ij}) = \frac{\partial}{\partial x_j} ((c^2 \rho' - p') \delta_{ij} - e_{ij} - \rho u_i u_j) \quad (2.10)$$

The RHS of the above equation represents a stress field that is the difference between the acoustic and realistic fluids, and hence represents the “extra” stress that would have to be artificially applied to an acoustic fluid in order to make it behave like a realistic one. This is the key step that makes Lighthill’s analogy so powerful. Instead of neglecting the aspects of the realistic flow that cannot be sustained by the acoustic flow by making limiting assumptions, they are rephrased as a source term and kept in the equations. If the manipulation used to derive Equation 2.4 is applied using the above momentum equation instead, the below equation is obtained.

$$\left( \frac{1}{c^2} \frac{\partial^2}{\partial t^2} - \frac{\partial^2}{\partial x_i^2} \right) (c^2 \rho') = \frac{\partial^2}{\partial x_i \partial x_j} ((p' - c^2 \rho') \delta_{ij} + e_{ij} + \rho u_i u_j) \quad (2.11)$$

This is an inhomogeneous wave equation that is a direct rearrangement of the Navier-Stokes equations without any further assumptions being made. The source term on the RHS is typically referred to as “Lighthill’s stress tensor”, and is denoted  $T_{ij}$  as defined below.

$$T_{ij} = (p' - c^2 \rho') \delta_{ij} + e_{ij} + \rho u_i u_j \quad (2.12)$$

Because no further assumptions have been made, Equation 2.11 will be valid whenever the Navier-Stokes equations are valid. Hence, the equation allowed Lighthill to provide a basis for defining what aspects of a realistic flow can be considered sound sources as opposed to pure sound propagation.

It is important to understand that Equation 2.11 is not linear in general. The wave variable is  $c^2 \rho'$  and this is present in  $T_{ij}$ . However, it is clear from the discussion

following Equation 2.8 that  $T_{ij}$  vanishes for small, isentropic perturbations and hence the source field is restricted to a certain volume. Outside of the source field, Equation 2.8 is valid and hence  $c^2\rho'$  can be replaced with the more desirable  $p'$ . If the source field can be pre-calculated using CFD, then the equation is effectively linearised (as the source field is known without needing to know  $c^2\rho'$  everywhere) and can be solved using convolution with the appropriate Green function.

This is an incredibly powerful concept, as it paves the way for predicting the sound of highly complex flows without having to make any assumptions or simplifications to that flow. The resulting predictions can then be directly linked back to the flow phenomena causing them, offering excellent insight into how the sound was produced and ultimately how to mitigate it. It is this lack of assumption and the direct link to the underlying flow phenomena that make an aeroacoustic analogy such an attractive tool to aeroacousticians.

Unfortunately, this realism also leads to the analogy's biggest weakness in terms of using it to perform aeroacoustic calculations. The key problem is that the source field cannot be fully calculated in most, if not all, realistic problems of interest, and certainly in the case of open rotors. Non-linear flow phenomena such as wakes and vortices persist sufficiently far downstream that it is both computationally impractical and numerically infeasible to extend a mesh with enough resolution and accuracy to capture the entire source field. This inevitably means that at least some of the source field needs to be neglected, which in turn leads to the neglect errors identified as a key motivation for the work in this thesis.

While this effect cannot be entirely eliminated, there have been efforts to mitigate it. The key principle is to search for equivalent formulations of the source field that vary more stably depending on how much of the source field is included. For example, a source field that oscillates by 10% around the exact solution as the extent of the

source field is varied has less fidelity than a source field that oscillates by 1%. This will be discussed further in the next section, but at this point it is appropriate to acknowledge that there are alternatives to Lighthill's analogy that have been shown to mitigate neglect errors. In particular, it is not necessary to construct the inhomogeneous wave equation at the heart of the analogy with  $c^2\rho$  as the wave variable. As shown by Morfey [58], an alternative is to manipulate both the mass and momentum equations into the form given below.

$$\frac{\partial}{\partial t} \left( \frac{p'}{c^2} \right) + \frac{\partial}{\partial x_i} (\rho u_i) = \frac{\partial}{\partial t} \left( \frac{p'}{c^2} - \rho' \right) \quad (2.13)$$

$$\frac{\partial}{\partial t} (\rho u_i) + \frac{\partial}{\partial x_i} (p') = \frac{\partial}{\partial x_j} (-e_{ij} - \rho u_i u_j) \quad (2.14)$$

By applying the same manipulation to the above equations as to obtain Equation 2.11, the following equation is obtained.

$$\left( \frac{1}{c^2} \frac{\partial^2}{\partial t^2} - \frac{\partial^2}{\partial x_i^2} \right) (p') = \frac{\partial^2}{\partial t^2} \left( \frac{p'}{c^2} - \rho' \right) + \frac{\partial^2}{\partial x_i \partial x_j} (e_{ij} + \rho u_i u_j) \quad (2.15)$$

Comparing the above with Equation 2.11, it is clear that the wave variable has changed from  $c^2\rho'$  to  $p'$ , and that this has led to part of the stress source field in Lighthill's analogy being replaced with a density source field in Morfey's analogy. The reasons why this can be useful are discussed in the next section.

Other alternatives to Lighthill's analogy have been derived that make other flow properties the wave variable [39, 46, 54, 85], or allow the base flow from which perturbations are measured to not be stationary and uniform [40]. These are not relevant for the work presented in this thesis, and hence are not discussed further.

A second weakness of Lighthill's analogy is that it does not allow for the presence

of solid surfaces in the flow, which is clearly important for open rotor problems, and is typically required for most other problems of interest. This is where the FW-H equation (or, more properly, the method that extends Lighthill’s analogy to give the FW-H equation) comes in, and is the subject of the next section.

## 2.2 Surface Introduction

As discussed above, Lighthill’s aeroacoustic analogy provides a basis for defining how sound is generated and propagated in a fluid flow. What it lacks is an ability to handle solid surfaces in the flow, which almost invariably accompany any practical flow of interest, certainly in the case of open rotors. Lighthill’s analogy outlines an approach where the non-linear region of the flow is pre-calculated to determine a set of quadrupole sources that can be used to calculate  $c^2\rho'$  anywhere in the flow (and hence  $p'$  in the linear far-field). However, the effect of surfaces is to add additional sources into the flow, and hence Lighthill’s analogy needs to be extended to also allow these sources to be represented.

The FW-H equation [84] provides this extension by using generalised function theory [53] to derive the conservation equations for a new “discontinuous” flow that replaces the fluid within an arbitrary surface with fluid at the bulk condition while maintaining an identical external flow. The resulting surface sources required to maintain conservation represent the sound generated within the surface, and can be propagated analytically to any external observer using convolution with the appropriate Green function.

The original paper derives its equation under the assumption that the surface is coincident with a physical surface in the real flow. As acknowledged in the paper, this assumption is not necessary, and Ffowcs Williams later published a “permeable”

version of the equation in conjunction with other authors [19, 23]. The permeable version was also re-derived by di Francescantonio [22], who presented it as a hybrid of the FW-H equation with the Kirchhoff method (which is discussed later), however most agree that it should simply be called the permeable FW-H equation. The key advantage of the permeable version is it allows the surface to be placed to enclose as much of the source field as possible, rather than just the solid objects in the flow, mitigating the need for complex and costly volume integrals.

As will be discussed shortly, there have been numerous adaptations and extensions to the FW-H equation, as well as alternative methods that have many aspects in common with the FW-H equation. However, this section begins with a derivation of the permeable version of the original FW-H equation based on the derivation given by Brentner and Farassat [7] in order to give a firm grounding on the physical understanding of the method.

The only real difference in the derivation given here is a change in notation that this author finds more intuitive. In their paper, Brentner and Farassat distinguish between the original and discontinuous flows by defining differential operators as either “ordinary” or “generalised”. In addition to the fact that many mathematicians will find the use of the term “ordinary partial derivative” quite confusing, this author feels that it is not the differential operators that should be distinguished, but the flow properties they are operating on. “Ordinary differentiation” can be considered the same as the generalised equivalent but on a function with no generalised content, but the original flow is fundamentally different to the discontinuous one, and it is useful to understand when a flow property is from one or the other.

Hence, this thesis uses a bar above a variable (instead of the bar above a differential operator used by Brentner and Farassat) to denote that it refers to the discontinuous equivalent of the variable. This is consistent with notation used in

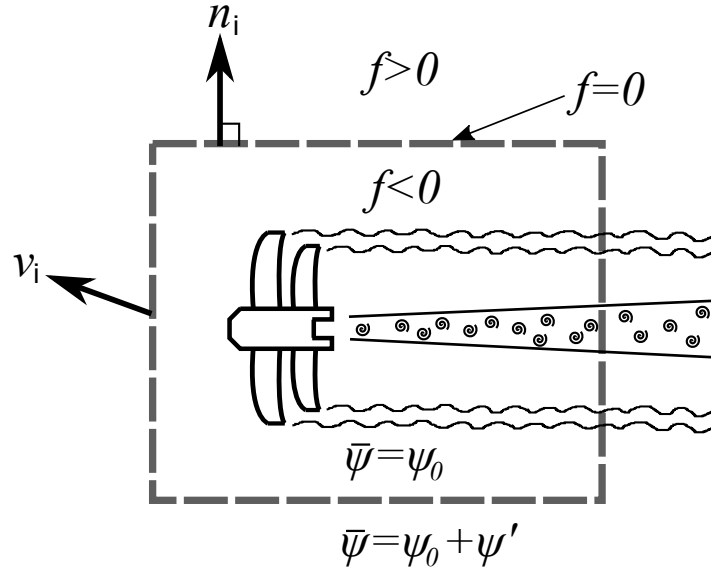


Figure 2.1: Illustration of FW-H surface discontinuity concept.

the original FW-H paper. By defining an arbitrary function,  $f(x_i, t)$ , that is zero on, negative inside, and positive outside the surface of interest, the continuous and discontinuous representations of any flow property,  $\psi$ , can be related using the below equation, where  $H(f)$  is the Heaviside step function operating on  $f$ , and hence equals zero inside the surface, and unity outside it. This concept is illustrated in Figure 2.1, which shows that any surfaces in the original flow (open rotor blades and hub in this thesis) can be enclosed by the arbitrary surface, as can as much of the flow as desired/possible.

$$\bar{\psi} = \psi_0 + \psi' H(f) \quad (2.16)$$

There is still a large amount of flexibility in the choice of  $f$ . It is convenient to assume that the gradient of  $f$  is equal to the unit outward normal of the surface,

which will be denoted  $n_i$ , though it should be noted that this does not change the final result, only avoids some slightly trickier manipulation during derivation. Some people find it helpful to imagine a specific function with this property, in which case the author suggests imagining  $f(x_i, t)$  to give the minimum distance to the surface of any point in space and time, with points inside the surface given a negative distance. Such a function would have all the desired properties described above.

At this point, it is useful to recognise two simple results from the differentiation of the surface function, given below. Note that the velocity of the surface at a given point is  $v_i$ , and its component in the direction of the outward surface normal is denoted by  $v_n$ , with this suffix being used to mean the same component of any vector in the rest of this thesis.

$$\frac{\partial f}{\partial t} = -v_n \quad (2.17)$$

$$\frac{\partial f}{\partial x_i} = n_i \quad (2.18)$$

These results allow time and space derivatives of a discontinuous flow property to be related to their continuous equivalents, as given in the equations below. Note that  $\delta(f)$  is the Dirac delta function representing a unit impulse on the surface boundary, which is distinct from the Kronecker delta,  $\delta_{ij}$ .

$$\frac{\partial \bar{\psi}}{\partial t} = \frac{\partial \psi'}{\partial t} H(f) - \psi' v_n \delta(f) \quad (2.19)$$

$$\frac{\partial \bar{\psi}}{\partial x_i} = \frac{\partial \psi'}{\partial x_i} H(f) + \psi' n_i \delta(f) \quad (2.20)$$

These two equations underline the fundamental concept behind using generalised derivatives in this derivation. The derivative of a discontinuous variable is shown to be constructed from two components, the first being the derivative of the original variable but restricted to the external flow, and the second representing the required discontinuous source strength on the surface to enforce the value of the underlying variable on the surface. In other words, the surface term replaces the variation of the variable inside the surface with a sudden introduction of the value on the surface, while the external volume term represents any further variation outside the surface.

If the LHS of Equation 2.1 (mass conservation) is written out with discontinuous flow variables, the above results can be used to expand these derivatives into continuous equivalents, as below.

$$\frac{\partial}{\partial t} (\bar{\rho}) + \frac{\partial}{\partial x_i} (\bar{\rho} u_i) = \left( \frac{\partial}{\partial t} (\rho) + \frac{\partial}{\partial x_i} (\rho u_i) \right) H(f) + (\rho u_n - \rho' v_n) \delta(f) \quad (2.21)$$

This equation has expressed conservation of mass in the discontinuous flow regime in terms of flow properties from its continuous counterpart, i.e. specifying a set of sources that are required to conserve mass in the discontinuous flow. As would be expected, the volume term is simply the continuous mass conservation equation restricted to the external volume, which is zero everywhere by definition and can be removed. This leaves a term on the surface that represents the mass that needs to be introduced into the external fluid at the surface in order to preserve conservation.

A similar approach for the momentum equation yields similar results, with the  $H(f)$  term being cancelled due to momentum conservation in the continuous flow, leaving a specification of the required momentum sources to sustain the external flow. The resulting mass and momentum equations, with the  $H(f)$  source terms

removed, are given below.

$$\frac{\partial}{\partial t} (\bar{\rho}) + \frac{\partial}{\partial x_i} (\bar{\rho} u_i) = (\rho u_n - \rho' v_n) \delta(f) \quad (2.22)$$

$$\frac{\partial}{\partial t} (\bar{\rho} u_i) + \frac{\partial}{\partial x_j} (\bar{p}_{ij} + \bar{\rho} u_i u_j) = (p'_{ij} n_j + \rho u_i (u_n - v_n)) \delta(f) \quad (2.23)$$

The terms on the RHS can be split into two groups. The  $\rho u_n$  and  $(p_{ij} n_j + \rho u_i u_n)$  terms represent the rates at which mass and momentum would be introduced into the surrounding fluid if the surface were stationary, while the  $-\rho' v_n$  and  $-\rho u_i v_n$  terms account for the rate at which mass and momentum are being “swallowed up” by the motion of the surface.

The FW-H equation is constructed from Equations 2.22 and 2.23 using the same manipulation used to get Equation 2.11. In order to simplify the notation, the source terms defined above are collated into a mass term,  $Q$ , and a momentum term,  $F_i$ .

$$Q = \rho u_n - \rho' v_n \quad (2.24)$$

$$F_i = p'_{ij} n_j + \rho u_i (u_n - v_n) \quad (2.25)$$

$$\left( \frac{1}{c^2} \frac{\partial^2}{\partial t^2} - \frac{\partial^2}{\partial x_i^2} \right) (c^2 \bar{\rho}') = \frac{\partial}{\partial t} (Q \delta(f)) - \frac{\partial}{\partial x_i} (F_i \delta(f)) + \frac{\partial^2}{\partial x_i \partial x_j} (T_{ij} H(f)) \quad (2.26)$$

Throughout the rest of this thesis, there will be references to both the “FW-H equation”, which is the equation above, and the “FW-H method”, which is the method by which Lighthill’s analogy is extended to include a surface discontinuity and give the above equation. In summary, this method is to derive the realistic

equations for conservation of mass and momentum for the discontinuous flow (i.e. the mass and momentum sources required on the surface discontinuity to satisfy conservation in the realistic fluid) and then perform the same reorganisation of terms that Lighthill used to obtain Equation 2.11.

Unsurprisingly, the rearrangement of the equations has led to the appearance of the same source term as Lighthill’s analogy, albeit for the discontinuous  $T'_{ij}H(f)$ . Instead of the internal half of the  $T_{ij}$  source field of Equation 2.11, the mass and momentum source terms have appeared as monopole and dipole distributions respectively. The power of this alternative formulation is that all source terms have now been limited to be either on or outside the surface. Any noise sources, non-linear propagation effects or solid surfaces occurring inside the surface have been replaced by an analogous set on the surface that preserves the external flow.

If the FW-H surface is placed sufficiently far from the underlying flow disturbance that all non-linearity is within the surface (i.e. the  $T_{ij}H(f)$  term can be neglected), then the entire source field is confined to the FW-H surface, the external  $c^2\rho'$  field is analogous to the pressure field, and it can be calculated using a convolved surface integral. As discussed in the previous section, it is rare that the entire source field can be captured by CFD, and hence the surface cannot be extended sufficiently to achieve the above ideal situation. This typically leads to the  $T_{ij}H(f)$  term being neglected entirely, as the surface should be extended as far as the CFD is trusted. This problem is often described as the effect of non-linear flow phenomena crossing the FW-H surface and generating “spurious” sound. This author does not like this description, as none of the source terms are spurious, it is the neglect of other terms that should accompany the surface terms that generates errors.

Many alternatives to the FW-H equation have been proposed, and much recent work has focused on trying to eliminate unstable density perturbations from the

source terms. This was noted as a key problem by Shur et al [74, 75], who found good improvements by replacing  $\rho'$  with  $p'/c^2$  as per Equation 2.8. However, this replacement is not justified in a physically meaningful way, as it is not made clear why it is appropriate to use a relationship to replace variables in an equation when that relationship is expressly not valid. After all, if the relationship were valid it would not be expected to make any difference to the final result.

A more mathematically robust approach was then developed by both Spalart and Shur [78] and Morfey and Wright [59]. In a similar manner to Lighthill's originally novel step of retaining terms as sources rather than neglecting/replacing them, both approaches rearranged the FW-H equation such that the surface terms were devoid of density perturbations, leading to extra terms being "assigned" to the external volume and neglected.

While these formulations are mathematically robust, i.e. neglected source terms are clearly identified and no extra assumptions are made, they are still not very physically intuitive, as the manipulations are rather complex and it is difficult to retain a clear physical understanding of what the resulting sources represent. Despite this, these formulations do appear to provide important improvements in stability and accuracy, as will be demonstrated in a moment.

A popular alternative to the FW-H equation is to use the approach developed by Kirchhoff [49], which was extended to allow surface motion by Morgans [61] and applied to aeroacoustics by Farassat and Myers [29]. The Kirchhoff equation is a general solution to the linear wave equation which, in a similar manner to the FW-H equation, allows effects within a surface to be replaced with an equivalent set of surface sources. The fundamental mathematics is very similar, but the surface discontinuity is applied directly to a linear wave equation rather than to the realistic mass and momentum conservation equations which underlie it. This approach is

summarised below for a generic wave variable  $\phi$ , which is typically taken to be  $p'$  in aeroacoustics, but any other wave variable can be specified.

$$\begin{aligned}
\frac{1}{c^2} \frac{\partial^2 \bar{\phi}}{\partial t^2} - \frac{\partial^2 \bar{\phi}}{\partial x_i^2} &= \frac{1}{c^2} \frac{\partial^2}{\partial t^2} (\phi H(f)) - \frac{\partial^2}{\partial x_i^2} (\phi H(f)) \\
&= \frac{1}{c^2} \frac{\partial}{\partial t} \left( \frac{\partial \phi}{\partial t} H(f) - \phi v_n \delta(f) \right) - \frac{\partial}{\partial x_i} \left( \frac{\partial \phi}{\partial x_i} H(f) + \phi n_i \delta(f) \right) \\
&= \left( \frac{1}{c^2} \frac{\partial^2 \phi}{\partial t^2} - \frac{\partial^2 \phi}{\partial x_i^2} \right) H(f) - \left( \frac{M_n}{c} \frac{\partial \phi}{\partial t} + \frac{\partial \phi}{\partial x_i} n_i \right) \delta(f) \\
&\quad - \frac{1}{c} \frac{\partial}{\partial t} (\phi M_n \delta(f)) - \frac{\partial}{\partial x_i} (\phi n_i \delta(f))
\end{aligned} \tag{2.27}$$

In the above equation, the external volume source field is the wave operator on the wave variable. As with the external source field in the FW-H equation, it is common for this term to be neglected. As a result, the Kirchhoff equation is often said to assume that the fluid is an acoustic fluid, and the FW-H equation is described as more “realistic”. This author does not like this description, as both equations are theoretically exact in a realistic fluid if all source terms are included. As with the variants of the FW-H equation discussed above, a better question is which formulation provides the best method of splitting the internal and external source fields such that neglect errors are mitigated as much as possible.

Probably the most widely referenced comparison of the FW-H and Kirchhoff methods for aeroacoustic applications is the work by Brentner and Farassat [8]. They attempt an analytical comparison of the two methods, but only really succeed in showing that they are equivalent if the surface encompasses the entire source field, i.e. the surface is entirely in the linear region of the flow and Equation 2.8 can be

assumed to be valid everywhere on and outside the surface, a situation that does not arise in realistic cases. They also argue that the key limitation of the Kirchhoff equation is that it assumes linearity, which has already been discussed above as being incorrect/misleading.

Despite this, they do show convincing results for a helicopter in hover that find that the integration surface can be placed much closer to the helicopter rotors when using the FW-H method to get convergence than when using the Kirchhoff method. Two key plots for these results are reproduced in Figures 2.2 and 2.3. They clearly show that the Kirchhoff method suffers from significant error when the surface is placed too close to the blade, whereas the FW-H method does not, i.e. it is more stable with surface placement.

This would appear to suggest that the FW-H method is a fundamentally more stable way of introducing a surface discontinuity into an aeroacoustic analogy than the Kirchhoff method. However, this is contradicted by results of the aforementioned work of Spalart and Shur [78]. Rather than a helicopter in hover, they used a stationary hot jet noise problem as their test case, and Figures 2.4 and 2.5 show the opposite effect when using surfaces of different radii. The traditional FW-H method gives entirely the wrong trend with directivity for all the surfaces considered, whereas the Kirchhoff method quickly moves towards correlation with the experimental data as the surface is expanded. Their adjusted FW-H method is even better, providing correlation of a similar quality to the Kirchhoff method even at the closest surfaces.

It is worth noting that these two pieces of work have applied the methods to two very different flow problems. Brentner and Farassat have applied the methods to a helicopter in hover calculated using a full potential flow solver, and hence the source field is steady in the rotating frame and there is no turbulence in the solution. The sound generated is entirely due to the motion of the source field relative to the

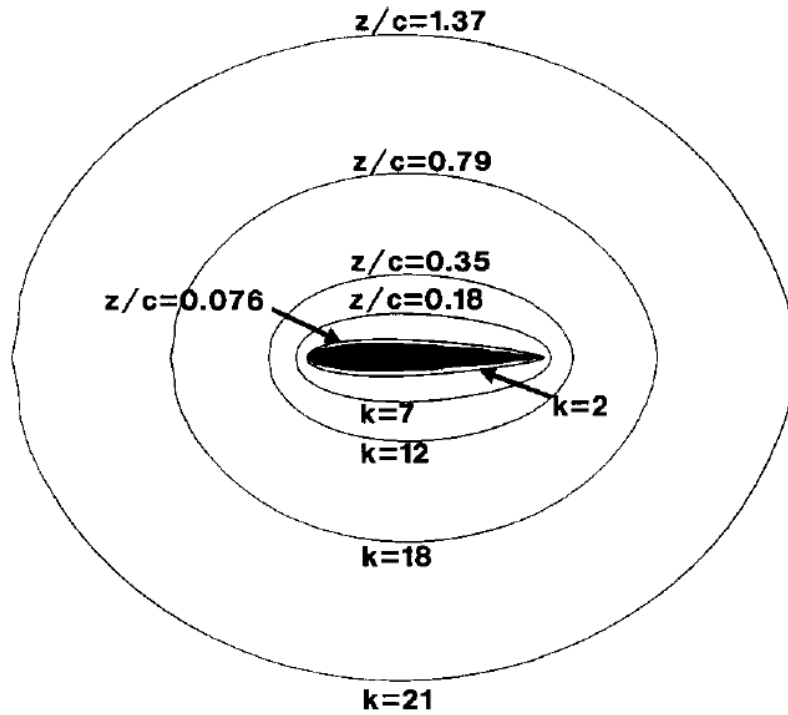


Figure 2.2: FW-H surface naming convention from Brentner and Farassat [8].

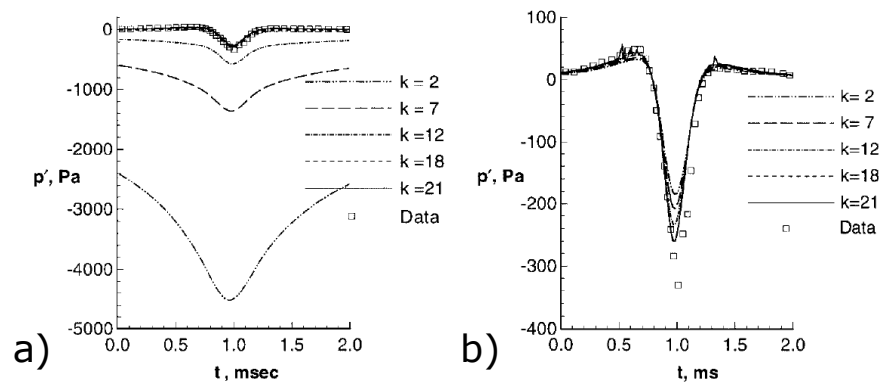


Figure 2.3: Noise results for a) Kirchhoff and b) FW-H methods from Brentner and Farassat [8].

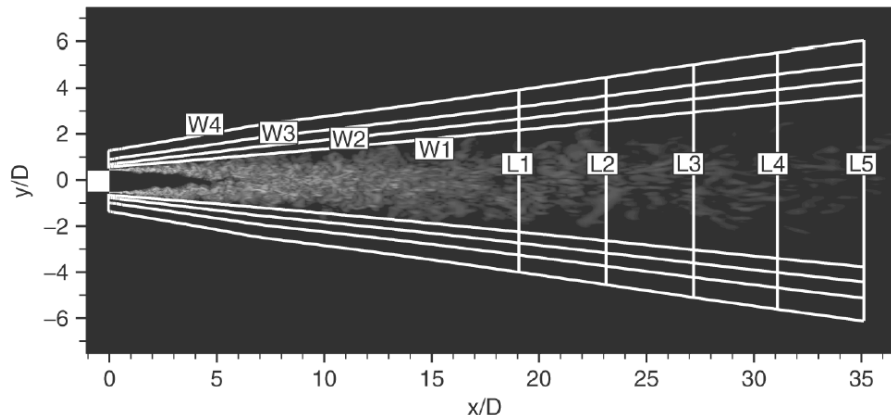


Figure 2.4: FW-H surface naming convention from Spalart and Shur [78].

stationary frame. In contrast, Spalart and Shur applied the methods to hot jet noise calculations using fully turbulent CFD. The sound generated is entirely due to the unsteady fluctuation of the flow properties on the surface. It is possible that the methods have different shortcomings that are exposed by these very different flow problems.

In summary, it has been shown that both the FW-H and Kirchhoff methods can have severe limitations for different flow problems. It appears that an FW-H method will converge to a result for smaller integration surfaces than the Kirchhoff method, but that the density fluctuations in the standard FW-H source terms can cause significant neglect errors and instability with surface placement for hot jets. What is lacking is a mathematically robust and physically intuitive method of mitigating neglect errors, as well as an equally clear understanding of the differences between this method and the FW-H and Kirchhoff methods. This is the motivation behind the work in Chapter 5, and is the fourth objective of this thesis.

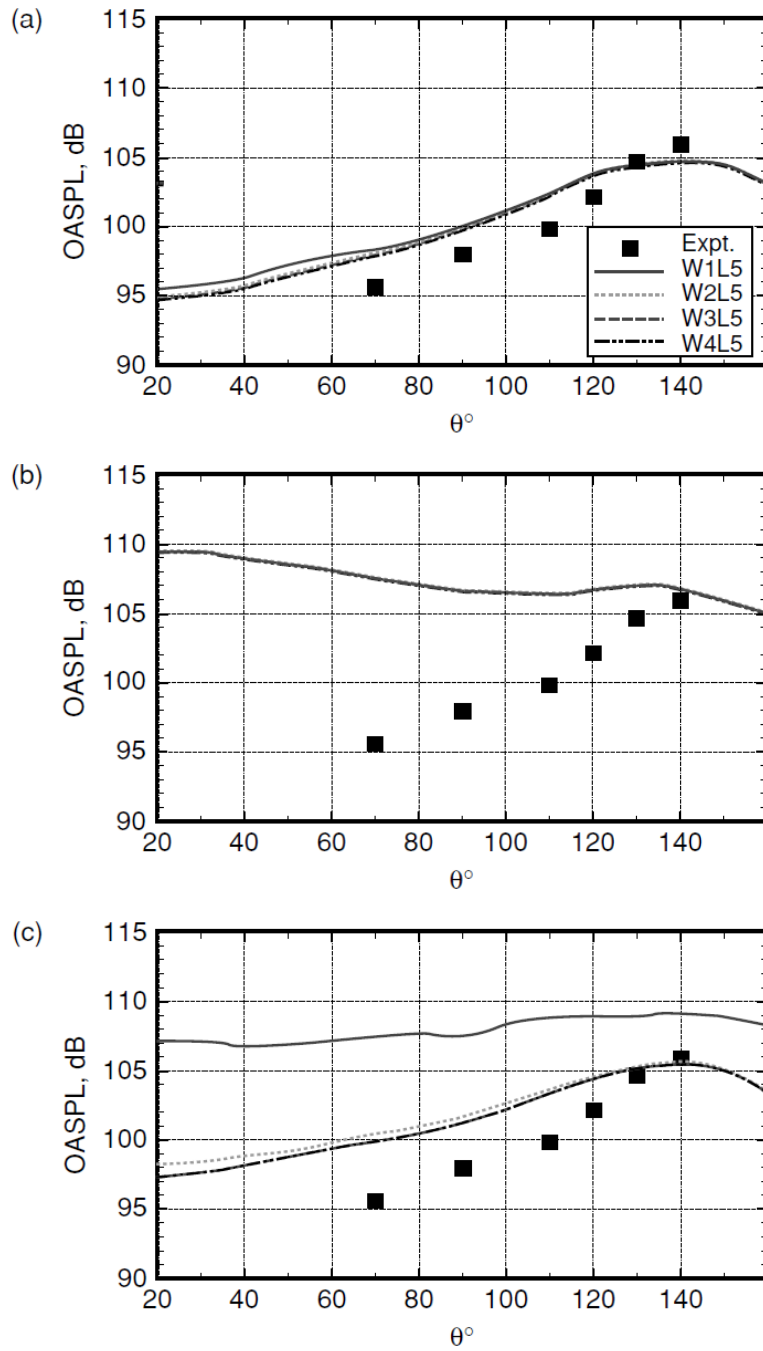


Figure 2.5: Noise results for a) adjusted FW-H b) traditional FW-H and c) Kirchhoff source terms from Spalart and Shur [78].

## 2.3 Formulations of Solution

Thus far, the governing FW-H equation has been derived and compared with alternative source field definitions. The next step is to discuss how solutions to these governing equations can be formulated such that they are suitable for numerical integration. By far the most popular formulations in use today are those given by Farassat [24]. All formulations begin from the same point, which is the fundamental convolution through space and time of the source field with the appropriate Green function. The variation comes from how the sifting of the various generalised functions and any derivatives of them are handled, with two basic types of formulations being discussed. The so-called “collapsing sphere” formulations are briefly discussed but discarded in favour of “emission time” formulations which are much easier to couple to CFD flow solutions. These emission time formulations are briefly derived in enough detail to understand their physical interpretation.

### 2.3.1 The Fundamental Convolution

In order to solve for the pressure at a particular observer outside the surface, all that is required is to integrate the contribution of the source field over its entire extent. The solution to this in free space is well known and documented [19], and will be briefly discussed here. It involves use of the free space Green function for the linear wave equation given below, where  $x$  is the magnitude of  $x_i$  (a convention used throughout this thesis for all vector terms) and  $g(x_i, t)$  is an important function that will be discussed in a moment.

$$g(x_i, t) = t - \frac{x}{c} \quad (2.28)$$

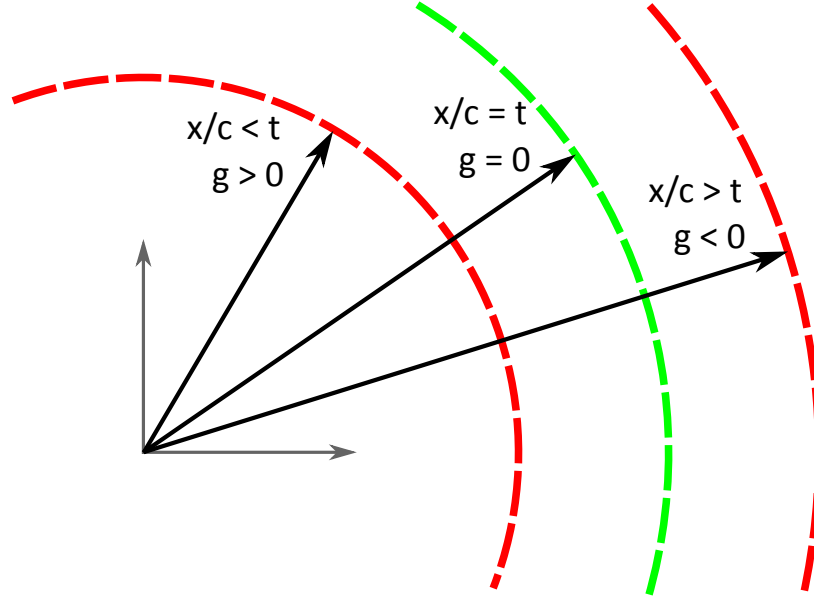


Figure 2.6: Illustration of sifting of  $\delta(g(x_i, t))$  term.

$$G(x_i, t) = \frac{\delta(g(x_i, t))}{4\pi x} \quad (2.29)$$

This Green function can be interpreted as the field that would result from a point impulse of unit magnitude at the origin. The  $\delta(g)$  sifts for points in time and space where the amount of time a wave would take to reach an observer from the origin,  $x/c$ , is equal to the actual time between source and observer,  $t$ , i.e.  $g(x_i, t) = 0$ . Times and locations that do not satisfy this condition represent points that either the wave has already passed through ( $g > 0$ ) or points that the wave has not got to yet ( $g < 0$ ). This is illustrated in Figure 2.6.

In performing the convolution, it is necessary to introduce ‘dummy’ integration variables to sum up the contribution from the entire source field. These variables can be physically interpreted as the time and location of the source point being

considered, which will be denoted  $\tau$  and  $y_i$  respectively. This distinction between source and observer times and locations can cause some confusion, and it becomes very important to keep track of which one a property is being evaluated at, what is being held constant in a given differentiation, and so on.

An important conceptual step, as explained by Farassat [26], is to introduce a set of co-ordinates which are fixed to the FW-H surface, denoted  $\eta_i$ , and to integrate through space using this co-ordinate system to represent volume elements. Note that all other vectors are still evaluated in the bulk stationary frame, they are just a function of  $\eta_i$  and  $\tau$  instead of  $y_i$  and  $\tau$ . These “body-fixed” co-ordinates allow a much simpler handling of terms involving  $f$ , although it is a slight abuse of notation (again see Farassat) to not rename functions like  $f$  when technically they are, from now on, different functions (i.e.  $f(\eta_i(x_i, t))$  instead of  $f(x_i, t)$ ).

The full solution to the FW-H equation as given in Equation 2.26 will be split into three components, based on the parts of the source field relating to  $Q\delta(f)$ ,  $F_i\delta(f)$  and  $T_{ij}H(f)$  respectively. For the sake of clarity, the governing equations for these components are written out below. Though the three components are denoted  $p'_Q$ ,  $p'_F$  and  $p'_T$ , it should be remembered that the solution is really for  $c^2\rho'$ , not  $p'$ .

$$\left(\frac{1}{c^2}\frac{\partial^2}{\partial t^2} - \frac{\partial^2}{\partial x_i^2}\right)p'_Q = \frac{\partial}{\partial t}(Q\delta(f)) \quad (2.30)$$

$$\left(\frac{1}{c^2}\frac{\partial^2}{\partial t^2} - \frac{\partial^2}{\partial x_i^2}\right)p'_F = -\frac{\partial}{\partial x_i}(F_i\delta(f)) \quad (2.31)$$

$$\left(\frac{1}{c^2}\frac{\partial^2}{\partial t^2} - \frac{\partial^2}{\partial x_i^2}\right)p'_T = \frac{\partial^2}{\partial x_i\partial x_j}(T_{ij}H(f)) \quad (2.32)$$

Writing out the convolutions in full for these terms leads to the integrals given

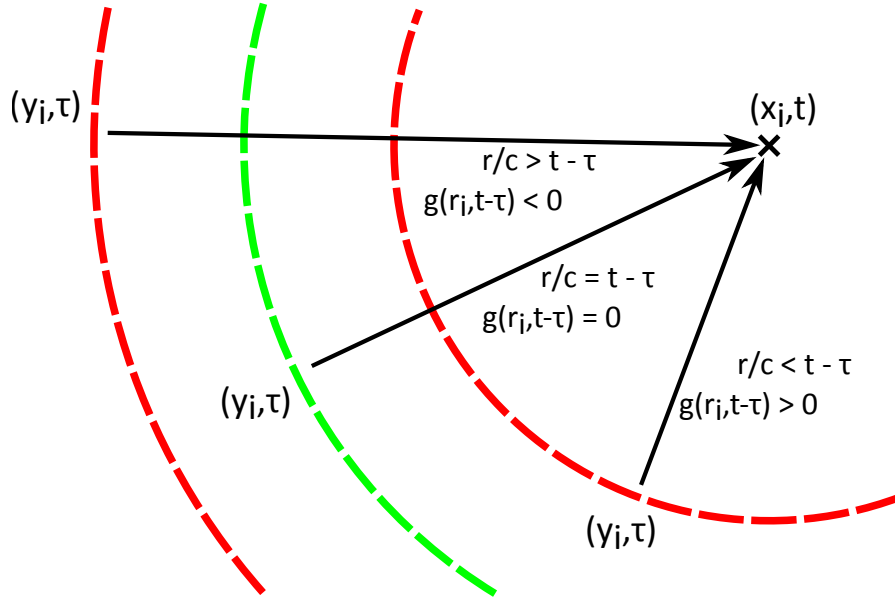


Figure 2.7: Illustration of sifting of  $\delta(g(r_i, t - \tau))$  term.

below, with the derivatives being kept outside of the integrals using standard convolution rules (i.e.  $L(A) * B = L(A * B)$  where  $L$  is a linear operator on two functions  $A$  and  $B$ ). Note that  $r_i = x_i - y_i$ , which is often referred to as the “radiation vector” as it represents the line a wave would travel along from the source to the observer. Also, care is taken to specify exactly what a property depends on, in particular to underline that flow properties are evaluated at the source, whereas derivatives are taken at the observer. The  $\delta(g(r_i, t - \tau))$  terms now sift through time and space for source points  $(y_i, \tau)$  at which a wave can be emitted to arrive at the desired observer time  $(x_i, t)$ , as illustrated in Figure 2.7.

$$p'_Q(x_i, t) = \frac{\partial}{\partial t} \bigg|_{x_i} \int_{-\infty}^t \int_{R^3} \frac{Q(\eta_i, \tau) \delta(f(\eta_i)) \delta(g(r_i, t - \tau))}{4\pi r} d\eta_i d\tau \quad (2.33)$$

$$p'_F(x_i, t) = - \left. \frac{\partial}{\partial x_i} \right|_t \int_{-\infty}^t \int_{R^3} \frac{F_i(\eta_i, \tau) \delta(f(\eta_i)) \delta(g(r_i, t - \tau))}{4\pi r} d\eta_i d\tau \quad (2.34)$$

$$p'_T(x_i, t) = \left. \frac{\partial^2}{\partial x_i \partial x_j} \right|_t \int_{-\infty}^t \int_{R^3} \frac{T'_{ij}(\eta_i, \tau) H(f(\eta_i)) \delta(g(r_i, t - \tau))}{4\pi r} d\eta_i d\tau \quad (2.35)$$

The approach for solving each of the above integrals is very similar, with the fundamental theory being given by Farassat [24]. The most important choice is in how the sifting of the generalised functions  $\delta(f)$ ,  $\delta(g)$  and  $H(f)$  are applied. This leads to two different types of formulation. For reasons discussed below, only the emission time type of formulation will be investigated in this thesis. Formulations of this type are almost invariably based on Farassat's "Formulation 1" and "Formulation 1A" [26], which differ only in how time derivatives of source fields are handled. Neither formulation includes a solution for  $p_T$ , but the mathematics is very similar and solutions for this term are also given from previous work, both by Dowling in Chapter 14 of Crighton et al [19] and by Farassat and Brentner [27].

### 2.3.2 Collapsing Sphere Formulations

The first type of formulation is typically referred to as the "collapsing sphere" type. If the source time is fixed, then the  $\delta(g)$  term sifts for points on a sphere of radius  $c(t - \tau)$  centred at the observer, as illustrated in Figure 2.7. The  $\delta(f)$  terms sift through this sphere for points on the intersection with the FW-H surface, leading to a formulation that is a line integral along this intersection which is then integrated through source time. The  $H(f)$  terms sift through the sphere for the part of the sphere that is outside the FW-H surface, leading to a formulation that is a surface integral over the external part of the sphere which is also integrated through source

time. Establishing the line and surface of intersection can require quite complicated interpolation and offers very few advantages over the alternative method which will be discussed in a moment.

Farassat and others have used these types of formulations to handle an FW-H surface that is moving supersonically [25, 31] which will be seen to be a weakness of the alternative formulation type discussed in a moment. However, such motion only arises in open rotor calculations if the surface is rotating with the rotors (as the forward motion of an open rotor is subsonic). As will be seen later in this thesis, avoiding a rotating surface is advantageous for a variety of other reasons as well. This makes collapsing sphere methods unattractive in general for the work in this thesis, and they are given no more consideration here. However, it is worth noting that much of the work presented in this thesis is just as applicable to assessing solvers based on a collapsing sphere formulation as any other FW-H solver.

### 2.3.3 Emission Time Formulations

The second type of formulation is described as the “emission time” formulation in this thesis. It is often referred to as the “retarded time” formulation, but this name is more strongly linked to a particular methodology used to solve the formulation, as discussed in a moment and for which there are alternatives. Emission time formulations use a change of integration variable from  $\tau$  to  $g$  which allows the sifting of the  $\delta(f)$  and  $\delta(g)$  terms to be applied differently such that they lead to integrals over the FW-H surface or the volume external to it, with the key task being to calculate the “emission time” at which a given source point is evaluated.

This technique is more attractive than the collapsing sphere method because the integrals performed can be over the panels and cells of the original CFD mesh,

avoiding the need for any complicated interpolation to establish the intersection with a sphere. It should be noted that any source point is evaluated at the same time and location in both types of formulation. The advantage of an emission time formulation is not the locus of source times and locations that are integrated, but the way in which it is discretised.

The vast majority of modern emission formulations are based on Farassat’s “Formulation 1” and “Formulation 1A” [5, 24, 30]. Formulation 1 requires the calculation of time derivatives at the observer, i.e. the integrals need to be evaluated several times to get the pressure at a particular point in space and time. This is computationally inefficient and this formulation was extended to bring any derivatives inside the integrals (which can be considered as shifting them from observer to source), leading to Formulation 1A. A good starting point for the derivation of the formulations is the lecture by Farassat [26], however it should be noted that the expressions derived in this lecture are for an impermeable surface. For a permeable FW-H surface derivation, most people refer to the work of di Francescantonio [22], though as already noted above the permeable version of the FW-H equation had already been suggested by Ffowcs Williams and Hawkings themselves [84], and derived by related future work [19, 23].

The mathematics for deriving the formulations is not overly lengthy, however it is very subtle, and none of the steps below are trivial to make. A very brief description of the derivations of the two formulations taken from the above referenced work will be given here, with the important conceptual steps explained.

The first step in the derivation is to replace the spatial derivative in the  $p_F$  convolution with some terms that are easier to handle. This is achieved by noticing that only  $\delta(g)$  and  $r$  depend on  $x_i$  in the convolution, and hence applying the spatial derivative leads to the expression below. Note that the dependency of variables has

been dropped for the sake of brevity and that a hat ( $\hat{\phantom{x}}$ ) over a vector denotes the unit vector in the same direction (although  $n_i$  is already a unit vector).

$$p'_F = - \int_{-\infty}^t \int_{R^3} \frac{F_i \delta(f)}{4\pi} \left( \frac{1}{r} \frac{\partial}{\partial x_i} \Big|_t (\delta(g)) - \frac{\hat{r}_i \delta(g)}{r^2} \right) d\eta_i d\tau \quad (2.36)$$

This does not appear overly helpful at first, however a useful identity, given below, allows the spatial derivative of  $\delta(g)$  to be replaced with an equivalent time derivative.

$$\frac{\partial}{\partial x_i} \Big|_t (\delta(g)) = \frac{-\hat{r}_i}{c} \frac{\partial}{\partial t} \Big|_{x_i} (\delta(g)) \quad (2.37)$$

Substituting this result into 2.36, and then moving the time derivative outside the integrals, leads to the new expression for  $p_F$  given below. Importantly, the validity of moving the observer time derivative outside the source time integration is more subtle than it may appear due to  $t$  being the upper limit of the integral (hence the “width” of the integral, as well as the magnitude of the function being integrated, varies with  $t$ ). As is well explained by Farassat [26], use of Leibniz’s rule for differentiation under an integral sign results in an extra term appearing, but this can be shown to be zero, meaning the time derivative can indeed be simply moved outside. Moving the time derivative outside the spatial integral is fine because the limits (which are infinite) are not a function of observer time. In addition, moving observer spatial derivatives in and out of the integrals, as performed above to derive Equation 2.36, is also fine because none of the limits depend on  $x_i$ .

$$p'_F = \frac{\partial}{\partial t} \int_{-\infty}^t \int_{R^3} \frac{F_i \hat{r}_i \delta(f) \delta(g)}{4\pi c r} d\eta_i d\tau + \int_{-\infty}^t \int_{R^3} \frac{F_i \hat{r}_i \delta(f) \delta(g)}{4\pi r^2} d\eta_i d\tau \quad (2.38)$$

Applying the sifting of the  $\delta(f)$  terms in the convolutions leads to the volume

integrals reducing to surface integrals. The new convolution integrals for  $p_Q$  and  $p_F$  are then as given below, where  $S$  symbolises the FW-H surface.

$$p'_Q = \frac{\partial}{\partial t} \Big|_{x_i} \int_{-\infty}^t \int_S \frac{Q\delta(g)}{4\pi r} dS d\tau \quad (2.39)$$

$$p'_F = \frac{\partial}{\partial t} \Big|_{x_i} \int_{-\infty}^t \int_S \frac{F_i \hat{r}_i \delta(g)}{4\pi cr} dS d\tau + \int_{-\infty}^t \int_S \frac{F_i \hat{r}_i \delta(g)}{4\pi r^2} dS d\tau \quad (2.40)$$

In order to derive Formulation 1, all that is left to do is apply the sifting of the  $\delta(g)$  term. This involves swapping the order of integration and then using the following relationship to change the inner integration variable from  $\tau$  to  $g$ . Because this change occurs inside the surface integral, it is for a fixed  $\eta_i$  as well as for a fixed  $x_i$  and  $t$ , which are still independent of  $\tau$  and  $g$  as no sifting of these variables has been applied, and they are therefore still dummy variables. Note that  $M_i$  is the Mach number of the surface velocity and  $M_r$  is the component in the direction of  $r_i$ , known as the radiation Mach number.

$$d\tau = \frac{\partial \tau}{\partial g} \Big|_{\eta_i, x_i, t} dg \quad (2.41)$$

$$= \frac{1}{1 - M_r} dg \quad (2.42)$$

This expression can be substituted into the convolutions, and the  $\delta(g)$  sifting applied to give Formulation 1 as below.

$$p'_Q = \frac{\partial}{\partial t} \Big|_{x_i} \int_S \left[ \frac{Q}{4\pi r(1 - M_r)} \right]_{g=0} dS \quad (2.43)$$

$$p'_F = \frac{\partial}{\partial t} \Big|_{x_i} \int_S \left[ \frac{F_i \hat{r}_i}{4\pi c r(1 - M_r)} \right]_{g=0} dS + \int_S \left[ \frac{F_i \hat{r}_i}{4\pi r^2(1 - M_r)} \right]_{g=0} dS \quad (2.44)$$

The corresponding solution for the  $p_T$  term is derived using a very similar approach for handling the spatial derivatives as for the  $p_F$  contribution, the only difference being that there is an additional derivative to handle. An equation similar to Equation 2.37 can be derived as below.

$$\begin{aligned} \frac{\partial^2}{\partial x_i \partial x_j} \Big|_t \left( \frac{\delta(g)}{r} \right) &= \frac{3\hat{r}_i \hat{r}_j - \delta_{ij}}{r^3} \delta(g) + \frac{\partial}{\partial t} \Big|_{x_i} \left( \frac{3\hat{r}_i \hat{r}_j - \delta_{ij}}{c r^2} \delta(g) \right) \\ &+ \frac{\partial^2}{\partial t^2} \Big|_{x_i} \left( \frac{\hat{r}_i \hat{r}_j}{c^2 r} \delta(g) \right) \end{aligned} \quad (2.45)$$

This can be used to rewrite the the  $p_T$  contribution defined in Equation 2.35 as follows, where  $T'_{ij} \hat{r}_i \hat{r}_j = T'_{rr}$  and  $T'_{ij} \delta_{ij} = T'_{ii}$ .

$$\begin{aligned}
p'_T(x_i, t) &= \int_{-\infty}^t \int_{R^3} \frac{(3T'_{rr} - T'_{ii})H(f)\delta(g)}{4\pi r^3} d\eta_i d\tau \\
&+ \frac{\partial}{\partial t} \Big|_{x_i} \int_{-\infty}^t \int_{R^3} \frac{(3T'_{rr} - T'_{ii})H(f)\delta(g)}{4\pi cr^2} d\eta_i d\tau \\
&+ \frac{\partial^2}{\partial t^2} \Big|_{x_i} \int_{-\infty}^t \int_{R^3} \frac{T'_{rr}H(f)\delta(g)}{4\pi c^2 r} d\eta_i d\tau
\end{aligned} \tag{2.46}$$

The  $H(f)$  term sifts for an integral over the volume external to the FW-H surface, and the  $\delta(g)$  sifting can be handled as for the  $p_Q$  and  $p_F$  terms to give the solution below.

$$\begin{aligned}
p'_T(x_i, t) &= \int_{f>0} \left[ \frac{(3T'_{rr} - T'_{ii})}{4\pi r^3(1 - M_r)} \right]_{g=0} d\eta_i + \frac{\partial}{\partial t} \Big|_{x_i} \int_{f>0} \left[ \frac{(3T'_{rr} - T'_{ii})}{4\pi cr^2(1 - M_r)} \right]_{g=0} d\eta_i \\
&+ \frac{\partial^2}{\partial t^2} \Big|_{x_i} \int_{f>0} \left[ \frac{T'_{rr}}{4\pi c^2 r(1 - M_r)} \right]_{g=0} d\eta_i
\end{aligned} \tag{2.47}$$

Several of the integrals in Equations 2.43, 2.44 and 2.47 need to be differentiated with respect to observer time for a fixed  $x_i$ , i.e. for a point that is stationary relative to the bulk fluid. For an observer that moves with the FW-H surface (e.g. wind tunnel microphones and passengers on a plane), this means that the time history at that observer cannot be numerically differentiated for the required result, as that time history is for a moving point, not a fixed one. This means extra integrals for other points have to be calculated in order to evaluate the formulation, which signifi-

cantly slows down computation time. This is the key motivation behind Formulation 1A, which uses a simple relationship to replace the differentiation of the integral with respect to observer time with an equivalent differentiation of the integrand with respect to source time. Because this source time differentiation is for a point convected on the surface, the derivatives can be easily taken from the given CFD time history, making this a much more computationally efficient formulation.

The key step in achieving this is to notice that the source time in the integrands of Equations 2.43 and 2.44 is linked to the observer time via the  $g = 0$  condition, i.e. if the observer time is varied, the source time at a particular point on the surface must vary accordingly to maintain  $g = 0$ . Furthermore, there is no direct dependence of the integrands on the observer time (only on observer position via  $r_i$ ), and so a simple chain rule can be used to convert the observer time derivative to a source time derivative. Note that, as with Equation 2.42, being inside the surface integral implies being at a fixed  $\eta_i$ , meaning that moving a derivative from outside of the integral to inside implies holding this constant in addition to anything else, leading to source time derivatives for the point convected with the surface. This process is summarised below using a generic function  $\psi$  which could represent either integrand, and the notation for the convective source time derivative will be simplified using a dot ( $\dot{\cdot}$ ) over a variable.

$$\begin{aligned} \frac{\partial}{\partial t} \Big|_{x_i} \int_S [\psi(x_i, \eta_i, \tau)]_{g=0} dS &= \int_S \frac{\partial \tau}{\partial t} \Big|_{x_i, \eta_i, g=0} \frac{\partial \psi}{\partial \tau} \Big|_{x_i, \eta_i, g=0} dS \\ &= \int_S \left[ \frac{\dot{\psi}}{1 - M_r} \right]_{g=0} dS \end{aligned} \quad (2.48)$$

Using the above equation to substitute into Formulation 1, the source time derivatives of kinematic properties can be taken analytically by noting that  $\dot{r}_i = -v_i$ . After some rearrangement, the following version of Formulation 1A for a permeable FW-H surface is found. Note that a kinematic property,  $K_M$ , is defined for ease of notation.

$$K_M = \dot{M}_i r_i + c (M_r - M^2) \quad (2.49)$$

$$p_Q = \frac{1}{4\pi} \int_S \left[ \frac{\dot{Q}}{r(1 - M_r)^2} + \frac{Q K_M}{r^2(1 - M_r)^3} \right]_{g=0} dS \quad (2.50)$$

$$p_F = \frac{1}{4\pi} \int_S \left[ \frac{\dot{F}_i \hat{r}_i}{cr(1 - M_r)^2} + \frac{F_i (\hat{r}_i - M_i)}{r^2(1 - M_r)^2} + \frac{F_i \hat{r}_i K_M}{cr^2(1 - M_r)^3} \right]_{g=0} dS \quad (2.51)$$

A corresponding expression for  $p_T$  has also been derived by Brentner [6], but is rather lengthy and unused in this thesis, and hence is not given here. The Formulation 1A method is by far the most popular method in use in modern research, and hence is the one investigated in this thesis. As already discussed for collapsing sphere methods, much of the work presented in this thesis around validating and assessing different solvers is just as applicable to Formulation 1 methods and other approaches, which is an area for potential future work.

## 2.4 Solver Methodologies

The formulation of solution that will be used in this thesis is defined by Equations 2.50 and 2.51. This section will discuss how this formulation can be solved, i.e. the solver methodologies that can be implemented to numerically integrate the formu-

lation. Three basic types of solver methodology are presented, which differ in how the  $g = 0$  condition is handled, i.e. how the propagation from source to observer is represented. This is referred to as the “propagation algorithm” for the solver methodology.

### 2.4.1 Observer Dominant Methodologies

As already discussed, emission time formulations are often referred to as “retarded time” formulations. This name really refers to a particular type of propagation algorithm for these formulations. In addition, this author prefers the term “observer dominant” to “retarded time”, as it more directly describes the difference between this type of algorithm and those that will be discussed in a moment. The key characteristic of an observer dominant methodology is how it represents the propagation from source to observer, i.e. applies the  $g = 0$  condition in evaluating the integrals. Observer dominant methodologies were the standard methodology for emission time formulations until Casalino presented his “source dominant” or “advanced time” methodology which will be discussed in the next section [12].

Each of the integrals in Equations 2.50 and 2.51 has an integrand that must be evaluated such that  $g = 0$ , i.e. the source and observer times are consistent with a wave being emitted by the source at the source time and received by the observer at the observer time. If the observer time is fixed, then the relevant emission time for each point on the surface needs to be calculated, the corresponding integrands can then be constructed, and a surface integral performed to calculate the noise at the observer at the given time. The fact that it is the observer time that is fixed and the corresponding source time calculated to account for propagation is the reason for describing the methodology as “observer dominant”.

How the emission time is calculated depends on the motion of the surface. Inspecting Equation 2.28, it is clear that the  $g(r_i, t - \tau) = 0$  condition corresponds to the following requirement.

$$t - \tau - \frac{r(x_i, \eta_i, \tau)}{c} = 0 \quad (2.52)$$

The dependence of  $r$  on  $\tau$  means that there is no general closed form solution to the above equation for  $\tau$ . However, there are some special cases which are relevant to this thesis, and are discussed in more detail in Chapter 3. For a stationary surface,  $r$  does not depend on  $\tau$  and the emission time is trivially calculated as  $\tau = t - r/c$ . For a surface with a constant velocity, the Garrick triangle [28] provides a slightly more complicated but still exact solution. The other type of motion investigated in this thesis is helicoidal, i.e. a constant forward velocity plus a rotation. Unfortunately, there is no known closed form solution for rotating source motion, and hence such surfaces require an iterative solution to the above equation.

As will be discussed in Chapter 3, this iterative solution is significantly slower than the closed form solutions, meaning that avoiding the need for it is very advantageous in terms of computational speed. If the surface is axisymmetric, then it can be interpolated onto a non-rotating surface, allowing a closed form solution to be used. An alternative is to change the propagation algorithm, as discussed below.

### 2.4.2 Source Dominant Methodologies

In observer dominant methodologies, the observer time and location are fixed, and then the emission time of each panel on the FW-H surface is calculated. The flow properties are interpolated from the times known in the CFD solution, and the relevant surface integral applied.

Using an observer dominant algorithm has two important consequences in the context of open rotors. Firstly, it is the motion of the source which has to be accounted for in evaluating the correct source time. As discussed above, this can introduce significant computational cost if the surface is rotating, due to the need to use an iterative solution for the retarded time. Secondly, different points on the integration surface will need to be evaluated at different source times, and hence require use of different time steps from the original CFD solution. This can lead to significant memory usage due to needing to hold large amounts of the flow solution in memory at one time [37].

A useful alteration to the standard observer dominant algorithm was proposed by Casalino [12] that helps to alleviate these two issues. Instead of fixing observer time and finding the appropriate source time, Casalino fixed the source time and then calculated the appropriate observer time. Casalino refers to this as an “advanced time” algorithm as opposed to the retarded time algorithm, but this author prefers the term “source dominant”.

In such an algorithm, it is the observer’s motion that needs to be accounted for in calculating propagation time. Because this is rarely a rotating motion (most observers are either stationary on the ground or a passenger/wind tunnel microphone flying with the open rotor) the analytical solution for rectilinear motion can be used instead, which can make a source dominant methodology much faster than an observer dominant one if the surface rotates.

Also, because each timestep of the underlying CFD is handled independently, only one timestep (or a few depending on how time derivatives are handled) needs to be kept in memory at a time, which gives a significant memory saving over observer dominant algorithms if the code implementing the solver is written to take advantage of it [37].

Another consequence of switching to a source dominant algorithm is that different advanced times are calculated at the observer for each panel, and hence interpolation is required to find a common time history for the surface as a whole. This essentially swaps interpolation through the source flow history in an observer dominant algorithm for interpolation through the calculated panel pressure signal in a source dominant algorithm. Whether there is any notable penalty or advantage in doing so in terms of discretisation error will be investigated by this thesis in Chapter 4.

### 2.4.3 Frequency Domain Methodologies

Both observer and source dominant methodologies propagate effects from source to observer in the time domain. However, it is possible to perform this propagation in the frequency domain, as shown by Shur et al [75]. A brief overview of the derivation and its implications will be given here.

In their paper, Shur et al make a far field approximation, however it is reasonably trivial to extend the derivation to include all terms contributing to  $p_Q$  and  $p_F$ . This will be done here using Formulation 1A as given in Equations 2.50 and 2.51 as an example, but the same method can be used to find frequency domain formulations for any emission time formulation, provided the restrictions on source and observer motion applied below are met.

Also, Shur et al assume the frequency content is given as a Fourier transform. A significant aspect of the work presented in this thesis will revolve around the fact that this is often not a good way to characterise the frequency content of a counter-rotating open rotor and that a more flexible set of frequencies can be useful (see Chapter 3). Hence, this limitation will not be made here, however this only demands a slightly more general (and unfortunately less concise) notation to that used by Shur et al,

there is no new mathematics. It will be assumed that the source time history of any flow property at a given point on the FW-H surface,  $\psi(\eta_i, \tau)$ , has been broken down into cosine and sine components for  $N_\omega$  frequencies, as described below, with the constant component denoted  $\psi_{\omega=0}(\eta_i)$ . The cosine and sine components for a given frequency  $\omega_k$  are denoted  $\psi_c$  and  $\psi_s$  respectively.

$$\psi(\eta_i, \tau) = \psi_{\omega=0}(\eta_i) + \sum_{k=1}^{N_\omega} (\psi_c(\eta_i, \omega_k) \cos(\omega_k \tau) + \psi_s(\eta_i, \omega_k) \sin(\omega_k \tau)) \quad (2.53)$$

If the observer moves coincidentally with the FW-H surface at a constant velocity (this assumption is only true for non-rotating surfaces with “fly-along” observers), then the propagation time, and hence the radiation vector are constant. This means that the cosine and sine components of  $p_Q$  and  $p_F$  for a given frequency are only a function of the corresponding components of  $Q$ ,  $\dot{Q}$ ,  $F_i$  and  $\dot{F}_i$ , with a phase shift of  $\alpha_k = -\omega_k(t - \tau)$  applied for each frequency. This leads to the equations below for a frequency domain implementation of Farassat’s Formulation 1A with  $K_Q$ , etc. being defined and the dependency of each variable left out for ease of notation.

$$K_Q = \frac{K_M}{r^2(1 - M_r)^3} \quad (2.54)$$

$$K_{\dot{Q}} = \frac{1}{r(1 - M_r)^2} \quad (2.55)$$

$$K_{F,i} = \frac{\hat{r}_i - M_i}{r^2(1 - M_r)^2} + \frac{\hat{r}_i K_M}{cr^2(1 - M_r)^3} \quad (2.56)$$

$$K_{\dot{F},i} = \frac{\hat{r}_i}{cr(1 - M_r)^2} \quad (2.57)$$

$$\begin{pmatrix} p_{Q,c} \\ p_{Q,s} \end{pmatrix}_k = \int_S \left[ \begin{pmatrix} \cos\alpha_k & -\sin\alpha_k \\ \sin\alpha_k & \cos\alpha_k \end{pmatrix} \begin{pmatrix} \dot{Q}_c & Q_c \\ \dot{Q}_s & Q_s \end{pmatrix} \begin{pmatrix} K_{\dot{Q}} \\ K_Q \end{pmatrix} \right]_{g=0} dS \quad (2.58)$$

$$\begin{pmatrix} p_{F,c} \\ p_{F,s} \end{pmatrix}_k = \int_S \left[ \begin{pmatrix} \cos\alpha_k & -\sin\alpha_k \\ \sin\alpha_k & \cos\alpha_k \end{pmatrix} \begin{pmatrix} \dot{F}_{c,i} & F_{c,i} \\ \dot{F}_{s,i} & F_{s,i} \end{pmatrix} \begin{pmatrix} K_{\dot{F},i} \\ K_{F,i} \end{pmatrix} \right]_{g=0} dS \quad (2.59)$$

The first matrix on the RHS of each of the above equations applies the required phase shift, while the second and third matrices assemble the cosine and sine components based on the source time from the underlying components of  $Q$  and  $F_i$ . Remember that a repeated  $i$  suffix in any product implies a summation.

It should also be reiterated that the equations are fundamentally the same as those given by Shur et al, the only distinctions being that this author has used explicit sine and cosine components, rather than expressing magnitude and phase using  $e^{i\omega t}$ , and that no far-field assumption has been made.

Other work on frequency domain FW-H solvers appears to be quite sparse and immature compared to the extensive use of time domain methods. Farassat and Casper [28] have recently derived their so-called Formulation 2B which is intended for broadband turbulence noise prediction. The development of the formulation appears to be in its early stages, with no numerical results given in the paper, but the formulation's apparent ability to derive a velocity potential is certainly interesting.

Sharma and Chen [72] have applied Shur et al's work to open rotor tonal noise prediction, as will be done in this thesis. Their results were based on a flow solution derived using steady RANS calculations for rotor alone tones and a linearised frequency domain method for extracting interaction frequencies in the blade gap, whereas this thesis will use unsteady RANS calculations. Differences between these two approaches would be an investigation into input errors, and as already discussed

these are outside the scope of this thesis.

Also, Tang et al [81] appear to have duplicated the derivation of Shur et al with the extension of deriving a frequency domain formulation for  $p_T$ , although it does not appear to be used in the paper. The  $p_Q$  and  $p_F$  terms are then validated against some basic analytical solutions.

Another frequency domain approach has been developed by Gennaretti et al [35]. This implementation allows for rotating source motion, and results in using several matrices to account for the additional frequency content of the radiation vector,  $r_i$ , and its dependent terms. This means that a single frequency in the underlying flow solution is distributed to several frequencies in the output. This has its merits in terms of identifying the rotating properties responsible for a given tone, but it greatly increases the computational complexity of the program. Also, their derivation is for single rotation applications such as isolated helicopter rotor discs and marine propellers, meaning that all frequency content appears as harmonics of the rotation speed. Extending this analysis to a counter-rotating open rotor, with different front and rear rotational speeds, such as is investigated in this thesis, is expected to be far from trivial and is not covered by this thesis.

## 2.5 Verification and Validation

Thus far, the FW-H equation and similar alternatives have been discussed, as have the various formulations of solution for solving such problems and the solver methodologies used to calculate the associated integrals. The integrals are quite complex, and have subtle aspects that need to be handled carefully, particularly in terms of handling frames of reference and observer/source interaction correctly. Hence it is essential that the solver is thoroughly checked to ensure it is working as intended,

and that no mistakes have been made in its development.

It is common for analytical flow solutions to be used for this purpose. Input errors are eliminated because the flow solution is known exactly and the same solution can be used to evaluate the expected noise at the observer. In addition, these solutions are directly for an acoustic fluid (i.e. satisfy Equations 2.1 and 2.3), hence  $T_{ij} = 0$  and there are no neglect errors. This means that only discretisation errors are present, and the noise can be calculated almost exactly provided a detailed enough surface is used. These solutions are an excellent tool in verifying a particular solver, and in investigating/validating improvements made to discretisation error sensitivity.

This thesis uses one particular type of analytical solution, referred to as an “acoustic monopole”. As will be seen shortly, it can be conceived as a point mass source that can move relative to the bulk flow and emits a varying amount of mass into the surrounding fluid. Because the flow solutions are linear, it is easy to create quite complex flow solutions by superposing several acoustic monopoles, and varying the motion and fluctuation frequency of each source. This section will present a brief derivation of the flow solution and also discuss previous work that has used such solutions in assessing FW-H solvers.

One of the first derivations of the monopole in an acoustic context, and utilising the generalised functions which are prevalent today, is that of Lowson [55], however the derivation begins in the stationary frame and applies a conversion to derive the field of a source in motion. A more direct derivation, and the one that will be used here, is given by Crighton et al [19] and is well summarised by Morgans [60]. It is similar to the derivation of the  $p_Q$  components of Formulations 1 and 1A above.

Beginning with mass and momentum conservation as defined in Equations 2.1 and 2.2, the first step is to apply the necessary assumptions to linearise the problem, namely to assume small and isentropic (and therefore inviscid) perturbations from

an otherwise stationary, uniform bulk fluid. The new mass and momentum equations are then as given below, and can be recognised as the well-known linearised Euler equations for a stationary bulk fluid.

$$\frac{\partial \rho'}{\partial t} + \rho_0 \frac{\partial u_i}{\partial x_i} = 0 \quad (2.60)$$

$$\rho_0 \frac{\partial u_i}{\partial t} + \frac{\partial p'}{\partial x_i} = 0 \quad (2.61)$$

Clearly, to model a point mass source involves adding source terms to the RHS of Equation 2.60. As the equation is phrased in terms of creation of mass per unit volume, it is unsurprising that the required term can be expressed as  $Q_M(t)\delta(x_i - Y_i(t))$  where  $Q_M(t)$  represents the strength of the source and  $Y_i(t)$  is the location of the source at a given time (note that this is intentionally defined differently from the dummy convolution variable  $y_i$ ). This gives the following new equation for conservation of mass in the presence of a point mass source.

$$\frac{\partial \rho'}{\partial t} + \rho_0 \frac{\partial u_i}{\partial x_i} = Q_M(t)\delta(x_i - Y_i(t)) \quad (2.62)$$

These two equations can then be manipulated in the same way as for constructing Equations 2.11 and 2.26 from their mass and momentum equations to give the following result.

$$\left( \frac{1}{c^2} \frac{\partial^2}{\partial t^2} - \frac{\partial^2}{\partial x_i^2} \right) (c^2 \rho') = \frac{\partial}{\partial t} (Q_M(t)\delta(x_i - Y_i(t))) + \frac{\partial^2}{\partial x_i^2} (p' - c^2 \rho') \quad (2.63)$$

The second term on the RHS of the above equation is the equivalent of the

Lighthill stress tensor for the linearised Euler equations (i.e.  $e_{ij}$  and the  $\rho u_i u_j$  have been neglected). At this point, the assumption of isentropic perturbations allows the currently arbitrary constant  $c$  to be defined such that  $p' = c^2 \rho'$  (see Equation 2.9 and the surrounding discussion for details). This removes the Lighthill-type term from the RHS of the equation and leaves the LHS as a linear wave operator on  $p'$  instead of  $c^2 \rho'$ , as given below.

$$\left( \frac{1}{c^2} \frac{\partial^2}{\partial t^2} - \frac{\partial^2}{\partial x_i^2} \right) p' = \frac{\partial}{\partial t} (Q_M(t) \delta(x_i - Y_i(t))) \quad (2.64)$$

The derivation continues almost identically to that for  $p_Q$ , with the source term being convolved with the free space Green function and the sifting of the delta functions applied to give a form of solution reminiscent of Formulation 1. Note that the delta function in the source will sift for the single location of the source at a given  $\tau$ , so the volume integral reduces to a single point, rather than a surface integral. A form similar to Formulation 1A is then obtained by using Equation 2.48. The resulting expressions are given below, where the need to set the source location to  $Y_i$  is given alongside the  $g = 0$  condition, underlining why it was mathematically useful to define  $Y_i$  in the first place. All other terms are exactly as defined for Equation 2.50.

$$p'(x_i, t) = \frac{\partial}{\partial t} \left[ \frac{Q_M}{r(1 - M_r)} \right]_{g=0, y_i=Y_i} \quad (2.65)$$

$$= \left[ \frac{\dot{Q}_M}{r(1 - M_r)^2} + \frac{Q_M K_M}{r^2(1 - M_r)^3} \right]_{g=0, y_i=Y_i} \quad (2.66)$$

This solution for the pressure field is widely known, and allows the exact signal at

an observer to be calculated. This means the error in the results of an FW-H solver can be measured exactly. However, in order to be able to also calculate the exact flow solution used as input to an FW-H solver, it is clear from Equations 2.24 and 2.25 that the density and velocity fields are also required. In addition, the appearance of convective derivatives of  $Q$  and  $F_i$  in Equations 2.50 and 2.44 mean that both time and spatial derivatives of pressure, density and velocity are required to evaluate  $\dot{Q}$  and  $\dot{F}_i$  analytically in Formulation 1A.

The density field is trivially established from use of  $p' = c^2 \rho'$ . The velocity field can be established using the well-known relationship between its time derivative and the gradient of pressure in the linearised Euler equations, as given below.

$$\frac{\partial u_i}{\partial t} = \frac{-1}{\rho_0} \frac{\partial p'}{\partial x_i} \quad (2.67)$$

Noting the form of Equation 2.64, it is clear the corresponding governing equation for  $u_i$  is as follows.

$$\left( \frac{1}{c^2} \frac{\partial^2}{\partial t^2} - \frac{\partial^2}{\partial x_i^2} \right) u_i = \frac{-1}{\rho_0} \frac{\partial}{\partial x_i} (Q_M(t) \delta(x_i - Y_i(t))) \quad (2.68)$$

This is of a similar form to that for the  $F_i$  term in the FW-H equation, and hence the Formulation 1- and 1A-esque solutions are very similar to the  $p_F$  solutions given in Equations 2.44 and 2.51, and lead to the following equivalent solutions for the monopole velocity field.

$$u_i = \frac{1}{4\pi\rho_0} \frac{\partial}{\partial t} \bigg|_{x_i} \left[ \frac{Q_M \hat{r}_i}{cr(1-M_r)} \right]_{g=0, y_i=Y_i} + \frac{1}{4\pi\rho_0} \left[ \frac{Q_M \hat{r}_i}{r^2(1-M_r)} \right]_{g=0, y_i=Y_i} \quad (2.69)$$

$$= \frac{-1}{4\pi\rho_0} \left[ \frac{\dot{Q}_M \hat{r}_i}{cr(1-M_r)^2} + \frac{Q_M (\hat{r}_i - M_i)}{r^2(1-M_r)^2} + \frac{Q_M \hat{r}_i K_M}{cr^2(1-M_r)^3} \right]_{g=0, y=Y_i} \quad (2.70)$$

As with Formulations 1 and 1A, the above solutions also struggle to handle transonic motion. Derivations of monopole solutions for transonic and supersonic motion do exist [48], however only in the frequency domain, and are not used in this thesis.

Many researchers have used analytical flow solutions to check their formulations, and the most comprehensive use of them known to this author is that of Casalino [12]. The paper presented the first use of a source dominant methodology, and analytical solutions were used to verify that the solver correctly predicted various different analytical test cases while also performing some basic investigation of discretisation error. Specifically, the variation of error with time step of the input flow solution was investigated. Part of the study is reproduced in Figures 2.8, 2.9 and 2.10. The test case consists of a set of monopoles rotating about two different axes and with a sinusoidal strength fluctuation, and it demonstrates that even a simple case like this can require significant resolution in time to provide an accurate answer. Even at 200 steps per acoustic period the error is close to 10%.

While this study is sufficient to verify that the advanced time formulation can work and produce accurate results, it does not look to validate that this solver provides an improvement over an equivalent observer dominant methodology or make any other comparisons or conclusions using the solutions. The study itself is also quite simplistic, as it only varies the time step of the given solution, and does not investigate other important effects such as spatial discretisation and surface motion.

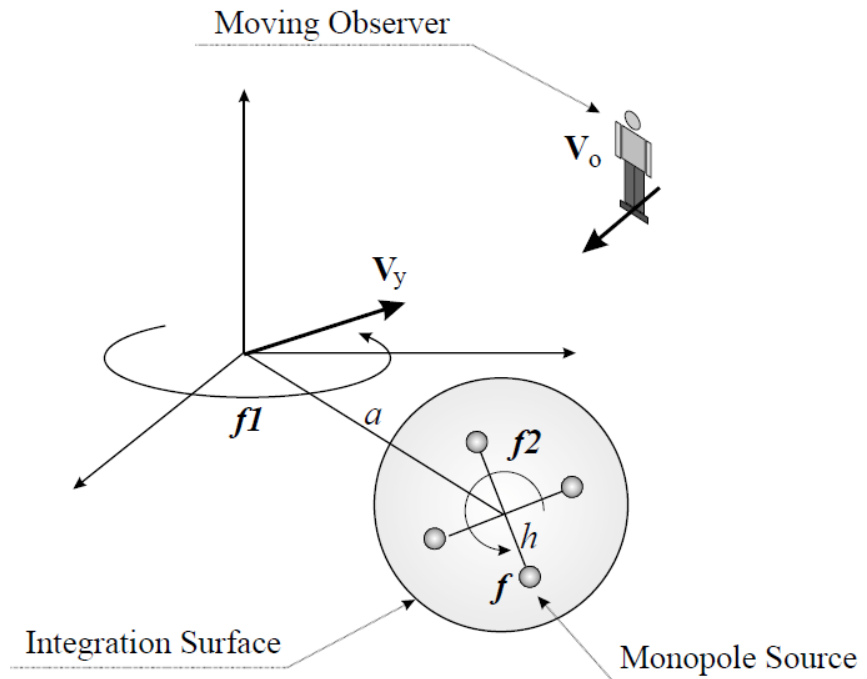


Figure 2.8: Illustration of analytical test case from Casalino [12].

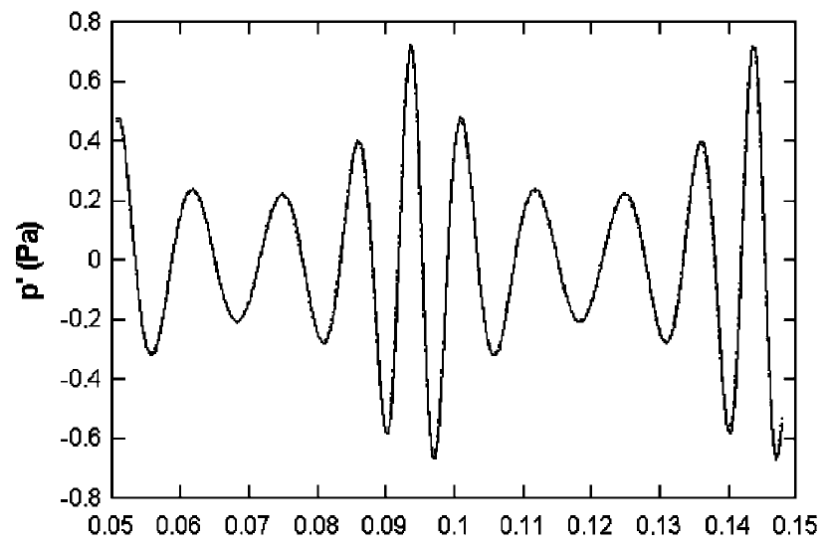


Figure 2.9: Calculated time signal for the test case from Casalino [12].

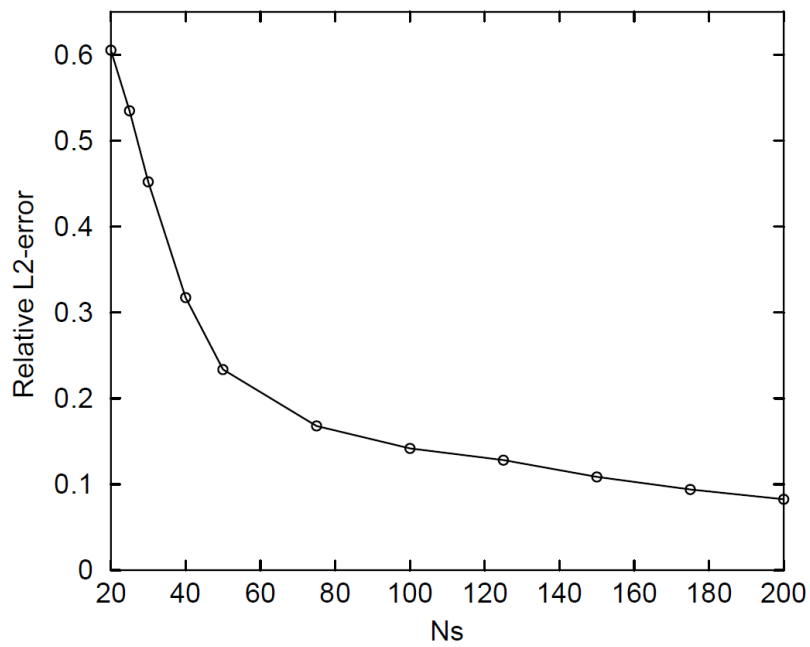


Figure 2.10: Plot of RMS error vs. step size from Casalino [12].

Other notable uses of analytical solutions have been by Morgans [60], Najafi-Yazdi [62], Ghorbaniasl and Hirsch [36] and Tang et al [81]. The extent of their use of the solutions, and of the use made by other research, appears to be in justifying that their formulations are correct, with often some small investigation of effects such as speed of motion or resolution on the FW-H surface. However, these studies are invariably basic and do not appear to be used in directly guiding choices made when developing solver methodologies. In other words, solvers are typically verified, but there are still a wide range of different solver methodologies in current use, and very little effort appears to have been devoted to comparing or understanding these different methodologies in terms of their sensitivity to discretisation error.

This lack of detailed research presents an opportunity to greatly improve the understanding of discretisation errors and the use of analytical flow solutions in assessing FW-H solvers. This is the fundamental motivation behind the work presented in Chapter 4, and the associated objectives defined at the start of this thesis.

## 2.6 Open Rotors

Open rotor noise sources are normally split based on two fundamental characteristics. Firstly, the terms “tonal” and “broadband” are used to differentiate between noise that is restricted to discrete sets of frequencies (or tones) and noise that is spread over a range of frequencies respectively. Secondly, the terms “rotor alone”, “interaction” and “installation” are used to separate effects that can be considered a direct product of a single row of rotors, effects due to the interaction of two rows of rotors, and effects due to the surrounding environment respectively.

Broadband noise prediction using an FW-H based approach would require a detailed solution for the random turbulent effects ingested and created by an open

rotor. The computational requirements of such research is beyond the reach of this author and hence not considered further in this thesis. Hence, only tonal rotor alone, interaction and installation effects are investigated here.

### 2.6.1 Rotor Alone Effects

At low speeds typical of a take-off condition, the rotor alone noise is dominated by so-called “thickness” and “loading” noise sources, caused by volume displacement and rotating blade forces respectively. These can also be thought of as the effect of the potential field of the rotors. Early work on thickness noise was carried out in the context of conventional propellers by Lynam and Webb [56] and Bryan [10], while the first work on loading noise is normally accredited to Gutin [42].

Gutin represented a propeller as a stack of airfoils with a certain thickness, as illustrated in Figure 2.11. A frequency domain approach was used to extract results for each harmonic of the blade passing frequency, and it is clear from Figures 2.12 and 2.13 that this approach produced remarkably realistic directivity plots given the simplicity of the model. In particular, it clearly mimics the expected vanishing of the tones close to the rotation axis of the propeller.

Open rotor research began in earnest in the eighties, and built heavily on the work that had been done for traditional propellers. In particular, NASA undertook a wide-ranging program covering aerodynamic, aeroacoustic and aeroelastic considerations. The initial research focused mainly on single rotation configurations, as these were the simplest to evaluate and least commercially sensitive. Some good early studies are those of Jeracki et al [47], Rohrbach et al [69] and Barton et al [2]. Figures 2.14 and 2.15 show the predicted noise of the NASA SR-3 blade design from Rohrbach et al’s work compared with experimental results. This again demonstrates the ability

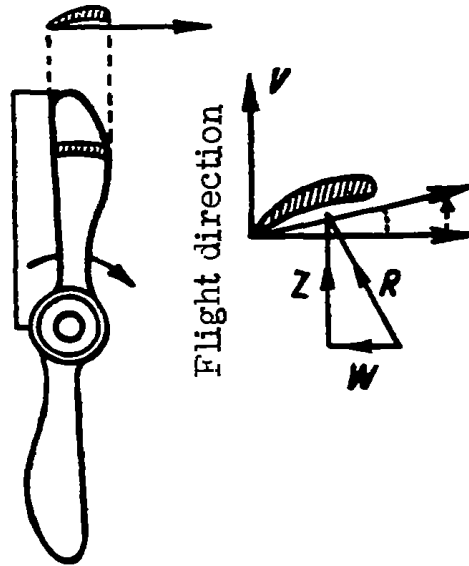


Figure 2.11: Representation of a propeller blade as a stack of airfoils from Gutin [42].

of simplified analytical models to produce plausible trends.

By definition, rotor alone effects must be steady in the frame of reference rotating with the relevant blade row. Hence, the frequency content of the generated noise field is purely a product of its rotation. Assuming a uniform tangential distribution of identical blades, such as is investigated in this thesis, means that all rotor alone frequency content must occur at integer harmonics of the so-called “blade passing frequency” (BPF) for that row, which is equal to the number of blades multiplied by the rotational speed.

In the context of the FW-H equation, the  $p_Q$  and  $p_F$  components of the solution are often described as the thickness and loading noise, however it is important to note that this is only applicable if the FW-H surface is coincident with the actual blade surface, and hence impermeable. As this thesis will exclusively use a permeable

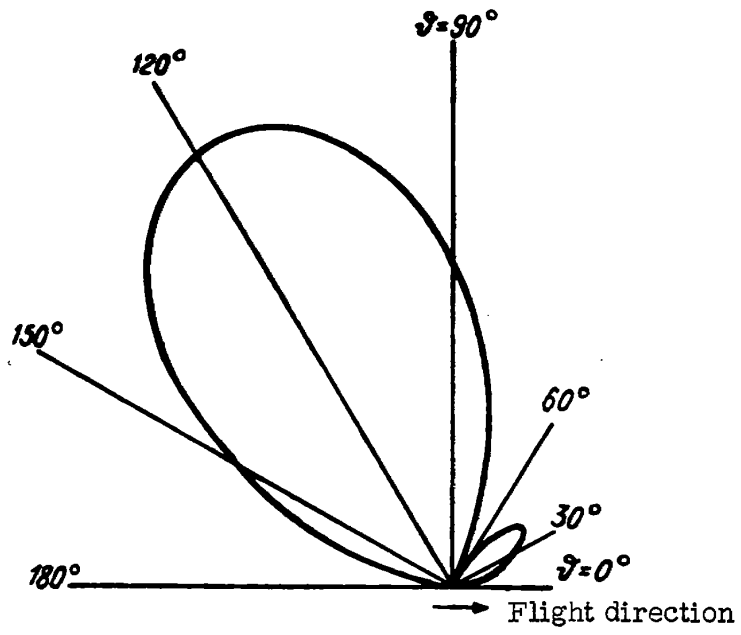


Figure 2.12: Calculated variation of noise with directivity from Gutin [42].

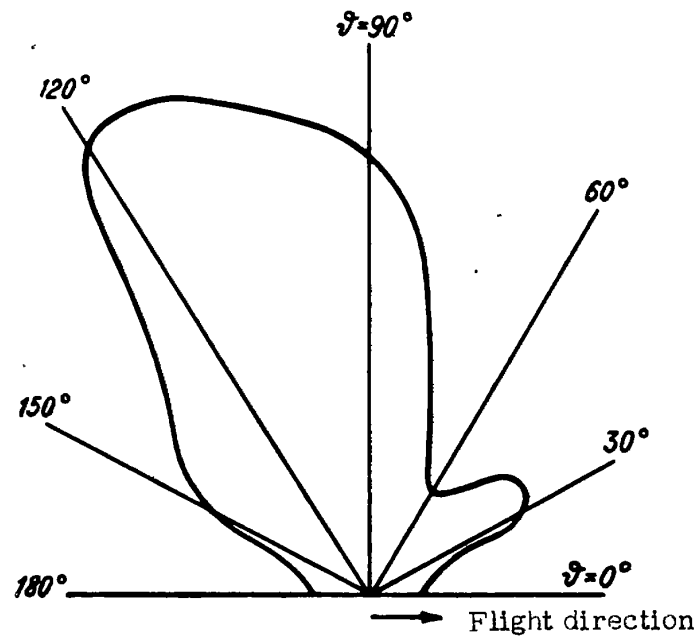


Figure 2.13: Experimental variation of noise with directivity from Gutin [42].

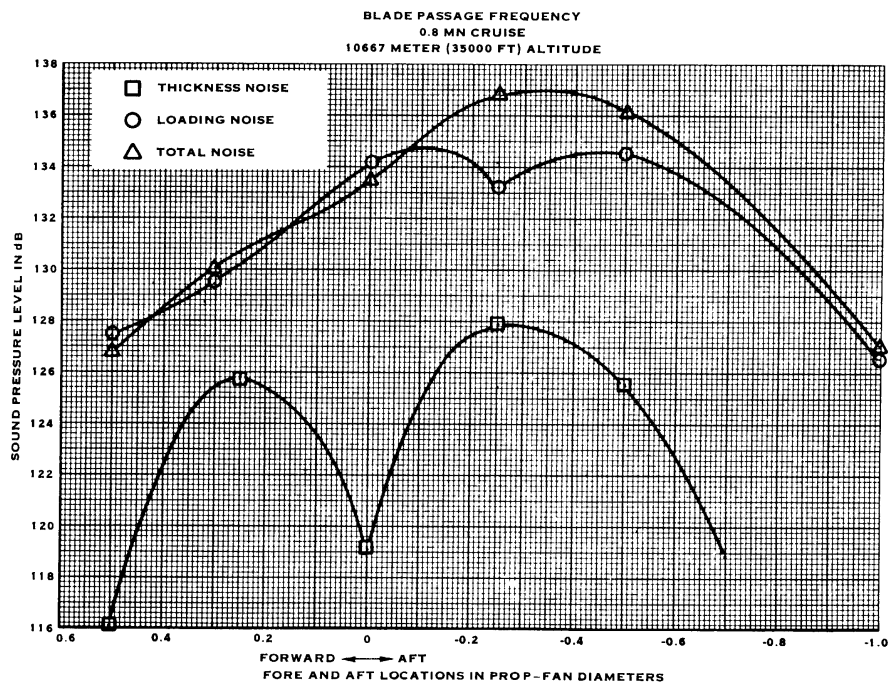


Figure 2.14: Predicted variation of noise with axial location from Rohrbach et al [69].

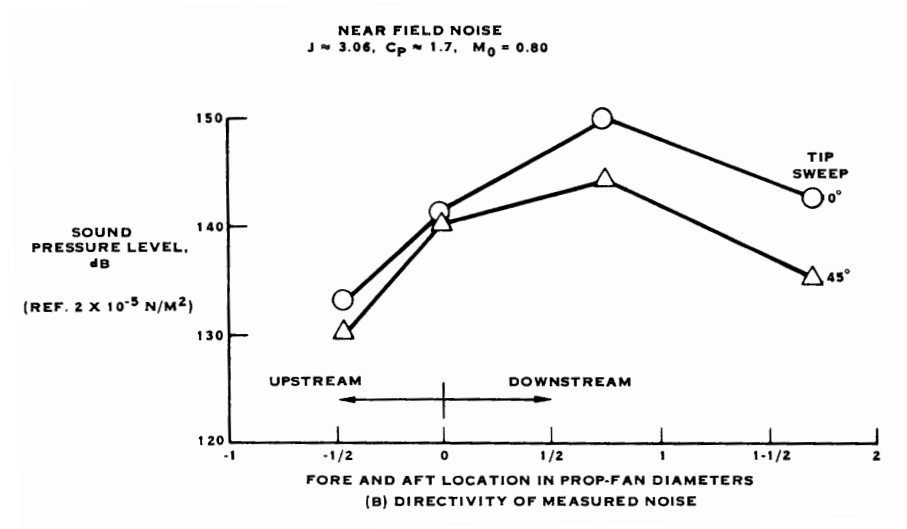


Figure 2.15: Experimental variation of sound with axial location from Rohrbach et al [69].

FW-H surface not coincident with the blade surface, the  $p_Q$  and  $p_F$  components will not be labelled as thickness and loading noise.

## 2.6.2 Interaction Effects

The interaction noise generated by an open rotor falls into two main categories. Firstly, the potential field of one set of rotors influences the flow over the other, leading to fluctuation of loading and hence extra frequency content. Secondly, the wakes and vortices shed by the front rotors can interact strongly with the rear rotor, and hence cause further fluctuation of the loading and the noise generated by the rear rotors.

Work on counter-rotating open rotors began to gather speed in the late eighties and early nineties, with some good aerodynamic studies being those of Celestina et

al [13], Podboy and Krupa [67] and Shin et al [73]. Also at this time, Magliozzi et al released an excellent summary of propeller aeroacoustics in general, with good discussion of the sources and relative importance of different aspects of propeller noise, both tonal and broadband [57]. Computational resources meant that use of the FW-H equation for noise prediction of these effects was quite impractical, and most prediction methods relied on the work of Hanson [44] and Parry and Crighton [65].

A good example of an early experimental study of the noise of counter-rotating open rotors is that of Woodward [86]. An open rotor with eleven and nine blades on the front and rear rows respectively was tested at a take-off condition for a range of configurations. The experimental set up is pictured in Figure 2.16. The measured frequency content for a microphone at a directivity of  $90^\circ$  is shown in Figure 2.17, with many of the rotor alone and interaction tones highlighted. It is clear that the frequency content is extremely complex and highly tonal. In addition to the harmonics of the blade passing frequencies, a large number of interaction tones are present and significant.

The variation of the two fundamental rotor alone tones and the simplest interaction tone with directivity are plotted in Figure 2.18. It shows the expected vanishing of the rotor alone tones towards the rotation axis, while the interaction tone is significant at all directivities. Woodward also showed results that found that interaction tones were heavily affected by the spacing of the blade rows, which is as expected as a larger gap would weaken the interaction of one blade row with the other. Conversely, rotor alone tones were less affected by the gap.

It is clear that the frequency content of counter-rotating open rotors is significantly more complicated than for single rotation. A single rotation problem is steady in the frame rotating with the blades, but the addition of a second blade row with a

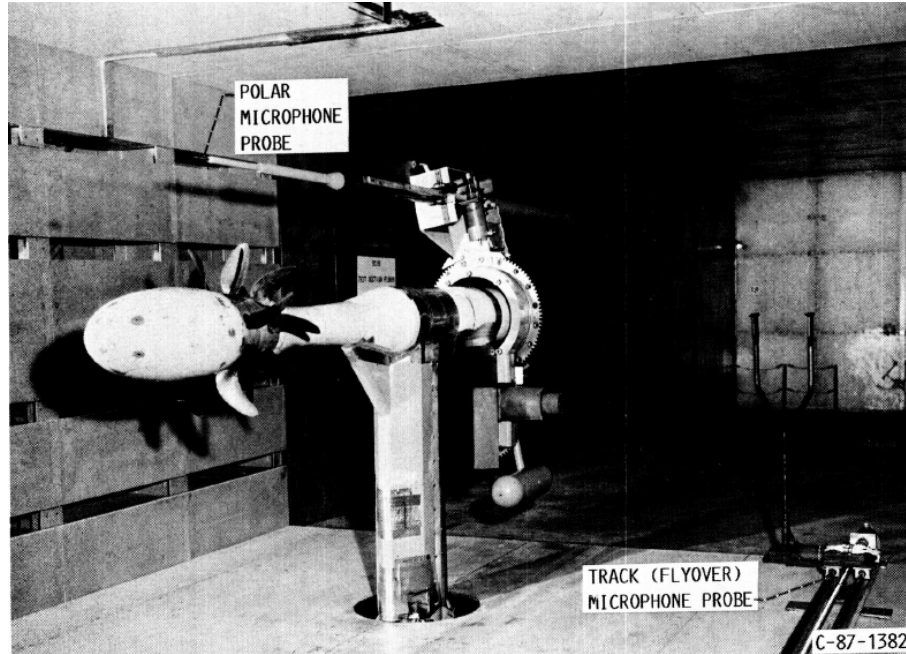


Figure 2.16: Experimental set up from Woodward [86].

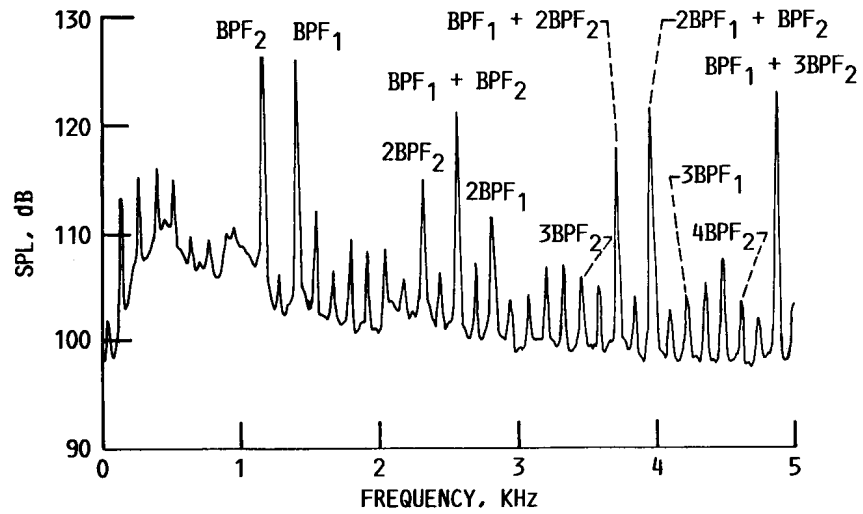


Figure 2.17: Typical open rotor frequency content from Woodward [86].

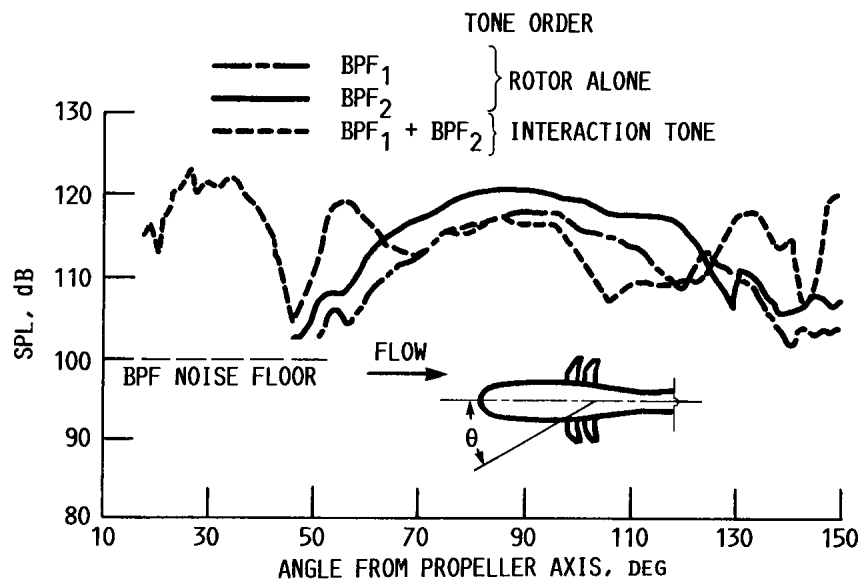


Figure 2.18: Directivity of rotor alone and interaction tones from Woodward [86].

different rotational speed means this is not the case for counter-rotation. However, provided the open rotor is uninstalled (see below) the flow will still be periodic in the rotating frame of reference, with the period being the time taken for a point on the second blade row to do one full rotation relative to the first blade row, i.e. the time for the relative alignment of the two blade rows to repeat itself. If the numbers of blades on the two blade rows have a common factor, then the period will be reduced by this factor, i.e. the flow solution will have spatial periodicity. This is summarised by the equation below, where  $T_P$  is the period of the flow solution in the relative frame,  $\Omega_F$  and  $\Omega_R$  are the front and rear rotational speeds (assumed to have the same sense), and  $N_{HCF}$  is the highest common factor of the front and rear blade numbers.

$$T_P = \frac{2\pi}{N_{HCF}|\Omega_F - \Omega_R|} \quad (2.71)$$

Hence, in the rotating frame, the frequency content will be harmonics of the fundamental periodicity frequency. Unfortunately, this is not true in the non-rotating frame in general. This is illustrated in Figure 2.19, which shows the rotation of an 8/6 bladed open rotor with different front and rear rotational speeds. The (1,1) and (5,4) blade pairs are initially aligned and the front and rear blade numbers have a common factor of 2 (i.e.  $N_{HCF} = 2$ ), so the flow solution will repeat twice around the rotation axis. In a frame rotating with the rear row, the above equation shows that the relative rotation of the front row during a period of  $T_P$  is  $180^\circ$  and leads to the (1,4) and (5,1) blade pairs being aligned, at which point the flow solution is identical to its initial state. In the absolute frame, the front and rear blade rows rotate by  $\Omega_F T_P$  and  $\Omega_R T_P$  respectively.

If  $\Omega_F = -\Omega_R$ , then the above equation shows that each blade row would rotate by  $90^\circ$  in opposite directions in the absolute frame, so after  $2T_P$  the flow solution will be identical in the absolute frame as well. However, it is common for the front and rear rotational speeds to be different, and this means that the amounts that each blade row rotates after  $T_P$  are different and the absolute orientation of the blades may never repeat itself.

As a result, the rotating harmonic frequency content is far more complex in the absolute frame, and is composed of sum and difference combinations of the harmonics of the relative periodic frequency,  $N_{HCF}|\Omega_F - \Omega_R|$ , and harmonics of the rotation frequency, which is either  $\Omega_F$  or  $\Omega_R$ . This can also be represented in terms of integer combinations of  $\Omega_F$  and  $\Omega_R$ . The rotor alone tones are a subset of this frequency content, corresponding to the sum and difference combinations

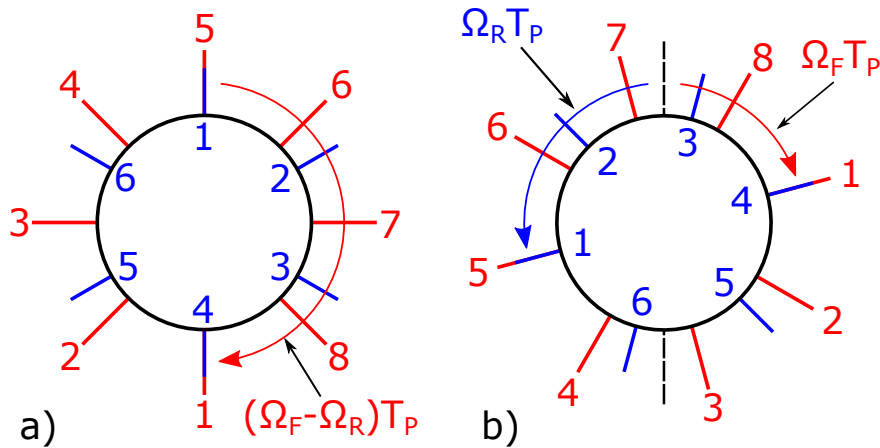


Figure 2.19: Blade row rotations for an 8/6 bladed open rotor in the a) rotating and b) absolute frames.

of the constant component of the relative frequency harmonics with the rotation harmonics that correspond to the blade passing frequencies. It should be noted that other harmonics of either rotation frequency can also be present, but are generally small compared to the rotor alone tones, i.e. the fluctuations caused by each passing blade are significantly stronger than the variation of this effect from one blade to the next.

For the same reason, the loudest interaction tones tend to be integer combinations of the two blade passing frequencies, i.e. interactions of the rotor alone tones. Hence a common notation that is used in this thesis for referring to different tones is  $(M, N)$  where  $M$  and  $N$  are the harmonics of the front and rear blade passing frequencies respectively.

### 2.6.3 Installation Effects

The previous two sections have considered effects of so-called “isolated” or “uninstalled” open rotors, i.e. open rotors that exist entirely by themselves in a flow and no angle of attack. Clearly this is never true in a realistic situation.

When installed on a plane, effects such as ingestion of wakes from upstream wings and pylons and the induced incidence on the open rotor from nearby wings, as well as the potential field and scattering effects of the fuselage and the engine centrebody, can all have significant effects on the generated noise. When installed in a wind tunnel, extra interaction effects (aside from any that are being modelled in the experiment) can include wind tunnel walls and shear layers, the potential field of the mounting of the model, any instrumentation in the flow and upstream turbulence creation. As many of these effects are not axisymmetric and do not rotate with either set of blade rows, they can introduce entirely new sets of frequencies.

Work on installation effects using FW-H methodologies appears somewhat sparse at the moment. Stuermer and Yin [80] have done some work looking at pylon interaction and the effect of open rotors on each other (in terms of sense of rotation). Also, Brandvik et al [3] and Sohoni et al [77] have demonstrated the aerodynamic effects of angle of attack and highlighted its potential impact on conventional methods of controlling tip vortex interaction (i.e. requiring more cropping or smaller rotor row spacing to avoid such interaction than for a zero incidence case), however the resulting effects on the actual noise prediction have not been calculated.

The frequency content for a pressure transducer on a rear blade for zero and  $12^\circ$  angle of attack are reproduced from Sohoni et al in Figure 2.20. The plots clearly show that the frequency content of the zero angle of attack flow solution in the rotating frame is composed of strong tones at harmonics of the relative blade

passing frequency of the front blades plus some broadband background noise, while the  $12^\circ$  angle of attack case also contains a large number of side bands to these tones representing the once per rotation effects. Investigation of installation effects is beyond the scope of this thesis, but it is an important area of study that the work in this thesis can be extended to investigate.

### 2.6.4 Modern Research

Open rotor research tapered somewhat during the nineties, but interest has been gradually increasing over the last decade or so as oil prices continue to rise. With the increased computational capabilities available today, many researchers are using unsteady CFD with an FW-H solver to predict the resulting noise. As the objectives of this thesis are around developing better solvers for open rotor noise, rather than directly researching open rotor noise itself, this section will concentrate on work that has examined how best to use FW-H solvers for this purpose.

One of the best recent end to end studies including examination of different CFD methodologies is that of Colin et al [14, 15, 16]. The first paper in the series compared the FW-H approach to one based on the semi-analytical theories of Sears [71] and Hanson [44]. Figure 2.21 shows the resulting predictions, with the chorochronic approach being shown to give good agreement with test data away from the rotation axis. However, all methods struggled to accurately predict the location of a “bump” at downstream directivities, giving good evidence of the importance of neglecting errors in realistic calculations.

The second paper in the series moved on to examine the importance of accurate propagation of the front rotor wakes for predicting the resulting unsteady loading of the rear rotor blades. Various different mesh topologies were examined, as were sev-

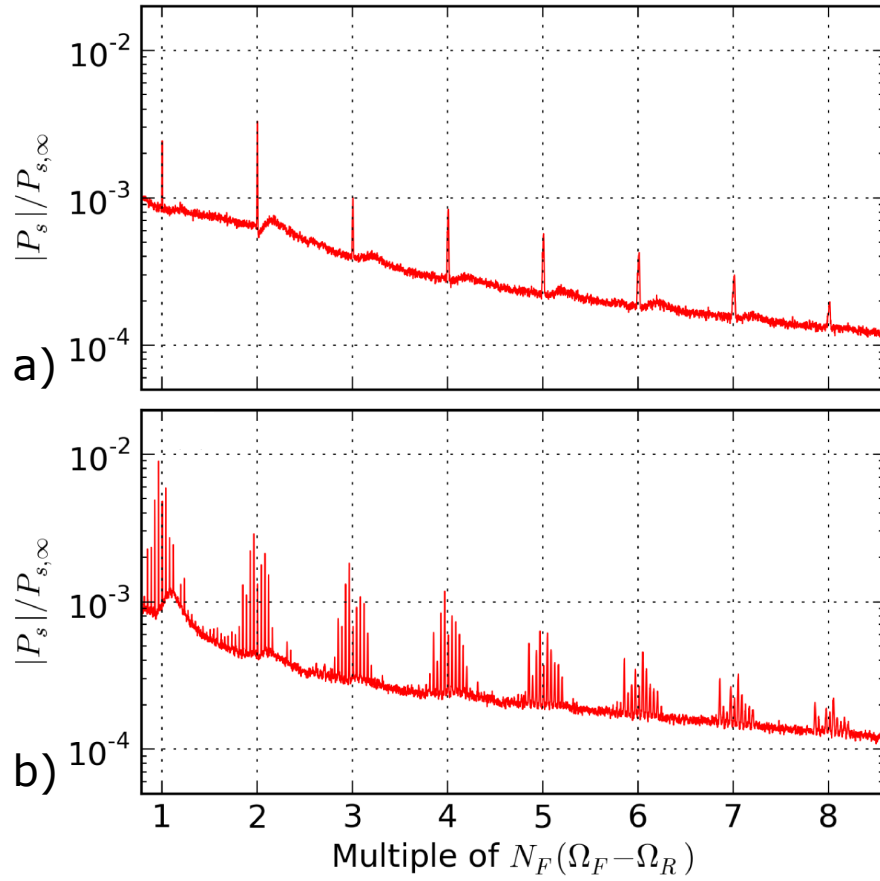


Figure 2.20: Pressure frequency content on a rear blade for a) zero and b)  $12^\circ$  angle of attack from Sohoni et al [77].

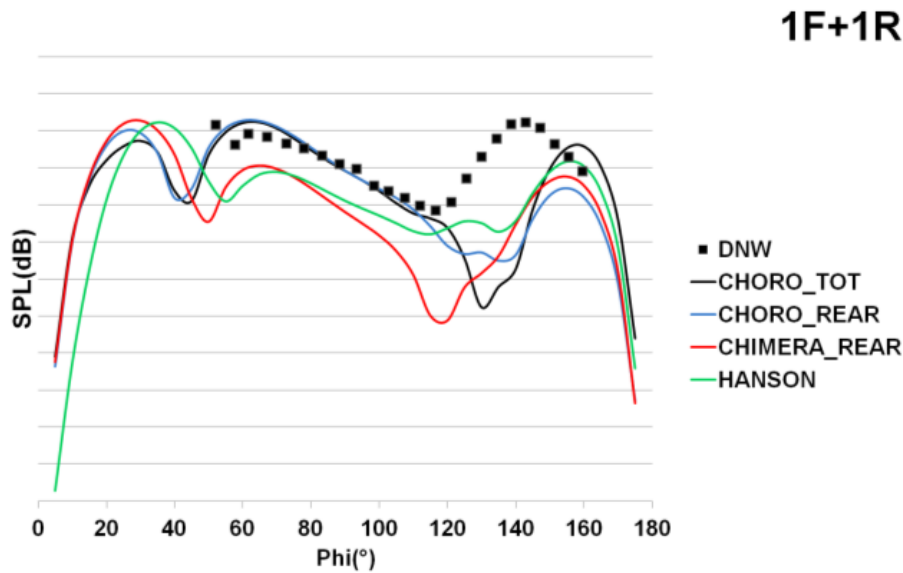


Figure 2.21: Experimental and calculated data for the (1,1) interaction tone from Colin et al [15].

eral different mesh resolutions. Figure 2.22 reproduces results for two different tones and three different mesh resolutions. Clearly, the (1,0) tone is far more consistently predicted as the mesh resolution is worsened than the (2,2) tone. What is less clear from the research is how much of this inconsistency is as a result of the input errors caused by inaccurate wake propagation as opposed to discretisation error within the FW-H solver itself due to the worse resolution on the integration surface.

This would have been an excellent opportunity to make use of analytical flow solutions to isolate discretisation error and decide whether this was the limiting factor or not. This understanding could feed back guidance on whether a fine CFD mesh could be coarsened on the integration surface to speed up the FW-H solver, or conversely if a coarse CFD mesh could provide accurate enough input but needed to be interpolated to a finer mesh in the FW-H solver to mitigate discretisation error.

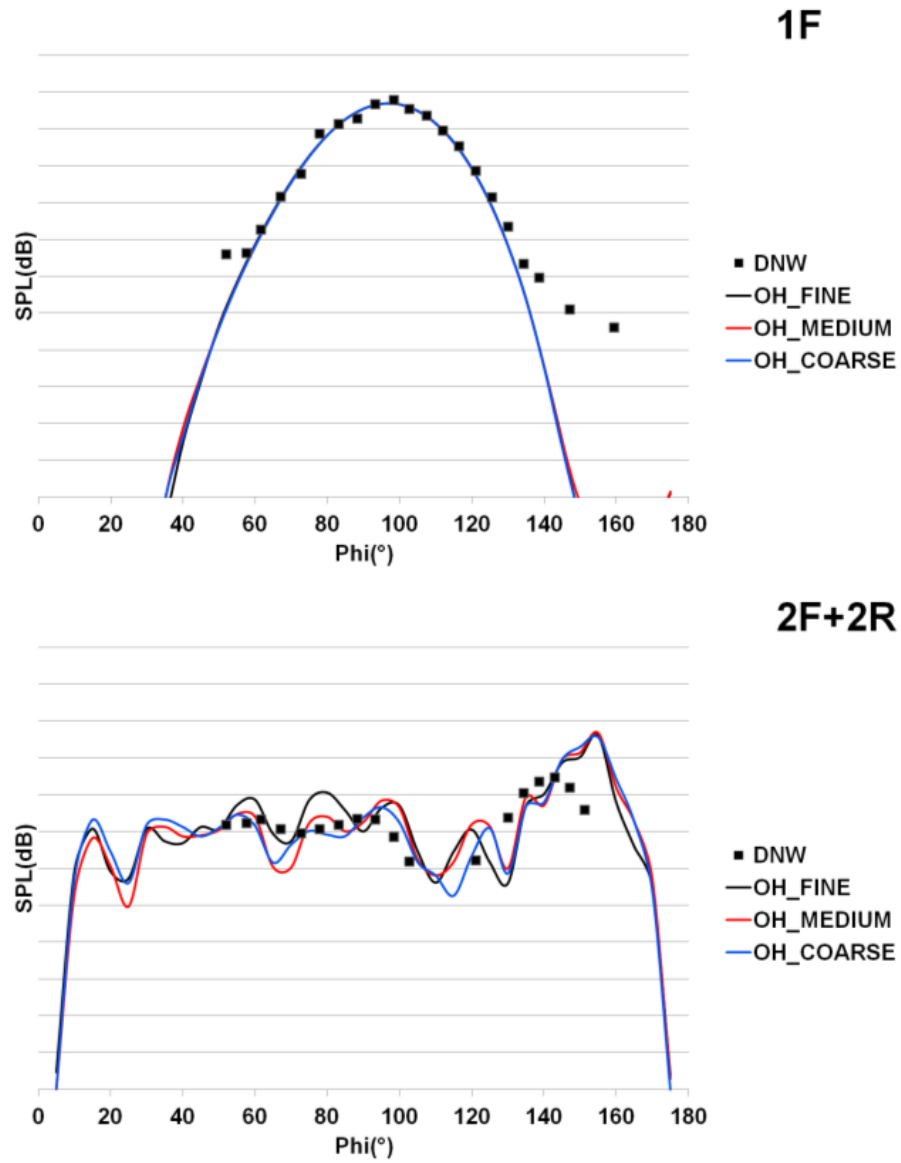


Figure 2.22: Experimental and calculated results for different mesh densities from Colin et al [14].

Among other things, the final paper in the series did some work on comparing different FW-H surface placements for noise prediction. In particular, a hypothesis for the cause of the misplacement of the downstream “bump” shown in Figure 2.21 was investigated by comparing a closed surface wrapped tightly around the open rotor blades with a cylindrical surface that extended much further downstream but was open at that end. The hypothesis was that the neglect of the downstream source field in the original results, in particular the effects of refraction through the tip vortices, was the cause of the misplaced bump and that extending the FW-H surface further downstream could mitigate this.

This concept is illustrated in Figure 2.23, Figure 2.24 shows the two different surfaces and Figure 2.25 shows the associated results for the (1,1) interaction tone. Clearly, the longer open surface predicts a better “location” for the bump, but underestimates its magnitude and has some oscillation with directivity, implying instability. The closed short surface gives a smoother, more accurate bump but at the wrong directivity. This seems to imply that the longer surface is correctly accounting for refraction, but the decision to leave it open at the downstream end, i.e. neglect this part of the source field, may have introduced other errors.

Other than this, the vast majority of current research predicting the noise of open rotors using an FW-H based approach simply couples a CFD result to an FW-H solver and looks at the results. As already discussed in general for FW-H solvers, it is very rare for the underlying methodology to be investigated in any depth, or for different methodologies to be compared. When comparisons are made, it is almost always for different CFD methodologies, i.e. investigating input errors, not neglect or discretisation errors. This underlines the need to investigate these errors, which has been identified as the fundamental motivation of the work in this thesis.

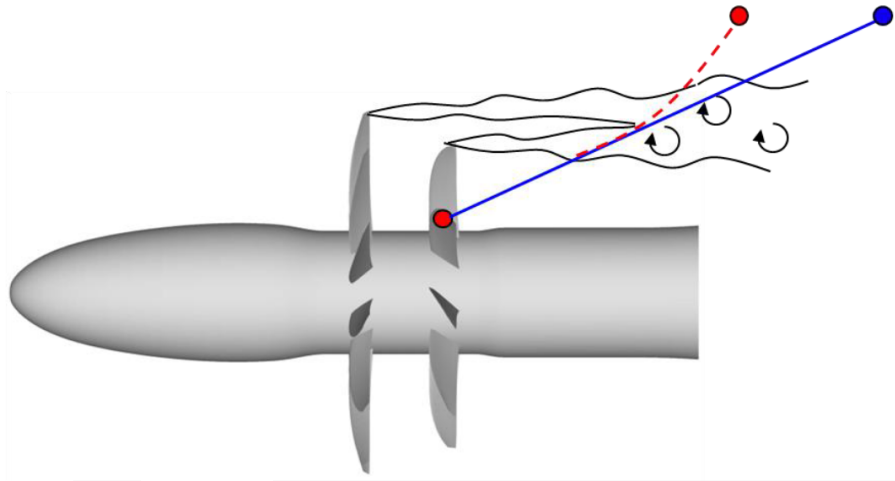


Figure 2.23: Illustration of refraction concept from Colin et al [16].

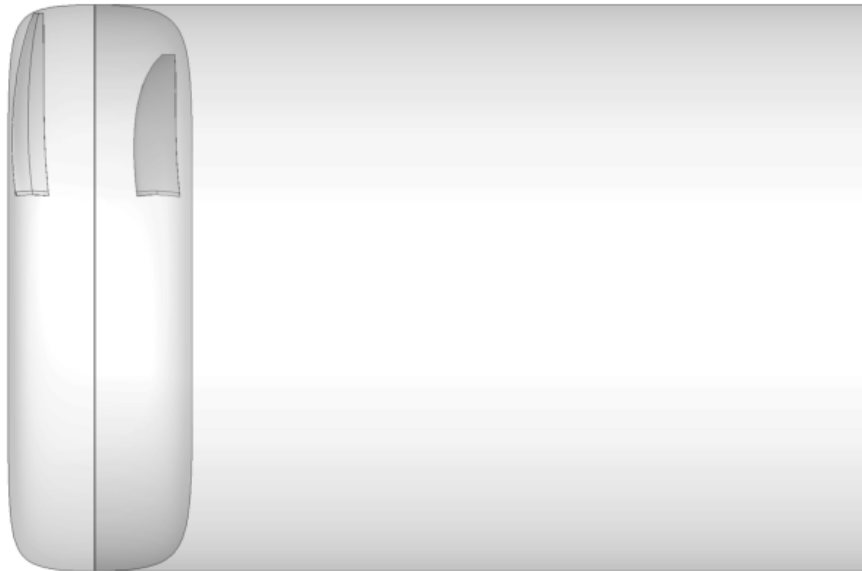


Figure 2.24: Open and closed surface placements from Colin et al [16].

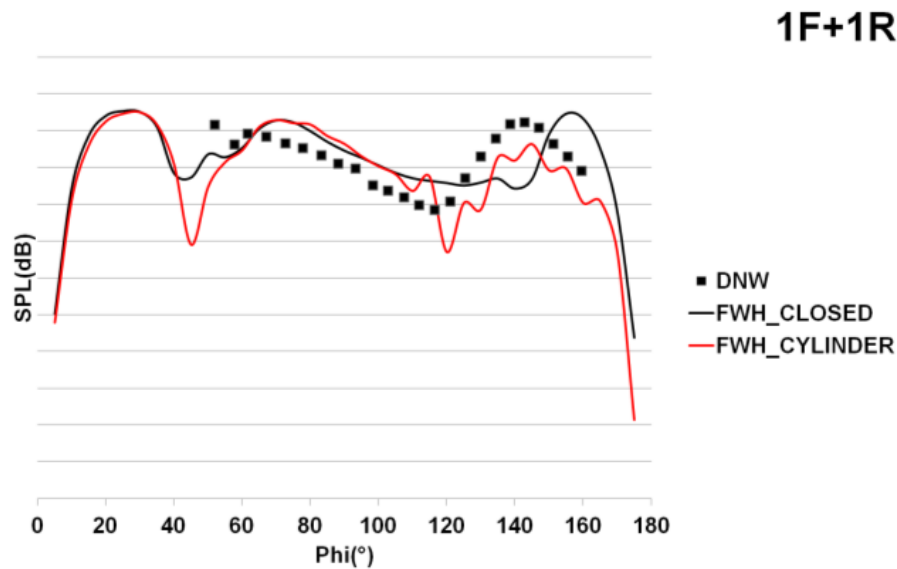


Figure 2.25: Experimental and calculated data for different surface placements from Colin et al [16].

### 2.6.5 Z-08 Test Case

This thesis develops a variety of methods for improving the fidelity of predicting open rotor noise using an FW-H based approach. The majority of the thesis uses analytical and semi-analytical solutions to quantify the improvements offered by these methods. However, it is still important to demonstrate these improvements on a more realistic flow solution, to give confidence that the conclusions drawn and any benefits extracted will translate to these cases. The test case selected for this purpose uses the Rolls Royce Z-08 design at an uninstalled take-off condition.

In the late eighties, Rolls Royce contributed to the aforementioned initial research on open rotors through the development of a design named Rig-140 [50]. By today's standards, it was a relatively primitive design, with seven blades on both front and rear rows. Two different builds, Build A and Build B, incorporated straight and

swept blade designs respectively. Very little of the original research is in the public eye, with the in house Rolls-Royce reports of Newman [63] and Hammerton and Knighton [43] being the main references of note, both of which suggested there was significant scope for improvement to the design.

As in other research centres, work on open rotors in Rolls Royce waned through the nineties and until recently, when a new design, Rig-145, was developed, based on the original Rig-140. The design went through two iterations, named Build 1 and Build 2. Unfortunately, these builds suffer from the same lack of information in the public eye as Rig-140, though brief overviews are given by Ricouard et al [68] and Parry et al [66]. Rig-145 Build 2 was also the subject of the studies by Colin et al described above [14, 15, 16, 17].

Further recent development and collaboration with Airbus has led to the Z-08 design used in this thesis, as described by Paquet et al [64]. A photograph of the experimental setup for an installed test case is reproduced from Paquet et al in Figure 2.26 and Figure 2.27 shows experimental results for the variation with directivity of the (2,1) and (2,2) interaction tones.

The test case used in this thesis is the zero angle of attack take-off case considered by Sohoni et al [77] and from which Sohoni kindly provided the CFD solution [76]. The CFD methodology used by Sohoni was based on that developed by Brandvik et al [3] who ran similar predictions for Rig-145 designs. The CFD solver used is the Turbostream solver developed by Brandvik and Pullan [4], which is a redevelopment of the TBLOCK solver developed by Denton [21] that takes advantage of GPU architectures to highly parallelise the solver and hence allow significantly faster calculation times. Turbostream is a URANS solver that is second order in both time and space.

Some key operating parameters are reproduced from Sohoni et al in Table 2.1.

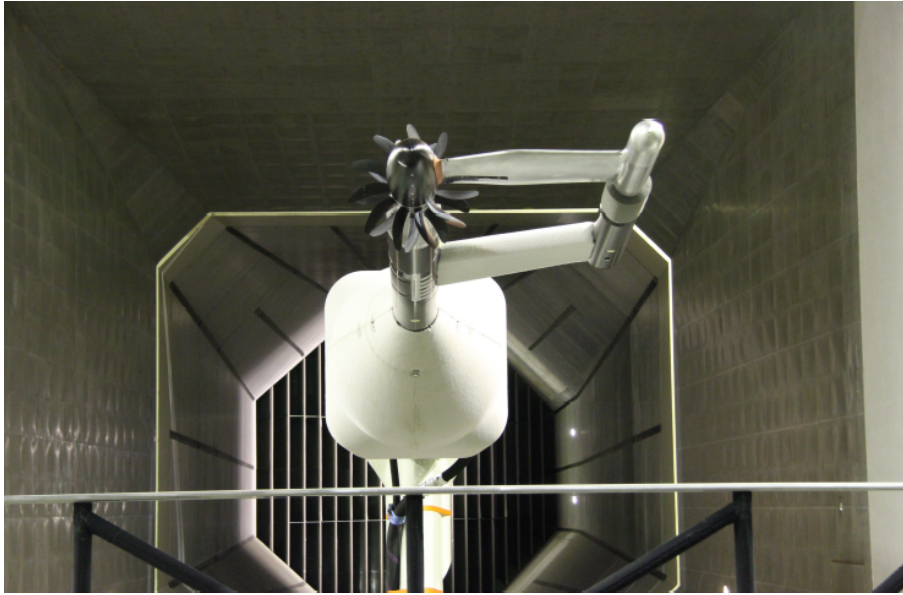


Figure 2.26: Experimental setup for an installed Z-08 case from Paquet et al [64].

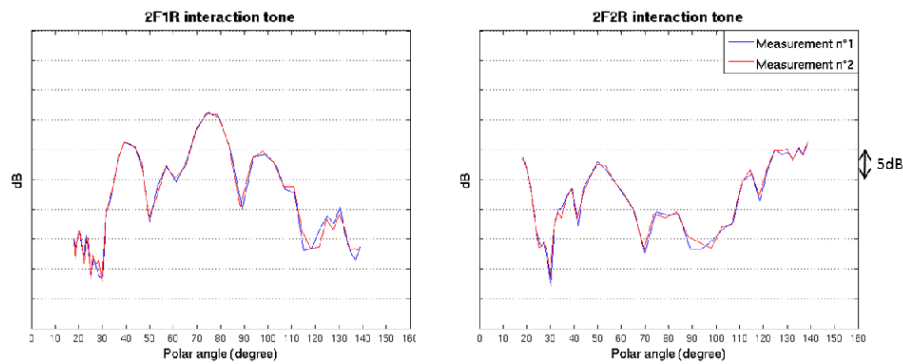


Figure 2.27: Experimental data for the (2,1) and (2,2) interaction tones for the Z-08 test case from Paquet et al [64].

	<b>Front Row</b>	<b>Rear Row</b>
Diameter (m)	0.610	0.518
Blade Count	12	9
Stagger at 70% span (°)	46.9	37.8
Advance Ratio	1.09	1.49
Forward Mach Number	0.219	
Upstream Stagnation Pressure (Pa)	104470	
Upstream Stagnation Temperature (K)	304.3	

Table 2.1: Key characteristics of Z-08 test case, reproduced from Sohoni et al [76, 77].

Some details of the meshing strategy and boundary conditions are given in Figure 2.28. The use of a non-rotating upstream mesh zone allowed a simpler boundary condition to be specified there (otherwise the required stagnation profile at the inlet would vary with radius), but this was not necessary downstream due to the static boundary condition there. The mesh itself was the finer of the two grids used by Sohoni et al, with approximately 170 million nodes for the full annulus case. A more detailed discussion of the particular CFD solution used is given in Chapter 6.

## 2.7 Summary

This chapter has described relevant previous work with respect to the development, understanding and use of the FW-H equation as well as the specific application of FW-H solvers to open rotors. In discussing the derivation and physical understanding of the FW-H equation, it has been shown that a significant problem with the method is the need to neglect the source field external to the surface discontinuity. These neglect errors have been seen to make FW-H calculations very sensitive to surface placement, with instability of the prediction persisting further downstream than it is practical to extend a CFD mesh. An alternative is provided by the Kirch-

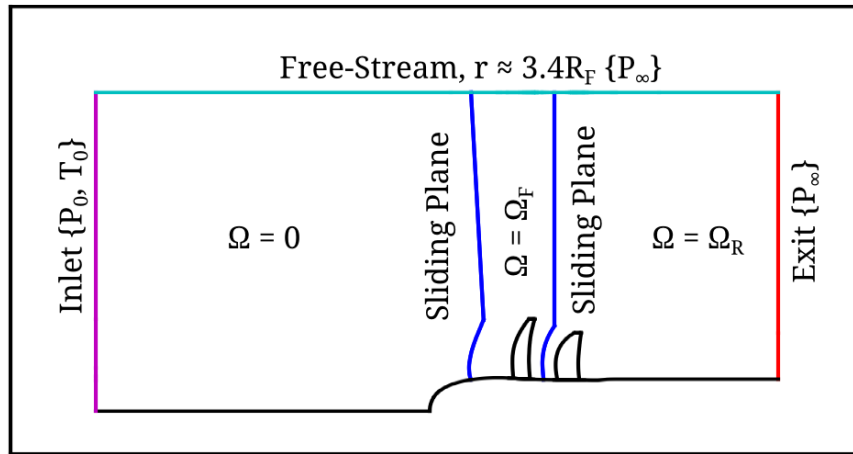


Figure 2.28: Meshing strategy and boundary conditions for Z-08 test case from Sohoni et al [77].

hoff equation, but it has been shown that there are conflicting opinions over which is better, and the differences between them are not clearly understood. Previous attempts to adjust the FW-H source terms to behave more stably have given promising results but the methods used are not physically meaningful and hence are also poorly understood. This justifies the associated objective defined at the start of this thesis, which is addressed by the work in Chapter 5.

Regardless of which particular governing equation is used, it has been shown that there are a variety of different ways of formulating a solution, with Farassat's Formulation 1A being selected as the formulation to be used in this thesis. Even having specified this formulation, there are still a wide range of solver methodologies that can be employed to perform the calculations. It has been shown that there has been almost no research directly comparing different solver methodologies and quantifying their relative performance. The discretisation errors that solvers generate regardless of the accuracy of their input are poorly understood and there are no clear

guidelines on how much resolution is required in an input solution to get acceptable accuracy in the output. Understanding discretisation errors, developing a standard process for comparing different solver methodologies and identifying a best practice methodology for open rotor noise prediction have all been identified as key objectives for this thesis, and they are addressed by the work in Chapter 4.

The key characteristics of open rotors in terms of how they generate noise have been discussed. In particular, it is important to acknowledge that the time history of a counter-rotating, uninstalled open rotor will be periodic in a frame rotating with either blade row, but non-periodic in the absolute frame. Finally, the Rolls Royce Z-08 design has been presented as an appropriate modern open rotor design to be used as a realistic test case for demonstrating the various improvements developed in this thesis, which is the final objective of the thesis. The history of the design has been discussed, as has the CFD methodology used to generate flow solutions, with specifics of the particular solution used and the associated operating point given alongside the actual demonstrations in Chapter 6.

# Chapter 3

## Numerical Methods

This chapter will describe and validate the numerical methods used in the rest of this thesis. The objectives of this thesis require a range of different solver methodologies, source term constructions and input flows to be available, and hence the methods and the various file formats they use can be configured in a variety of ways. The names of the codes developed, and a brief description of their purposes are given in Table 3.1.

This chapter discusses some key concepts behind how the codes work before discussing each code in turn and presenting basic validation that they work as expected. In particular, the validation of the solvers themselves is particularly important, because this also provides end to end validation of the other codes.

Code Name	Description
<code>fwh_input</code>	Acoustic monopole input generation.
<code>fwh_ts2fwh</code>	Turbostream file conversion.
<code>fwh_interp</code>	Surface interpolation.
<code>fwh_p2q</code>	Source term construction.
<code>fwh_t2freq</code>	Frequency domain conversion.
<code>fwh_ret</code>	Observer dominant (retarded time) solver.
<code>fwh_adv</code>	Source dominant (advanced time) solver.
<code>fwh_freq</code>	Frequency domain solver.

Table 3.1: Description of FW-H solver codes.

## 3.1 Key Concepts

### 3.1.1 Periodicity

In the absence of installation effects, it was shown in Chapter 2 that the flow solution for a counter-rotating open rotor will be periodic in time in the rotating frame (see Equation 2.71), and that if the front and rear blade numbers share a common factor, the solution will also be rotationally periodic. All the codes in this thesis assume that provided flow solutions are periodic in time, hence care must be taken when using a non-periodic flow solution that sufficient time history is provided. The codes can also take advantage of any rotational periodicity in the flow solution. This allows significant savings in disc space and computation time.

### 3.1.2 Panel Averaging

In order to perform the surface integrals of Formulation 1A, a necessary step is to average the given node data to get representative values for each panel, in order to then multiply the resulting integrands by the panel area to perform the surface integral.

The solvers support two different types of panel averaging: “raw” averaging which averages the quantities directly read in by the solver, e.g.  $p'$  or  $n_i$  and “integrand” averaging which constructs the required integrands at each node and then averages these integrands for each panel. These two options form part of the solver study conducted in Chapter 4.

### 3.1.3 Propagation Time Calculation

As discussed in Chapter 2, an important part of the FW-H solvers is the calculation of the propagation time for the given source and observer pair. If the source does not rotate, there is an analytical solution for the propagation time called the Garrick triangle [28]. The triangle can be used both to calculate an emission time (observer dominant) or a reception time (source dominant), with some slight adjustments. For an observer dominant calculation, this triangle is illustrated in Figure 3.1, where  $A$  represents the location of the observer at the given time,  $B$  is the location of the source at the observer time, and  $C$  is the location of the source at the emission time.

The distance  $AB$  (denoted  $R_0$ ) and the angle  $\theta$  are known a priori because the current time and the kinematics of both source and observer are known. The distances  $AC$  and  $BC$  are a function of the propagation time  $\Delta t$ , with  $BC$  representing the distance travelled by the source point during the propagation time, and  $AC$  representing the true propagation distance. Normalising the sides of the triangle by  $c\Delta t$  leaves  $AB$ ,  $BC$  and  $AC$  equal to  $R_0/(c\Delta t)$ ,  $M$  and 1 respectively, with only  $\Delta t$  unknown. Applying the cosine rule to the normalised triangle leads to the following equation.

$$\Delta t = \frac{c}{AB \left( -M \cos \theta \pm \sqrt{M^2 \cos^2 \theta + 1 - M^2} \right)} \quad (3.1)$$

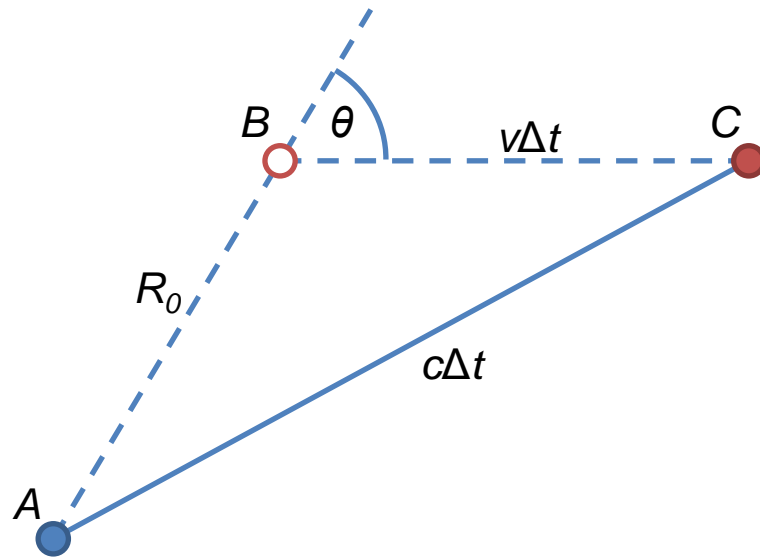


Figure 3.1: Illustration of the Garrick triangle.

Clearly, there are two solutions to this equation. The positive solution corresponds to the propagation time for a wave leaving the observer and arriving at the source, whereas the negative solution is the opposite way round, and is clearly the desired solution in this case.

In a source dominant solution, it is the source point whose time is fixed, and the observer time which is calculated as a result. Hence, the advanced time solution can be understood by reinterpreting Figure 3.1, with  $A$  representing the source location and  $B$  and  $C$  representing the locations of the observer at the source and reception times respectively. It should be clear that the positive solution represents a wave travelling from  $A$  to  $C$ , i.e. from source to observer, and is the correct solution in this case.

When the source is rotating, the observer dominant case of the above equation

cannot be applied, and there is no known, closed form solution to the problem. An iterative solution must be used, and it has been found that a damped Newton-Raphson approach based on the  $g = 0$  condition discussed in Chapter 2 is sufficient. Having fixed the observer location at time  $t$ , the problem becomes purely a function of the source time, and a given guess of the source time,  $\tau_n$ , can be used to find an improved guess,  $\tau_{n+1}$ , using the equations below. The damping factor of 0.25 was found to be sufficient to give robust behaviour for all cases considered in this thesis, with the only exception being cases that involved transonic motion, which cannot be handled by this approach as there are several valid emission times for a given source point.

$$g(\tau) = \tau - t + \frac{r(\tau)}{c} \quad (3.2)$$

$$g'(\tau) = 1 - M_r(\tau) \quad (3.3)$$

$$\tau_{n+1} = \tau_n - 0.25 \frac{g(\tau_n)}{g'(\tau_n)} \quad (3.4)$$

Due to the need to re-evaluate the source location for each iteration and the fact that each source time calculation requires several iterations, this iterative formula is much slower than using the Garrick triangle for a non-rotating point. Hence, interpolating a rotating surface to a non-rotating equivalent leads to much faster computation times in the FW-H solver. An important question to answer, which this thesis investigates in Chapter 4, is how this affects the accuracy of the calculation.

### 3.1.4 Surface Files

The geometry and kinematics of the FW-H surface can be specified in two formats. Inspection of Equations 2.50 and 2.51 should be sufficient to convince the reader that three things need to be known about the surface: the absolute frame position of the surface point and its associated time derivatives, the outward normal of the surface point and the area of a given panel of the surface.

For simple surface geometries, such as the spherical and cylindrical ones used in this thesis, all of these properties can be evaluated analytically for a given node distribution. Hence, the “full” format gives a list of nodes on each patch, giving body-fixed co-ordinates and outward normals for each one, as well as a list of panel areas. The codes can read this data in and calculate the effects of any surface motion (i.e. velocity, acceleration, etc.).

However, it is not possible to know normals and areas analytically in general, and this thesis briefly investigates the drawbacks of using complex FW-H surface shapes that require numerical evaluation of these properties in Chapter 4. Hence, the “simple” format gives just the node co-ordinates, and the codes use cross products of panel diagonals and/or mesh lines to calculate the associated normals and areas.

### 3.1.5 Flow Files

The format of the flow files is governed by two choices: whether the solution is time or frequency domain and whether the flow terms given are  $p'$ ,  $\rho'$  and  $u_i$  or  $Q$  and  $F_i$ . Each flow file specifies what combination of the above options it uses. The `fwh_freq` solver has specific requirements on the type of flow solution it can accept which are discussed later, but `fwh_ret` and `fwh_adv` can accept any combination of the above options.

## 3.2 Codes

Having defined the key concepts which underpin the structure and functionality of the different codes, this section now discusses each code in turn. The basic architecture of each code and any topics which are specific to its functionality are discussed first, before some validation that the code works as expected is presented. The FW-H solvers themselves are discussed as a group, as they have very similar basic architectures, and it is useful to validate all three at the same time.

### 3.2.1 Acoustic Monopole Input

The primary task of `fwh_input` is to generate flow solutions for acoustic monopole cases, but it can also generate its own surface and observer files as well. A broad overview of the resulting structure of the code is given in Figure 3.2.

The most important validation of the output of `fwh_input` is to confirm that the FW-H solvers can predict the generated noise to near perfection, i.e. to confirm that they have eliminated input and neglect errors. The checks presented here are intended to demonstrate two things that are important for this to be the case: that the relationship  $p' = c^2 \rho'$  is valid and that the linearised mass and momentum equations in Equations 2.60 and 2.61 are satisfied. A test case involving a single rotating, fluctuating monopole source and a rotating surface was created, as this represents the most complex motion required for both source and surface points.

The resulting pressure field on the  $(x, y)$  plane at  $\tau = 0$  is plotted in Figure 3.3, with the intersection with the surface patch also plotted. In order to examine convective derivatives and mass and momentum conservation, a single point on the surface, which is also marked in Figure 3.3, was selected.

Figure 3.4 plots  $p'$  and  $c^2 \rho'$ , confirming that the  $p' = c^2 \rho'$  condition is satisfied

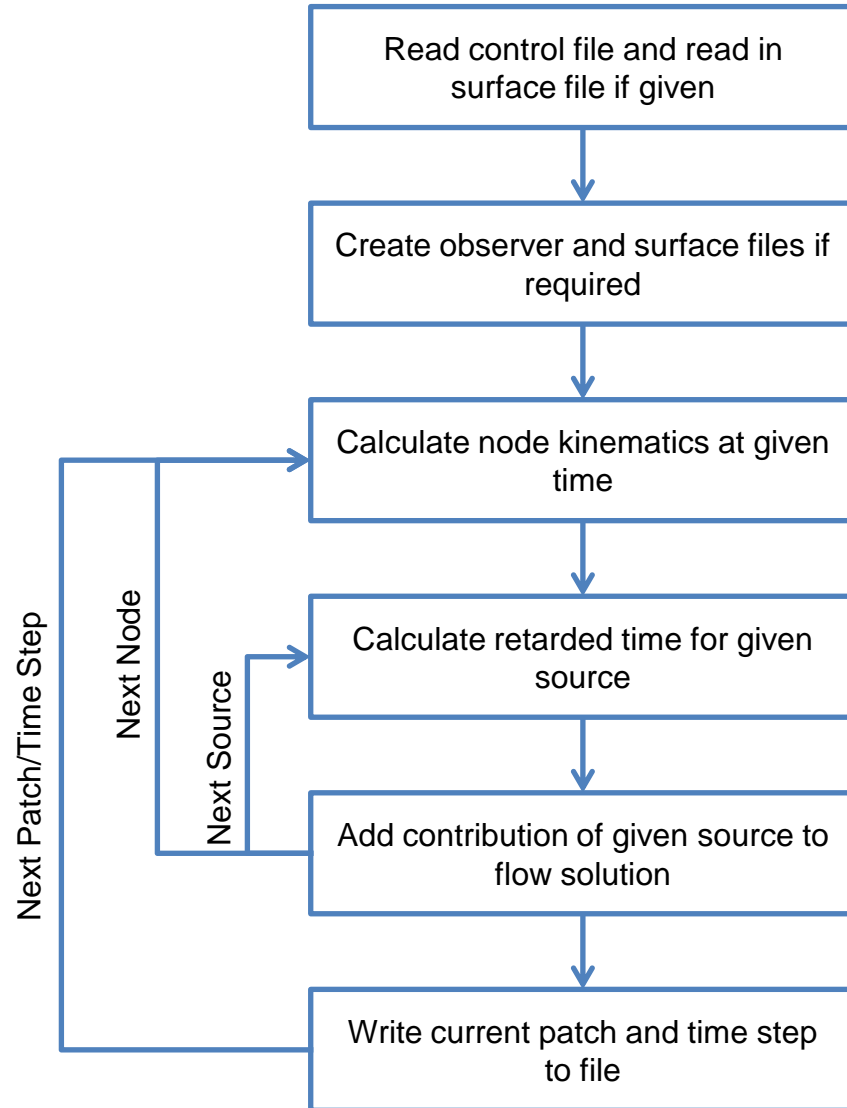


Figure 3.2: Basic schematic of `fwh_input` functionality.

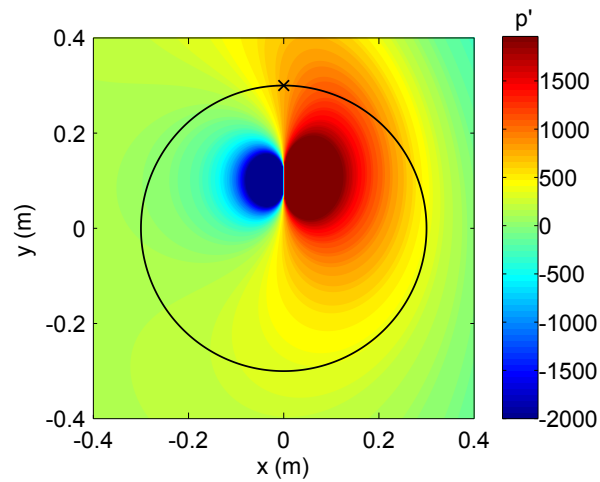


Figure 3.3: Pressure field, surface intersection (black line) and comparison point (red cross) for a rotating monopole.

with excellent accuracy. Figures 3.5 and 3.6 plot the time derivatives in Equations 2.60 and 2.61 against the negative spatial derivatives, and again the accuracy is excellent. This validates that the flow solutions output by `fwh_input` satisfy the  $p' = c^2 \rho'$  condition and the linearised Euler equations, as desired.

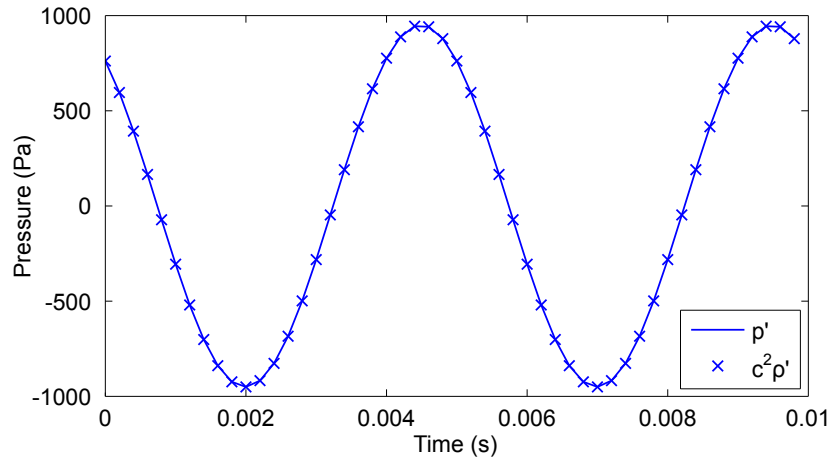


Figure 3.4: Comparison of  $p'$  and  $c^2 \rho'$  for a rotating monopole.

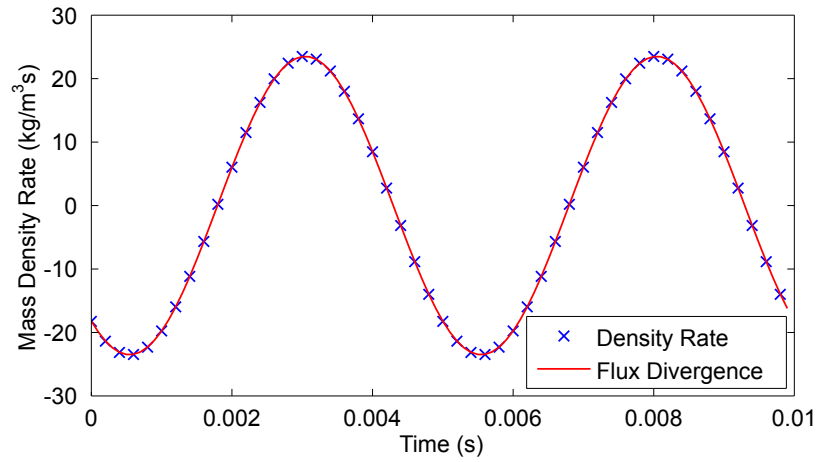


Figure 3.5: Mass conservation for a rotating monopole.

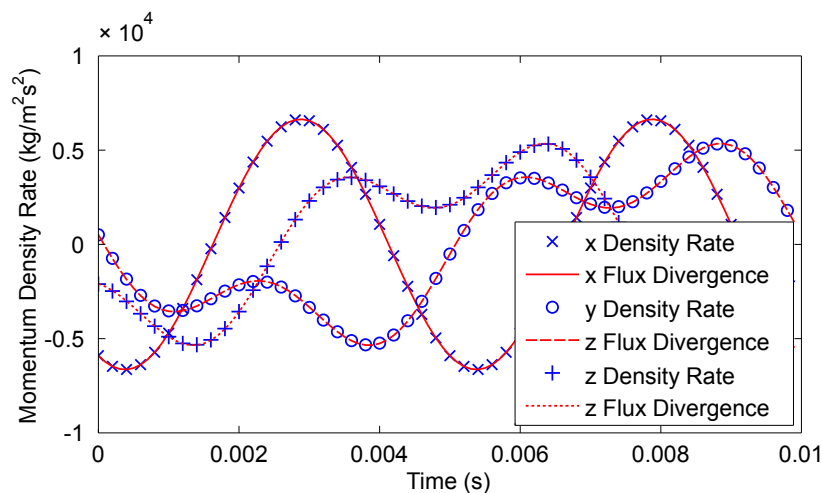


Figure 3.6: Momentum conservation for a rotating monopole.

### 3.2.2 Turbostream Input

In addition to generating input files from acoustic monopole cases, the codes also have to deal with flow solutions extracted from Turbostream runs. This was achieved using the `fwh_ts2fwh` code and some supporting MatLab scripts that are discussed below. The data output by Turbostream differed from the format required by the programs used in this thesis in two respects. Firstly, the extracted cut planes were specified in terms of an unstructured set of triangles, whereas data was required to be in a structured, quadrilateral format. Secondly, the flow solution at a given node was specified in a different form to the one required. How `fwh_ts2fwh` handles these two tasks is discussed, followed by a brief validation that the flow variables are correctly converted.

The basic architecture of `fwh_ts2fwh` is illustrated in Figure 3.7. It was possible to find a set of unstructured nodes to take from the input cuts to create structured surface patches because the meshes in Turbostream were structured, and the cut

data had been constructed from intersections of mesh lines with the cut surface. By isolating the nodes corresponding to two dimensions of the mesh lines, not the third, a structured grid could be recovered. An example of this is given in Figures 3.8 and 3.9, showing how some nodes corresponding to unwanted mesh lines are removed, and triangles in the input cut are amalgamated to create quadrilateral panels in the structured output.

In order to be consistent with the output of `fwh_input`, flow solutions need to be provided to the FW-H solvers in terms of  $p'$ ,  $\rho'$  and  $u_i$  and with vector terms evaluated in body-fixed, right-handed, Cartesian co-ordinates. However, Turbostream cut data is given in terms of the conserved properties  $\rho$ ,  $\rho u_i$  and  $\rho e$ , where  $e$  represents the total internal and kinetic energy of the fluid per unit mass. Additionally,  $\rho u_i$  is given in the frame of reference that convects with the surface but does not rotate, and in terms of left-handed cylindrical co-ordinates.

The density and velocity are trivially obtained from  $\rho$  and  $\rho u_i$ , however the pressure requires a little more effort. As air is treated as an ideal gas throughout this thesis, the appropriate expression for  $e$ , and the resulting required conversion for  $p$  (in terms of the conserved properties), are given in the below equations.

$$e = \frac{p}{(\gamma - 1)\rho} + \frac{1}{2}u_i^2 \quad (3.5)$$

$$p = (\gamma - 1) \left( \rho e - \frac{1}{2} \frac{(\rho u_i)^2}{\rho} \right) \quad (3.6)$$

Having calculated  $p'$ ,  $\rho'$  and  $u_i$  from the input data, all that is needed is to convert  $u_i$  to the correct Cartesian reference frame. In order to check these conversions, one of the cuts from the zero angle of attack take-off CFD case that is investigated

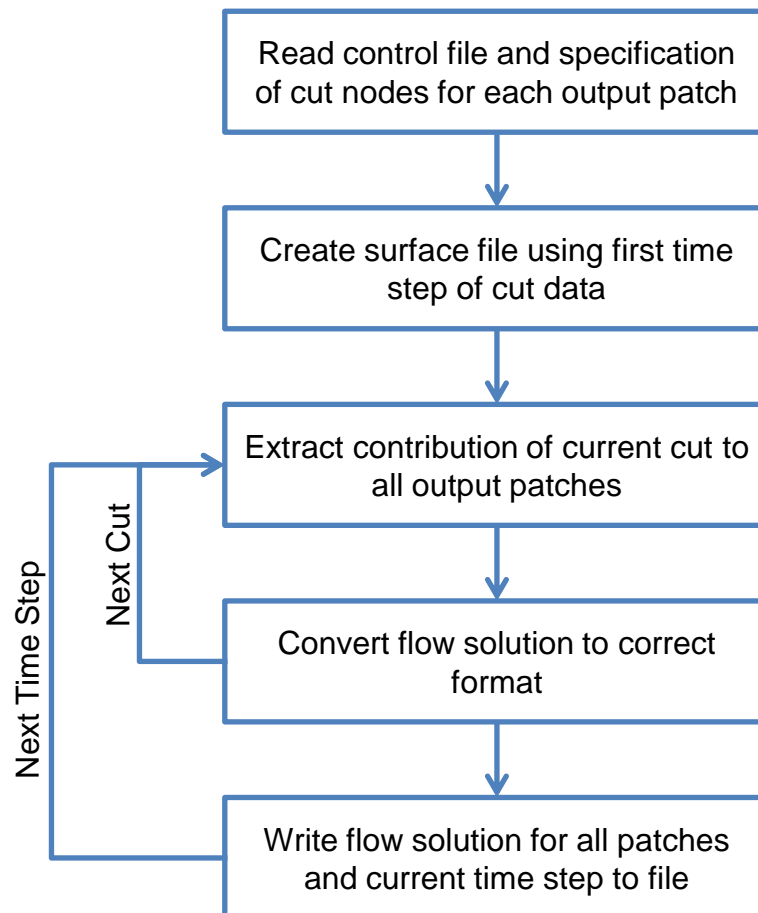


Figure 3.7: Basic schematic of `fwh_ts2fwh` functionality.

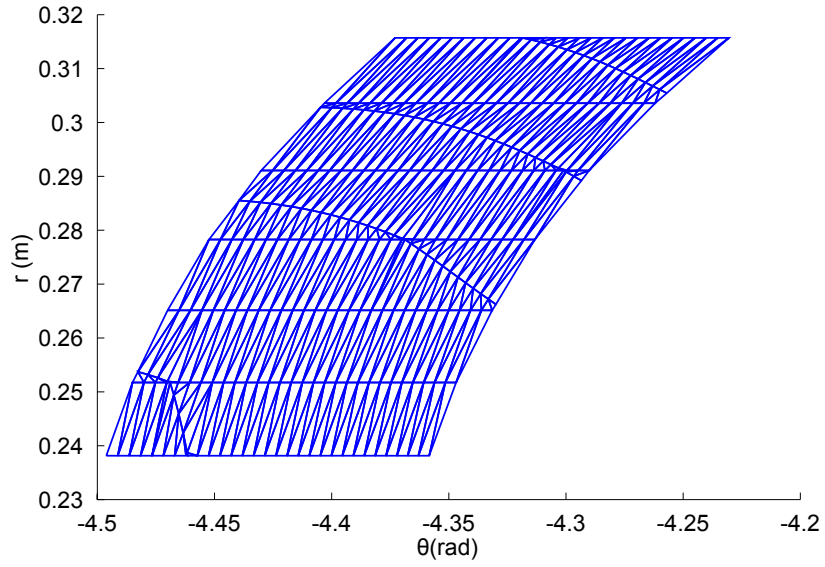


Figure 3.8: Unstructured cut taken from Turbostream.

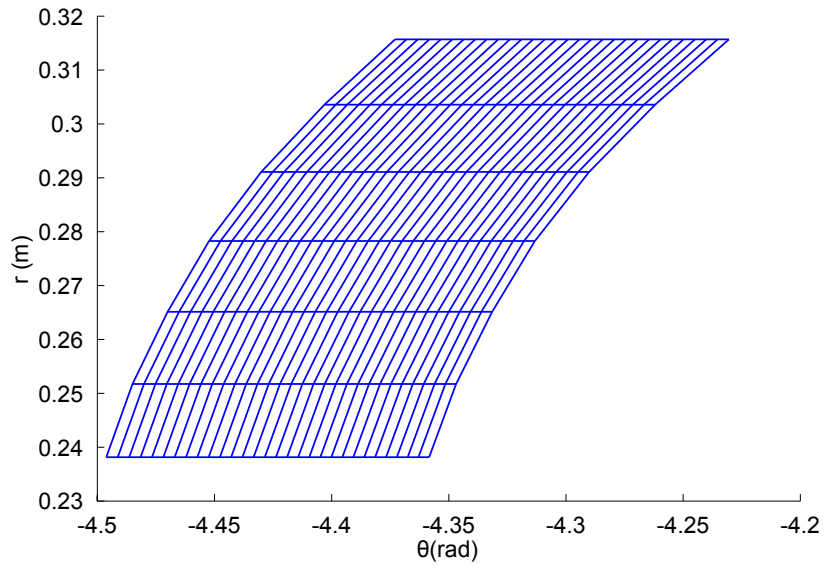


Figure 3.9: Structured cut output by mesh conversion algorithm.

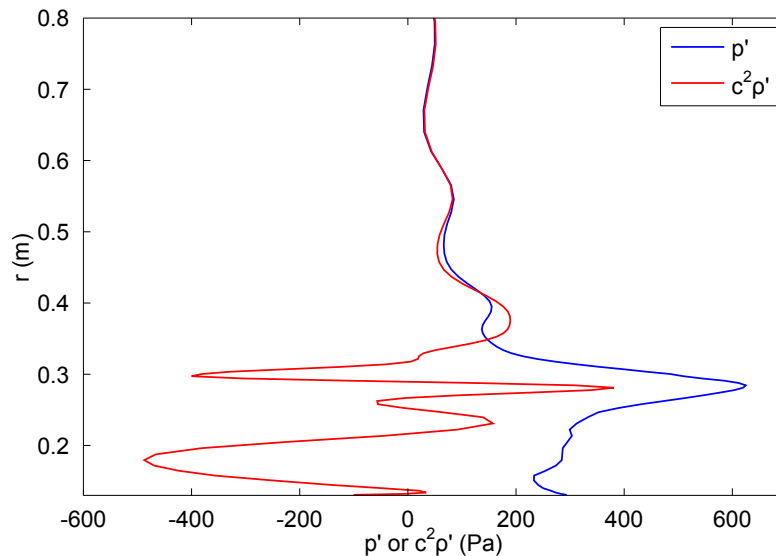


Figure 3.10: Pressure and density variation in output of `fwh_ts2fwh`.

in Chapter 6 was used. A single line of nodes running roughly radially and just downstream of the rear blade row was considered, and its flow solution was extracted for a single time step of the solution. The variation of  $p'$  and  $c^2 \rho'$  along the node line is plotted in Figure 3.10. The results are encouraging because the  $p' = c^2 \rho'$  condition appears well satisfied outside the source region. The velocity components are plotted in Figure 3.11, and the fact that these tend to zero away from the open rotor is good evidence that the conversion of reference frame is being performed correctly.

### 3.2.3 Surface Interpolation

As will be demonstrated in Chapter 4, the rotation of an FW-H surface introduces significant extra computational demand on an FW-H solver. Hence, it can be useful to interpolate a rotating flow solution onto a non-rotating one. Also, the surface

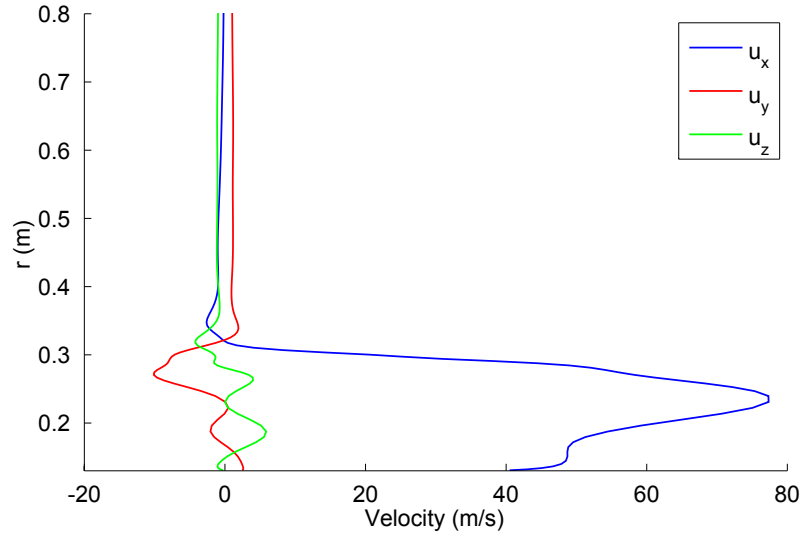


Figure 3.11: Velocity variation in output of `fwh_ts2fwh`.

patches created from Turbostream data extend through the entirety of the original CFD mesh domain, and hence a different set of structured patches need to be obtained which can be cropped at the relevant radius or axial position to construct a contiguous FW-H surface. These interpolations were performed using `fwh_interp`. The basic architecture of the code is illustrated in Figure 3.12.

A key assumption made by `fwh_interp` is that the surface is axisymmetric. This assumption is necessary to be able to interpolate a surface onto an equivalent one that is rotating at a different speed. As a result, the basic shape of the surface, rather than the specific locations of nodes on that surface, can be parametrised as a function of axial and radial co-ordinates, denoted  $(\eta_X, \eta_R)$ . The three-dimensional node co-ordinates are then parametrised in two dimensions, using the tangential angle,  $\theta$ , and the distance along the shape profile, which will be referred to as  $s$ . Hence, rotation of a given surface patch was trivially handled by incrementing the

value of  $\theta$  for each point.

The main task of `fwh_interp` is to establish the location of each desired output point on the input surface and interpolate the flow solution onto that point. The algorithm used to perform this search is illustrated in Figure 3.13, showing how the algorithm would treat two input patches, A and B, when looking for overlap with an output patch, C. The algorithm uses a “divide and conquer” approach to first examine whether an entire input and output patch have any overlap, before recursing into smaller pieces of each patch. Patch A is immediately disregarded because its  $\theta$  range does not overlap with that of patch C. However, the  $\theta$  and  $s$  ranges of patch B are within the ranges of patch C, and hence the code would recurse into this combination. At this point, B and C are split into smaller pieces that are individually compared, and the only pair of pieces which do not fail the range tests are B4 and C3. The code would then further recurse into this combination and so on until the individual input panels which the overlapping output nodes are in are found. Bicubic Hermite interpolation is then used to find the flow solution at each output node.

As with `fwh_input`, the most important validation of `fwh_interp` is that the flow solutions it gives lead to accurate results from the FW-H solvers, which will be demonstrated later. For now, it will simply be shown that an analytical flow solution derived on a rotating surface can be interpolated to a non-rotating surface, and that the output flow solution is consistent with the flow solution for the non-rotating surface as derived directly by `fwh_input`.

The input flow solution used was the same as that used in the validation of `fwh_input` above. This flow solution was interpolated onto an output surface identical to the input surface in every respect except that it did not rotate, and the exact flow solution on this output surface was also calculated directly using `fwh_input`. The time histories of  $p'$  for the same point as used in the `fwh_input` validation for the

three different surfaces are compared in Figures 3.14. It is clear that the interpolated solution is almost identical to the analytical equivalent even though the equivalent point on the rotating surface has an entirely different solution. This confirms that the interpolation algorithm has successfully tracked the motion of the non-rotating point across the rotating surface, and calculated the correct corresponding solution.

### 3.2.4 Source Term Construction

The flow solutions output by `fwh_input` and `fwh_interp` are given in terms of  $p'$ ,  $\rho'$  and  $u_i$ . In order to be able to use `fwh_freq`, it is useful to be able to specify the flow solution in terms of  $Q$  and  $F_i$ . The code used to perform this conversion is called `fwh_p2q`. It reads in a surface and flow solution, converts that flow solution to the desired format, and writes it out to a set of output files. The way in which  $Q$  and  $F_i$  are formed depends on the conservation equations being used and the method for constructing acoustic source terms from them, as discussed in Chapter 5. This leads to six different possible outputs for a given input flow solution. The easiest way to validate the output of this code is to demonstrate its accuracy when used as input to the FW-H solvers, and so the validation of the solvers given later acts as implicit validation of `fwh_p2q`.

### 3.2.5 Frequency Domain Conversion

Frequency domain flow solutions are used extensively throughout this thesis, and the most common method for extracting the frequency content of a signal is the Fast Fourier Transform (FFT). However, an FFT assumes that the given signal is periodic over the sampling period, and hence that the signal is formed from a set of integer harmonics of the periodic frequency. As discussed in Chapter 2, this is often

not true for time histories in open rotor flow solutions, due to the different front and rear rotational speeds as well as installation effects.

The consequences of this problem are demonstrated in Figures 3.15 and 3.16, which show the results of using an FFT on a sinusoid of unit magnitude and frequency 1Hz. The signal is sampled at 40Hz for periods of 1s (periodic) and 1.5s (non-periodic). The resulting frequency content gives the desired single tone at 1Hz for the periodic case, but the non-periodic case gives a range of frequency components. Plotting the signals given by the inverse FFT from each case against the original time signal shows how the FFT has forced the frequency content to reflect a periodic signal, creating a step discontinuity for the 1.5s case that explains the unwanted frequency content.

Hence, a different method for extracting frequency content is used in `fwh_t2freq`. The method will be referred to as Least Squares Spectral Analysis (LSSA), but has also been referred to as the Vanicek method [83] in other research. The methodology requires prior knowledge of the expected frequency components, and calculates a set of discrete mode shapes at the given sample times, before finding a least squares fit of the modes to the data.

If the frequencies which compose the signal are known or assumed in advance, then the original signal must be composed of a sum of pairs of cosine and sine components for each frequency, plus a constant offset. If the original sample set of points from the signal is denoted by the vector  $q_i$ , the sample times  $t_i$  and the required magnitudes of each mode shape  $k_j$ ,  $q_i$  and  $k_j$  must be related by a matrix of the mode shapes, denoted  $A_{ij}$ . This relationship is defined below, as well as defining how the mode shapes are constructed from the given vector of angular frequencies,  $\omega_i$ .

$$q_i = A_{ij}k_j \quad (3.7)$$

$$A_{i,1} = 1 \quad (3.8)$$

$$A_{i,2j} = \cos(\omega_j t_i) \quad (3.9)$$

$$A_{i,2j+1} = \sin(\omega_j t_i) \quad (3.10)$$

Unlike the FFT, Equation 3.7 cannot always be solved exactly for  $k_j$ , i.e.  $A_{ij}$  is rarely square, let alone invertible. Instead, a least squares solution can be used to get the “best guess” for the solution, i.e. the solution for  $k_j$  which gives an estimate of  $q_i$  which is as close as possible to the original  $q_i$ .

The least squares solution can be found using Q-R factorisation [33, 34], which itself can use Gram-Schmidt orthogonalisation [32] for establishing a set of orthogonal basis vectors. Having found the least squares fit for  $k_j$ , the resulting estimate of the original  $q_i$  can be found, and hence the “residual” signal, i.e. the part of the original signal which is unaccounted for, can be calculated and investigated to check it is suitably negligible. If a tone is found in the residual at a frequency that was not included in the least squares fit, it can be added to the fit and the analysis rerun.

In order to check the implementation of the LSSA algorithm in `fwht2freq` and demonstrate its worth, the periodic and non-periodic sample sets used in Figures 3.15 and 3.16 were analysed using LSSA with the exact same frequency components as used by their respective FFT’s. The resulting frequency component magnitudes are plotted in Figure 3.17. As expected, the results are identical to those obtained from the corresponding FFT, validating that LSSA can reproduce an FFT if used with

the same sample set and frequency content. The LSSA for the non-periodic sample set was then re-run with only the 1Hz tone specified. Clearly, this still correctly calculates the magnitude of tone, without needing the extra tones in the frequency set or a periodic signal. This demonstrates the key advantage of LSSA over the FFT, that it can recover accurate frequency information even with a sparse, non-periodic frequency content.

As a more onerous test, Figure 3.18 shows how the residual signals can be used to identify missed frequency content. A signal composed of a unit cosine of frequency 1.5 Hz and a cosine of frequency 2.3 Hz and magnitude of 0.1 was sampled at 20 Hz over a period of 1 s. Initially, an FFT is performed to give a rough idea of the frequency content, and clearly shows a peak near 1.5 Hz, but the spreading of this tone by the FFT has “drowned out” the 2.3 Hz tone to a large extent. Imagining that the physics of the problem is understood well enough to know that a tone at 1.5 Hz is plausible, the LSSA method was run with just this frequency component specified.

Even without specifying the 2.3 Hz tone, it is clear from Figure 3.18 that the LSSA method has still resolved the 1.5 Hz tone better than the FFT. Also, inspection of the FFT of the residual of this run highlights a tone at around 2.3 Hz. Including this in the LSSA method leads to accurate prediction of both frequency components and a negligible residual signal, as expected and desired. This process of identifying which tones are important in a given flow solution is useful because it allows the minimum set to be extracted, which both saves disk space taken up by flow solutions and minimises calculation time in the FW-H solvers.

### 3.2.6 Solvers

Three different solvers of Farassat's Formulation 1A have been developed, with the key difference between each being their use of observer dominant (`fwh_ret`), source dominant (`fwh_adv`) and frequency domain (`fwh_freq`) propagation algorithms. The basic architecture of all three solvers is illustrated in Figure 3.19.

Both the time domain codes can use either time or frequency domain flow solutions. If a time domain flow solution is used, all interpolation and calculation of time derivatives not specified in the input files is performed using cubic Hermite interpolation. For frequency domain flow solutions and the frequency domain solver, properties are evaluated analytically from the given frequency components.

As discussed in Section 2.3, the frequency domain approach relies on only one element in each of the Formulation 1A integrands containing frequency content. The two important limitations this places on `fwh_freq` is that both the FW-H surface and the observer must move at the same constant velocity (i.e. no surface rotation), such that propagation times and kinematic terms do not vary with source or observer time, and that the flow solution provided must be a frequency domain solution in  $(Q, F_i)$  format. For a rotating input surface, this requires all three pre-processing codes, `fwh_interp`, `fwh_p2q` and `fwh_t2freq`, to be used.

It should be noted that `fwh_freq` requires no interpolation through a time history, whereas `fwh_ret` needs to interpolate through the source time history, and `fwh_adv` needs to interpolate through the observer time history. While this seems like a big advantage over these other codes, the steps required to produce a non-rotating, frequency domain flow solution have their own numerical methods attached to them (i.e. the need to use `fwh_interp` and `fwh_t2freq`). Hence it is important to examine which approach is better, as will be the subject of Chapter 4.

As has been discussed in the preceding sections, many of the codes, and the file formats they can accept, can be configured and run in different ways. These different possibilities are listed as follows:

- Simple or full surface file formats can be used.
- The flow solution can be interpolated onto a non-rotating surface.
- The flow solution can be converted to the frequency domain.
- $Q$  and  $F_i$  can be constructed in six different ways.
- Panel averaging can be performed in two different ways.
- Three different propagation algorithms can be used.

In theory, all of the above options can be picked in any combination and the codes will still run, giving 288 combinations that could be used. This section will only seek to demonstrate that the three solvers can each predict the frequency content of a given source distribution accurately from the same rotating input flow solution. Solving this using `fwf_freq` necessitates the use of `fwf_interp`, `fwf_p2q` and `fwf_t2freq`, and hence these codes are implicitly validated by these results. In addition, the rotating solution requires use of the iterative propagation time solution, whereas the interpolated solution uses the Garrick triangle method, validating that both of these are capable of producing accurate results. All methodologies use a simple surface format, no analytical time derivatives, the original FW-H method of constructing acoustic source terms and raw panel averaging. More advanced methodologies using the other options are examined in Chapter 4, and the results act as validation of those approaches.

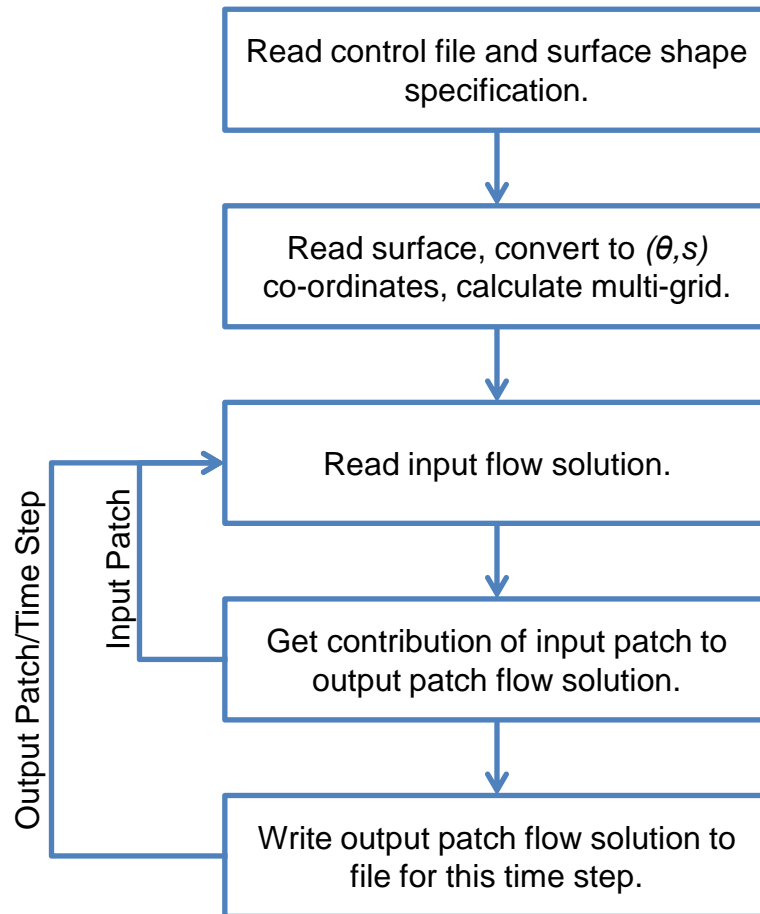
The surfaces and time domain flow solutions are the same as used in validating `fwh_interp`. The observer moves at the same forward speed as the surface, and is initially located at  $x_i = (1, 1, 0)$ . The flow solution, and hence the observer pressure signal, is periodic in the non-rotating frame with a period of 0.01 s. Observer time histories are calculated at a rate of 20 kHz, or 200 points per period. The original, rotating flow solution was first interpolated onto an equivalent, non-rotating surface. Then, it was passed through `fwh_p2q` before being converted to a frequency domain flow solution using `fwh_t2freq`, which looked for a set of harmonics of the fundamental 100 Hz tone up to 1.8 kHz. Note that the Nyquist limit for the given sampling rate of 20 kHz is 10 kHz, and therefore the frequency set used represents a heavily cropped set compared to the theoretically complete set that would be calculated by an FFT. The accurate results presented below demonstrate that the decomposition is perfectly valid for this application, and it is worth noting that it replaces 200 snapshots in a time domain flow solution with just 37 in the frequency domain solution.

The original flow solution, as well as the interpolated output of `fwh_interp` and the final frequency domain flow solution, were all run through both `fwh_ret` and `fwh_adv`, and the frequency domain solution was also run through `fwh_freq`. The time domain results are split between `fwh_ret` and `fwh_adv` and are compared with the analytical solution in Figures 3.20 and 3.21. Note that only every fourth sample of the observer time histories is plotted for the sake of clarity. The associated frequency content and the results for the `fwh_freq` run are plotted in Figure 3.22.

It is clear that all of the results give highly accurate predictions, with accuracy only failing at high frequencies and several orders of magnitude below the loudest tones. This is excellent validation that all the solvers and the associated pre-processing codes are working as expected.

### **3.3 Summary**

This chapter has presented the main numerical methods used in this thesis. It has been shown that a wide range of solver methodologies can be investigated using these methods, and that a flow solution based on a set of acoustic monopoles can be extremely accurately predicted by the methods if resolution on the surface is high enough. In other words, acoustic monopoles have no input or neglect errors and hence are a useful way of isolating the discretisation errors generated by a given solver methodology. It has also been shown that the CFD flow solutions obtained from Turbostream on an unstructured grid can be accurately converted to the required format.

Figure 3.12: Basic schematic of `fwh_interp` functionality.

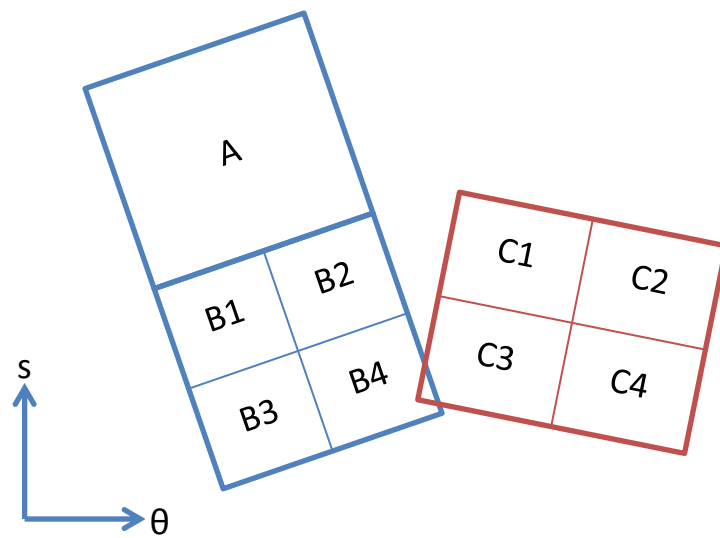
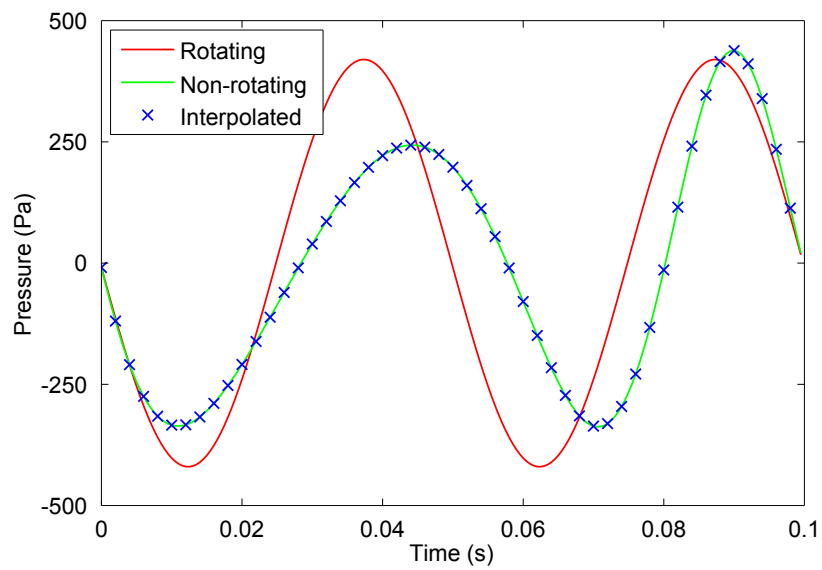
Figure 3.13: Illustration of `fwh_interp` overlap algorithm.

Figure 3.14: Pressure signals for rotating, non-rotating and interpolated surfaces.

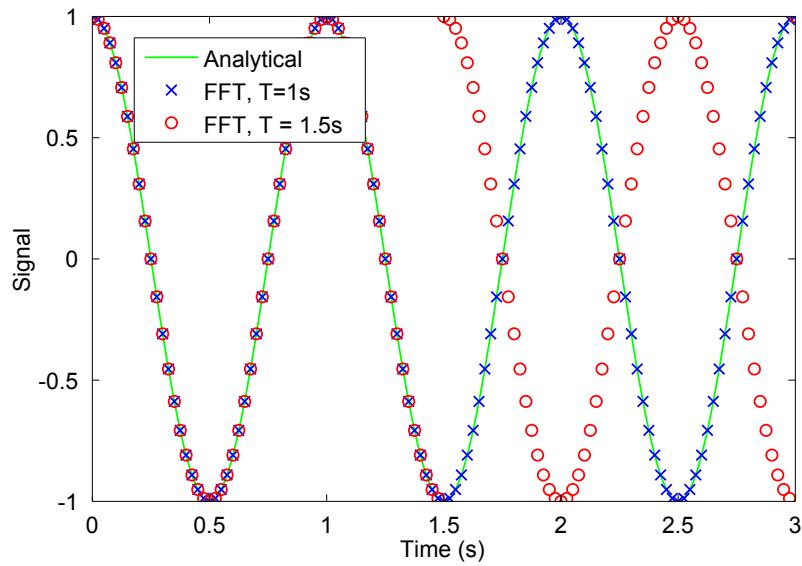


Figure 3.15: Time domain comparison for FFTs using different sample periods.

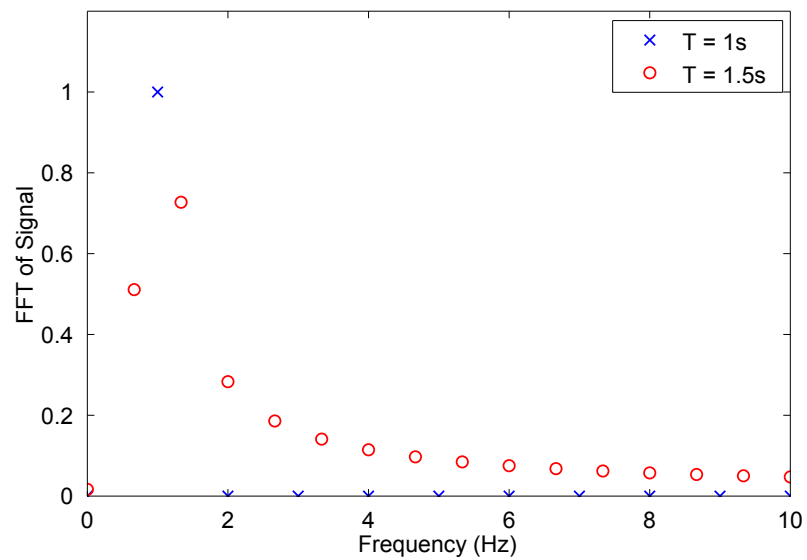


Figure 3.16: Frequency domain comparison for FFTs using different sample periods.

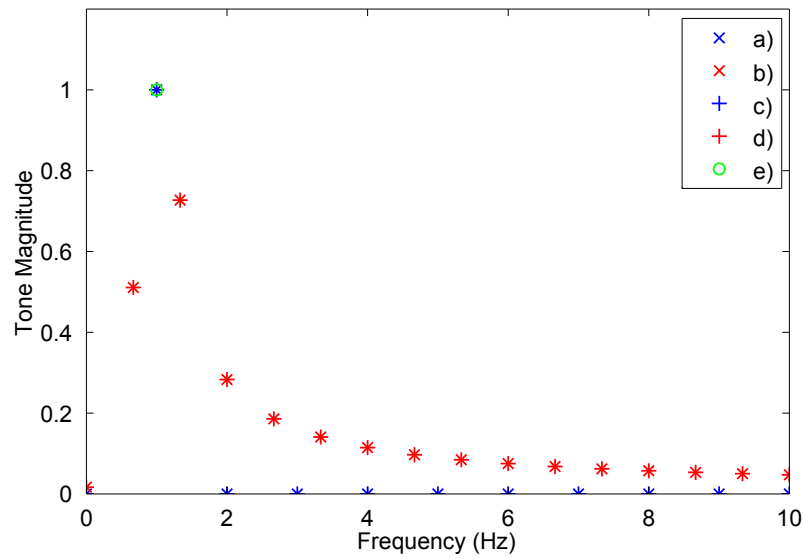


Figure 3.17: Frequency components calculated by a) FFT and periodic sample, b) FFT and non-periodic sample, c) LSSA with periodic sample and all tones, d) LSSA with non-periodic sample set and all tones, and e) LSSA with non-periodic sample set and the 1 Hz tones.

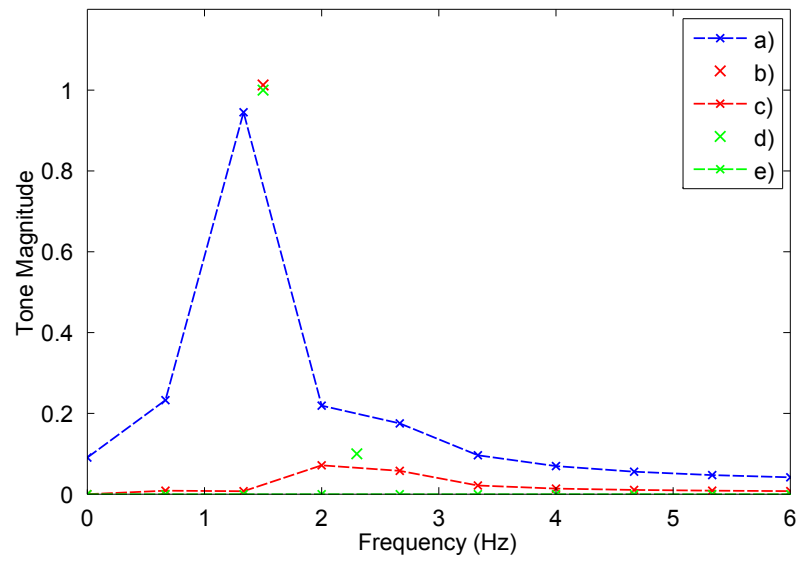


Figure 3.18: Results of LSSA method refinement, showing a) original FFT, b) LSSA using one tone, c) FFT of the corresponding residual, d) LSSA using both tones, and e) FFT of the corresponding residual.

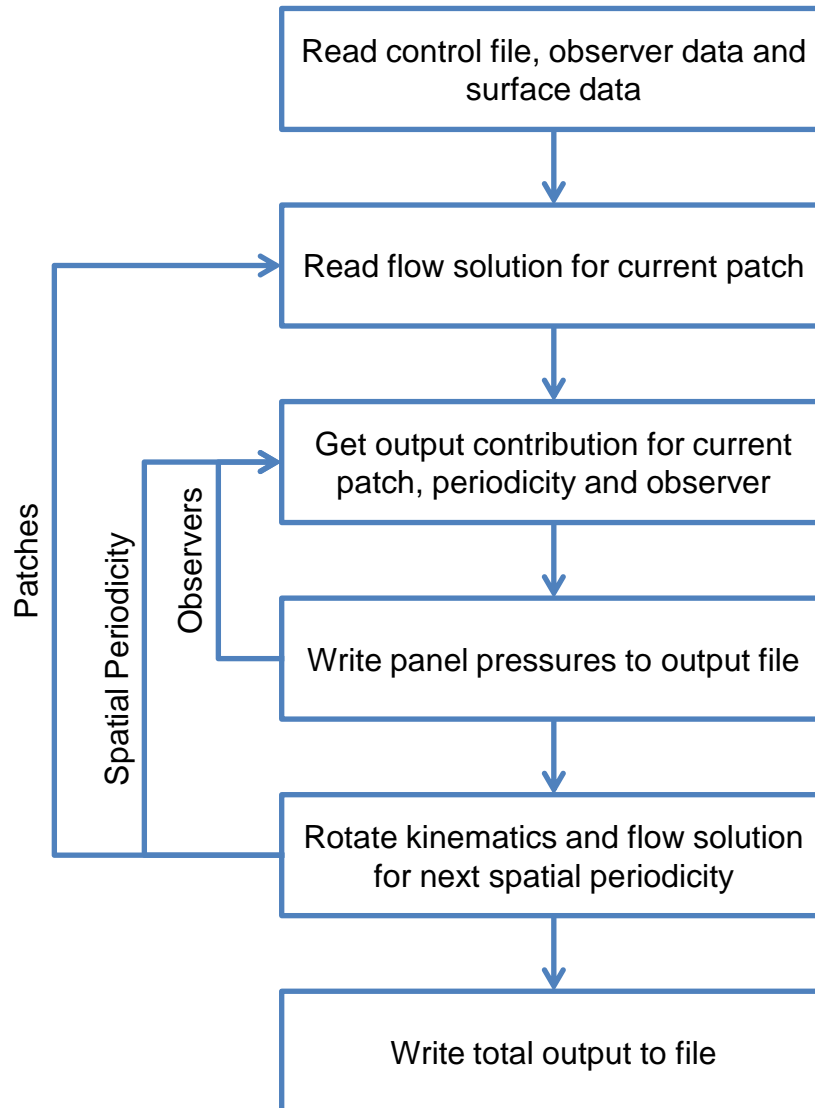
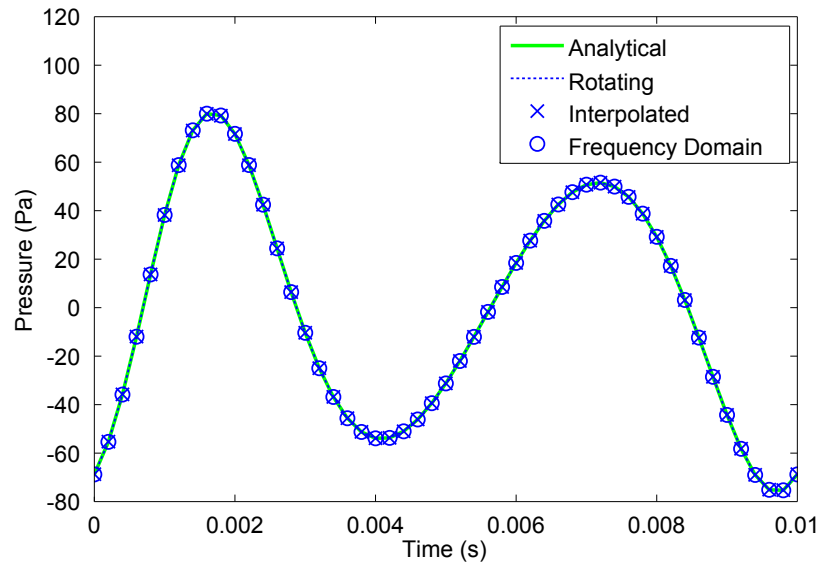
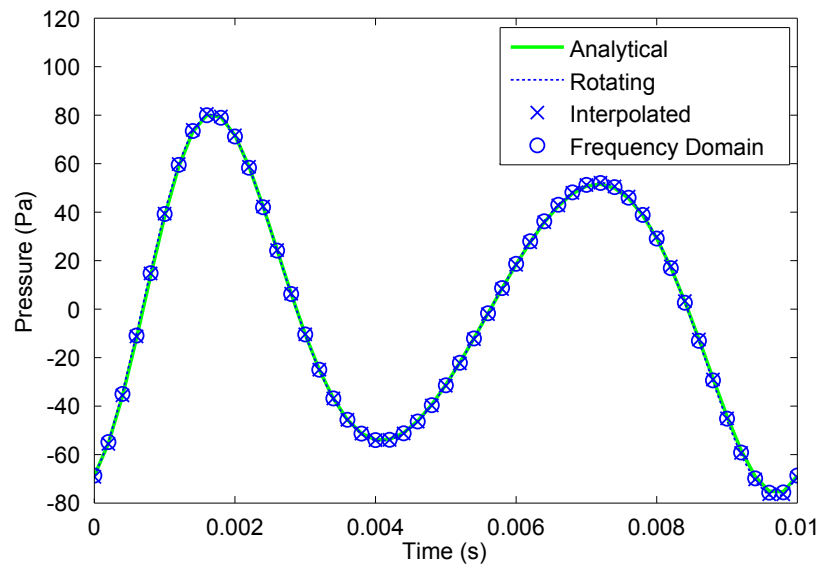


Figure 3.19: Basic schematic of FW-H solver functionality.

Figure 3.20: Time domain validation results for `fwh_ret`.Figure 3.21: Time domain validation results for `fwh_adv`.

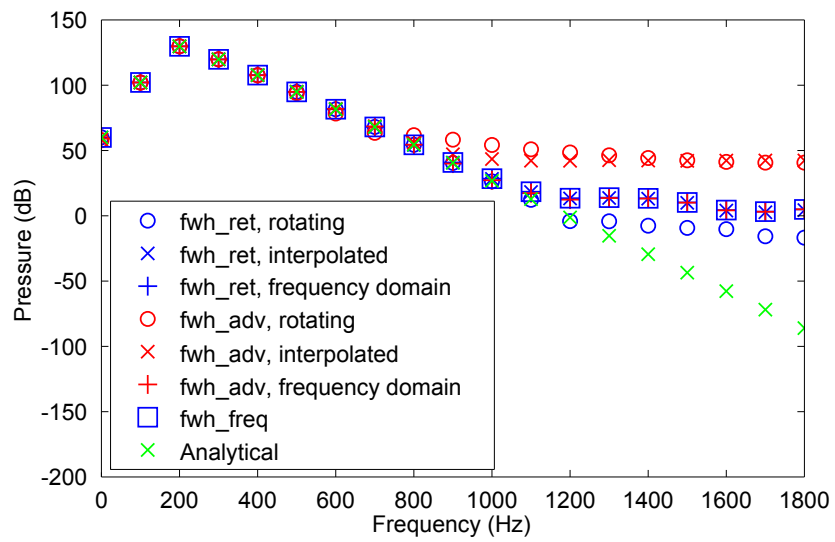


Figure 3.22: Frequency domain validation results for all codes.



# Chapter 4

## Discretisation Errors

This chapter presents research into understanding and mitigating discretisation errors. It has been shown in Chapter 2 that there has been very little previous work investigating discretisation errors, which underlines the need for a detailed approach to the problem from first principles.

In particular, three key objectives have been defined in Chapter 1 relating to discretisation errors. Firstly, a proper understanding of the causes of discretisation errors needs to be given, as well as any phenomena which affect a problem's sensitivity to these errors. Secondly, dimensional analysis needs to be used to develop a rigorous process for parametrising and investigating discretisation errors in FW-H solvers. Finally, this process needs to be used to investigate the various solver methodologies presented in the Chapter 3 in order to select a best practice methodology for open rotor noise prediction.

In line with these objectives, this chapter defines a categorisation of discretisation errors and presents simple demonstrations of each type that lead to the definition of key non-dimensional metrics. It also demonstrates the significant effect that surface

motion has on a problem's sensitivity to discretisation error, in particular surface rotation. Having established a clear understanding of discretisation errors, it is acknowledged that there are two subtly different types of investigation that engineers may want to undertake, and it is shown that dimensional analysis should be applied slightly differently depending on which type of study is being undertaken.

In order to apply this analysis to open rotor noise prediction, an analytical test case that is more representative of an open rotor than any known previous work is presented. The above dimensional analysis is performed on the test case, leading to a rigorous definition of the non-dimensional groups governing the problem. As acknowledged in the previous chapter, the number of options available in configuring a particular solver methodology is large, and hence some intuition is used in selecting a progression of methodologies that begin with an industry standard methodology, gradually introducing improvements until a best practice methodology is established. Thus, all three objectives are fully satisfied by the work presented in this chapter.

## 4.1 Basic Principles

The first objective of this thesis is to develop a clear understanding of the sources of discretisation error. This section addresses this objective by assuming that the problem is composed of a flow solution, a discretised surface placed in that flow solution and an observer placed outside of that surface. It is further assumed that only the flow solution is discretised in time, whereas the variation of any geometric and observer parameters in time is known analytically. This allows discretisation errors to be categorised in terms of “geometric”, “flow” and “observer” resolution, i.e. how well terms in the formulation of solution pertaining to each of these components are resolved in the surface integral being solved, with an accurate answer only being

possible if all resolutions are good enough. This section presents discussion and simple demonstrations of each type of discretisation error, as well as the effect of surface motion on a problem’s sensitivity to discretisation error.

### 4.1.1 Geometric Resolution

Geometric resolution describes how accurately the shape of the surface is defined by its discretised form. The terms in the formulations of solution that this will affect are the panel normals and areas. A simple test case to demonstrate the importance of this is defined in Table 4.1 and illustrated in Figure 4.1. The surface had the same number of panels in the latitudinal and longitudinal directions, denoted  $N_P$ , which was varied and the corresponding observer signals compared to the analytical solution.

As discussed in Chapter 3, two different surface formats can be used. The “full” surface format contains the node co-ordinates as well as the analytical solution for the normals and panel areas for a spherical surface, whereas the “simple” surface only gives the node co-ordinates, requiring the solvers to calculate the normals and panel areas numerically. Both surface formats were tested using `fwh_ret`.

The symmetry of the source terms and the low frequency (and hence long wavelength) of the source fluctuation meant that the flow resolution in space was extremely good. The high sampling frequency meant the same was true of the flow resolution in time, and the large distance to the observer meant the observer resolution was also excellent. All components of the problem were stationary, and hence the only thing significantly affected by varying  $N_P$  was the accuracy or the panel area calculation for the simple surface geometry. The error metric used was the root mean squared (RMS) of the error between the calculated and analytical observer

Variable	Description	Units	Value
$c$	Bulk speed of sound	$\text{m s}^{-1}$	340
$\rho_0$	Bulk density	$\text{kg m}^{-3}$	1.2
$Q_M$	Magnitude of source strength fluctuation	$\text{kg s}^{-1}$	1
$\omega$	Frequency of source strength fluctuation	$\text{rad s}^{-1}$	$\pi$
$v_X$	Forward velocity of source/surface/observer	$\text{m s}^{-1}$	0
$R$	Radius of surface	m	0.3
$\Omega$	Rotational velocity of surface	$\text{rad s}^{-1}$	0
$L$	Source/observer separation	m	100
$\theta$	Directivity of observer (in $x$ - $z$ plane)	$^\circ$	0
$N_P$	Number of latitudinal/longitudinal panels	-	2 - 40
$\Delta t$	Flow solution time step	s	0.01

Table 4.1: Parameters for geometric resolution test case.

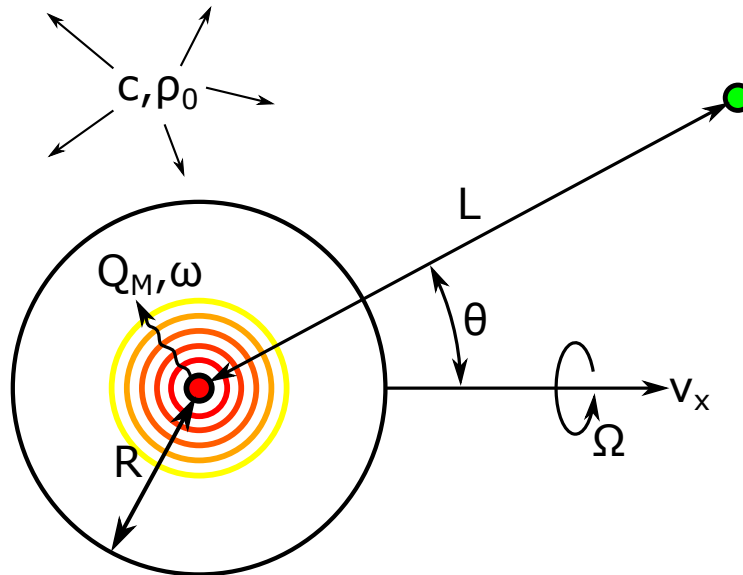


Figure 4.1: Illustration of simple acoustic monopole test case.

pressure signals, normalised by the RMS of the analytical signal, denoted  $\epsilon_{RMS}$  and defined below.

$$\epsilon_{RMS} = \frac{(p'_{calculated} - p'_{analytical})_{RMS}}{p'_{analytical,RMS}} \quad (4.1)$$

The effect of varying  $N_P$  on  $\epsilon_{RMS}$  for the two different surface types is given in Figure 4.2. Clearly, the full surface geometry (including analytically calculated panel areas) remains accurate regardless of the value of  $N_P$ , whereas the simple surface is heavily affected at low  $N_P$  due to its inability to accurately calculate the panel normals and areas. This demonstrates that geometric resolution can cause significant errors in an acoustic integral solver. It also shows that a full surface format using the analytical solutions for geometric quantities can greatly mitigate these errors. All the integration surfaces considered in this thesis are either spherical or cylindrical, and hence a full surface format can be used. Hence, geometric resolution is not expected to be important for the work presented in this thesis. This is likely to be the case for many problems of interest, where the integration surface is a reasonably simple shape with a large number of panels ( $N_P \gg 40$ ). It is possible that cases where the integration surface is made coincident with a real physical surface with a complex shape, e.g. an open rotor blade, would be more susceptible to these errors.

### 4.1.2 Observer Resolution

Observer resolution describes the ability of the discretisation of the surface to accurately resolve the variation of the relative observer position (i.e. the magnitude and direction of  $r_i$ ) on the surface. This can also be thought of as describing the resolution of the propagation of the sources on the surface to the observer. If the magnitude and/or direction of  $r_i$  varies strongly from one panel to another (i.e. if the

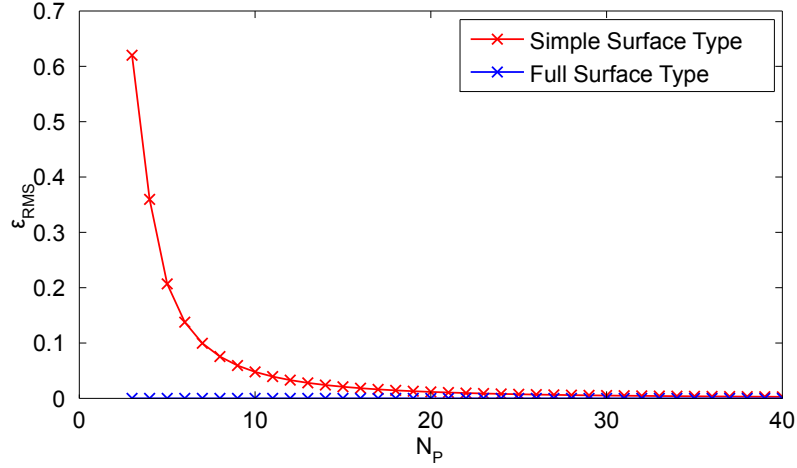
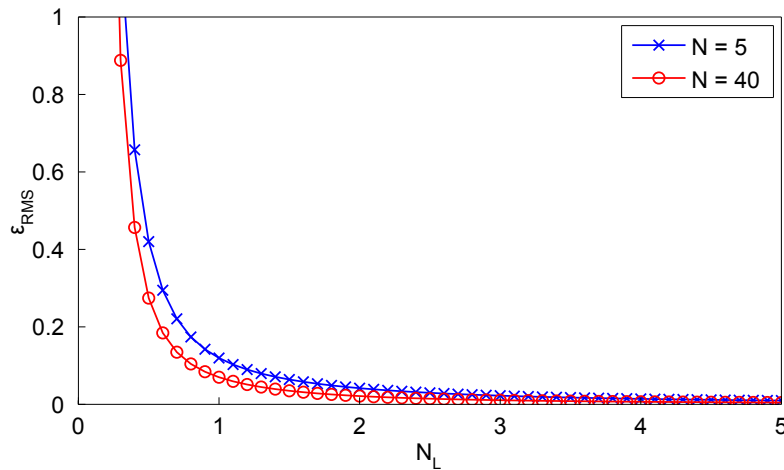


Figure 4.2: Variation of  $\epsilon_{RMS}$  with  $N_P$ .

observer is close to a part of the surface), the surface integral will be poorly resolved compared to a more distant observer.

A test case similar to that used for demonstrating geometric resolution was used to demonstrate observer resolution, the only differences being that  $L$  was varied for  $N_P = 5$  and  $N_P = 40$ , and that only the full surface specification was used, so that the geometric resolution was excellent in all cases. The key cause of observer resolution error is the distance to the observer becoming too small relative to the size of the panels on the surface, and hence the minimum distance from the surface to the observer,  $L - R$ , was normalised by a panel length scale,  $\lambda_P$ , defined below. This length scale represents the square root of the average panel area. The normalised parameter is denoted  $N_L$  and represents the minimum number of panel length scales between the surface and the observer.

Figure 4.3: Variation of  $\epsilon_{RMS}$  with  $N_L$ .

$$\lambda_P = \sqrt{\frac{4\pi R^2}{N_P^2}} \quad (4.2)$$

$$N_L = \frac{L - R}{\lambda_P} \quad (4.3)$$

The variation of  $\epsilon_{RMS}$  against  $N_L$  is shown in Figure 4.3 for the two values of  $N_P$ . It is clear that the observer only needs to be a few panel length scales away from the surface for observer resolution to be very good. As with geometric resolution, this means that observer resolution is unlikely to be significant in this thesis and many other problems of interest. This is because it is rare to want to calculate the noise very close to the integration surface, as this can usually be extracted directly from the underlying CFD.

### 4.1.3 Flow Resolution

As already discussed, the resolution of the flow solution differs from the other two types of resolution in that it is discretised in both space and time. As for the observer resolution demonstrations, the number of panels corresponding to a particular length scale is a useful metric for flow resolution in space. The obvious choice for the length scale is the wavelength of the flow perturbations, and the resulting non-dimensional parameter is defined as  $N_\lambda$  below. The observer resolution test case was used with  $L = 100$  and with  $\omega$  set to the value defined below, such that  $N_P = N_\lambda$ . As a result, varying  $N_P$  was equivalent to varying  $N_\lambda$  (a full surface specification was used so that geometric errors were negligible). Finally, the discretisation in time can be parametrised in a similar way, by defining  $N_T$  as the number of time steps per period of the flow fluctuations, as below.

$$\omega = \frac{2\pi c}{\sqrt{4\pi R^2}} \quad (4.4)$$

$$N_\lambda = \frac{2\pi c}{\omega \lambda_P} \quad (4.5)$$

$$N_T = \frac{2\pi}{\omega \Delta t} \quad (4.6)$$

The variation of  $\epsilon_{RMS}$  with  $N_\lambda$  and  $N_T$  is given in the contour plot of Figure 4.4. As expected, bad resolution of the flow solution in either space or time leads to significant discretisation errors, i.e. the size of the panels relative to the wavelength of the flow solution and the size of the time step relative to the period of the flow solution both need to be sufficiently small. The flow solutions of interest in this thesis are comprised of an infinite spectrum of discrete tones, and hence there will always

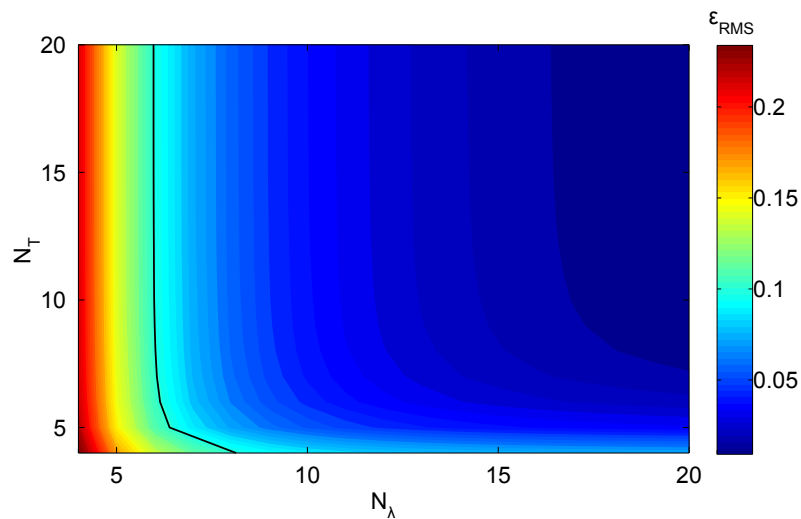


Figure 4.4: Variation of  $\epsilon_{RMS}$  with  $N_\lambda$  and  $N_T$ , and contour for  $\epsilon_{RMS} = 0.1$ .

be a limit to the tone that can be predicted accurately by a given CFD solution, even if inaccuracies in the CFD itself are disregarded.

Plots such as Figure 4.4 are an excellent way to guide the resolution requirements for a given problem of interest. As an example, the contour for  $\epsilon_{RMS} = 0.1$  has been plotted. If an error level of 10% were considered acceptable, the plot could be used to decide how fine a mesh was required to predict the noise to that level of accuracy. It is important to note that this is only in terms of the mitigation of discretisation error, it says nothing about whether the input CFD is accurate enough or if neglect errors are significant. It would also require an analytical test case to be used that sufficiently represents the complexity of the realistic flow field.

#### 4.1.4 Surface Motion

The three types of resolution above are sufficient to categorise the errors generated by an FW-H solver, however surface motion can have a significant effect on the sensitivity of a given problem to discretisation errors. Because the emission time varies across the surface, the locus of surface points at their emission time for a given observer time is not the same as the instantaneous shape of the surface. In other words, surface motion has the effect of distorting the surface shape being integrated. This distorted surface is commonly known as the “influence surface”. This in turn affects the resolution on the surface, and hence affects the discretisation errors. In other words, while a stationary surface with a given amount of discretisation error may be able to give an accurate answer, if that same surface is given motion it can become extremely inaccurate, as will be demonstrated shortly.

All the surfaces investigated in this thesis will be axisymmetric, and any surface motion will be a combination of constant forward motion and constant rotation about the forward motion direction (i.e. helicoidal motion). The motion was characterised by the “forward Mach number”,  $M_X = v_X/c$ , and a “rotational Mach number”,  $M_\Omega = \Omega R/c$ . In order to illustrate the effect of these parameters, the case used for demonstrating flow resolution was altered such that  $M_X = 0.5$ ,  $M_\Omega = 0.5$ ,  $N_P = 10$ ,  $L = 1$  and  $\theta = \pi/2$ .

The resulting influence surface, and the distribution of  $p'$  on it is shown in Figure 4.5. Clearly the forward motion has caused distortion of the overall surface shape (both a stretch along the axis of motion and a shear effect due to the observer directivity) while the rotation has caused the distribution of nodes around a given annulus to cluster and spread out on either side of the surface, depending on whether the rotation has induced motion away from or towards the observer respectively.

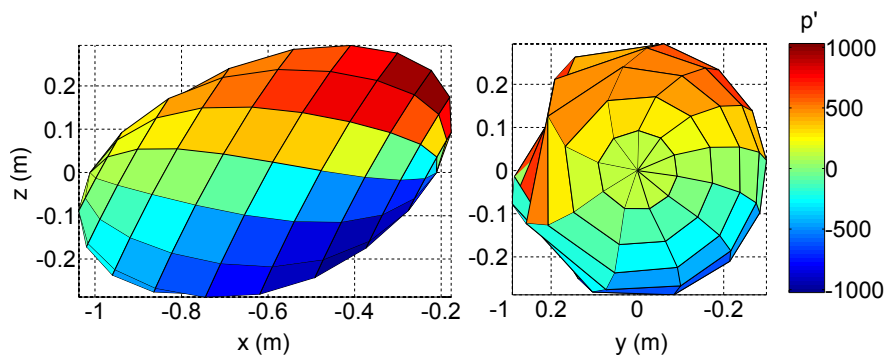


Figure 4.5: Illustration of influence surface distortion for  $M_X = 0.5$  and  $M_\Omega = 0.5$ .

These effects harm the surface's ability to accurately represent the integrands of the given formulation, making it more susceptible to discretisation error than its stationary equivalent.

The two Mach number parameters were investigated by varying  $v_X$  and  $\Omega$ , with the resulting effect on  $\epsilon_{RMS}$  given in Figure 4.6. The inaccuracy of the solution rapidly increases as either parameter increases, and as noted in Chapter 3 the propagation time algorithm fails to converge at all for cases which lead to transonic motion in the direction of the observer. It is clear that rotation of the surface can significantly impair the ability of an FW-H solver to accurately predict a given solution, even if the underlying flow solution is axisymmetric. Hence, interpolating a flow solution from a rotating surface onto a stationary one could give significant benefits in handling discretisation error, however the interpolation will also introduce errors and it is important to understand the trade off between these two effects. This will be investigated later in this chapter.

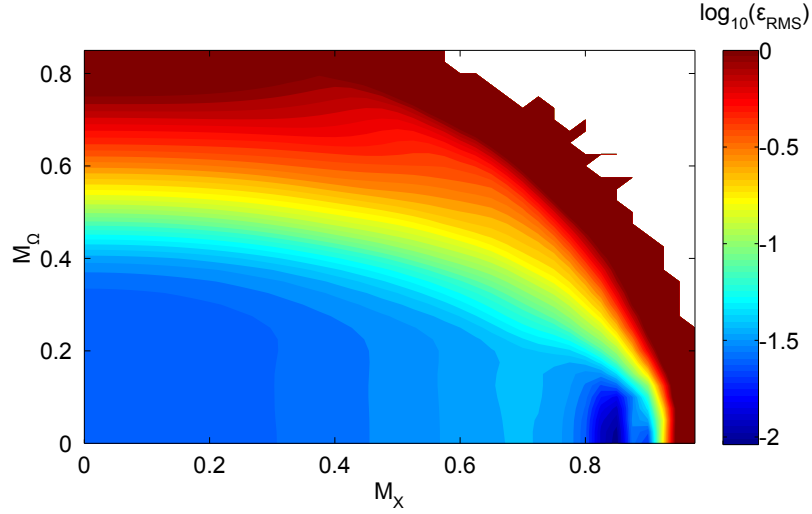


Figure 4.6: Variation of  $\epsilon_{RMS}$  with  $M_X$  and  $M_\Omega$ .

## 4.2 Error Study Framework

The second objective of this thesis is to use dimensional analysis to develop a rigorous process for investigating discretisation errors. The previous section has provided a solid understanding of discretisation errors and four key parameters ( $N_P$ ,  $N_L$ ,  $N_\lambda$  and  $N_T$ ) that quantify them, but it is important to make sure all aspects of a given problem of interest are being controlled when performing error studies. Dimensional analysis, as pioneered by Buckingham [11], provides an excellent framework for deriving such a set of non-dimensional groups.

Before defining this process, it is important to recognise that there are two fundamental types of study that might be undertaken when investigating discretisation errors. The first will be referred to as a “method study”, where the objective is to compare different methods to assess their accuracy and suitability for a given type of problem. In a method study, the four different resolution parameters need to be

varied independently, and the results of the different methods compared for relative accuracy. The second will be referred to as a “problem study”, where there is a very specific problem that needs to be predicted, and the objective is to assess what resolution should be set on the surface in order to achieve a desired level of accuracy, i.e. minimise discretisation errors below a certain threshold. In a problem study, the underlying problem is held constant and the resolution of the surface is varied in order to establish the required resolution.

In an ideal situation, a single dimensional analysis would derive a set of non-dimensional groups which would allow both types of study to be undertaken by fixing and varying different groups. Unfortunately, it will be seen that this is not possible in practice as the number of independent parameters that govern the discretisation of the problem ( $N_P$  and  $\Delta t$ ) is fewer than the number of groups governing the different types of resolution ( $N_P$ ,  $N_L$ ,  $N_\lambda$  and  $N_T$ ). If all the resolution parameters are to be included in the set of non-dimensional groups, some parameters governing the underlying problem being solved have to be neglected. In other words, independently controlling the individual sources of discretisation error is not possible without varying the underlying problem being solved, and vice versa.

This can be demonstrated using the examples from the previous section. A helpful technique when performing dimensional analysis is to try to break the problem down into its constituent parts and incorporate each in turn. In this case, a good starting point is to write down the parameters affecting just the analytical solution, i.e. with no concept of an integration surface. This is given below.

$$p' = f_1(c, \rho_0, A, \omega, v_X, L, \theta) \quad (4.7)$$

This equation has eight parameters and three dimensions (mass, length and time)

and hence Buckingham's  $\Pi$  theorem dictates five independent groups need to be formed. A suitable set is given below.

$$\frac{p'L}{\omega A} = f_2\left(\frac{\omega A}{c^2 \rho_0 L}, \frac{2\pi c}{\omega L}, M_X, \theta\right) \quad (4.8)$$

If the concept of an integration surface is introduced, but without any discretisation (i.e. assuming it can be solved perfectly),  $R$  and  $\Omega$  need to be introduced, leading to two further non-dimensional groups. Because the integration surface is now a "middle man" between the source and observer, the uses of  $L$  on the RHS of the above equation are replaced with  $R$  (this can be thought of as parametrising the flow solution on the surface rather than at the observer), and the two new groups  $L/R$  and  $M_\Omega$  are introduced to fully specify the problem, as given below.

$$\frac{p'L}{\omega A} = f_3\left(\frac{\omega A}{c^2 \rho_0 R}, \frac{2\pi c}{\omega R}, M_X, M_\Omega, \frac{L}{R}, \theta\right) \quad (4.9)$$

Finally, discretisation can be introduced. Two more parameters,  $N_P$  and  $\Delta t$ , now need to be incorporated. This only allows for two extra non-dimensional groups to be defined, whereas four resolution parameters are expected ( $N_P$ ,  $N_L$ ,  $N_\lambda$  and  $N_T$ ). Hence, there is a choice in how to complete the dimensional analysis, and this is where the concepts of method and problem studies is important. In a problem study, the underlying problem needs to be held constant, meaning that only two of the resolution parameters can be formed. As discussed in the previous section, it is expected that  $N_\lambda$  and  $N_T$ , i.e. the flow resolution, are the significant sources of discretisation error in the problems investigated in this thesis, and hence they are retained at the expense of  $N_P$  and  $N_L$  as below.

$$\frac{p'L}{\omega A} = f_4\left(\frac{\omega A}{c^2 \rho_0 R}, \frac{2\pi c}{\omega R}, M_X, M_\Omega, \frac{L}{R}, \theta, N_\lambda, N_T\right) \quad (4.10)$$

In a method study, all four resolution parameters need to be retained, but it is acceptable for the underlying problem to vary (in fact, it is useful to compare different solvers across a range of different problems). Hence, two groups from Equation 4.9 need to be neglected. There is actually no choice over which two are neglected, as there is only one combination that still gives an independent set of groups, as given below.

$$\frac{p'L}{\omega A} = f_5\left(\frac{\omega A}{c^2 \rho_0 R}, M_X, M_\Omega, \theta, N_P, N_L, N_\lambda, N_T\right) \quad (4.11)$$

It is important to understand that Equations 4.10 and 4.11 have been derived for a specific type of problem, i.e. an acoustic monopole moving at a constant velocity and wrapped in a spherical FW-H surface. However, the basic process used to derive them of forming groups without any surface terms, then including the surface shape and finally including discretisation terms differently depending on whether a method or problem study is being undertaken is applicable to any FW-H solver and underlying flow problem. As such, a general framework for performing such studies has been defined, and the second objective of the thesis has been satisfied.

### 4.3 Analytical Test Case

The third objective of this thesis is to compare a range of different solver methodologies in order to select a best practice methodology for open rotor noise prediction. In order to use the error study framework presented in the previous section to do so, an analytical test case that is representative of an open rotor is required. This

section presents a test case designed to have many characteristics in common with an uninstalled open rotor at a typical take off condition. The “datum” configuration for the test case (which is based on the realistic test case used in Chapter 6) is described and the required dimensional analysis is performed to give the set of non-dimensional parameters used in the method study of the next section.

### 4.3.1 Description

In order to have a test case that could be considered representative of an uninstalled open rotor at take-off, and bearing in mind the discussion of open rotor noise sources in Chapter 2, five key characteristics were identified that needed to be present in the solution:

1. The source kinematics should represent the counter-rotation of the two blade rows.
2. The test case should generate rotor alone tones for each blade row that vanish close to axial directivities.
3. The test case should generate interaction tones that are present at all directivities.
4. The test case should be periodic in time in the rotating reference frame, and also have rotational periodicity in space.
5. The test case should involve a rotating integration surface to emulate the CFD domain.

The test case modelled each blade of an open rotor using a single acoustic monopole at the tip radius, giving two counter-rotating “blade rows” which were

rotated in opposite directions about a common axis. Each monopole had the same strength fluctuation composed of constant and harmonic components. The constant component modelled rotor alone tones, while the harmonic component (whose frequency was the (1,1) interaction tone) modelled interaction tones, as defined below. Choosing this interaction tone guaranteed periodicity in time in the rotating frame of reference.

$$Q_M(t) = A_0 + A_1 \cos((N_F\Omega_F - N_R\Omega_R)t) \quad (4.12)$$

A spherical surface was wrapped around the sources and centred around the midpoint between the two centres of rotation. As will be seen in the next section, surface rotation presented significant problems and hence the surface was initially non-rotating, i.e. it was assumed the flow had been precisely interpolated to the non-rotating frame. The variables defining the test case, and their datum values, are described in Table 4.2. The geometric and kinematic terms are illustrated in Figure 4.7. Note that  $M_X$  is considered positive in the negative  $x$ -direction while the sense of rotation for both blade rows is right-handed based on the positive  $x$ -direction.

The pressure field at  $t = 0$  on the  $x = 0$  plane for the datum case is plotted in Figure 4.8. The pressure fluctuation for the observer defined in Table 4.2 is plotted in Figure 4.9. The resulting FFT is plotted in Figure 4.10 as well as the tones given by LSSA on the same time domain signal. The residual time signal from the LSSA is plotted against the original signal in Figure 4.9 and is clearly negligible. Finally, the variation of some of these tones with directivity is then plotted in Figure 4.11.

These plots show the other required characteristics of an open rotor flow solution. The contour plot shows that the flow field is periodic in space as expected from the blade numbers. The time domain plot shows that the time history at an observer is

Variable	Description	Datum Value
$c$	Bulk speed of sound	$340 \text{ m s}^{-1}$
$\rho_0$	Bulk density	$1.2 \text{ kg m}^{-3}$
$A_0$	Magnitude of constant component of source strength fluctuation	$1 \text{ kg s}^{-1}$
$A_1$	Magnitude of harmonic component of source strength fluctuation	$0.01 \text{ kg s}^{-1}$
$R_S$	Radius of sources	0.3 m
$X_S$	Gap between front and rear source rows	0.2 m
$N_F$	Number of sources in front row	12
$N_R$	Number of sources in rear row	9
$M_X$	Forward Mach number of source/surface/observer	0.2
$\Omega_F$	Rotational velocity of front sources	$700 \text{ rad s}^{-1}$
$\Omega_R$	Rotational velocity of rear sources	$-600 \text{ rad s}^{-1}$
$R$	Radius of surface	0.5 m
$L$	Distance from centre of surface to observer	100 m
$\theta$	Directivity of observer (in $x$ - $z$ plane)	$\pi/2 \text{ rad}$
$N_P$	Number of latitudinal/longitudinal panels on surface	240
$\Delta t$	Flow solution time step	$\frac{2\pi}{500\Omega_R} \text{ s}$

Table 4.2: Variables and datum values for solver methodology test case.

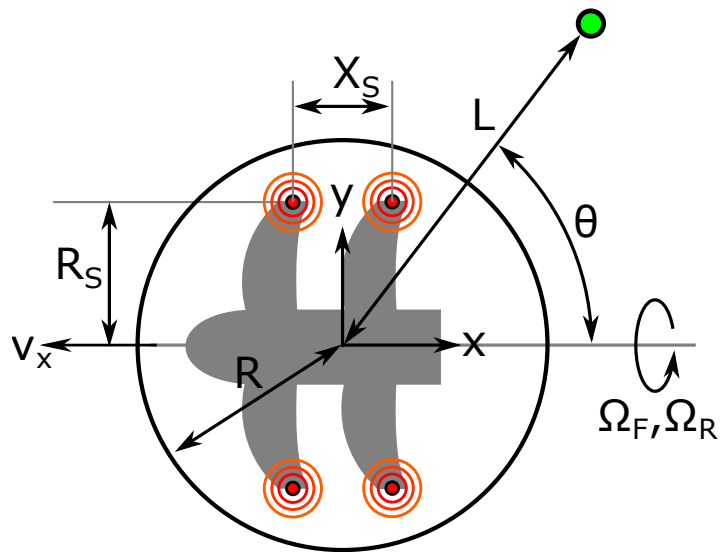


Figure 4.7: Illustration of analytical open rotor test case kinematics.

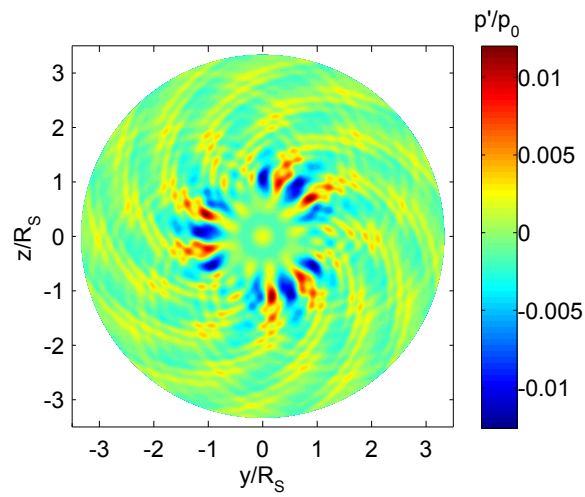


Figure 4.8: Instantaneous pressure perturbation for datum test case on the  $x = 0$  plane.

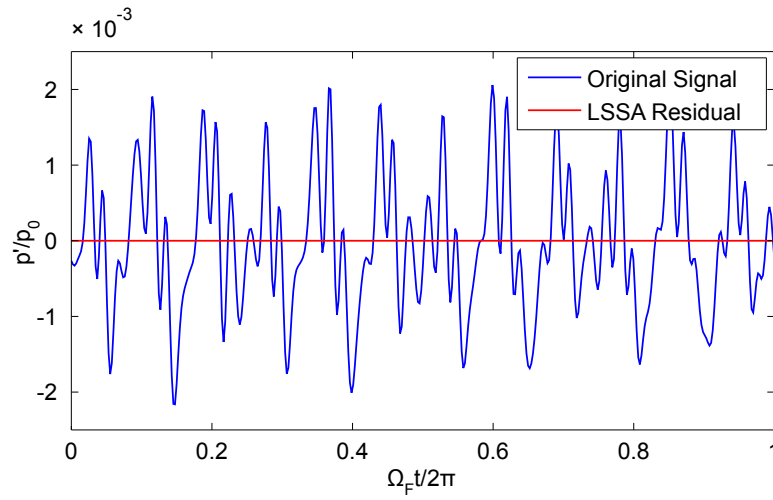


Figure 4.9: Time domain variation of pressure fluctuation and LSSA residual for the datum test case.

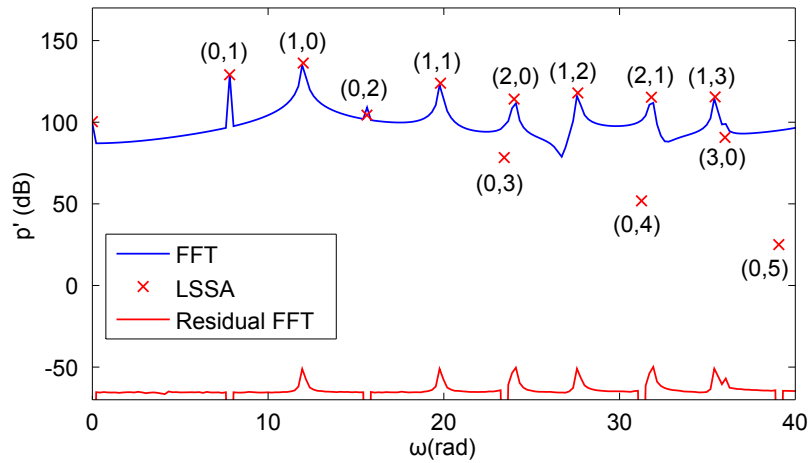


Figure 4.10: FFT, LSSA and residual FFT of pressure fluctuation for datum test case.

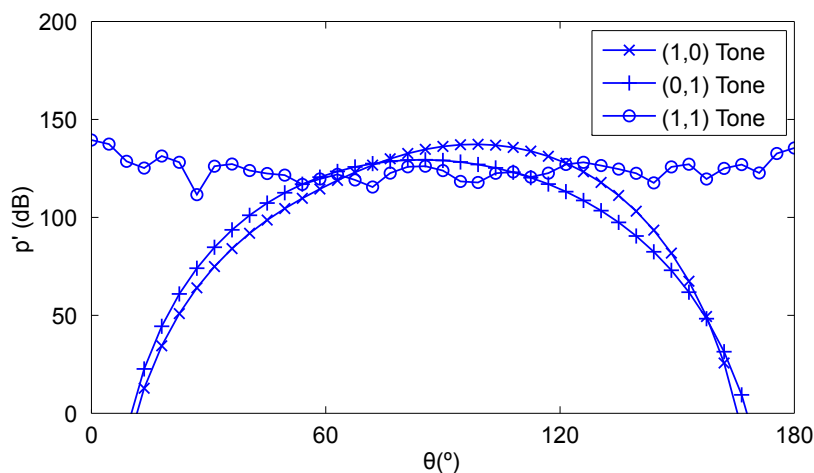


Figure 4.11: Variation of the (1,0), (0,1) and (1,1) tones with directivity for the datum case.

very complex and not periodic, as expected for a non-rotating point. Comparing the frequency content to Figure 2.17, it is clear that there is less frequency content than a realistic open rotor, but there are still a range of both rotor alone and interaction tones. Finally, the directivity plot confirms that the rotor alone and interaction tones vary as expected, with both rotor alone tones vanishing near the rotation axis while the interaction tone remains comparatively constant with directivity (compare with Figure 2.22). Hence, this test case is well suited for use in assessing different FW-H solvers for open rotor noise prediction.

In addition, the time and frequency domain plots show how effective the LSSA approach is at establishing frequency content. While the FFT has exhibited similar “drowning out” of quiet tones to that seen in Figure 3.18, the LSSA has very accurately resolved the frequency content using only a few tones, as evidenced by the negligible residual signal. Even extremely quiet tones such as the (0,5) tone have been resolved well compared to the residual signal. This is excellent evidence of the

improvements possible when LSSA is used in place of an FFT.

### 4.3.2 Dimensional Analysis

Having developed the datum test case and demonstrated that it is a good representation of an open rotor, this section performs the dimensional analysis to establish the parameter set for use in the method study of the next section. For the sake of brevity, the first two steps of the process defined in the previous section are combined to give the list of parameters affecting the underlying problem without discretisation (i.e. everything except  $N_P$  and  $\Delta t$ ), as given below.

$$p' = f_0(c, \rho_0, A_0, A_1, R_S, X_S, N_F, N_R, M_X, \Omega_F, \Omega_R, R, L, \theta) \quad (4.13)$$

The above equation contains fifteen variables in three dimensions, and hence Buckingham's  $\Pi$  theorem dictates twelve independent non-dimensional groups can be formed. The equation below provides a suitable set of groups.

$$\frac{p'L}{\Omega_R A_1} = f_1\left(\frac{A_0}{c\rho_0 L^2}, \frac{\Omega_R A_1}{c^2 \rho_0 L}, \frac{R_S}{X_S}, N_F, N_R, M_X, \frac{\Omega_F}{\Omega_R}, \frac{2\pi c}{\Omega_R R}, \frac{R}{R_S}, \frac{L}{R}, \theta\right) \quad (4.14)$$

The above equation describes the terms which affect the exact solution for  $p'$ . Once the discretisation parameters are introduced the calculated answer can be parametrised as well and hence the error. Because the intention is to use the parameter set in a method study, independent control over  $N_P$ ,  $N_L$ ,  $N_\lambda$  and  $N_T$  needs to be maintained and two of the above groups need to be neglected. As with the derivation of Equation 4.11, the neglected terms are prescribed by the need to maintain independence of the different terms. The rear blade passing frequency is used for

Variable	Description	Datum Value
$\frac{A_0}{c\rho_0L^2}$	Rotor alone source component	0.00245
$\frac{\Omega_R A_1}{c^2\rho_0L}$	Interaction source component	$4.505 \times 10^{-5}$
$\frac{R_S}{X_S}$	Ratio of source radius and gap	1.5
$N_F$	Front blade number	12
$N_R$	Rear blade number	9
$M_X$	Forward Mach number	0.2
$\frac{\Omega_F}{\Omega_R}$	Ratio of front and rear rotational speeds	1.152
$\frac{R}{R_S}$	Ratio of source and FW-H surface radii	1.67
$N_P$	Geometric resolution	240
$N_L$	Observer resolution	67.70
$N_\lambda$	Flow resolution in space	51.42
$N_T$	Flow resolution in time	60

Table 4.3: Values of non-dimensional groups for datum test case.

$N_\lambda$  and  $N_T$ . These are defined below, as is the final set of non-dimensional groups. The values of each group for the datum case and a brief description of their physical interpretation are given in Table 4.3.

$$N_\lambda = \frac{2\pi c}{N_R \Omega_R \lambda_P} \quad (4.15)$$

$$N_T = \frac{2\pi}{N_R \Omega_R \Delta t} \quad (4.16)$$

$$\epsilon = f_2 \left( \frac{A_0}{c\rho_0L^2}, \frac{\Omega_R A_1}{c^2\rho_0L}, \frac{R_S}{X_S}, N_F, N_R, M_X, \frac{\Omega_F}{\Omega_R}, \frac{R}{R_S}, \theta, N_P, N_L, N_\lambda, N_T \right) \quad (4.17)$$

## 4.4 Method Study

This section addresses the third objective of this thesis, which is to compare a range of different solver methodologies in order to select a best practice methodology for open rotor noise prediction. The range of options available for configuring a particular solver methodology have already been presented in Chapter 3. Of these options, the benefits of using a full surface specification have already been demonstrated earlier in this chapter, and the choice of source term construction is investigated separately in Chapter 5. Hence, the remaining options that need to be investigated are:

- Whether to use “raw” or “integrand” averaging.
- Whether to use a time or frequency domain flow solution.
- Which propagation algorithm (and hence solver) to use.
- Whether to interpolate onto a non-rotating surface or not.

A set of methodologies were developed to investigate each of these effects in turn, as summarised in Table 4.4. The dimensional analysis given in the previous section was used to independently vary the four resolution parameters from the datum point, and the error for each methodology was calculated and compared. Methodology A represents an industry standard methodology, with each subsequent methodology changing one aspect at a time and hence allowing the improvement offered by each alteration to be quantified. This author is not aware of any other study that compares a range of different FW-H solver methodologies using analytical flow solutions, particularly for an open rotor application. The initial methodology will be discussed first, and then the different improvements made in the various methodologies are in-

investigated in turn. This leads to a final “best practice” methodology being selected that satisfies the third objective of this thesis.

<b>Name</b>	<b>Propagation</b>	<b>Averaging</b>	<b>Flow Domain</b>	<b>Motion</b>
A	Observer dominant	Raw	Time	Non-rotating
B	Observer dominant	Integral	Time	Non-rotating
C	Source dominant	Integral	Time	Non-rotating
D	Source dominant	Integral	Frequency	Non-rotating
E	Frequency domain	Integral	Frequency	Non-rotating
F	Frequency domain	Integral	Frequency	Interpolated
G	Source dominant	Integral	Time	Rotating

Table 4.4: Definition of solver methodology options.

#### 4.4.1 Initial Methodology

The initial methodology is essentially that used in Chapter 4. The flow solution is calculated on a non-rotating surface using `fw_h_input` and a full surface specification. The sound at the observer is then calculated using `fw_h_ret` with raw averaging of panel data and source terms formed using the FW-H method with linear Euler governing equations (see Chapter 5 for discussion of this).

The flow solution on the surface at  $t = 0$  for the datum test case is plotted in Figure 4.12, again showing the complex interference pattern already seen in Figure 4.8. The resulting prediction for  $\theta = \pi/2$  is then plotted in time and frequency domains in Figures 4.13 and 4.14 respectively, showing that the datum case is predicted well but not perfectly. In particular, it is clear from the frequency domain plot that some of the higher frequency tones are being under-predicted, as would be expected due to these tones not being well enough resolved on the surface to be propagated accurately. The variation of  $\epsilon_{RMS}$  with  $\theta$  is plotted in Figure 4.15, showing that

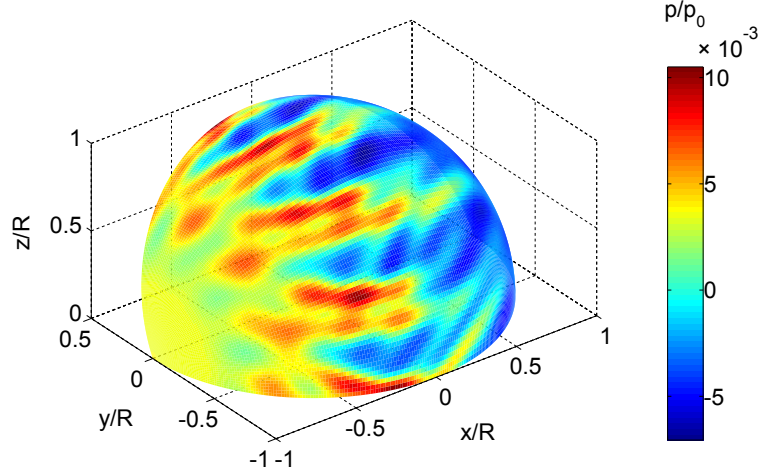


Figure 4.12: Instantaneous pressure perturbation on datum test case integration surface.

$\theta = \pi/2$  is the most onerous case for the solver to predict. At this point, a new error metric is defined below that is the maximum value of  $\epsilon_{RMS}$  seen in a sweep through  $\theta$ . This is a useful metric when running error studies as it is assumed that a given solver methodology needs to be accurate at all directivities, and hence it is the most onerous case encountered for each methodology that should be compared.

$$\epsilon_{\theta} = \max_{0 \leq \theta \leq \pi} (\epsilon_{RMS}) \quad (4.18)$$

The variation of  $\epsilon_{\theta}$  for each methodology and each resolution parameter is given in Figure 4.19, found at the end of this chapter.

#### 4.4.2 Panel Averaging

Methodology A used “raw” averaging, where each quantity defined in the input to the solver is averaged immediately, whereas Methodology B used “integrand” averaging,

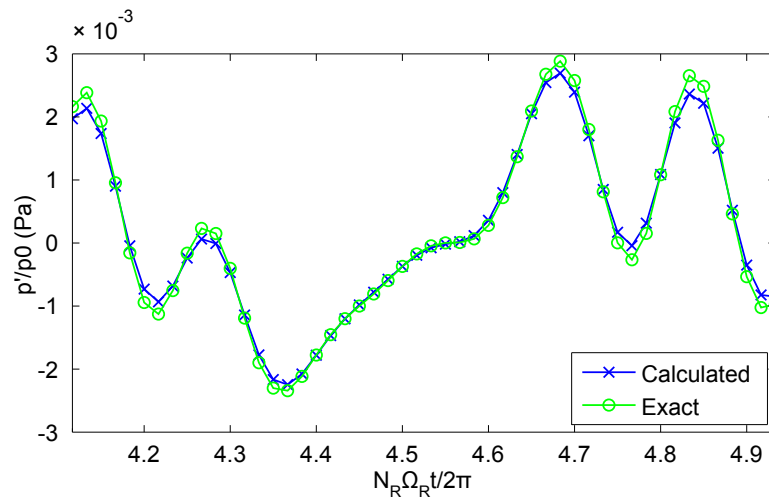


Figure 4.13: Calculated and exact observer signals for datum test case.

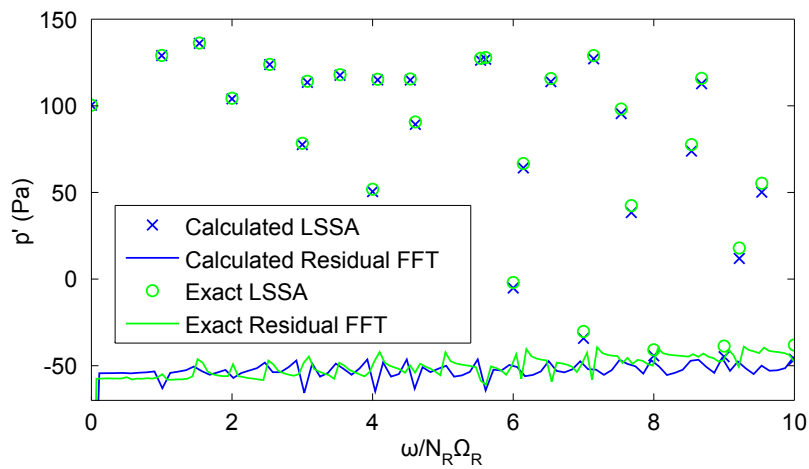


Figure 4.14: FFT, LSSA and residual FFT for calculated and exact datum test cases.

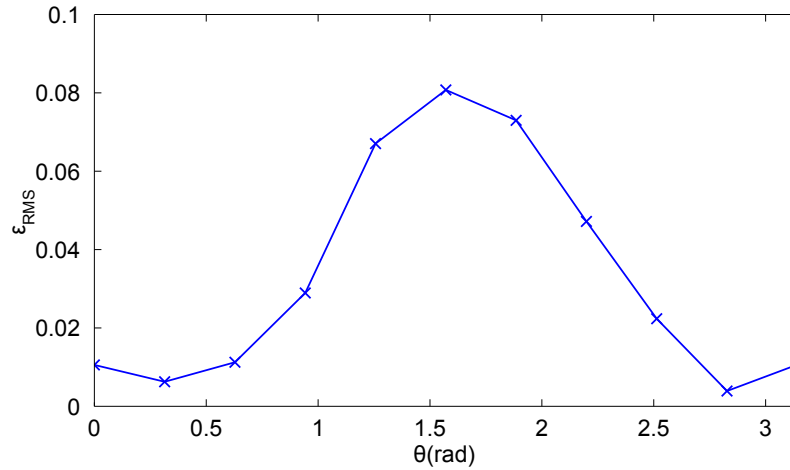


Figure 4.15: Variation of RMS error with directivity for datum test case.

which uses node values throughout the solver and only averages the final integrands in order to calculate the surface integrals. A general principle of numerical solutions is that averaging introduces errors, and hence it would be expected that integrand averaging would give better accuracy.

It is clear from all four plots in Figure 4.19 that this change gives a sizeable benefit. The error roughly halves for variations of  $N_P$ ,  $N_L$  and  $N_\lambda$  but is slightly less effective for variations of  $N_T$ . This is to be expected as the first three parameters deal with the resolution of quantities in space, which would be directly affected by how they were averaged across the surface, whereas variation of  $N_T$  deals with resolution in time, which should be less affected by spatial averaging. Integrand averaging does not appear to have been investigated by any previous study, certainly not to the same level of detail.

### 4.4.3 Observer and Source Dominant Propagation

Methodologies A and B use `fwh_ret` as their FW-H solver, which uses an observer dominant propagation algorithm that fixes the desired observer time, finds the associated emission time on the surface, and interpolates through the given flow solution for the desired flow properties. Also available is `fwh_adv` which uses a source dominant propagation algorithm that fixes the emission time based on the available flow solution, builds the received signal at the observer and then interpolates onto the desired observer time history.

In terms of accuracy, there are two important differences between the solvers. Firstly, an observer dominant methodology has to account for source motion when calculating propagation time whereas a source dominant methodology has to account for observer motion. As already discussed in Chapter 3, finding an accurate propagation time when rotating motion is involved requires an iterative solution, whereas rectilinear motion has an analytical solution. Hence `fwh_ret` could theoretically suffer from errors caused by inaccurate propagation time calculation when a rotating surface is used, whereas `fwh_adv` would resolve the propagation exactly.

Secondly, the two solvers interpolate through two different time histories. In `fwh_ret`, the time history of the flow solution is regularly spaced, and is interpolated to calculate the flow solution at the desired retarded time. In `fwh_adv`, it is the calculated observer time history that is interpolated to find the desired observer time history.

Methodology C was identical to Methodology B except that `fwh_adv` was used instead of `fwh_ret`. It is clear from the plots of Figure 4.19 that neither of the above differences are having any noticeable effect on  $\epsilon_\theta$  as the results appear identical between the two solvers. It will be seen later that `fwh_adv` handles rotating surface

motion better than `fwh_ret`, and hence it is selected as the better choice for now.

#### 4.4.4 Flow Solution Domain

Methodologies A to C all use a time domain flow solution. However, both `fwh_ret` and `fwh_adv` can also use a frequency domain flow solution as produced by `fwh_t2freq` using LSSA. For harmonic flow solutions that can be well described by a set of individual tones this has the potential to allow near perfect interpolation and extrapolation of the signal with the added benefit of reducing a long, detailed time history to a much smaller set of frequency components.

Methodology D was identical to methodology C except that the flow solution was converted to the frequency domain. It is clear from Figure 4.19 that this offers another significant improvement over the previous methodologies, with the error mostly being reduced by more than an order of magnitude compared to methodology C. Most impressively, using a frequency domain methodology appears to all but eliminate errors due to flow resolution in time, as shown by the variation with  $N_T$ . An important consequence of this behaviour is that FW-H solvers could be run using flow solutions with much larger time steps than the underlying CFD without any effect on the accuracy of prediction, greatly reducing the disk space and computational effort required for such runs.

The only place where the frequency domain flow solution does not appear to behave as well is for low values of  $N_\lambda$ , where the error actually exceeds the original methodology. In order to understand this problem, the frequency content for the edge cases  $N_\lambda = 40$  and  $N_\lambda = 50$  at  $\theta = \pi/2$  are compared in Figure 4.16, which normalises the tone frequency by the rear blade row rotational speed and normalises the pressure perturbation by the magnitude of the (1,0) tone (i.e. the front blade

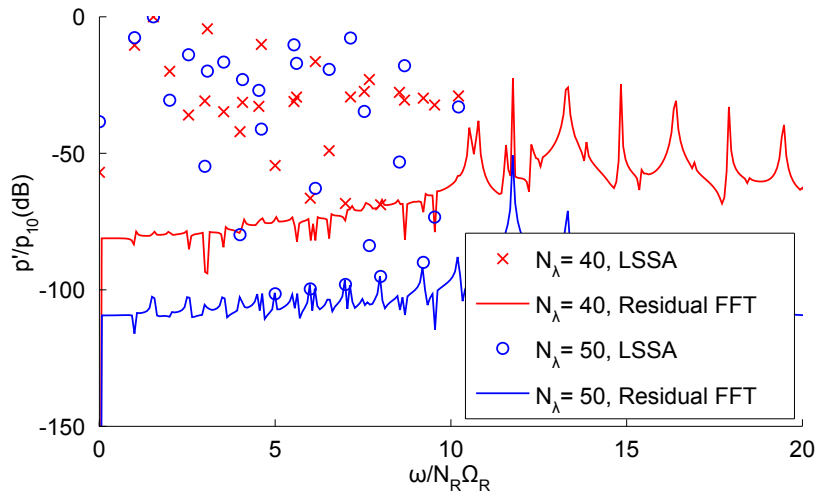


Figure 4.16: Comparison of frequency content for  $N_\lambda = 40$  and  $N_\lambda = 50$ .

passing frequency), denoted  $p_{10}$ .

The unexpected behaviour is an interesting demonstration of the inherent drawback of method studies, i.e. that it is impossible to isolate the different resolution parameters without also varying the underlying problem. The study varied  $N_\lambda$  while keeping  $R$ ,  $c$  and  $\rho_0$  constant, meaning  $\Omega_R$  and hence  $M_\Omega$  had to change in order to produce the required change in characteristic wavelength. It is clear from Figure 4.16 that this led to louder high frequency tones (particularly the (4,1) and (1,4) interaction tones) for  $N_\lambda = 40$ . However, the LSSA has not captured these tones, leading to large amounts of high frequency content being “missed” for this case.

Figure 4.17 shows that Methodologies C and D are inaccurate for  $N_\lambda = 40$  for two different reasons. For Methodology C, it is clear that the full frequency content present in the exact signal is being predicted to some extent, but several tones are predicted inaccurately, particular at high frequency. In contrast, tones that were not included in the LSSA when creating the frequency domain flow solution

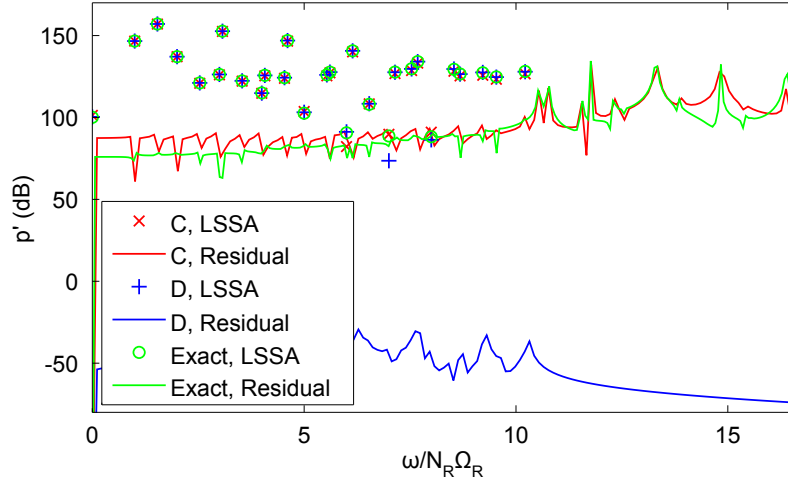


Figure 4.17: Comparison of frequency content for methodologies C and D at  $N_\lambda = 40$  and  $\theta = \pi/2$ .

for Methodology D are entirely absent from the calculated signal, and the residual is negligible. The tones that are present are more accurately predicted than for Methodology C, and the missing tones are the source of the errors. Including higher frequency tones in the LSSA would have mitigated this problem and confirmed the superiority of frequency domain flow solutions obtained using LSSA.

#### 4.4.5 Frequency Domain Propagation

In addition to the two time domain solvers discussed above, `fwh_freq` offers the ability to perform the propagation from source to observer in the frequency domain. As discussed in Chapter 3, an important limitation of this solver is that the surface and observer must have the same non-rotating motion so that the geometric and propagation terms in the integrands are constant. In addition, the flow solution must be converted to a  $(Q, F_i)$  format using `fwh_p2q` before being converted to the fre-

quency domain so that each term in the integrand has a single harmonic component multiplied by constant terms.

Methodology E only differed from methodology D in that `fwh_freq` was used instead of `fwh_adv`, and it is clear from Figure 4.19 that it gives similarly excellent accuracy. The key advantage of frequency domain propagation over time domain propagation is that the calculation scales with the number of frequency components in the flow solution, rather than the number of time steps in the flow solution (source dominant) or observer time history (observer dominant). Because the number of frequency components is over an order of magnitude smaller than the number of time steps (the datum test case uses 739 flow time steps and 536 observer time steps, but only 27 frequency components), `fwh_freq` is typically faster than the time domain solvers by roughly the same amount. In addition, the output solution is also in the frequency domain, meaning that any time signal of any length or resolution can be easily generated for comparison from the output.

#### 4.4.6 Surface Rotation

All of the methodologies investigated so far have calculated the flow solution on a non-rotating sphere directly from `fwh_input`. One of the required characteristics defined at the start of this section was that the input flow solution needed to be specified on a rotating surface. Figure 4.6 has already demonstrated that surface rotation can introduce significant discretisation error and even cause solvers to fail. The surface can be interpolated to the non-rotating frame of reference, but this will also introduce errors. As a result, it has been left until last to enable the other effects to be investigated first.

Chapter 3 showed that `fwh_interp` allowed a rotating flow solution to be inter-

polated to a non-rotating frame of reference. An obvious caveat for this process is that the surface must be axisymmetric, and this is the case for all surfaces considered in this thesis. For the current test case, the rotational speeds of the blade rows were such that both front and rear sources moved subsonically, allowing `fwh_input` to correctly calculate the flow solution. If the test case were to fully mimic a CFD test case, then part of the surface would rotate with the front blade row, while the other half would rotate with the rear.

As a slightly simpler but similarly onerous test, the entire surface was rotated at the front blade row rotational speed and the corresponding flow solution calculated. Methodology F then interpolated this flow solution onto the original, non-rotating surface and ran the same pre-processing and solver options as methodology E. It is clear from Figure 4.19 that this interpolation introduces a small amount of extra error (less than 0.5%) compared to using an exact input flow solution, but still represents a massive improvement over methodology A.

By contrast, trying to directly use the original flow solution in the solvers was very difficult. For the datum test case, the rotation of the surface gave a rotational Mach number of  $M_\Omega = 1.066$ , meaning that transonic motion of the sources towards the observer would occur at directivities close to  $\theta = \pi/2$ . The iterative solution for the propagation time in `fwh_ret` was unable to handle this motion and hence the solver failed at these points. However, `fwh_adv` did complete and hence was used in Methodology G, but the presence of  $1 - M_r$  in the denominator of the integrands, which would oscillate around zero at these directivities, generated huge errors where  $\epsilon_{RMS} \approx 10^7$ . This meant extracting a meaningful value of  $\epsilon_\theta$  was impossible, hence methodology G does not feature in Figure 4.19. Nevertheless, it was still possible to get meaningful calculations at more axial directivities, and these are compared to methodology A in Figure 4.18. Until the directivity becomes unmanageable,

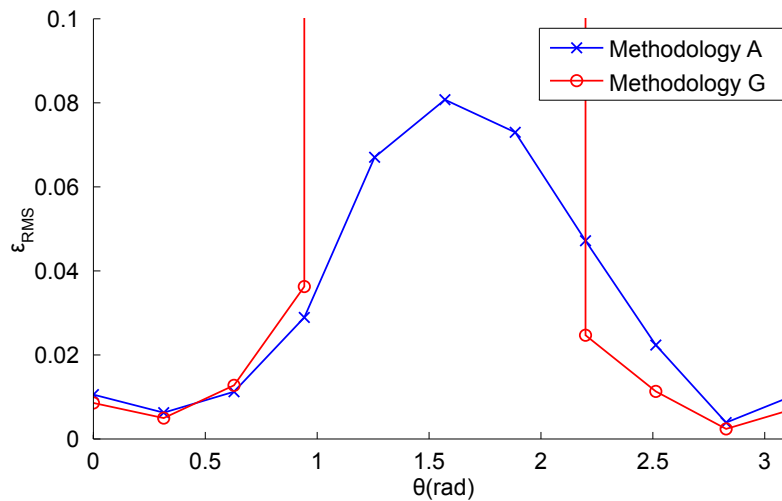
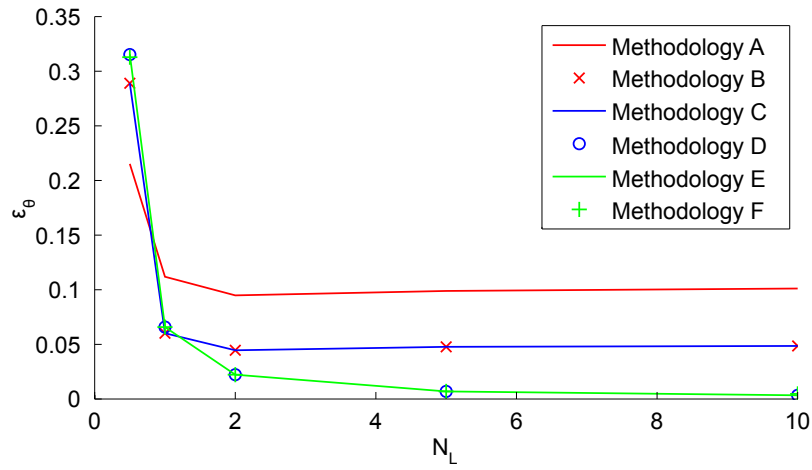


Figure 4.18: Comparison of methodologies A and G for datum test case.

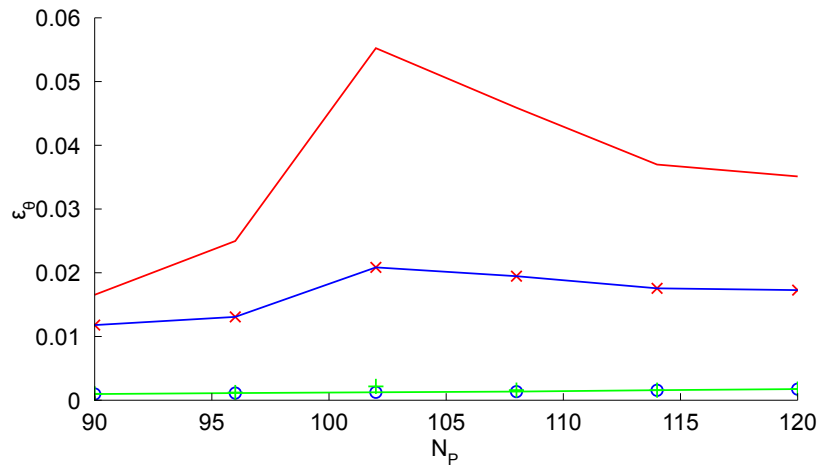
methodology G produces results that are roughly as accurate as methodology A, and hence significantly worse than methodology F. This shows that the errors introduced by interpolating to a non-rotating surface are negligible compared to the errors caused by surface rotation, and hence methodology F is selected as the best practice solver methodology for prediction of open rotor tonal noise at take-off.

## 4.5 Summary

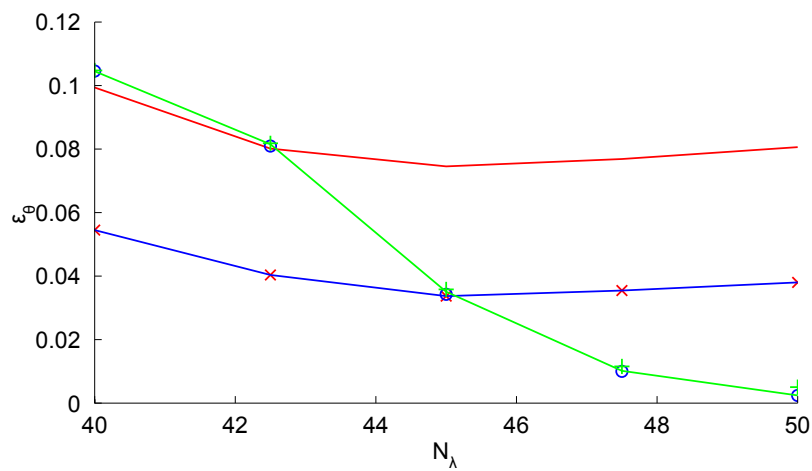
This chapter has addressed the first three objectives of this thesis. The first objective has been addressed by giving a detailed understanding of the sources of discretisation error, in particular introducing the concepts of geometric, observer and flow resolution and the non-dimensional parameters  $N_P$ ,  $N_L$ ,  $N_\lambda$  and  $N_T$  as useful metrics for these effects. These different types of error have been demonstrated using acoustic monopole test cases, and surface motion has been shown to greatly affect



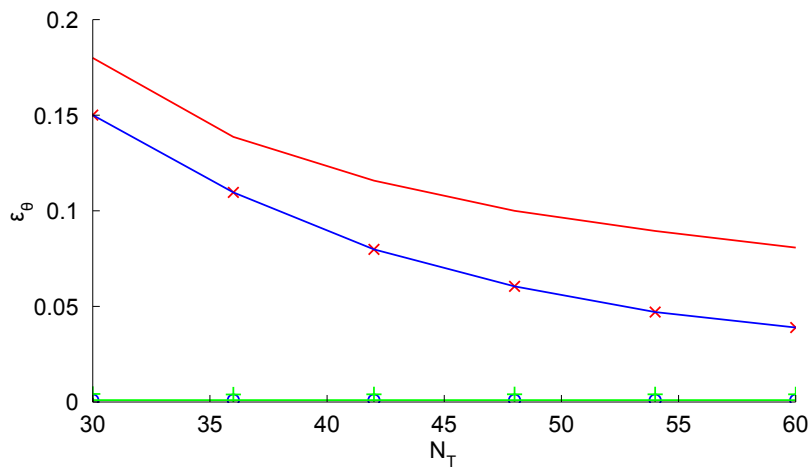
(a) Observer resolution.



(b) Geometric resolution.



(c) Flow resolution in space.



(d) Flow resolution in time.

Figure 4.19: Variation of discretisation error with resolution parameters for different solver methodologies.

the sensitivity of a problem to discretisation error.

The second objective has been addressed by using dimensional analysis to develop a clear framework for establishing an appropriate set of groups to use in running error studies. Two different types of study have been identified that require different pragmatic choices to be made in how the dimensional analysis is conducted. So-called “method” studies compare different FW-H solvers in order to select the best approach for a given class of problem. In the case of this thesis that class of problem is open rotor noise prediction. All the resolution parameters are retained and controlled so that the different methods can be compared in terms of their susceptibility to different types of error. An engineer can then vary the different resolution parameters independently, compare the results for different solver methodologies, and select the best one.

In order to enable this independent variation of discretisation parameters, other

parameters governing the underlying problem have to be ignored, meaning that varying the discretisation parameters also varies the underlying problem being investigated. This is fine in a method study as it is useful to compare results from across the design space. However, the second type of study, referred to as a “problem” study, is aimed at understanding what level of resolution is required for an accurate answer for a particular problem, and hence the associated parameters need to be fixed. This means only two resolution parameters can be retained, and it has been argued that  $N_\lambda$  and  $N_T$  are the appropriate choice as they are likely to be the most significant in realistic problems. Plots similar to Figure 4.4 can then be used to decide how much resolution in space and time to have on the surface in order to get a desired level of accuracy.

The third objective has been addressed by investigating a range of solver methodologies using an analytical test case that represents a counter-rotating open rotor at take-off. In particular, a “best practice” methodology that interpolates the rotating flow solution to the non-rotating frame, converts this non-rotating flow solution to the frequency domain, performs the propagation in the frequency domain using integrand averaging has been shown to offer over an order of magnitude improvement in accuracy over an industry standard approach. This also demonstrates the importance of discretisation errors in FW-H solvers, as even for the simplified analytical test case the industry standard methodology gave errors of up to 10%.

The detailed understanding of discretisation errors, the categorisation of the different types of error, the four key resolution parameters, the concept of method and problem studies, the error study framework and the best practice methodology are all novel contributions provided by this thesis. This is also the first time that acoustic monopoles have been used to represent an open rotor in such a detailed fashion in an FW-H solver methodology study. It is also the first time that analytical flow

solutions have been used to compare a range of different solver methodologies. The error study framework and the distinction between method and problem studies has allowed a wide range of techniques to be compared clearly and quantitatively. It is strongly recommended that such a process is used in any future work to develop new and improved FW-H solver methodologies.



# Chapter 5

## Neglection Errors

This chapter presents work on understanding and mitigating neglect errors in FW-H solvers, as per the fourth objective defined in Chapter 1. Chapter 2 has shown that avoiding density perturbations in the surface source terms has given promising results, but that there is no clear physical understanding of what these adjustments represent. It has also been shown that the Kirchhoff equation presents an alternative to the FW-H equation, but that the differences between the two are also not well understood, and contrasting results have been seen for their relative susceptibility to neglect errors.

As a result, this chapter investigates new methods for defining aeroacoustic analogies that mitigate neglect errors in a physically meaningful way. In particular, it is expected that such a method would enable density perturbations to be avoided in the surface source terms while retaining a clear physical interpretation of what those source terms represent. Also, there should be a mathematically rigorous and physically informed comparison of any new method with the FW-H and Kirchhoff equations, and the results for all three should be compared for different surface lo-

cations to assess their ability to mitigate neglect errors.

This chapter begins by presenting a generic aeroacoustic analogy that is agnostic of the exact form of the realistic and acoustic fluids being analogised. This provides a much clearer picture of the relationship between the realistic and acoustic fluids, and makes it easier to discuss the physical understanding of what an aeroacoustic analogy represents. This physical understanding is then used to derive a new method for incorporating a surface discontinuity into an aeroacoustic analogy. This method is compared with the FW-H and Kirchhoff methods, and a semi-analytical flow solution is used to compare results for the different methods.

## 5.1 Generic Aeroacoustic Analogy

As discussed in Chapter 2, an aeroacoustic analogy provides a definition of what aspects of a realistic flow can be considered sound propagation, and what must be considered a source term. Lighthill’s “density” analogy [52] is the original analogy, but there are others such as Morfey’s “pressure” analogy [58]. These analogies are all derived using the same basic process, and this section presents a generic aeroacoustic analogy that allows any realistic and acoustic conservation equations to be chosen to get a specific aeroacoustic analogy. Both Lighthill’s and Morfey’s analogies are specific examples of this generic analogy. While the mathematics has already been presented in Chapter 2, the generic notation and the physical arguments highlighted during the derivation are important in supporting the rest of the work in this chapter.

The derivation begins with generic versions of the mass and momentum conservation equations in a realistic fluid. These are as given below, where the mass density is still denoted  $\rho$ , the momentum density (which is assumed to be the same as the mass flux) is  $m_i$  and the stress field is  $s_{ij}$ .

$$\frac{\partial \rho}{\partial t} + \frac{\partial m_i}{\partial x_i} = 0 \quad (5.1)$$

$$\frac{\partial m_i}{\partial t} + \frac{\partial s_{ij}}{\partial x_j} = 0 \quad (5.2)$$

Using this generic notation of  $\rho$ ,  $m_i$  and  $s_{ij}$  means the results derived from this equation can be applied for any form of realistic conservation equations, such as the Euler or Navier-Stokes momentum equations. For clarity, the necessary substitutions to recover the Navier-Stokes equations (with no gravity field) are as given below.

$$m_i = \rho u_i \quad (5.3)$$

$$s_{ij} = p_{ij} + \rho u_i u_j \quad (5.4)$$

Next, we define generic versions of the corresponding mass and momentum conservation equations in an acoustic fluid. These are as given below, where  $\phi$  is the desired wave variable,  $\mu_i$  is the momentum density/mass flux in the acoustic fluid, and  $c$  is a constant.

$$\frac{1}{c^2} \frac{\partial \phi}{\partial t} + \frac{\partial \mu_i}{\partial x_i} = 0 \quad (5.5)$$

$$\frac{\partial \mu_i}{\partial t} + \frac{\partial \phi}{\partial x_i} = 0 \quad (5.6)$$

The divergence of Equation 5.6 can be subtracted from the time derivative of

Equation 5.5 (thus eliminating terms involving  $\mu_i$ ) to give a linear wave equation for  $\phi$ , as given below. The physical significance of  $c$  is now clearly defined as the speed of sound in the acoustic fluid.

$$\left( \frac{1}{c^2} \frac{\partial^2}{\partial t^2} - \frac{\partial^2}{\partial x_i^2} \right) \phi = 0 \quad (5.7)$$

The key conceptual step in establishing an aeroacoustic analogy is to reorganise the realistic Equations 5.1 and 5.2 into inhomogeneous forms of the acoustic Equations 5.5 and 5.6. This leads to the following set of equations, which are mathematically equivalent to the original realistic equations, with no further assumptions whatsoever made. For ease of notation, three quantities  $\alpha$ ,  $\gamma_i$  and  $\beta_{ij}$  are introduced to represent the source terms arising from the differences in mass density, mass flux/momentum density and stress fields respectively between the realistic and acoustic fluids.

$$\alpha = \frac{\phi'}{c^2} - \rho' \quad (5.8)$$

$$\beta_{ij} = \phi' \delta_{ij} - s'_{ij} \quad (5.9)$$

$$\gamma_i = \mu'_i - m'_i \quad (5.10)$$

$$\frac{1}{c^2} \frac{\partial \phi}{\partial t} + \frac{\partial \mu_i}{\partial x_i} = \frac{\partial \alpha}{\partial t} + \frac{\partial \gamma_i}{\partial x_i} \quad (5.11)$$

$$\frac{\partial \mu_i}{\partial t} + \frac{\partial \phi}{\partial x_i} = \frac{\partial \gamma_i}{\partial t} + \frac{\partial \beta_{ij}}{\partial x_j} \quad (5.12)$$

The equations show that the realistic fluid can be thought of as an ideal acoustic fluid with appropriate source terms added to make it behave like the realistic one.

The physical interpretation of these source terms is important. Mathematically, it is clear that it is the time and spatial derivatives of  $\alpha$ ,  $\gamma_i$  and  $\beta_{ij}$  that affect  $\phi$  and  $\mu_i$ , not their values, i.e. there are a range of choices of  $\alpha$ ,  $\gamma_i$  and  $\beta_{ij}$  that would satisfy Equations 5.11 and 5.12. Physically, there are two ways of interpreting this fact that will both be important later.

Firstly, the fact that only the derivatives matter implies that the equation should be understood in terms of addition of extra mass and momentum to the acoustic fluid, which is what the derivatives represent, rather than the imposition of extra density and stress fields, which is what the underlying variables represent. This makes physical sense, as it is easier to conceive of adding mass and momentum to a fluid than directly imposing a density or stress field. Secondly, the values of the underlying terms serve to link the properties of the acoustic fluid to the properties of the realistic fluid. The fact that these values do not matter to the acoustic fluid can be understood as representing the fact that the acoustic fluid does not care what physical laws govern the realistic fluid, and that any physical understanding of the above equations and hence an aeroacoustic analogy in general needs to be in the context of the acoustic fluid.

With these points in mind, the above equations can be manipulated in the normal way to eliminate  $\mu_i$  and construct an inhomogeneous wave equation for  $\phi$ , as given below.

$$\left( \frac{1}{c^2} \frac{\partial^2}{\partial t^2} - \frac{\partial^2}{\partial x_i^2} \right) \phi = \frac{\partial^2 \alpha}{\partial t^2} - \frac{\partial^2 \beta_{ij}}{\partial x_i \partial x_j} \quad (5.13)$$

Because  $\beta_{ij}$  is a tensor, the corresponding term in the above equation is often referred to as a quadrupole source field. However, keeping the above discussion in mind, this author argues it is more intuitive to describe it as a dipole source field as

it is not the underlying extra stress field that matters, but the resulting momentum source field. Similarly, the term involving  $\alpha$  should be thought of as a monopole term as it is not the underlying extra density field that matters but the resulting mass source field.

The derivation has outlined a generic process for establishing sources of sound in a fluid that is abstracted from the choices of realistic and acoustic conservation equations. By defining  $\phi = c^2\rho$  and using the Navier-Stokes equations defined in Equations 5.3 and 5.4, Lighthill's density analogy can be recovered by defining  $\alpha$  and  $\beta_{ij}$  as given below.

$$\alpha = 0 \tag{5.14}$$

$$\beta_{ij} = -(p - c^2\rho)\delta_{ij} - e_{ij} - \rho u_i u_j \tag{5.15}$$

Clearly,  $\beta_{ij}$  is the negative of  $T_{ij}$ , and is the only sound source under Lighthill's analogy. There is no need to select  $c^2\rho$  as the wave variable, when it is actually  $p$  that is of interest. If  $\phi$  is set directly to  $p$ , a different set of  $\alpha$  and  $\beta_{ij}$  are derived, as given below. This is the same result as given by Morfey's pressure analogy [58].

$$\alpha = \frac{p}{c^2} - \rho \tag{5.16}$$

$$\beta_{ij} = -e_{ij} - \rho u_i u_j \tag{5.17}$$

Obviously, it is important to understand the differences between the two analogies. They give two different source fields, even though the result is the same in the

far field (where  $p' = c^2 \rho'$ ) if the full source field is convolved. If only part of the source region is convolved, the resulting prediction is inaccurate in general, causing neglect errors. Furthermore, the pressure and density analogies will give different answers to each other, as the source fields are different. This raises the question of which analogy should be used in such situations.

In summary, this section has derived a more generic aeroacoustic analogy than has been given previously. It has also been argued that the source terms in the analogy should be thought of in terms of addition of mass and momentum rather than addition of density and stress. Finally, it has been noted that different analogies will give different solutions when part of the source field is neglected, raising the possibility that one analogy may be better suited to mitigating neglect errors than another.

## 5.2 New Surface Discontinuity Method

Having derived the generic aeroacoustic analogy, this section will present a new method for incorporating a surface discontinuity into an aeroacoustic analogy. It is shown that this method provides a simple and physically intuitive means of avoiding density perturbations in surface source terms. The new method is then compared to the FW-H and Kirchhoff methods using the physical arguments presented in the previous section, and the new method is shown to have some conceptual advantages over both the traditional methods.

### 5.2.1 Derivation

The derivation given here will start with the generic mass and momentum conservation equations for a realistic fluid, and the process applied will be as per the FW-H method described in Chapter 2 except for a small but important difference which leads to the new method. The comparison of this new method with the FW-H and Kirchhoff methods will be handled later, but the physical interpretation of the new method will be discussed in detail during the derivation.

As discussed in the previous section, the basic concept of an aeroacoustic analogy is the idea of adding mass and momentum sources to an acoustic fluid in order to make it behave like a realistic one. Generic versions of these inhomogeneous mass and momentum conservation equations for an acoustic fluid have been defined in Equations 5.11 and 5.12. The task now is to introduce a surface discontinuity in order to replace the internal part of the source field with an equivalent set of surface source terms that preserve the external flow solution. As also discussed in the previous section, the analogy should have a clear physical interpretation in the acoustic fluid. Hence, the discontinuity is applied to the acoustic fluid, with the resulting equations given below.

$$\frac{1}{c^2} \frac{\partial \bar{\phi}}{\partial t} + \frac{\partial \bar{\mu}_i}{\partial x_i} = \left( \frac{\phi'}{c^2} \frac{\partial H}{\partial t} + \mu'_i \frac{\partial H}{\partial x_i} \right) + \left( \frac{1}{c^2} \frac{\partial \phi}{\partial t} + \frac{\partial \mu_i}{\partial x_i} \right) H \quad (5.18)$$

$$\frac{\partial \bar{\mu}_i}{\partial t} + \frac{\partial \bar{\phi}}{\partial x_i} = \left( \mu'_i \frac{\partial H}{\partial t} + \phi' \frac{\partial H}{\partial x_i} \right) + \left( \frac{\partial \mu_i}{\partial t} + \frac{\partial \phi}{\partial x_i} \right) H \quad (5.19)$$

Note that the derivatives of  $H(f)$  have not been replaced using Equations 2.17 and 2.18 as it helps retain understanding of the origin of resulting terms. The volume terms are the LHS of the continuous conservation equations, and hence can

be replaced with the corresponding source terms from the RHS, as below.

$$\frac{1}{c^2} \frac{\partial \bar{\phi}}{\partial t} + \frac{\partial \bar{\mu}_i}{\partial x_i} = \left( \frac{\phi'}{c^2} \frac{\partial H}{\partial t} + \mu'_i \frac{\partial H}{\partial x_i} \right) + \left( \frac{\partial \alpha}{\partial t} + \frac{\partial \gamma_i}{\partial x_i} \right) H \quad (5.20)$$

$$\frac{\partial \bar{\mu}_i}{\partial t} + \frac{\partial \bar{\phi}}{\partial x_i} = \left( \mu'_i \frac{\partial H}{\partial t} + \phi' \frac{\partial H}{\partial x_i} \right) + \left( \frac{\partial \gamma_i}{\partial t} + \frac{\partial \beta_{ij}}{\partial x_j} \right) H \quad (5.21)$$

The surface terms in the above equations define the mass and momentum sources that must be introduced at the surface discontinuity in order to represent the effect of the internal source field on the external fluid, while the volume terms define the extra mass and momentum that must be added in the external volume to force the acoustic fluid to behave like the realistic one. Put another way, neglecting the volume terms is akin to neglecting any mass or momentum added to the acoustic fluid in the external volume. If the same manipulation used to derive Equation 5.13 is applied to the above equations, the following result is obtained.

$$\begin{aligned} \left( \frac{1}{c^2} \frac{\partial^2}{\partial t^2} - \frac{\partial^2}{\partial x_i^2} \right) \bar{\phi} &= \frac{\partial}{\partial t} \left( \frac{\phi'}{c^2} \frac{\partial H}{\partial t} + \mu'_i \frac{\partial H}{\partial x_i} \right) - \frac{\partial}{\partial x_i} \left( \mu'_i \frac{\partial H}{\partial t} + \phi' \frac{\partial H}{\partial x_i} \right) \\ &+ \frac{\partial}{\partial t} \left( \left( \frac{\partial \alpha}{\partial t} + \frac{\partial \gamma_i}{\partial x_i} \right) H \right) - \frac{\partial}{\partial x_i} \left( \left( \frac{\partial \gamma_i}{\partial t} + \frac{\partial \beta_{ij}}{\partial x_j} \right) H \right) \end{aligned} \quad (5.22)$$

As expected, the mass and momentum sources have manifested as monopole and dipole source terms. As already discussed, the volume terms on the second line of the above equation represent the external mass and momentum that need to be added to the acoustic fluid to make it behave like the original non-linear one. Hence the surface terms must represent the effect of the mass and momentum added to the acoustic

fluid inside the surface. This is an important point in the context of this paper, so the source terms in Equations 5.11 and 5.12 are split into internal and external contributions using  $H(-f)$  and  $H(f)$  to demonstrate this clearly. The resulting conservation equations, and the associated wave equation are as given below.

$$\frac{1}{c^2} \frac{\partial \phi}{\partial t} + \frac{\partial \mu_i}{\partial x_i} = \left( \frac{\partial \alpha}{\partial t} + \frac{\partial \gamma_i}{\partial x_i} \right) H(-f) + \left( \frac{\partial \alpha}{\partial t} + \frac{\partial \gamma_i}{\partial x_i} \right) H(f) \quad (5.23)$$

$$\frac{\partial \mu_i}{\partial t} + \frac{\partial \phi}{\partial x_i} = \left( \frac{\partial \gamma_i}{\partial t} + \frac{\partial \beta_{ij}}{\partial x_j} \right) H(-f) + \left( \frac{\partial \gamma_i}{\partial t} + \frac{\partial \beta_{ij}}{\partial x_j} \right) H(f) \quad (5.24)$$

$$\begin{aligned} \left( \frac{1}{c^2} \frac{\partial^2}{\partial t^2} - \frac{\partial^2}{\partial x_i^2} \right) \phi &= \frac{\partial}{\partial t} \left( \left( \frac{\partial \alpha}{\partial t} + \frac{\partial \gamma_i}{\partial x_i} \right) H(-f) \right) - \frac{\partial}{\partial x_i} \left( \left( \frac{\partial \gamma_i}{\partial t} + \frac{\partial \beta_{ij}}{\partial x_j} \right) H(-f) \right) \\ &+ \frac{\partial}{\partial t} \left( \left( \frac{\partial \alpha}{\partial t} + \frac{\partial \gamma_i}{\partial x_i} \right) H(f) \right) - \frac{\partial}{\partial x_i} \left( \left( \frac{\partial \gamma_i}{\partial t} + \frac{\partial \beta_{ij}}{\partial x_j} \right) H(f) \right) \end{aligned} \quad (5.25)$$

The above equation clearly splits the source field into the internal and external parts of the mass and momentum source field. Comparing Equation 5.25 with Equation 5.22 shows that the external terms are identical, with the internal terms of Equation 5.25 being replaced by the surface terms in Equation 5.22 that give an identical external flow. Hence, those surface terms predict the sound generated by the internal mass and momentum sources, and neglecting the external terms represents neglecting any mass and momentum added to the acoustic fluid outside the surface. As discussed in the derivation of Equation 5.13, it is physically intuitive to understand aeroacoustic analogies in terms of addition of extra mass and momentum to the acoustic fluid, and hence this new method is a physically intuitive way of splitting the internal and external source fields.

Introducing the discontinuity has also led to source terms that depend on  $\mu_i$  and  $\gamma_i$ . Isolating the external volume terms, the following equation shows that they reduce to a set of surface terms. In other words, the choice of  $\mu_i$  only affects how the internal and external parts of the source field are split, it does not have an overall effect on the noise, as already seen in Equation 5.13.

$$\begin{aligned} \frac{\partial}{\partial t} \left( \frac{\partial \gamma_i}{\partial x_i} H \right) - \frac{\partial}{\partial x_i} \left( \frac{\partial \gamma_i}{\partial t} H \right) &= \left( \frac{\partial \gamma_i}{\partial x_i} \frac{\partial H}{\partial t} + \frac{\partial^2 \gamma_i}{\partial t \partial x_i} H \right) - \left( \frac{\partial \gamma_i}{\partial t} \frac{\partial H}{\partial x_i} + \frac{\partial^2 \gamma_i}{\partial x_i \partial t} H \right) \\ &= \frac{\partial \gamma_i}{\partial x_i} \frac{\partial H}{\partial t} - \frac{\partial \gamma_i}{\partial t} \frac{\partial H}{\partial x_i} \end{aligned} \quad (5.26)$$

While the choice of  $\mu_i$  does not affect the overall source field, the fact that it affects the split means that when the external source field is neglected, the choice of  $\mu_i$  does affect the calculated answer. This is clear from the surface terms of Equation 5.22, which only depend on  $\phi$  and  $\mu_i$ . Selecting the definition of these two variables defines the acoustic fluid being used in the analogy. Hence, density perturbations can be avoided by setting these variables appropriately, for example  $\phi = p$  and  $\mu_i = \rho_0 u_i$ . The choice of  $\phi$  represents what realistic flow property is being analogised as sound, and the choice of  $\mu_i$  represents how momentum is being defined in the acoustic fluid, which affects how the internal and external parts of the source field are split at the discontinuity. This is a far simpler and more physically intuitive method of avoiding density perturbations in surface source terms than the adjusted FW-H methods of previous work [59, 78].

In summary, this section has derived a new method for incorporating a surface discontinuity into an aeroacoustic analogy. Its physical interpretation is in keeping with the principles of an aeroacoustic analogy in that the source terms are split

based on the extra mass and momentum that need to be added to the acoustic fluid in order for it to behave like the realistic fluid. It has also been shown that density perturbations can be avoided in surface source terms with a clearer, simpler physical interpretation than in previous work.

### 5.2.2 Comparison with FW-H and Kirchhoff Methods

Having derived the new surface discontinuity method, this section will compare it with the FW-H and Kirchhoff methods. The generic notation used in this chapter allows these different methods to be shown to be mathematically identical, with the only difference being how the internal and external source fields are split. The physical implications of neglecting the external source terms for each method are discussed, and it is argued that both the FW-H and Kirchhoff methods neglect external effects in a less physically intuitive way than the new method.

The standard FW-H equation has already been derived as given in Equation 2.26. However, it is useful to derive it using the generic notation of this chapter. The key difference to the derivation of the new method above is that the discontinuity is applied to the realistic conservation equations defined in Equations 5.1 and 5.2, rather than their inhomogeneous acoustic equivalents. Because the RHS of these equations are zero, the external volume source term is zero, hence only surface terms are required, as given below.

$$\frac{\partial \bar{\rho}}{\partial t} + \frac{\partial \bar{m}_i}{\partial x_i} = \rho' \frac{\partial H}{\partial t} + m'_i \frac{\partial H}{\partial x_i} \quad (5.27)$$

$$\frac{\partial \bar{m}_i}{\partial t} + \frac{\partial \bar{s}_{ij}}{\partial x_j} = m'_i \frac{\partial H}{\partial t} + s'_{ij} \frac{\partial H}{\partial x_j} \quad (5.28)$$

Similarly to other analogies, the  $\overline{m}_i$  terms are eliminated and a wave equation assembled, leading to a generic equivalent of the original FW-H equation as below.

$$\begin{aligned} \left( \frac{1}{c^2} \frac{\partial^2}{\partial t^2} - \frac{\partial^2}{\partial x_i^2} \right) \overline{\phi} = & \frac{\partial}{\partial t} \left( \rho' \frac{\partial H}{\partial t} + m'_i \frac{\partial H}{\partial x_i} \right) - \frac{\partial}{\partial x_i} \left( m'_i \frac{\partial H}{\partial t} + s'_{ij} \frac{\partial H}{\partial x_j} \right) \\ & + \frac{\partial^2}{\partial t^2} (\alpha H) - \frac{\partial^2}{\partial x_i \partial x_j} (\beta_{ij} H) \end{aligned} \quad (5.29)$$

This equation and the new method defined by Equation 5.22 have both been derived without assumption from the same realistic mass and momentum conservation equations. Hence they should be mathematically identical. This is not immediately obvious by comparing the two equations, but the equivalence can be demonstrated by using Equations 5.8, 5.9 and 5.10 to substitute for  $\rho'$ ,  $s'_{ij}$  and  $m'_i$  in the surface terms of the above equation and expanding the inner derivative of each volume term, as given below.

$$\begin{aligned} \left( \frac{1}{c^2} \frac{\partial^2}{\partial t^2} - \frac{\partial^2}{\partial x_i^2} \right) \overline{\phi} = & \frac{\partial}{\partial t} \left( \left( \frac{\phi'}{c^2} - \alpha' \right) \frac{\partial H}{\partial t} + (\mu'_i - \gamma'_i) \frac{\partial H}{\partial x_i} \right) \\ & - \frac{\partial}{\partial x_i} \left( (\mu'_i - \gamma'_i) \frac{\partial H}{\partial t} + (\phi' \delta_{ij} - \beta_{ij}) \frac{\partial H}{\partial x_j} \right) \\ & + \frac{\partial}{\partial t} \left( \frac{\partial \alpha}{\partial t} H + \alpha' \frac{\partial H}{\partial t} \right) - \frac{\partial}{\partial x_i} \left( \frac{\partial \beta_{ij}}{\partial x_j} H + \beta'_{ij} \frac{\partial H}{\partial x_j} \right) \end{aligned} \quad (5.30)$$

Some terms involving  $\alpha$  and  $\beta_{ij}$  in the above equation cancel, and the following identity can be used to replace the terms involving  $\gamma_i$ , leaving Equation 5.22.

$$\frac{\partial}{\partial t} \left( -\gamma'_i \frac{\partial H}{\partial x_i} \right) - \frac{\partial}{\partial x_i} \left( -\gamma'_i \frac{\partial H}{\partial t} \right) \equiv \frac{\partial}{\partial t} \left( \frac{\partial \gamma_i}{\partial x_i} H \right) - \frac{\partial}{\partial x_i} \left( \frac{\partial \gamma_i}{\partial t} H \right) \quad (5.31)$$

At this point, it is important to recall the discussion following Equations 5.11 and 5.12, which argued that the physical interpretation of the source terms of an aeroacoustic analogy can be looked at from two different perspectives. These two different perspectives also provide two different ways of interpreting the differences between the FW-H and new methods.

The first perspective is that the source field should be conceived as the addition of extra mass and momentum to an acoustic fluid, rather than the imposition of the underlying extra density and stress fields. The new method was shown to split the source field in terms of the extra mass and momentum, and hence neglecting the external half represents ignoring the effects of the mass and momentum added in the external part of the flow. A similar approach can be used to investigate how the FW-H method splits the source field. Instead of splitting the RHS of Equations 5.11 and 5.12 in terms of the added mass and momentum, they are split in terms of the underlying extra density and stress fields and the associated wave equation constructed, as given below.

$$\frac{1}{c^2} \frac{\partial \phi}{\partial t} + \frac{\partial \mu_i}{\partial x_i} = \frac{\partial}{\partial t} (\alpha H(-f) + \alpha H(f)) + \frac{\partial}{\partial x_i} (\gamma_i H(-f) + \gamma_i H(f)) \quad (5.32)$$

$$\frac{\partial \mu_i}{\partial t} + \frac{\partial \phi}{\partial x_i} = \frac{\partial}{\partial t} (\gamma_i H(-f) + \gamma_i H(f)) + \frac{\partial}{\partial x_j} (\beta_{ij} H(-f) + \beta_{ij} H(f)) \quad (5.33)$$

$$\begin{aligned} \left( \frac{1}{c^2} \frac{\partial^2}{\partial t^2} - \frac{\partial^2}{\partial x_i^2} \right) \phi &= \frac{\partial^2}{\partial t^2} (\alpha H(-f)) - \frac{\partial^2}{\partial x_i \partial x_j} (\beta_{ij} H(-f)) \\ &+ \frac{\partial^2}{\partial t^2} (\alpha H(f)) - \frac{\partial^2}{\partial x_i \partial x_j} (\beta_{ij} H(f)) \end{aligned} \quad (5.34)$$

It is clear that the external volume source field of Equation 5.34 is the same as the equivalent term in Equation 5.29. This demonstrates that the FW-H method can be understood as splitting the internal and external source fields in terms of the underlying extra density and stress fields, rather than the extra mass and momentum sources. As already discussed, this is not physically intuitive as it is difficult to conceptualise “adding” density and stress to a fluid.

An alternative criticism of the physical interpretation of the FW-H method comes from the second perspective discussed in the previous section. This perspective highlighted that the acoustic fluid knows nothing about the physical laws of the realistic fluid, and hence any source field in the acoustic fluid should be understood in terms of the acoustic fluid, not the realistic one.

As described in its derivation, the FW-H method applies the discontinuity to the realistic fluid, not the acoustic one. As a result, the surface source terms represent the mass and momentum sources required to satisfy conservation in the realistic fluid, not the acoustic one. Hence, these surface sources have no physical interpretation in the context of the acoustic fluid. This is made clear by noticing that the surface terms of the FW-H equation defined in Equation 5.29 are defined entirely in terms of the properties of the realistic fluid, i.e.  $\rho$ ,  $m_i$  and  $s_{ij}$ . An interesting consequence of this is that the surface terms are entirely unaffected by what acoustic fluid is chosen, i.e. they are the same regardless of how  $\phi$  and  $\mu_i$  are defined. This explains why previous research has struggled to adjust the FW-H equation to avoid density perturbations.

Moving on to the Kirchhoff method, its derivation begins by applying the discontinuity directly to the wave equation rather than the underlying mass and momentum conservation equations. This means all source terms are defined in terms of  $\phi$ .

$$\begin{aligned} \left( \frac{1}{c^2} \frac{\partial^2}{\partial t^2} - \frac{\partial^2}{\partial x_i^2} \right) \bar{\phi} &= \frac{1}{c^2} \frac{\partial}{\partial t} \left( \phi' \frac{\partial H}{\partial t} \right) - \frac{\partial}{\partial x_i} \left( \phi' \frac{\partial H}{\partial x_i} \right) \\ &+ \frac{1}{c^2} \frac{\partial \phi}{\partial t} \frac{\partial H}{\partial t} - \frac{\partial \phi}{\partial x_i} \frac{\partial H}{\partial x_i} \\ &+ \left( \frac{1}{c^2} \frac{\partial^2 \phi}{\partial t^2} - \frac{\partial^2 \phi}{\partial x_i^2} \right) H \end{aligned} \quad (5.35)$$

Clearly, the first two terms of the above equation are monopole and dipole terms respectively, and hence can be conceptualised as mass and momentum source terms. However, the other terms are not so easy to interpret physically, as will be discussed shortly. Demonstrating that this equation is mathematically equivalent to Equation 5.22 is a little more involved than for the FW-H comparison. The first step is to substitute for the derivatives of  $\phi$  using Equations 5.11, 5.12 and 5.13. This leads to the following equation.

$$\begin{aligned} \left( \frac{1}{c^2} \frac{\partial^2}{\partial t^2} - \frac{\partial^2}{\partial x_i^2} \right) \bar{\phi} &= \frac{1}{c^2} \frac{\partial}{\partial t} \left( \phi' \frac{\partial H}{\partial t} \right) - \frac{\partial}{\partial x_i} \left( \phi' \frac{\partial H}{\partial x_i} \right) \\ &+ \left( \frac{\partial \alpha}{\partial t} + \frac{\partial \gamma_i}{\partial x_i} - \frac{\partial \mu_i}{\partial x_i} \right) \frac{\partial H}{\partial t} - \left( \frac{\partial \gamma_i}{\partial t} + \frac{\partial \beta_{ij}}{\partial x_j} - \frac{\partial \mu_i}{\partial t} \right) \frac{\partial H}{\partial x_i} \\ &+ \left( \frac{\partial^2 \alpha}{\partial t^2} - \frac{\partial^2 \beta_{ij}}{\partial x_i \partial x_j} \right) H \end{aligned} \quad (5.36)$$

The second step uses the following identity involving  $\mu_i$ , which can be easily

proven by expanding the derivatives on the RHS.

$$\left(\frac{\partial\mu_i}{\partial x_i}\frac{\partial H}{\partial t}\right) - \left(\frac{\partial\mu_i}{\partial t}\frac{\partial H}{\partial x_i}\right) \equiv \frac{\partial}{\partial x_i}\left(\mu_i\frac{\partial H}{\partial t}\right) - \frac{\partial}{\partial t}\left(\mu_i\frac{\partial H}{\partial x_i}\right) \quad (5.37)$$

This identity can be used to replace the terms involving  $\mu_i$  in Equation 5.36 as below.

$$\begin{aligned} \left(\frac{1}{c^2}\frac{\partial^2}{\partial t^2} - \frac{\partial^2}{\partial x_i^2}\right)\bar{\phi} &= \frac{1}{c^2}\frac{\partial}{\partial t}\left(\phi'\frac{\partial H}{\partial t} + \mu_i\frac{\partial H}{\partial x_i}\right) - \frac{\partial}{\partial x_i}\left(\mu_i\frac{\partial H}{\partial t} + \phi'\frac{\partial H}{\partial x_i}\right) \\ &+ \left(\frac{\partial\alpha}{\partial t} + \frac{\partial\gamma_i}{\partial x_i}\right)\frac{\partial H}{\partial t} - \left(\frac{\partial\gamma_i}{\partial t} + \frac{\partial\beta_{ij}}{\partial x_j}\right)\frac{\partial H}{\partial x_i} \\ &+ \left(\frac{\partial^2\alpha}{\partial t^2} - \frac{\partial^2\beta_{ij}}{\partial x_i\partial x_j}\right)H \end{aligned} \quad (5.38)$$

It should be clear that the above equation can be rearranged into Equation 5.22 by noting the following results.

$$\frac{\partial\alpha}{\partial t}\frac{\partial H}{\partial t} + \frac{\partial^2\alpha}{\partial t^2}H = \frac{\partial}{\partial t}\left(\frac{\partial\alpha}{\partial t}H\right) \quad (5.39)$$

$$\frac{\partial\gamma_i}{\partial x_i}\frac{\partial H}{\partial t} - \frac{\partial\gamma_i}{\partial t}\frac{\partial H}{\partial x_i} = \frac{\partial}{\partial t}\left(\frac{\partial\gamma_i}{\partial x_i}H\right) - \frac{\partial}{\partial x_i}\left(\frac{\partial\gamma_i}{\partial t}H\right) \quad (5.40)$$

$$\frac{\partial\beta_{ij}}{\partial x_j}\frac{\partial H}{\partial x_i} + \frac{\partial^2\beta_{ij}}{\partial x_i\partial x_j}H = \frac{\partial}{\partial x_i}\left(\frac{\partial\beta_{ij}}{\partial x_j}H\right) \quad (5.41)$$

This shows that the Kirchhoff method is just a rearrangement of the new method, and hence also the FW-H method. The split between internal and external source

fields in the Kirchhoff method can be understood in a similar manner to the other equations. However, this time it is the source terms of Equation 5.13, rather than Equations 5.11 and 5.12, that are split into internal and external contributions, as given below.

$$\left(\frac{1}{c^2} \frac{\partial^2}{\partial t^2} - \frac{\partial^2}{\partial x_i^2}\right) \phi = \left(\frac{\partial^2 \alpha}{\partial t^2} - \frac{\partial^2 \beta_{ij}}{\partial x_i \partial x_j}\right) H(-f) + \left(\frac{\partial^2 \alpha}{\partial t^2} - \frac{\partial^2 \beta_{ij}}{\partial x_i \partial x_j}\right) H(f) \quad (5.42)$$

The above equation shows that the Kirchhoff method splits the internal and external contributions to the source field in terms of fundamental sound sources. By comparing the Kirchhoff method of Equation 5.38 with the new method of Equation 5.22, it is clear that the difference between the two is whether the middle line of Equation 5.38 is considered part of the internal (Kirchhoff) or external (new method) source fields.

Again recalling the first perspective for understanding aeroacoustic analogies, these terms cannot be conceptualised as mass and momentum sources by themselves, they represent the sound generated by the boundary of the external mass and momentum volume sources. Hence, it is unphysical to assign them to the internal source field, as this means neither the internal nor external source fields can be conceptualised in terms of mass or momentum. In other words, when the external source field is neglected, the remaining surface sources do not conserve mass or momentum.

Turning to the second perspective, all the source terms of the Kirchhoff method are defined by the choice of  $\phi$ , i.e. the choice of  $\mu_i$  makes no difference. This means that the Kirchhoff method has no concept of a fluid at all as it has no concept of momentum, and so cannot be understood in terms of an acoustic fluid.

In summary, the new method has been shown to be more physically intuitive

than the FW-H and Kirchhoff methods from two different perspectives. The first perspective shows that the new method represents splitting the internal and external source fields in terms of the physically intuitive addition of mass and momentum, whereas the FW-H method splits the source field in terms of the physically unintuitive imposition of extra density and stress fields, and the Kirchhoff method in terms of fundamental noise sources which are incapable of being conceived as mass and momentum sources. The second perspective shows that the new method splits its source terms based on conservation in the acoustic fluid, which is in keeping with the basic principle of an aeroacoustic analogy, whereas the FW-H method splits its source terms based on conservation in the realistic fluid, which has no meaning in the acoustic fluid, and the Kirchhoff equation has no concept of representing a fluid at all. It is important to emphasise that the three methods have been shown to have identical overall source fields, with the only difference being how the methods split the source field between internal and external contributions. This only matters because the external part is neglected from all methods in realistic applications, and the objective of this chapter is to understand and mitigate the errors that result from this neglect.

### 5.3 Semi-Analytical Test Case

The previous sections have derived a new method for incorporating a surface discontinuity into an aeroacoustic analogy and compared it to the FW-H and Kirchhoff methods. It has been shown that it is easily formulated to avoid density perturbations in the surface source terms, something which is believed to be a significant source of neglect error, and it has been shown that the new method has a much clearer physical interpretation than either the FW-H or Kirchhoff methods. All of

these results are important and give the new method fidelity in terms of it being clearly understood, but it is critical to investigate which method is least sensitive to neglect error, i.e. which method is most stable as the extent of the integration surface is varied.

This section addresses this need by using a semi-analytical flow solution to compare the different methods. It is semi-analytical in that analytical solutions for  $\alpha$ ,  $\gamma_i$  and  $\beta_{ij}$  are defined which must then be numerically integrated to get the solution for  $\phi$ . Because the source terms are known exactly, there are no input errors, but discretisation still needs to be handled. It is also important to understand that these flow solutions cannot be interpreted as realistic fluids, as they will not respect conservation of energy in the realistic fluid.

In order to investigate the difference between pressure and density analogy versions of the methods, it is useful to note the following relationship between the source fields, which is obtained by comparing Equations 5.14 and 5.15 with Equations 5.16 and 5.17. Note that an extra subscript to denote which analogy is being used is introduced.

$$\alpha_\rho = 0 \tag{5.43}$$

$$\beta_{\rho,ij} = \beta_{p,ij} - c^2 \alpha_p \delta_{ij} \tag{5.44}$$

Hence, defining  $\alpha_p$  and  $\beta_{p,ij}$  implicitly defines the corresponding  $\alpha_\rho$  and  $\beta_{\rho,ij}$ . A moving surface was desired, and so a body-fixed frame,  $\eta_i(x_i, t) = x_i + v_i t$ , was defined for a constant surface velocity  $v_i$ . An axisymmetric, harmonic source field was then defined as below, where  $\eta_X$  and  $\eta_R$  are the axial and radial co-ordinates in

the body-fixed frame, respectively.

$$Q_1(\eta_X) = 0.5 (1 + \tanh(2\pi\eta_X)) \operatorname{sech}(\eta_X) \quad (5.45)$$

$$Q_2(\eta_R) = \operatorname{sech}(2\pi\eta_R) \quad (5.46)$$

$$Q_3(t) = \sin(\omega t) \quad (5.47)$$

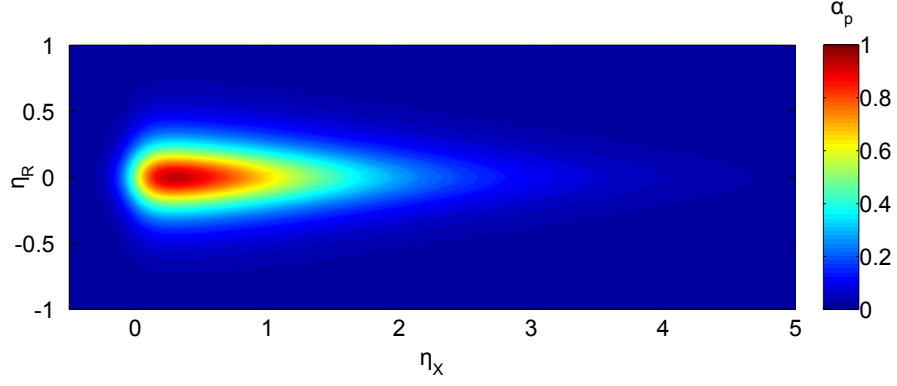
$$\alpha_p = Q_1(\eta_X)Q_2(\eta_R)Q_3(t) \quad (5.48)$$

$$\beta_{p,ij} = 0 \quad (5.49)$$

For simplicity, only the contribution of  $\alpha_p$  is considered, but it should be noted that its effect on  $\beta_{\rho,ij}$  remains, so both monopole and dipole fields are examined to some extent. The amplitude of  $\alpha_p$ , which is  $Q_1(\eta_x)Q_2(\eta_r)$ , is illustrated in Figure 5.1. Clearly, the  $Q_1$  and  $Q_2$  components limit the extent of the source field in the axial and radial directions respectively. Again, it should be emphasised that this source field is not based on a realistic flow.

The partial source fields resulting from retaining only the internal parts of Equations 5.25, 5.34 and 5.42 are as defined below. The subscripts  $K$ ,  $N$  and  $F$  are used to denote solutions using the Kirchhoff, new and FW-H surface methods respectively, and subscripts  $p$  and  $\rho$  are used to denote solutions using the pressure and density analogies respectively.

$$\left( \frac{1}{c^2} \frac{\partial^2}{\partial t^2} - \frac{\partial^2}{\partial x_i^2} \right) \phi_{K,p} = \frac{\partial^2 \alpha_p}{\partial t^2} H(-f) \quad (5.50)$$

Figure 5.1: Magnitude of  $\alpha_p$  for semi-analytical test case.

$$\left( \frac{1}{c^2} \frac{\partial^2}{\partial t^2} - \frac{\partial^2}{\partial x_i^2} \right) \phi_{N,p} = \frac{\partial}{\partial t} \left( \frac{\partial \alpha_p}{\partial t} H(-f) \right) \quad (5.51)$$

$$\left( \frac{1}{c^2} \frac{\partial^2}{\partial t^2} - \frac{\partial^2}{\partial x_i^2} \right) \phi_{F,p} = \frac{\partial^2}{\partial t^2} (\alpha_p H(-f)) \quad (5.52)$$

$$\left( \frac{1}{c^2} \frac{\partial^2}{\partial t^2} - \frac{\partial^2}{\partial x_i^2} \right) \phi_{K,\rho} = c^2 \frac{\partial^2 \alpha_p}{\partial x_i^2} H(-f) \quad (5.53)$$

$$\left( \frac{1}{c^2} \frac{\partial^2}{\partial t^2} - \frac{\partial^2}{\partial x_i^2} \right) \phi_{N,\rho} = c^2 \frac{\partial}{\partial x_i} \left( \frac{\partial \alpha_p}{\partial x_i} H(-f) \right) \quad (5.54)$$

$$\left( \frac{1}{c^2} \frac{\partial^2}{\partial t^2} - \frac{\partial^2}{\partial x_i^2} \right) \phi_{F,\rho} = c^2 \frac{\partial^2}{\partial x_i^2} (\alpha_p H(-f)) \quad (5.55)$$

The equations above can be solved by convolving the source fields with the appropriate Green function. This leads to separate volume integrals for each solution, with any derivatives encapsulating the step function being initially left out of the convolution before being “moved” from the observer to the source in a similar manner to the derivation Formulation 1A. The process for deriving each solution is very

briefly summarised below, with the manipulations required to move derivatives from source to observer being omitted for the sake of brevity. A slightly different notation is used in order to allow convective derivatives of source properties to be clearly distinguished from stationary derivatives, and two kinematic properties are defined for ease of notation.

$$\frac{D}{D\tau} = \frac{\partial}{\partial\tau} \Big|_{\eta_i} \quad (5.56)$$

$$K_1 = c(M_r - M^2) \quad (5.57)$$

$$K_2 = c(M_r^2 - M^2) \quad (5.58)$$

$$\phi_{K,p} = \frac{1}{4\pi} \int_V \left[ \frac{\frac{\partial^2 \alpha_p}{\partial \tau^2}}{r(1 - M_r)} \right]_{g=0} dV \quad (5.59)$$

$$\phi_{N,p} = \frac{1}{4\pi} \frac{\partial}{\partial t} \int_V \left[ \frac{\frac{\partial \alpha_p}{\partial \tau}}{r(1 - M_r)} \right]_{g=0} dV \quad (5.60)$$

$$= \frac{1}{4\pi} \int_V \left[ \frac{\frac{D}{D\tau} \left( \frac{\partial \alpha_p}{\partial \tau} \right)}{r(1 - M_r)^2} + \frac{\frac{\partial \alpha_p}{\partial \tau} K_1}{r^2(1 - M_r)^3} \right]_{g=0} dV \quad (5.61)$$

$$\phi_{F,p} = \frac{1}{4\pi} \frac{\partial^2}{\partial t^2} \int_V \left[ \frac{\alpha_p}{r(1 - M_r)} \right]_{g=0} dV \quad (5.62)$$

$$= \frac{1}{4\pi} \int_V \left[ \frac{\frac{D^2 \alpha_p}{D\tau^2}}{r(1 - M_r)^3} + \frac{\frac{D\alpha_p}{D\tau} (2K_1 + K_2)}{r^2(1 - M_r)^4} \right. \\ \left. + \frac{\alpha_p K_1 (2K_1 + K_2)}{r^3(1 - M_r)^5} + \frac{c\alpha_p K_2}{r^3(1 - M_r)^4} \right]_{g=0} dV \quad (5.63)$$

$$\phi_{K,\rho} = \frac{1}{4\pi} \int_V \left[ \frac{c^2 \frac{\partial^2 \alpha_p}{\partial y_i^2}}{r(1 - M_r)} \right]_{g=0} dV \quad (5.64)$$

$$\phi_{N,\rho} = \frac{1}{4\pi} \frac{\partial}{\partial x_i} \int_V \left[ \frac{c^2 \frac{\partial \alpha_p}{\partial y_i}}{r(1 - M_r)} \right]_{g=0} dV \quad (5.65)$$

$$\begin{aligned} &= \frac{-1}{4\pi} \int_V \left[ \frac{c \frac{D}{D\tau} \left( \frac{\partial \alpha_p}{\partial y_i} \right) \hat{r}_i}{r(1 - M_r)^2} + \frac{c^2 \frac{\partial \alpha_p}{\partial y_i} (\hat{r}_i - M_i)}{r^2(1 - M_r)^2} \right. \\ &\quad \left. + \frac{c \frac{\partial \alpha_p}{\partial y_i} K_1 \hat{r}_i}{r^2(1 - M_r)^3} \right]_{g=0} dV \end{aligned} \quad (5.66)$$

$$\phi_{F,\rho} = \frac{1}{4\pi} \frac{\partial^2}{\partial x_i^2} \int_V \left[ \frac{c^2 \alpha_p}{r(1 - M_r)} \right]_{g=0} dV \quad (5.67)$$

$$\begin{aligned} &= \frac{1}{4\pi} \int_V \left[ \frac{\frac{D^2 \alpha_p}{D\tau^2}}{r(1 - M_r)^3} + \frac{\frac{D \alpha_p}{D\tau} (2K_1 + K_2)}{r^2(1 - M_r)^4} \right. \\ &\quad \left. + \frac{\alpha_p K_1 (2K_1 + K_2)}{r^3(1 - M_r)^5} + \frac{c \alpha_p K_2}{r^3(1 - M_r)^4} \right]_{g=0} dV \end{aligned} \quad (5.68)$$

It is clear that  $\phi_{F,p} = \phi_{F,\rho}$ , though quite a lot of manipulation is required to get to this result for  $\phi_{F,\rho}$ . A solver was written to calculate these various different solutions for an observer moving in the body-fixed frame, with all derivatives of  $\alpha_p$  being taken analytically. Because  $\alpha_p$  was harmonic and all other aspects of the integral were constant in time, a frequency domain approach was used to propagate the sine and cosine components individually.

The solver was validated for a source field with a forward Mach number of -0.5 (i.e. moving in the negative axial direction), speed of sound  $340 \text{ m s}^{-1}$ , a frequency of  $600 \text{ rad s}^{-1}$  and an observer 20 m away from the body fixed origin at a range of

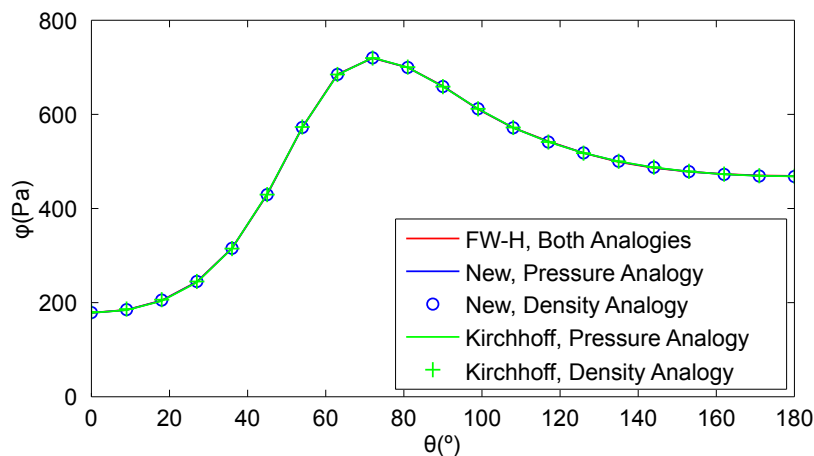


Figure 5.2: Variation of  $\phi$  with directivity for  $X_D = 6$ .

directivities. The integration region was cylindrical, with the upstream end of the volume located at  $\eta_X = -2\text{m}$  and the location of the downstream end, denoted  $X_D$ , being varied. The radial limit of the volume was  $\eta_R = 2\text{m}$ . The discretisation of the volume was checked to make sure errors were negligible.

Figures 5.3 and 5.2 show the variation of the calculated noise with directivity for the different methods and analogies for two different values of  $X_D$ . The fact that all six methods match closely for  $X_D = 6$ , i.e. when the external source field is negligible, confirms that the solver is correctly evaluating the various volume integrals defined above. However, it is clear from the results for  $X_D = 1$  that when a significant part of the source field is outside the surface discontinuity and is neglected, the different methods can give very different answers.

In order to more directly investigate the stability of different methods to neglect errors, Figures 5.4, 5.5 and 5.6 show the variation of  $\phi$  with  $X_D$  for an axially upstream, perpendicular and axially downstream observer respectively. Clearly, the directivity of the observer has a strong effect on the stability of the different methods,

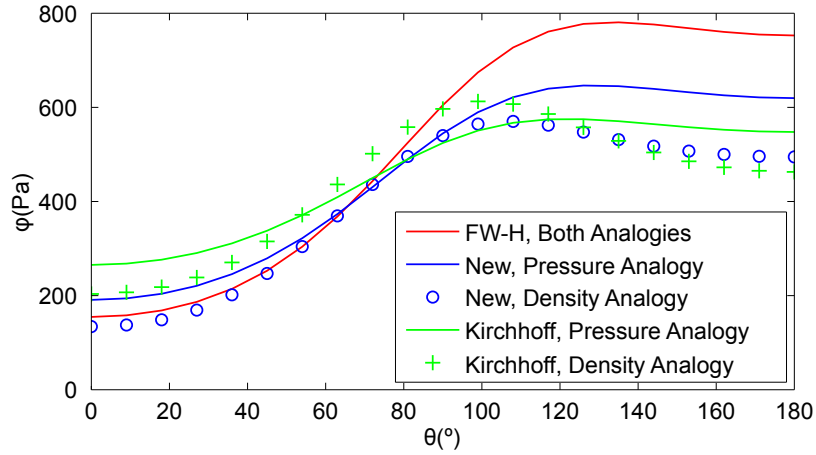


Figure 5.3: Variation of  $\phi$  with directivity for  $X_D = 1$ .

as is expected from previous work. However, the results also show that directivity affects the relative stability of the different methods, with either the Kirchhoff or FW-H methods being the most unstable and the new method being somewhere in between. This is an important new contribution of this thesis, as it raises the possibility of one method being more appropriate than another at different directivities.

The results for the upstream observer show the largest instabilities, as well as the largest variation between different methods. The FW-H method is the most unstable, followed by the other methods using a pressure analogy. Surprisingly, it is the Kirchhoff with density analogy method that is the most stable, almost completely eliminating the large oscillations which have affected the other signals. The perpendicular observer has the best correlation between the different methods, though again the FW-H method has the largest fluctuations. At the downstream observer it is a little harder to pick the best method. The Kirchhoff and new methods with a density analogy are quick to approach the correct answer, but are rather more unstable than their pressure analogy equivalents and the FW-H method.

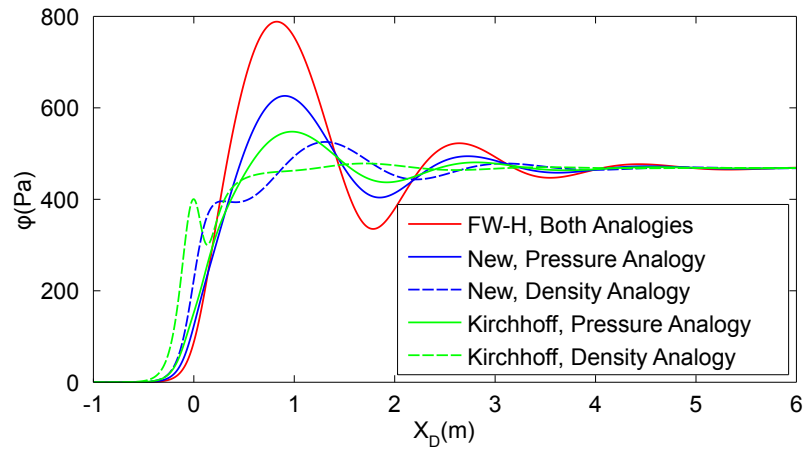


Figure 5.4: Comparison of different analogies and surface methods for an upstream observer location.

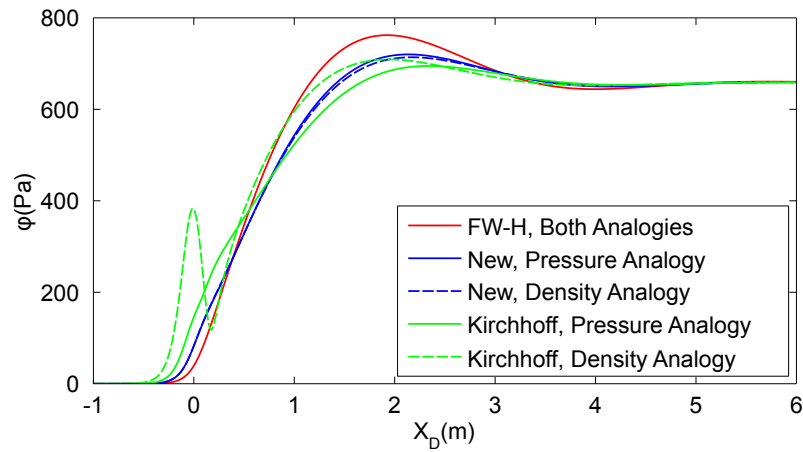


Figure 5.5: Comparison of different analogies and surface methods for a perpendicular observer location.

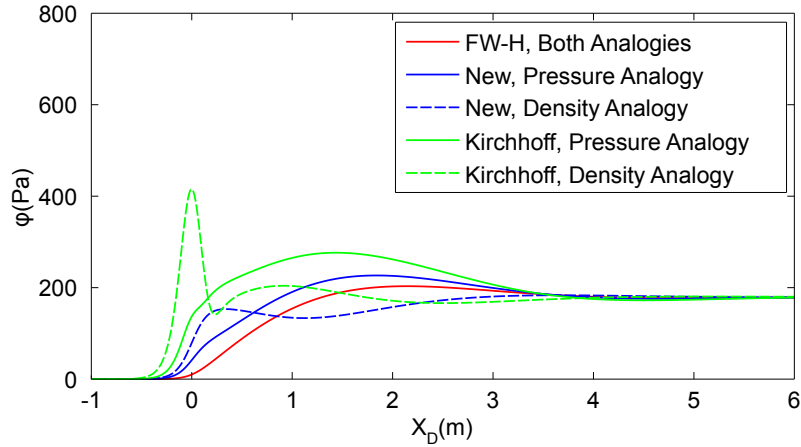


Figure 5.6: Comparison of different analogies and surface methods for a downstream observer location.

In order to better visualise the relative stability of the different methods as a function of directivity and downstream surface location, Figure 5.7 shows a set of contour plots. The above observations are clearly supported, in particular that it is actually the density analogy methods that most effectively mitigate the instabilities at upstream directivities seen for the FW-H method. This would appear to outweigh the increased “twitchiness” of the density analogy methods at downstream directivities, as these appear to be small in comparison to the improvements at upstream directivities.

The superiority of the density analogy methods is contradictory to the motivation for the work in this chapter, namely that eliminating density perturbations can give a stability benefit. It is important to reiterate that the source field these results are based on is not physically meaningful, and hence it is vital that these methods are tested on a more realistic test case. It has, however, demonstrated that neglection errors can vary significantly for a given test case depending on which aeroacoustic

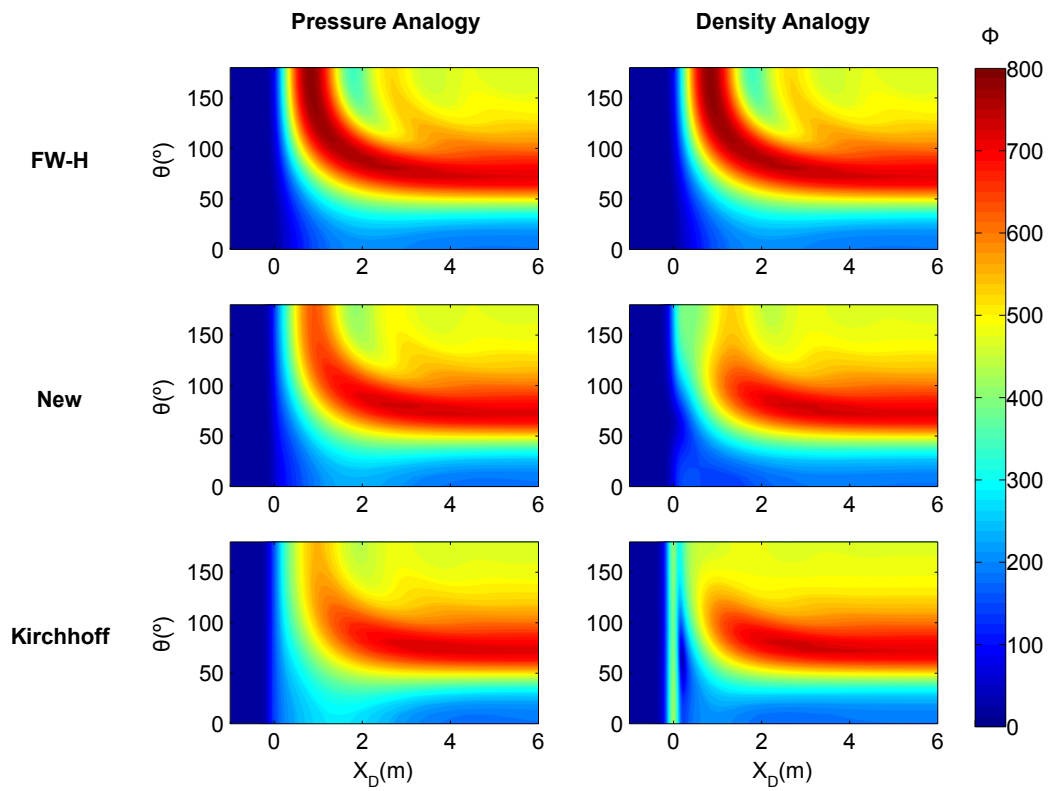


Figure 5.7: Variation of  $\phi$  for different surface methods and source constructions vs. directivity and downstream integration limit.

analogy and which surface discontinuity method are used. This underlines the importance of neglection errors and hence the relevance of the work presented in this chapter in deriving and understanding the new surface discontinuity method and how it compares to the FW-H and Kirchhoff methods.

## 5.4 Summary

The fourth objective of this thesis is to find new methods for defining aeroacoustic analogies that help to mitigate neglection errors while retaining a clear physical interpretation. This chapter has addressed this objective by deriving a generic version of an aeroacoustic analogy. This generic notation has demonstrated two different ways of understanding the physical interpretation of the source field in an aeroacoustic analogy. Firstly, the source field should be thought of in terms of addition of mass and momentum, rather than imposition of density and stress. Secondly, any source field should be understood in terms of its relationship to the acoustic fluid, not the realistic one.

With these perspectives in mind, a new method for introducing a surface discontinuity into an aeroacoustic analogy has been developed. The key difference to other methods is that the source field is split in terms of the mass and momentum added to the acoustic fluid, and hence neglecting the external part of this field has a clear physical interpretation in terms of ignoring addition of mass and momentum to the acoustic fluid outside the surface, which is in keeping with the above perspectives. It has also been shown that the new method allows density perturbations in the surface sources to be easily avoided by choosing appropriate definitions of the acoustic flow properties, meaning that this is also achieved with a clear physical understanding of what avoiding density perturbations represents.

The new method has been compared to the FW-H and Kirchhoff methods, and all three have been shown to be mathematically identical when no terms are neglected. However, all three have been shown to split the internal and external source fields differently. The FW-H method has been shown to split the source field in terms of the imposition of extra density and stress fields, and that the resulting surface sources only have a physical interpretation in the realistic flow, not the acoustic one. The Kirchhoff method has been shown to split the source field in terms of fundamental sound sources, not mass and momentum addition. It has also been shown that the source field cannot be interpreted in terms of an acoustic fluid. This means that both the FW-H and the Kirchhoff methods are inconsistent with the two fundamental perspectives and the new method is therefore considered more physically intuitive.

Finally, a semi-analytical flow solution has been used to investigate the relative stability of the different methods with downstream surface placement. Interestingly, it has been seen that the relative stability of the methods depends on observer directivity, which appears to be a new result of this thesis. The results also seem to favour the Kirchhoff method and the density analogy, both of which are surprising and contradictory to the motivation of this chapter. Because the source field is unphysical, it is difficult to draw any further conclusions from the results, but they demonstrate the importance of neglecting errors and the potential of the new surface discontinuity method to provide a viable alternative to the FW-H and Kirchhoff methods. It is imperative that these different methods are applied to a more realistic test case, in order to understand how valid the results from the semi-analytical test case are.

The generic notation used in this chapter, the clear way in which this demonstrates the split between realistic and acoustic fluids, the two perspectives highlighted as key to understanding aeroacoustic analogies, the new method of introducing a surface discontinuity, the comparisons of and resulting insight into the new, FW-H and

Kirchhoff methods and the use of the semi-analytical flow solution to investigate them are all new contributions provided by this thesis.

# Chapter 6

## Demonstration On Realistic Test Case

This thesis has presented novel work aimed at mitigating discretisation and neglect errors in FW-H solvers. The final objective of this thesis is to demonstrate the importance and validity of this work on a realistic open rotor test case. This chapter addresses this objective using the Rolls Royce Z-08 open rotor design presented in Chapter 2. Provided the test case can be considered representative of an open rotor in general, it can be used to compare different methods, which is the purpose of this chapter.

The chapter begins with a more detailed discussion of the Z-08 test case, including some brief examination of the available CFD flow solution. An important problem with the available CFD is identified, namely that it is not periodic in time in the rotating frame, which necessitates an unphysical “fix” that is a good compromise between altering the input flow as little as possible and overcoming the troublesome effect of non-periodicity. This adjusted flow solution is then used to calculate some

Variable	Description	Value	Units
$M_X$	Forward Mach number	0.218	-
$R_F$	Front rotor tip radius	0.305	m
$R_R$	Rear rotor tip radius	0.2509	m
$N_F$	Number of blades on front row	12	-
$N_R$	Number of blades on rear row	9	-
$J_F$	Front rotor advance ratio	1.09	-
$J_R$	Rear rotor advance ratio	1.52	-

Table 6.1: Key characteristics of Z-08 test case.

initial results that demonstrate that the test case is representative of an open rotor. Discretisation errors are examined in a simple method study that compares results for the “industry standard” and “best practice” methodologies from Chapter 4 using two different flow solution time steps. Finally, neglect errors are examined by comparing the new source term formulations derived in Chapter 5 with the original FW-H terms for a range of directivities and downstream integration limits.

## 6.1 Test Case

As described in Chapter 2, the test case chosen for this thesis is an uninstalled run of the Rolls Royce “Z-08” design, which is itself a descendant of the previous “Rig-140” [50] and “Rig-145” [68] designs. The CFD flow solution for the test case was kindly provided by Sohoni [76, 77]. While the full operating point of the test case is not in the public domain, some parameters are given in Table 6.1. These can be compared with those of Table 4.2 to show that the analytical test case used in examining different solver methodologies was representative of a realistic open rotor.

A basic illustration of the CFD domain is given in Figure 6.1. The mesh contained two sliding planes to account for the counter-rotation of the blades. A key

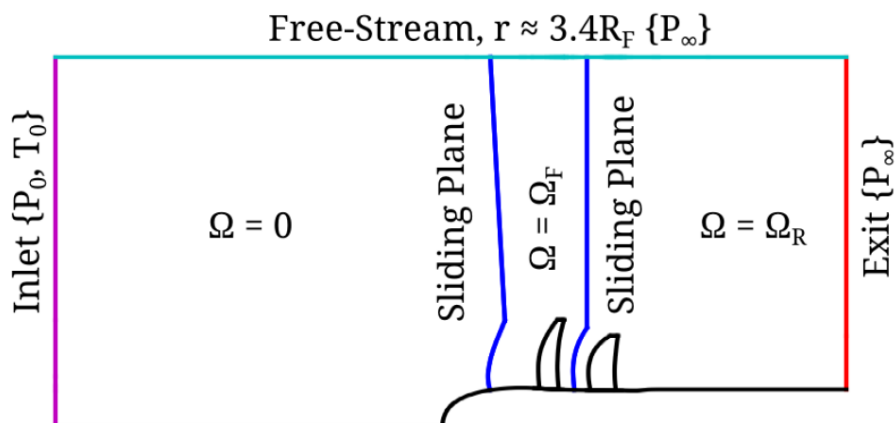


Figure 6.1: Illustration of CFD domain reproduced from Sohoni [77], showing sliding planes and boundary conditions.

motivation in the development of the CFD methodology was the accurate propagation of the front rotor wakes across the sliding plane between the blade rows, in order to accurately calculate its interaction with the rear rotors and the resulting interaction noise. The entropy contours across the sliding plane given in Figure 6.2 show no obvious discontinuity at the sliding plane, and it appears that the wakes are being propagated well. Sohoni defined a metric for measuring the quality of this propagation,  $K$ , which is defined as the ratio of the strength of a given wake harmonic just downstream of the sliding plane to just upstream of it. This metric is compared for the “fine” mesh used in Figure 6.2 and a “coarse” mesh in Figure 6.3. It is clear that the fine mesh is significantly better at preserving the wakes across the sliding plane, and this impressive result should not be underestimated.

In order to examine the effect of different integration surface placements on the calculation, several different downstream cut planes were extracted. The positions and naming convention for these cuts are plotted in Figure 6.4 and the locations of each cut are defined in Table 6.2.

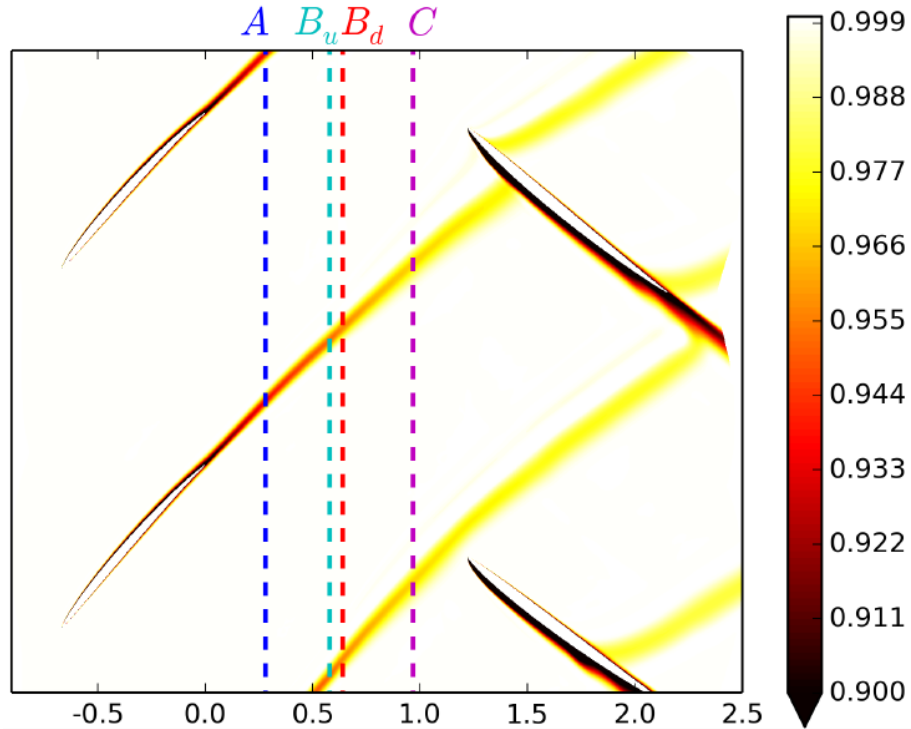


Figure 6.2: Entropy contours across inter-row sliding plane and wake comparison locations, reproduced from Sohoni [77].

Name	Type	Location
$U1$	Upstream Axial	$x/R_F = -0.213$
$D1$	Downstream Axial	$x/R_F = 0.807$
$D2$	Downstream Axial	$x/R_F = 0.925$
$D3$	Downstream Axial	$x/R_F = 1.044$
$D4$	Downstream Axial	$x/R_F = 1.163$
$D5$	Downstream Axial	$x/R_F = 1.282$
$R1$	Radial	$r/R_F = 1.013$

Table 6.2: Cut plane locations for Z-08 test case.

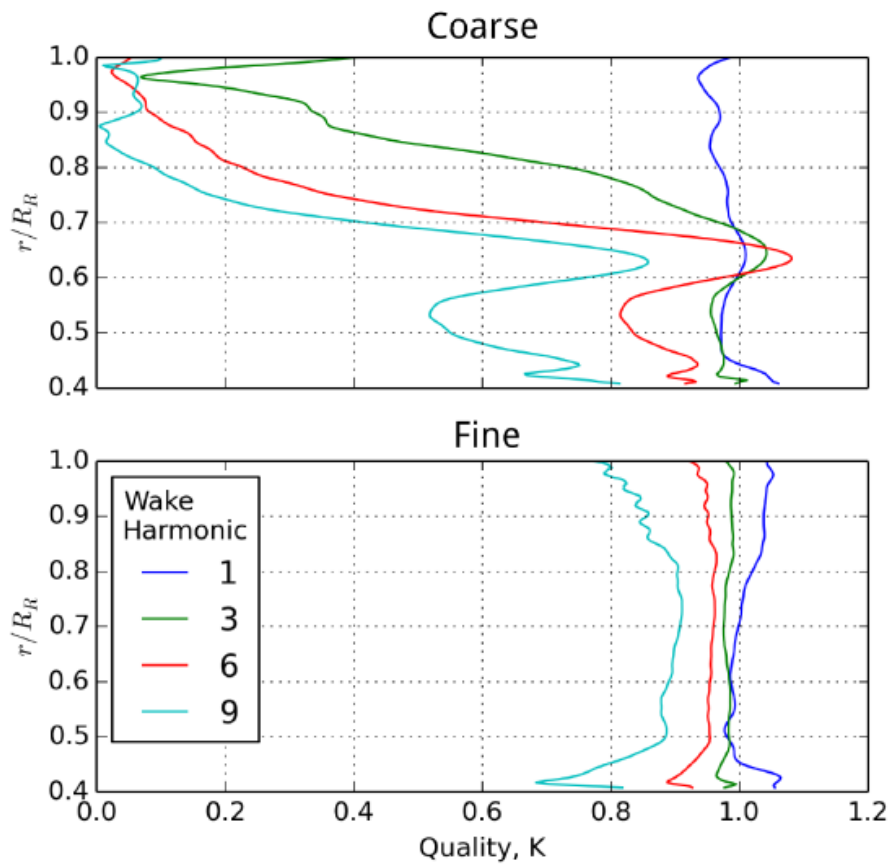


Figure 6.3: Plot of wake harmonic propagation quality across the inter-row sliding plane for two different mesh resolutions, reproduced from Sohoni [77].

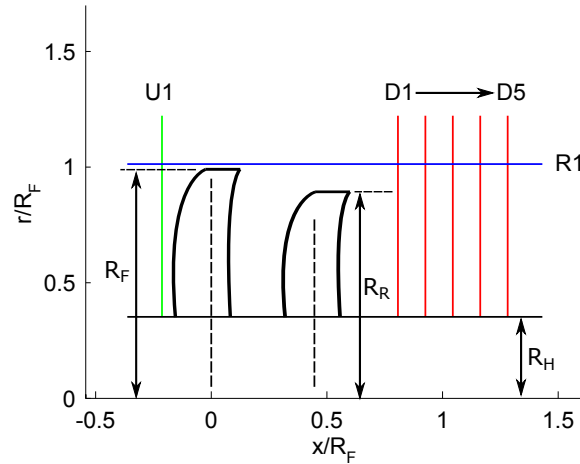


Figure 6.4: Plot of cut plane locations and names, as well as Z-08 geometry notation.

The Turbostream flow solution was converted using `fwh_ts2fwh` as described in Chapter 3. In order to check that this conversion was correct, and to assess the validity of the underlying CFD, some basic checks of the flow solution were made. Contours of the pressure perturbation and entropy on D1 for  $t = 0$  are plotted in Figures 6.5 and 6.6. This clearly shows that the pressure field is dominated by the rear tip vortices, where as the entropy plot highlights more flow features, including the front tip vortices, both sets of wakes and the hub interaction. To give an impression of the acoustic source field, contour plots of  $Q$  and the magnitude of  $F_i$  are given in Figures 6.7 and 6.8.

All four contour plots highlight a mesh line and two points on the line, A and B, which will be used for further analysis below. Point A is close to one of the rear tip vortices, while point B is at a midspan location. The mesh line also cuts across the rear wake and hence is considered a reasonably onerous choice in terms of flow field complexity.

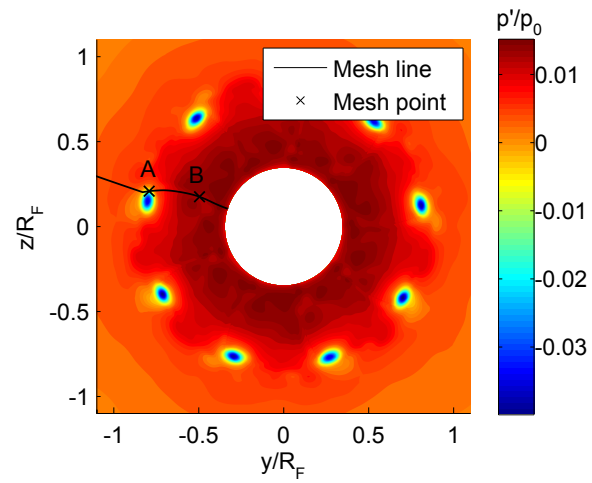


Figure 6.5: Contour plot of pressure perturbation on D1 cut plane, as well as mesh line and point sample locations.

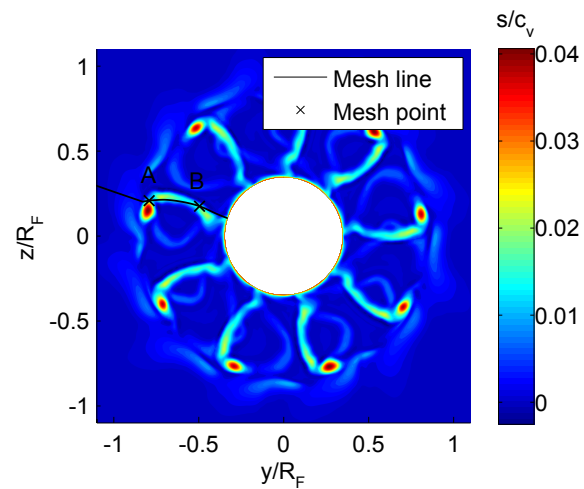


Figure 6.6: Contour plot of entropy on D1 cut plane, as well as mesh line and point sample locations.

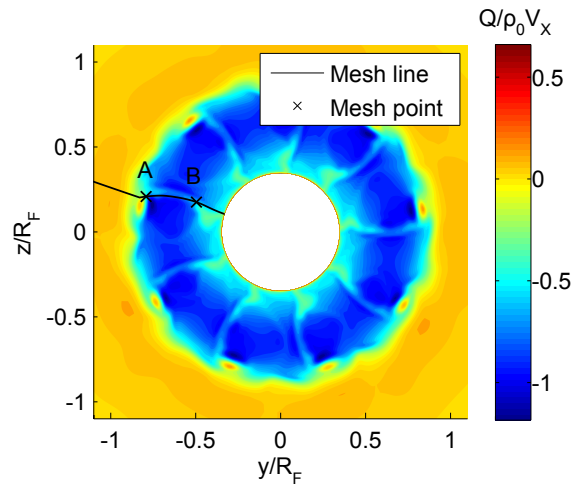


Figure 6.7: Contour plot of  $Q$  on D1 cut plane, as well as mesh line and point sample locations.

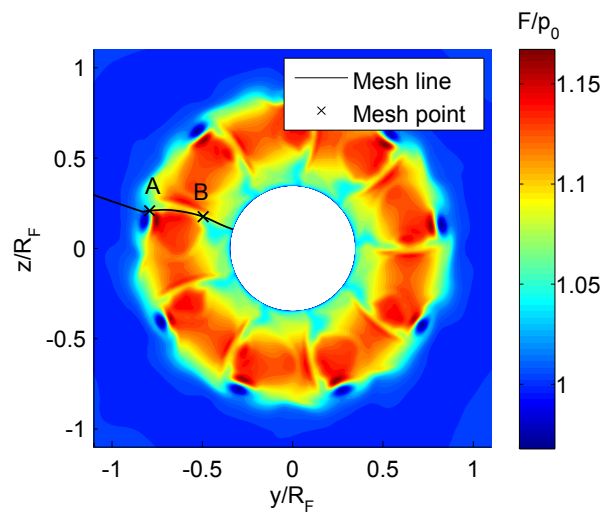


Figure 6.8: Contour plot of  $F$  on D1 cut plane, as well as mesh line and point sample locations.

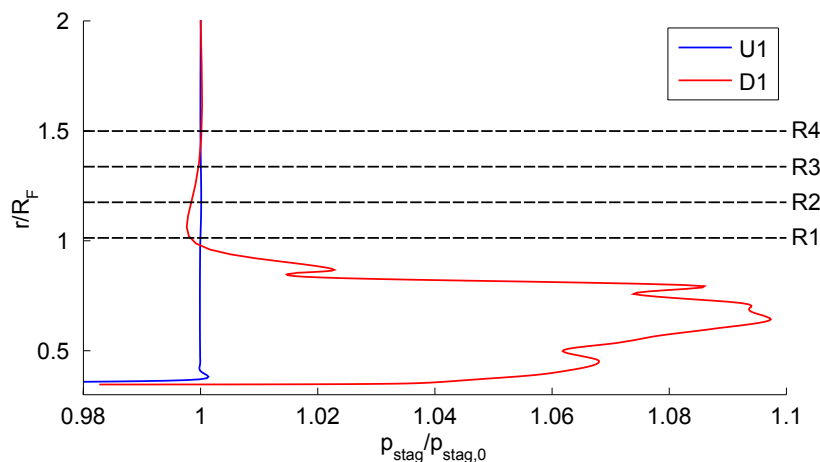


Figure 6.9: Radial plot of stagnation pressure on U1 and D1 cut planes.

The radial variation of stagnation pressure for the mesh line is compared with the equivalent for a mesh line on the U1 plane in Figure 6.9. This demonstrates that the stagnation pressure boundary condition is being maintained on the U1 plane, with the exception of the hub boundary layer, and that the stagnation pressure on D1 quickly returns to this value in the freestream. The “wiggles” in the D1 profile are due to the mesh line cutting across a wake, as discussed above.

A similar plot to judge the acoustic linearity of the flow on the upstream and downstream planes is given in Figure 6.10 by plotting  $p' - c^2\rho'$  for the same mesh line. It is clear that the upstream plane satisfies the  $p' = c^2\rho'$  condition everywhere except in the hub boundary layer, as would be expected, while the downstream plane only linearises in the freestream.

Thus far, only a single time step of the input CFD solution has been investigated. While the results are encouraging as they appear to respect the boundary conditions and give plausible acoustic source fields, it is important to examine the time history

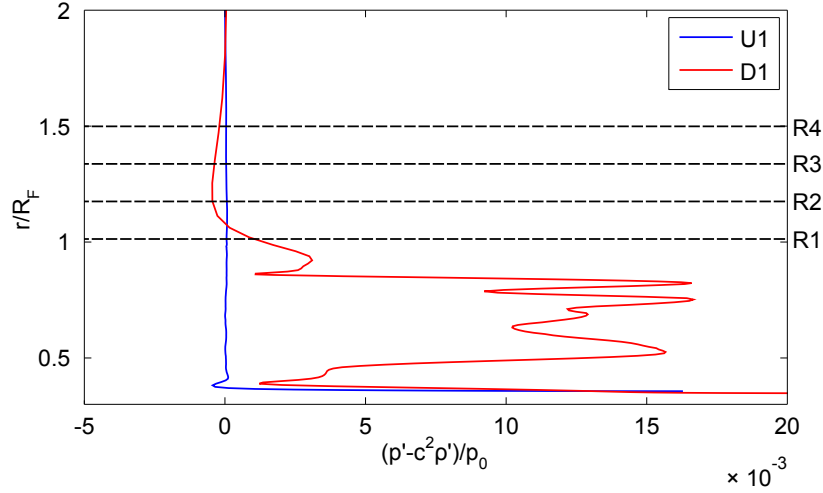


Figure 6.10: Radial plot of  $p' - c^2 \rho'$  on U1 and D1 cut planes.

of the flow solution and confirm that it is sufficiently well converged. This uncovers a problem with the periodicity of the flow solution that is examined in the next section.

## 6.2 Periodicity Problem

As has already been discussed in Chapter 2, the uninstalled nature of the test case means that the flow solution is expected to be periodic in the rotating reference frames for each blade row. The expected periodicity is given by Equation 2.71, but is repeated below for clarity (note that  $N_{HCF} = 3$  due to the blade numbers).

$$T_P = \frac{2\pi}{3(\Omega_F + \Omega_R)} \quad (6.1)$$

The CFD flow solution covered a time history of  $2T_P$ , with a time step of  $\Delta t = T_P/667$ , i.e. 1334 steps in total, and hence the time history should repeat itself twice.

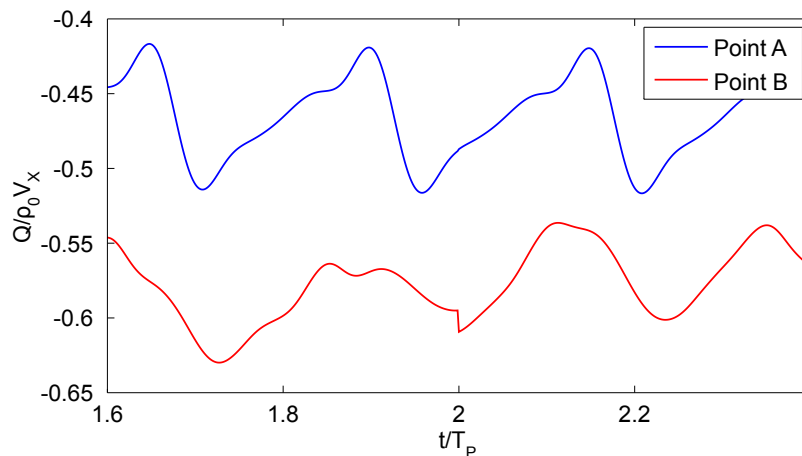


Figure 6.11: Plot of  $Q$  for points A and B on the D1 cut.

This periodicity in time needed to be taken advantage of in order to generate a time history in the non-rotating frame that was long enough to accurately resolve the frequency content. Hence the flow solution needed to be extrapolated past  $t = 2T_P$  (it was found that  $8T_P$  was sufficient), requiring the solution to “wrap around” to the  $t = 0$  point. The resulting time histories of the acoustic source term  $Q$  for points A and B from the previous section are plotted in Figure 6.11. It is clear that there is a large discontinuity in the time history for point B, and though point A seems much more periodic there is in fact a very small discontinuity there as well. These discontinuities led to large spikes in time derivatives, as shown in Figure 6.12.

This step discontinuity between the start and end of the time history was a significant problem for the proposed solver methodology. When the flow solution was interpolated as is, large discontinuities were created in the interpolated flow solution at integer multiples of  $2T_P$ . These were seen as extremely loud noise sources by the FW-H solvers and the resulting errors polluted the entire frequency content.

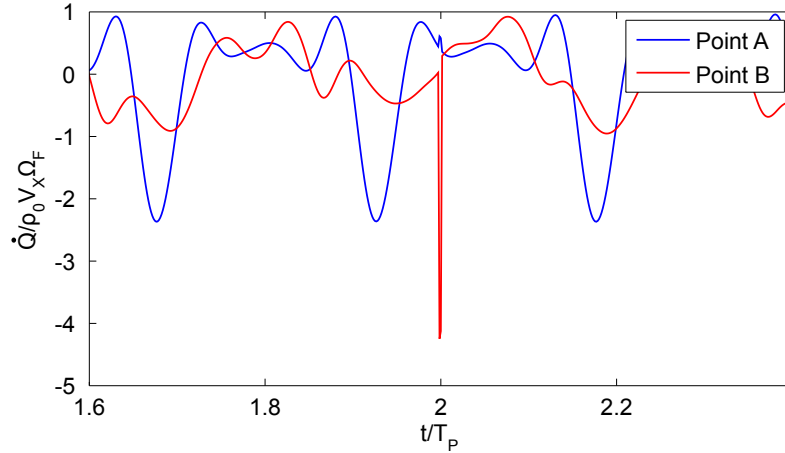


Figure 6.12: Plot of  $\dot{Q}$  for points A and B on the D1 cut.

In an ideal world, the available CFD would be perfectly converged and this problem could be entirely avoided. However, this is not a realistic solution, as all CFD inevitably has some imperfections. A more practical solution could be to extract a longer time history from the CFD, but this was not available to this author and would also require significantly longer CFD run times. Hence, the decision was taken to attempt to extract the periodic content from the flow solution and discard the non-periodic content causing the issues.

Figures 6.13 and 6.14 show the signal for point B around  $t = T_P$  and  $t = 2T_P$ , as well as the equivalent for two different methods of filtering. The first method was to simply perform LSSA on the signal with only the harmonics of the periodic frequency,  $2\pi/T_P$ , as input. Unfortunately it is clear from the plots that this only succeeded in splitting the discontinuity into two smaller discontinuities at  $t = T_P$  and  $t = 2T_P$ .

The second method adjusted the time history to remove the step discontinuity

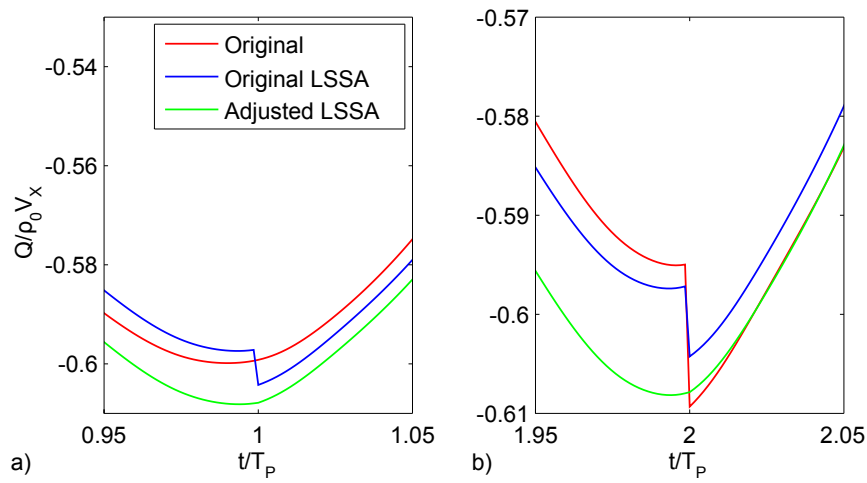


Figure 6.13: Plot of  $Q$  for point B compared to the results of the two filtering methods.

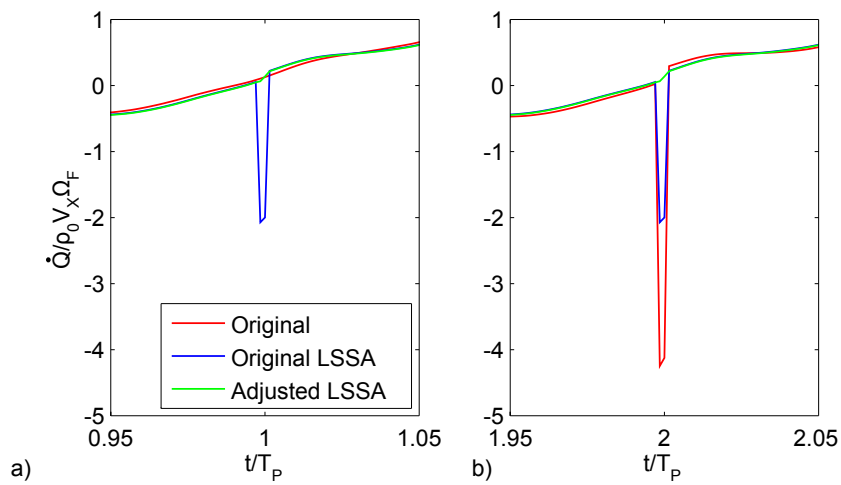


Figure 6.14: Plot of  $\dot{Q}$  for point B compared to the results of the two filtering methods.

before the LSSA was calculated. The adjustment was as defined below, and corresponded to removing a sawtooth wave of the correct magnitude from the signal. It is clear from Figures 6.13 and 6.14 that this has eliminated the discontinuity and guaranteed a smooth, periodic signal for interpolation.

$$\psi_{new}(t) = \psi_{old}(t) + \frac{t}{2T_0}(\psi_{old}(2T_0) - \psi_{old}(0)) \quad (6.2)$$

In order to understand the effect of this adjusted method on the frequency content, the FFTs of the three signals are given in Figure 6.15. It is clear that the effect of the original LSSA method is to remove the odd harmonics from the original FFT, while perfectly preserving the even tones, which are the tones which are periodic across  $T_P$ . While this forces the filtered signal to be periodic across  $T_P$ , the remaining tones are the same as for the FFT of a signal of length  $T_P$ , and hence discontinuities can exist in the result, and the LSSA has included some in order to get the best fit to the original signal. By removing the sawtooth content, the adjusted method prevents the LSSA from introducing the discontinuity, but also changes the periodic frequency content retained from the original signal.

Figure 6.16 shows the residual signal for each filtering method and the difference between the two. It is clear that this difference is a perfect square wave, i.e. the two methods remove the same non-periodic content except that the original method also removes a square wave of content that leads to the splitting of the original discontinuity between  $t = T_P$  and  $T = 2T_P$ . The reason that the difference is a perfect square wave is that the difference in input to the LSSA is a sawtooth wave, hence the difference in residuals is the odd harmonics of a sawtooth wave's FFT, which can be shown to be a square wave of half the magnitude of the original sawtooth.

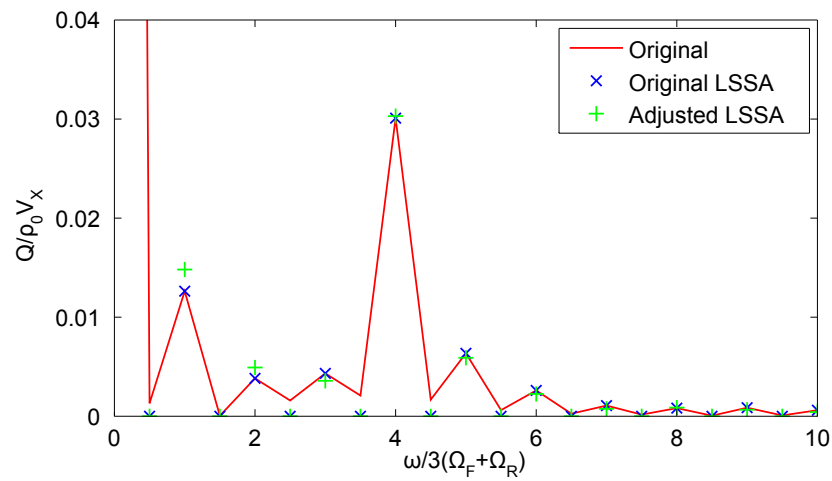


Figure 6.15: Frequency domain comparison of the original signal to the two filtering methods.

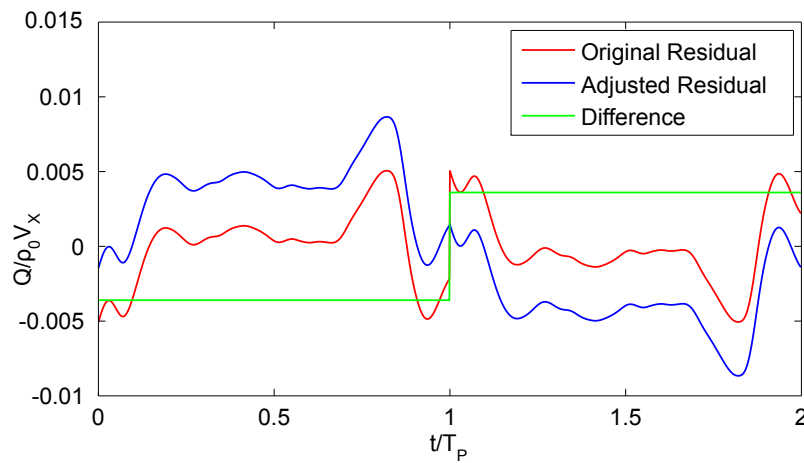


Figure 6.16: Comparison of the residual signals for the two filtering methods.

In summary, the provided CFD had small discontinuities between the start and end of the time history, despite being expected to be periodic. Because the required time history in the non-rotating flow solution needed to take advantage of this periodicity, these discontinuities needed to be dealt with to avoid significant errors in the calculated noise. By subtracting a sawtooth wave from the input time histories and then filtering for periodic content using LSSA, a flow solution was generated that was both smooth and precisely periodic, while having as similar a frequency content as possible to the original flow. It is important to recognise that this filtering is unphysical and will introduce input errors. However, these errors are small compared to those caused by retaining the discontinuities, and hence have to be accepted. An important area of future work is to investigate this problem further.

### 6.3 Surface Interpolation

Having developed a flow solution that was suitable for interpolation, the next decision was what spatial resolution to set on the non-rotating surface. The datum test case of Chapter 4 achieved reasonable results for  $N_\lambda \approx 50$  and  $N_T \approx 60$  based on the rear rotor alone tone, but the resolution of the CFD flow solution was much higher, at  $N_\lambda \approx 180$  and  $N_T \approx 480$ . Because this value of  $N_\lambda$  was skewed by the coarser mesh further from the blades, it was decided to aim for  $N_\lambda \approx 280$ . The resulting values of  $N_\lambda$  and  $N_T$  based on different tones are given in Table 6.3.

It is clear from these values that the (2,2) tone is quite close to the  $N_\lambda \approx 50$  limit. As will be seen shortly, the frequency content of the realistic case is more complex than the test case used in Chapter 4, and hence it was considered unlikely that tones above this frequency will be accurately predicted. Being able to assess the likely accuracy of a given mesh could be extremely useful when designing CFD

<b>Tone</b>	$N_\lambda$	$N_T$
(0,1)	277.7	478.7
(1,0)	180.6	311.3
(1,1)	109.4	188.7
(1,2)	78.5	135.3
(2,1)	68.1	117.5
(1,3)	61.2	105.5
(2,2)	54.7	94.3

Table 6.3: Resolution parameters based on different tones.

runs for use with an FW-H solver, and is an example of the power of analytical flow solutions in supporting such work.

The resulting interpolated flow solution at  $t = 2.25T_P$  is compared with the original flow solution at  $t = 0.25T_P$  in Figures 6.17 and 6.18. Also plotted is a constant radius line, and the solution along this line is compared in Figure 6.19. Clearly, the results are excellent and demonstrate that the flow solution has been correctly interpolated to the non-rotating frame, and that the calculation of the flow solution outside of the original time history has been handled correctly.

## 6.4 Initial Results

An initial set of results using this interpolated flow solution was obtained using the industry standard methodology from Chapter 4, i.e. the observer dominant solver `fwh_ret` was used with integral averaging and the time domain flow solution. The resulting time and frequency domain content for an observer at  $L = 10\text{m}$  and  $\theta = \pi/2\text{rad}$  using the D1 downstream cut are plotted in Figures 6.20 and 6.21. The time domain plot shows that the interpolated signal is not periodic and demonstrates the need to interpolate a long time history from the original rotating flow solution.

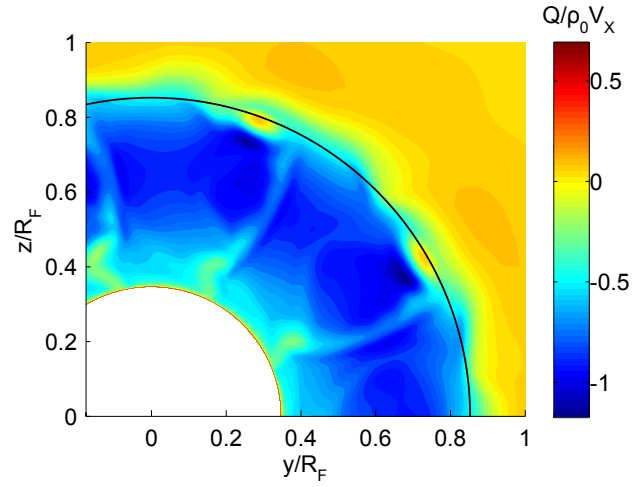


Figure 6.17:  $Q$  on D1 downstream cut in original flow solution at  $t = 0.25T_0$ .

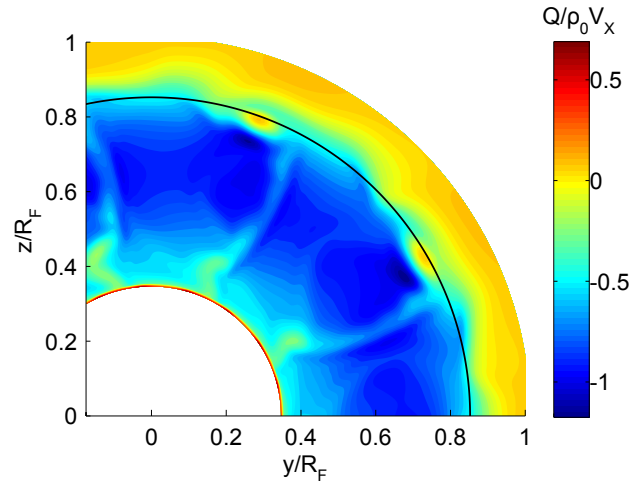


Figure 6.18:  $Q$  on D1 downstream cut in interpolated flow solution at  $t = 2.25T_0$ .

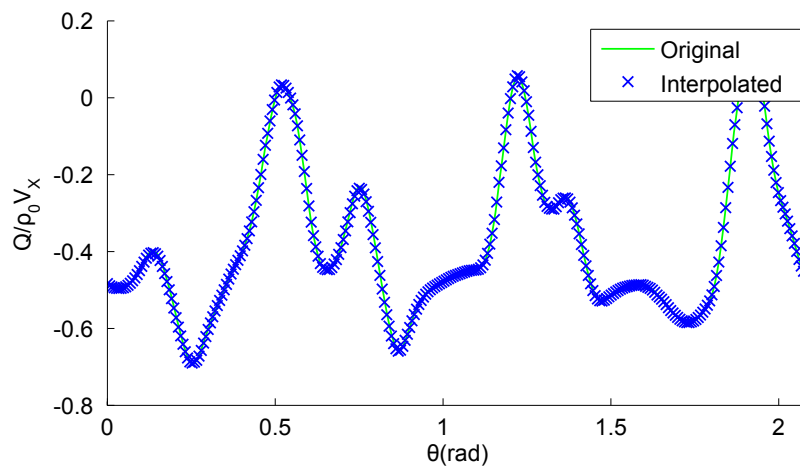


Figure 6.19:  $Q$  on D1 downstream cut in the original and interpolated flow solutions.

The frequency domain plot shows the FFT of the calculated signal and the associated LSSA and residual FFT, with the loudest tones labelled for clarity. The LSSA used 80 tones constructed from the first 9 and 12 front and rear rotor alone tones respectively, the first three positive interaction tones of each of these rotor alone tones (i.e. adding multiples of the other row's blade passing frequency), the first two harmonics of the rotating frame periodicity frequency (i.e.  $2\pi/T_P$  and  $4\pi/T_P$ ), and the (1,-1), (2,-2) and (-1,2) negative interaction tones. The remaining residual content was found to be primarily made up of other negative interaction tones, but including them in the results would have required a significantly longer interpolated flow solution and had a negligible effect on the louder tones that are further investigated in this chapter. However, it is important to acknowledge that the residuals are significantly louder than those seen for the analytical test cases of Chapter 4. This means that frequency content is being missed by the LSSA and this is an important area for future work.

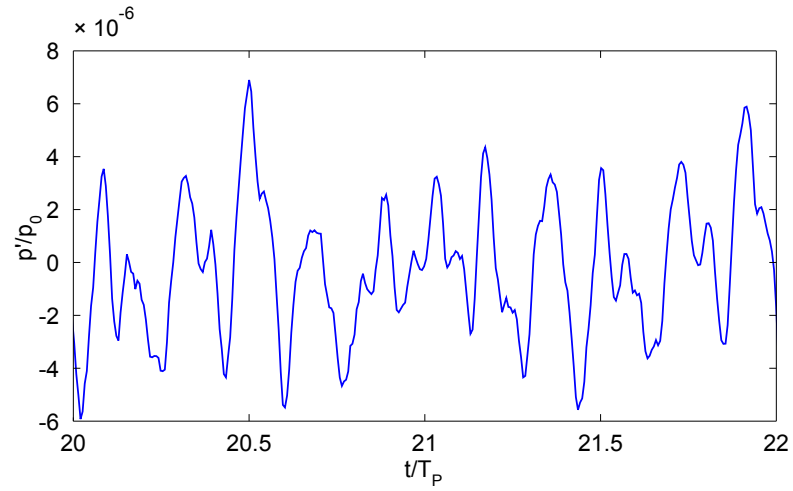


Figure 6.20: Time domain plot of initial results for the (U1,R1,D1) surface.

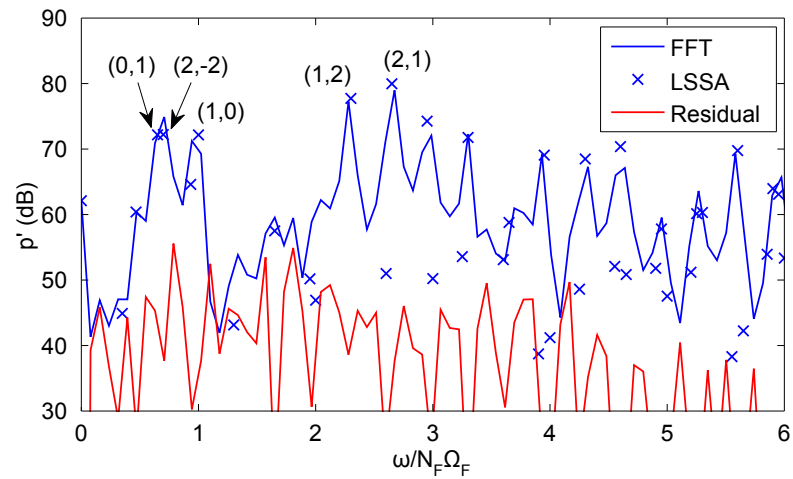


Figure 6.21: Frequency domain plot of initial results for the (U1,R1,D1) surface.

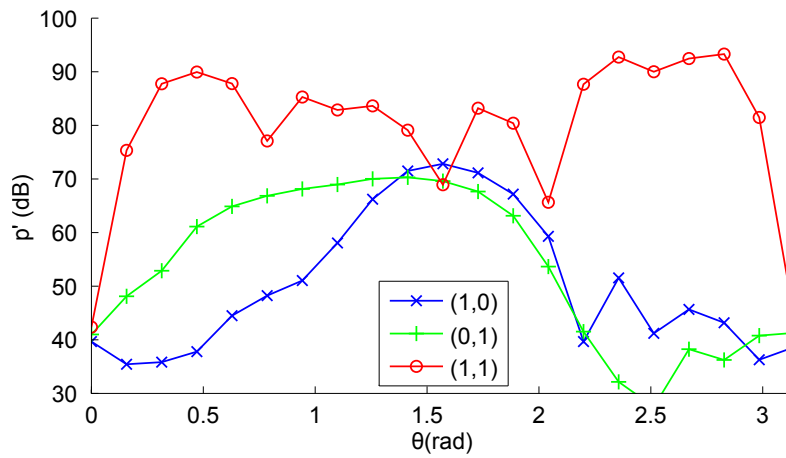


Figure 6.22: Directivity plot of initial results for the (U1,R1,D1) surface and industry standard methodology.

The variation of the (1,0), (0,1) and (1,1) tones with directivity is plotted in Figure 6.22. As expected, the rotor alone tones are only significant at close to perpendicular directivities, while the interaction tone is present at a much wider range of directivities. This is excellent validation that the right physics is being represented in the solutions, making them useful for studying the method improvements from previous chapters.

The same plot is presented for results based on the best practice methodology in Figure 6.23. The trends of the tones are clearly very similar, though at close to axial directivities the instability in the rotor alone tones is slightly different. This confirms that the best practice methodology also produces plausible results, but that there are noticeable differences between the methodologies which need to be investigated.

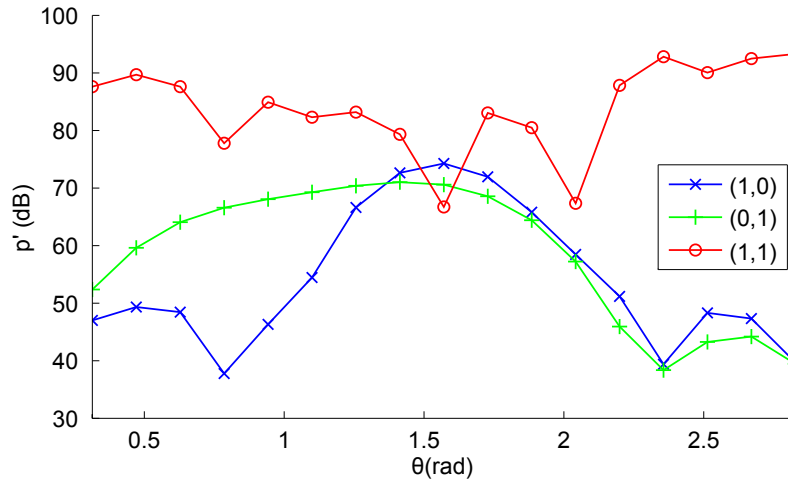


Figure 6.23: Directivity plot of initial results for the (U1,R1,D1) surface and best case methodology.

## 6.5 Discretisation Errors

Having developed a best practice methodology that significantly reduces discretisation errors compared to an industry standard methodology in Chapter 4, this section presents a simple demonstration that this superiority is also present for a realistic open rotor test case. As discussed in Chapter 4, it is expected that a key benefit of the best practice methodology is that it can be used with much longer time steps than methods based on a time domain flow solution, while still giving accurate results. In order to demonstrate this with the realistic test case of this chapter, a second set of interpolated flow solutions that only used every eighth time step of the original CFD flow solution (i.e. reduced the values of  $N_T$  given in Table 6.3 by a factor of eight) was calculated, and the corresponding results for both methodologies was compared with those for the original time step.

The best practice runs used the same frequency components in the LSSA as

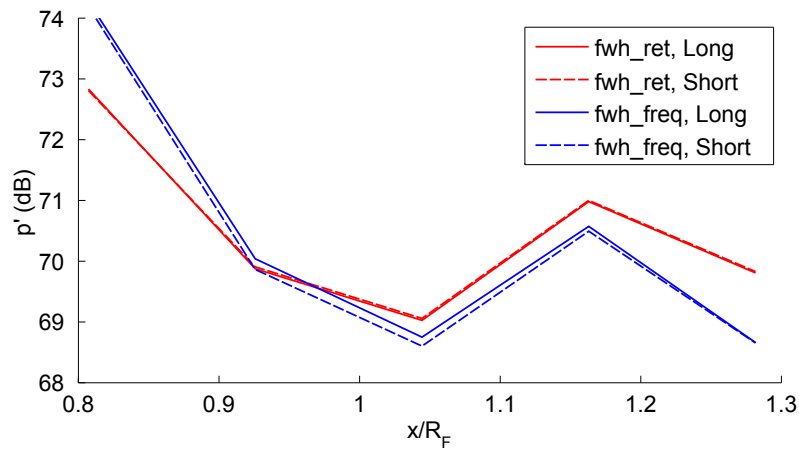


Figure 6.24: Variation of the (1,0) interaction tone for different solver methodologies and time steps.

Figure 6.21. The resulting variation of the (1,0) and (3,3) tones with downstream surface placement for each methodology/time step combination are given in Figures 6.24 and 6.25. Clearly, the results for the (1,0) tone are very consistent the different time steps for each solver, with the maximum variation across the different cases for a given downstream integration limit being about 1 dB. This is to be expected as the resolution of this tone is still quite high for the longer time step case.

However, the (3,3) tone is significantly less well resolved, leading to much larger differences both between the solvers and between the time steps. The differences between the solvers underlines how important discretisation errors are in realistic test cases, as the solution varies by up to 15 dB between the two solvers. The industry standard methodology varies by up to 10 dB for the two different time steps, whereas the best practice methodology only varies by up to about 3 dB. This clearly demonstrates the superiority of the best practice methodology in terms of its ability to handle significantly longer time steps than an industry standard methodology.

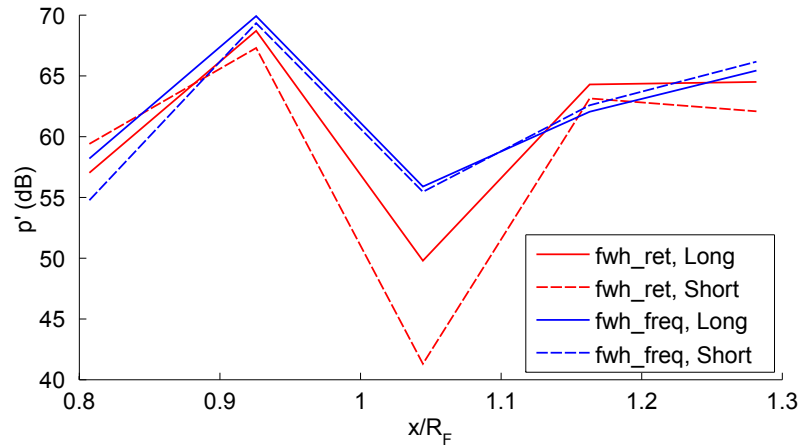


Figure 6.25: Variation of the (3,3) interaction tone for different solver methodologies and time steps.

In summary, it has been clearly demonstrated that different solver methodologies can have a large effect on the calculated noise, demonstrating the importance of selecting a solver that is well suited to the given problem and ensuring that discretisation errors are mitigated as much as possible. The superiority of the best practice methodology has been demonstrated in terms of its ability to handle longer time steps than the industry standard methodology.

## 6.6 Neglection Errors

It was seen in Chapter 5 that observer directivity had a significant effect on the relative stability of the different methods as downstream surface location was varied for a semi-analytical flow solution. A more surprising result was that the density analogy appeared to give better stability than the pressure analogy, demonstrating a need for investigating whether this was also seen in a realistic test case. This section

uses the best practice methodology and the short time step flow solution to demonstrate the importance of neglect errors in realistic test cases, and the usefulness of the work presented in Chapter 5 in mitigating these errors. Unfortunately, the Kirchhoff method could not be tested as its source terms contain spatial derivatives of flow properties, which were not given in the available CFD. However, the FW-H method and the new method using both pressure and density analogies could all be calculated and compared.

A similar study to that for the semi-analytical case was performed for the realistic test case, and the results for the (1,2) interaction tone at three different observer locations are presented in Figure 6.26. As for the semi-analytical flow solution, it is clear that the largest instabilities are seen at upstream observer locations, where predictions varied by up to 15 dB. Conversely, the downstream observer is the most stable, with predictions only varying by about 3 dB.

Moving on to comparing the different surface discontinuity methods, it is clear that the three methods are roughly similar in terms of stability for the downstream observer, and that the FW-H and new with pressure analogy methods are correlated, with the new with density analogy method following a different trend. For the perpendicular observer, the two new methods correlate very closely, with the FW-H method showing a slightly more extreme, less stable trend. Finally, the upstream observer clearly shows the new with pressure analogy method to be the most stable, as it varies by about 5 dB while the FW-H method varies by 10 dB and the new with density analogy method varies by 13 dB. This is a clear demonstration that density perturbations introduce significant instability to FW-H solvers, and that the new with pressure analogy method can, as intended, provide significant stability benefits compared to the FW-H method.

The above observations are all consistent with the results for the semi-analytical

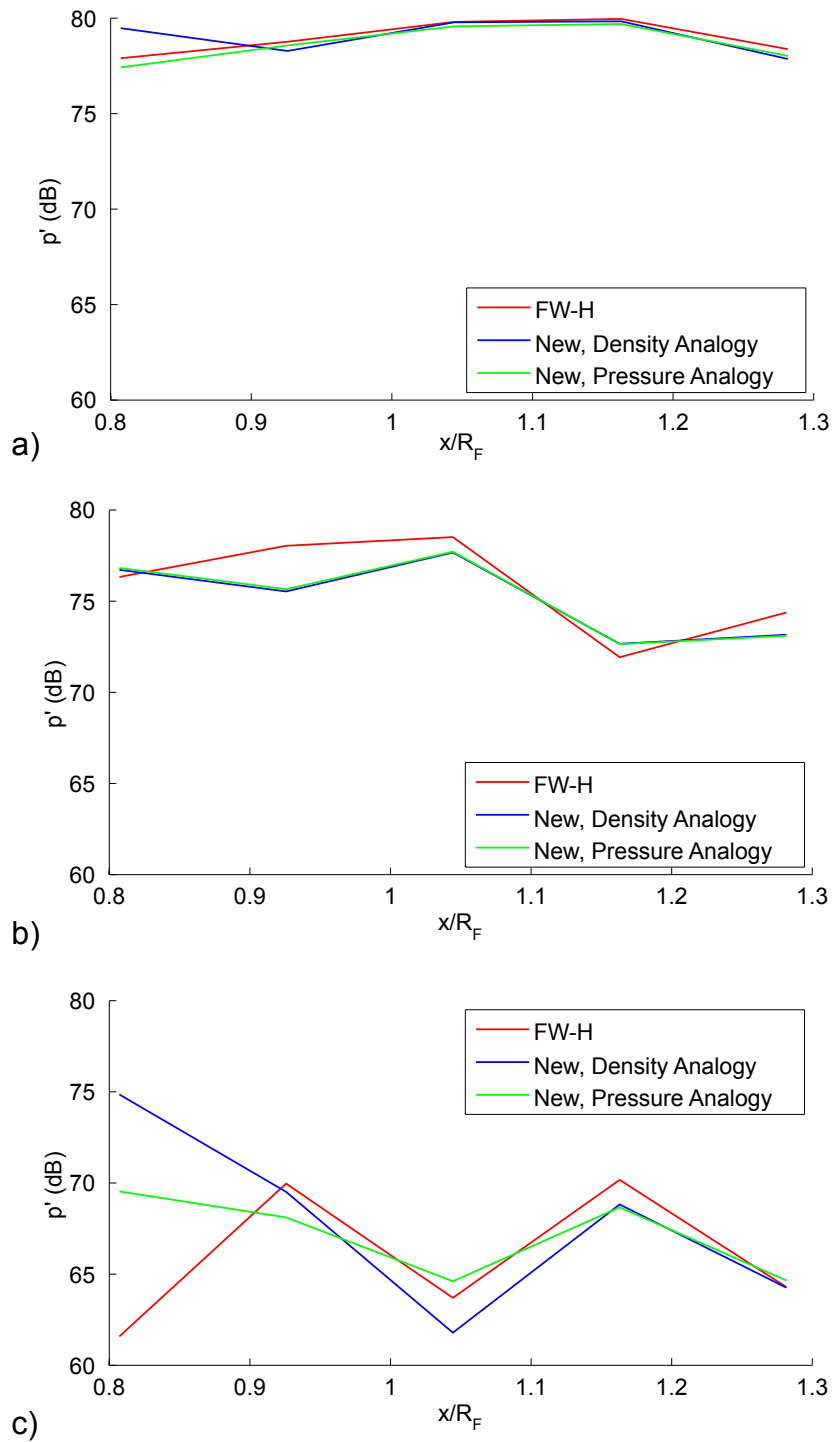


Figure 6.26: Variation of the (1,2) interaction tone for different source constructions at a)  $\theta = \pi/10$ , b)  $\theta = \pi/2$  and c)  $\theta = 9\pi/10$ .

case (see Figures 5.4, 5.5 and 5.6) except for the instability of the new with density analogy method at the upstream observer. For the semi-analytical case, this method was significantly more stable than both the FW-H and new with pressure analogy methods, and this was the key surprising result of Chapter 5. The fact that the results for the realistic test case so clearly contradict this result while much of the rest of the results are very consistent suggests that the semi-analytical case captures much of the physics of a realistic case, but is missing something fundamental to the instability caused by density perturbations. Remembering that many simplifications were made to the acoustic source field in the semi-analytical case (e.g. setting  $\alpha_p = 0$ ), it is possible that a different semi-analytical test case could be constructed that would more accurately represent a realistic test case. This is an important area for future work.

In summary, it has been shown that neglection errors are significant in a realistic open rotor test case, justifying the motivation for the work in Chapter 5. As expected from previous research, it has been confirmed that density perturbations can introduce significant instabilities in FW-H solvers, and that the new with pressure analogy method can significantly mitigate these instabilities. The surprising result from the semi-analytical test case of Chapter 5 that seemed to favour density analogy methods has been contradicted in the realistic test case, but many other aspects of the two sets of results were shown to be consistent. This suggests that the basic approach of the semi-analytical test case has merit, but that the particular source field needs to be made more realistic in order to better represent the physics of the problem.

## 6.7 Summary

As per the fifth and final objective of this thesis, this chapter has demonstrated the importance of the method improvements to conventional FW-H solvers developed in the previous chapters on a realistic open rotor test case. A significant problem with the periodicity of the available CFD was encountered and mitigated by using a simple but unphysical adjustment of the signals that removed large steps across the ends of the available time history. The initial results were shown to be representative of an open rotor, and hence the test case was confirmed to be useful in assessing the method improvements.

A simple method study examining the effect of increasing the time step in the interpolated flow solution was conducted to confirm a key point from Chapter 4, namely that using a frequency domain flow solution allowed significantly larger time steps to be used without detrimental effect on the accuracy. The fact that the results for the two different methods differed so much clearly demonstrated the importance of discretisation errors in realistic open rotor test cases. It was shown that higher frequency tones were affected exactly as expected, and that the best practice methodology did indeed handle the longer time steps significantly better than the industry standard methodology.

In addition, the new method of including a surface discontinuity into an aeroacoustic analogy that was developed in Chapter 5 was compared with the normal FW-H terms for both a pressure and a density analogy by varying the downstream extent of the integration surface. This demonstrated three important aspects of the work in Chapter 5. Firstly, it was seen that the new method using the pressure analogy gave the most stable predictions of the three methods, and that the new with density analogy was the least stable. This confirms that it is possible to mitigate

neglection errors by avoiding density perturbations in aeroacoustic analogies while maintaining a clear physical interpretation. Secondly, it was also confirmed that observer directivity greatly affects both the absolute and relative stability of the different methods, with upstream observers being the most unstable and hence onerous. Finally, it was seen that much of the behaviour of the different methods had been accurately predicted by the semi-analytical test case, with the important exception that the instability of density perturbations had not been seen in the semi-analytical case. This suggests that the semi-analytical case could be refined to better represent a realistic source field and then be used for further investigation of neglection errors.

The large differences seen between different solver methodologies and source term constructions has confirmed that discretisation and neglection errors need to be very carefully managed in FW-H solvers, and that it is not sufficient to simply concentrate on the accuracy of the input CFD solution. The benefits in mitigating these errors provided by the best practice methodology and the new with pressure analogy source terms clearly demonstrate the value of the work presented in this thesis. Hence, the final objective of this thesis has been satisfied.



# Chapter 7

## Conclusions and Further Work

This chapter summarises the main results and contributions provided by this thesis, and identifies important areas for future work. This thesis has presented relatively separate pieces of work in understanding and mitigating both discretisation and neglect errors in FW-H solvers, and hence this chapter is divided along the same lines.

### 7.1 Discretisation Errors

#### 7.1.1 Conclusions

The first objective of the thesis was to define the sources of discretisation error and the phenomena which affected them. This led to the definition of geometric, observer and flow resolution, and the associated metrics  $N_P$ ,  $N_L$ ,  $N_\lambda$  and  $N_T$  used to parametrise each error source. In addition, surface motion was shown to significantly affect the sensitivity of a solution to discretisation error.

The second objective of this thesis was to define a standard process by which

dimensional analysis could be used to investigate discretisation errors. Two different types of study were identified and it was shown that the dimensional analysis needs to be performed subtly differently in each case.

The third objective of the thesis was to use the above process to develop a “best practice” methodology that minimises discretisation errors as much as possible. An analytical test case consisting of two rows of counter-rotating acoustic monopole sources was developed and shown to be representative of an open rotor, with rotor alone tones vanishing at axial directivities and interaction tones present at all directivities.

A method study was performed using the above test case that began with a solver methodology that represented a current industry standard. This was gradually improved upon until arriving at a best practice methodology that reduced discretisation errors by over 90%.

The fifth objective of the thesis was to demonstrate any method improvements on a realistic open rotor test case. For the above work, this was achieved by comparing the industry standard and best practice methodology results using two CFD flow solutions for a modern open rotor design: one using every step and one using every eighth step of the CFD.

Differences between the two methodologies were up to 15 dB depending on surface location and the tone compared, but were less than 5 dB in most cases. This shows that discretisation is a significant effect in realistic test cases, justifying the work done in this thesis to understand and mitigate them. The variation of time step produced believable results, with low frequency tones being less affected than higher frequency ones. The best practice methodology was noticeably more stable as time step was varied than the industry standard, giving good confidence that the best practice methodology represents a significant improvement. However, more detailed

investigation of the methodologies is required to confirm this finding.

### 7.1.2 Future Work

Beginning with opportunities to improve the presented work, there are three key concerns which this author wishes to raise. All three relate to the application of the work of Chapter 4 to the realistic open rotor test cases in Chapter 6.

Firstly, a detailed method study was undertaken in order to select the best practice methodology, but no formal problem study was conducted in order to decide the resolution of the interpolated surface for the realistic test case. The analytical open rotor test case should be used in a problem study to calculate a plot similar to Figure 4.4. It should then be used to assess what limits the resolution of the available CFD places on the frequencies that can be accurately predicted.

Secondly, the selection of the best practice solver methodology was based entirely on the results of an analytical test case. This is a simplification compared to the more realistic/complex CFD test cases actually used and could mean important effects have been ignored. In particular, the LSSA was found to be significantly more accurate at representing the analytical flow solution than the realistic one. Hence the findings of this study should be confirmed with a realistic test case. A high resolution CFD solution should be used in order to eliminate input errors as much as possible, and this flow solution should then be coarsened and refined to perform a method study similar to the one given in this thesis.

Finally, it must be acknowledged that there has been no careful coupling of the FW-H solver and input CFD methodology, i.e. the input errors have not been investigated. In particular, the noise results have not been validated against any other data, so it is difficult to know whether the results are accurate or not. The

results should be compared to experimental data, as this will improve the fidelity of the solvers. It should be noted that it would not be expected to change the conclusions of this thesis, as they are based on the variation of prediction across different methods, rather than the accuracy of one specific method.

Moving onto potential extensions of the work, there is huge scope for applying this work to other areas. The general approach is agnostic to the type of solver being used and the underlying problem of interest, and hence can theoretically be applied to all of them. In terms of other solvers that could be examined, different formulations of solution such as Farassat's Formulation 1 or collapsing sphere formulations could be tested, as could the Kirchhoff method, and other interpolation methods or numerical schemes. In terms of applying it to different problems of interest, there are many other aspects of open rotors that are of interest, such as noise at cruise, broadband noise and installation effects, and many other technologies that FW-H solvers are used for, such as helicopters and wind turbines.

## 7.2 Neglection Errors

### 7.2.1 Conclusions

By using a novel generic notation that is agnostic of the form of both the realistic and acoustic conservation equations, a generic aeroacoustic analogy has been derived of which Lighthill's so-called "density" analogy and Morfey's similar "pressure" analogy are specific versions.

It was shown that the source terms in the acoustic fluid could be understood from two different physical perspectives. The first perspective is that the source field should be understood in terms of addition of mass and momentum, rather than

density and stress or other source fields. The second perspective is that the acoustic fluid has no concept of what the realistic fluid is, and hence the source field should be understood in the context of the acoustic fluid, not the realistic one.

With these perspectives in mind, a new surface discontinuity method was derived. The source field was shown to be split in terms of the mass and momentum sources required in the acoustic fluid. Hence, neglecting the external part of the source field represents neglecting the addition of mass and momentum to the acoustic fluid outside the surface. This is a clear physical interpretation that is in keeping with the above perspectives, and hence it is concluded that this method is the way of introducing a surface discontinuity that is most in keeping with the basic principles of an aeroacoustic analogy.

The generic notation allowed the new method to be directly compared to the FW-H and Kirchhoff methods in a novel manner. All three were shown to have the same overall source field, and only differed in how that source field was split at the discontinuity. It was shown that only the new method applied the discontinuity in a physically meaningful manner with respect to the above perspectives.

It was shown that avoiding density perturbations in the new method is simply a case of selecting an appropriate acoustic fluid to base the aeroacoustic analogy on. Hence, the new method appears to not only be the most physically intuitive way of introducing a surface discontinuity, but also of formulating that discontinuity to mitigate neglect errors.

In order to confirm whether the new surface discontinuity method provided any benefit compared to either the FW-H or Kirchhoff methods, a semi-analytical flow solution (where the mass and momentum source fields were analytically defined but the resulting solution needed to be numerically integrated) was used.

The contour plots of Figure 5.7 clearly show that the FW-H method suffers from

significant instabilities at upstream directivities that are mitigated somewhat by the new method and almost entirely eliminated by the Kirchhoff method. The reverse is true for downstream directivities, but this effect is less significant than for the upstream cases. Surprisingly, the density analogy methods seem to be more stable for the new and Kirchhoff methods than their pressure analogy counterparts. This underlines the importance of demonstrating the different methods on a realistic test case. Nevertheless, the test case has clearly demonstrated that the new method can mitigate these errors compared to the FW-H method while providing a superior physical basis for the source field.

In order to demonstrate the new method on the realistic test case of Chapter 6, the FW-H, new with pressure analogy and new with density analogy methods were applied to five different downstream surface locations and three observers. In some cases, the neglect errors were found to cause over 10 dB of oscillation as surface extent was varied, confirming that this is an important effect in realistic cases and hence justifying the work in this thesis towards understanding and mitigating them. It also demonstrated the strong dependence on observer directivity seen in the semi-analytical test case, with upstream cases being shown to be much less stable than downstream ones, which were quite stably predicted. The comparison of the different source term constructions was less conclusive, though for the upstream, most onerous case the new with pressure analogy method was noticeably more stable than the other methods. While this is very encouraging, it is important to acknowledge that these are only initial results based on a small number of surface locations.

### 7.2.2 Future Work

It is clear from comparing the results for the semi-analytical and realistic test cases that the semi-analytical test case is incorrectly favouring density analogy methods. The semi-analytical case is very simple, in that  $\beta_{p,ij} = 0$  and hence only some source terms were examined. In addition, the construction of the  $\alpha_p$  source field is rather simple and does not incorporate any rotating motion. It could well be that investigating more complex source fields that are more representative of a realistic fluid will enable the semi-analytical case to give far more relevant results. Hence this is an important area for future work.

Another opportunity arises from the Kirchhoff method not being examined for the realistic test case, due to spatial gradients not being available in the CFD. These gradients should be extracted to enable a Kirchhoff method to be compared to the others.

As for the discretisation error work, there is huge scope for applying the work of Chapter 5 to other problems. The adjusted methods of Morfey et al [59] and Spalart and Shur [78] and other variants of the new method using different aeroacoustic analogies could be investigated. The semi-analytical test case could be tailored to other problems of interest such as jet or helicopter noise. In particular, the detrimental effect of retaining density perturbations in surface source terms is believed to be especially important in hot jets, where temperature changes lead to significantly larger fluctuations in the density field than in the associated pressure field. Applying the new method with various underlying analogies to these other problems could present even more significant benefits than those seen for open rotor noise in this thesis.



# Bibliography

- [1] The GNU Fortran Project, <http://gcc.gnu.org/fortran/>.
- [2] J. M. Barton, O. Yamamoto, and L. J. Bober. Inviscid analysis of advanced turboprop propeller flow fields. 1985.
- [3] T. Brandvik, C. A. Hall, and A. B. Parry. Angle of attack effects on counter-rotating propellers at take-off. *Proceedings of ASME Turbo Expo, GT2012-69901*, 2012.
- [4] Tobias Brandvik and Graham Pullan. An accelerated 3d navier–stokes solver for flows in turbomachines. *Journal of Turbomachinery*, 133(2):021025, 2011.
- [5] K. S. Brentner. Prediction of helicopter rotor discrete frequency noise: A computer program incorporating realistic blade motions and advanced acoustic formulation. *NASA TM-87721*, 1986.
- [6] K. S. Brentner. An efficient and robust method for predicting helicopter high-speed impulsive noise. *Journal of Sound and Vibration*, 203(1):87–100, 1997.
- [7] K. S. Brentner and F. Farassat. Modeling aerodynamically generated sound of helicopter rotors. *Progress in Aerospace Sciences*, 39(2):83–120, 2003.

- [8] Kenneth S Brentner and F Farassat. Analytical comparison of the acoustic analogy and kirchhoff formulation for moving surfaces. *AIAA journal*, 36(8): 1379–1386, 1998.
- [9] Guillaume A Bres, Joseph W Nichols, Sanjiva K Lele, and Frank E Ham. Towards best practices for jet noise predictions with unstructured large eddy simulations. *Cell*, 1:M2, 2012.
- [10] G. H. Bryan. The acoustics of moving sources with application to airscrews. R. & M. No. 684. *British Aeronautical Research Committee*, 1920.
- [11] Edgar Buckingham. On physically similar systems; illustrations of the use of dimensional equations. *Physical Review*, 4(4):345–376, 1914.
- [12] D. Casalino. An advanced time approach for acoustic analogy predictions. *Journal of sound and vibration*, 261(4):583–612, 2003.
- [13] M. L. Celestina, R. A. Mulac, and J. J. Adamczyk. A numerical simulation of the inviscid flow through a counterrotating propeller. *Journal of Turbomachinery*, 108(2):187–193, 1986.
- [14] Y. Colin, F. Blanc, B. Caruelle, F. Barrois, and N. Djordjevic. Computational strategy for predicting cror noise at low-speed part ii: Investigation of the noise sources computation with the chorochronic approach. *18th AIAA/CEAS Aeroacoustics Conference*, 2012.
- [15] Y. Colin, B. Caruelle, T. Node-Langlois, M. Omais, and A. Parry. Computational strategy for predicting cror noise at low speed, part 1: Review of the numerical methods. *18th AIAA/CEAS Aeroacoustics Conference*, 2012.

- [16] Y. Colin, B. Caruelle, and A. B. Parry. Computational strategy for predicting rotor noise at low-speed part iii: Investigation of noise radiation with the fflowcs williams-hawkings analogy. *18th AIAA/CEAS Aeroacoustics Conference*, 2012.
- [17] Yann Colin, Fabien Wlassow, Bastien Caruelle, Thomas Nodé-Langlois, Magdi Omais, Pierre Spiegel, and Anthony B Parry. Installation effects on contra-rotating open rotor noise at high-speed. In *20th AIAA/CEAS aeroacoustics conference*, pages 16–20, 2014.
- [18] European Union Council. Directive 2008/101/ec.
- [19] D. G. Crighton, A. P. Dowling, J. E. Fflowcs Williams, M. Heckl, and F. G. Leppington. *Modern Methods in Analytical Acoustics*. Springer, 1992.
- [20] M. Czech and H. Thomas, Russell. Open rotor aeroacoustic installation effects for conventional and unconventional airframes. *AIAA*, 2185:2013, 2013.
- [21] J. D. Denton and D. C. Prince Jr. An improved time-marching method for turbomachinery flow calculation. *Journal of Engineering for Power*, 105(3): 514–524, 1983.
- [22] P. di Francescantonio. A new boundary integral formulation for the prediction of sound radiation. *Journal of Sound and Vibration*, 202(4):491–509, 1997.
- [23] A. P. Dowling and J. E. Fflowcs Williams. *Sound and sources of sound*. E. Horwood, 1983.
- [24] F. Farassat. Theory of noise generation from moving bodies with an application to helicopter rotors. *NASA TR-451*, 1975.

- [25] F. Farassat. The Kirchhoff formulas for moving surfaces in aeroacoustics - the subsonic and supersonic cases. *Journal of Sound and Vibration*, 230(2):460–462, 2000.
- [26] F. Farassat. Derivation of Formulations 1 and 1A of Farassat. *NASA TM 214853*, 2007.
- [27] F. Farassat and K. S. Brentner. The uses and abuses of the acoustic analogy in helicopter rotor noise prediction. 1987.
- [28] F. Farassat and J. Casper. Broadband noise prediction when turbulence simulation is available Derivation of Formulation 2B and its statistical analysis. *Journal of Sound and Vibration*, 331(10):2203–2208, 2012.
- [29] F. Farassat and M. K. Myers. Extension of Kirchhoff’s formula to radiation from moving surfaces. *Journal of Sound and Vibration*, 123(3):451–460, 1988.
- [30] F. Farassat and G. P. Succi. A review of propeller discrete frequency noise prediction technology with emphasis on two current methods for time domain calculations. *Journal of Sound and Vibration*, 71(3):399–419, 1980.
- [31] F. Farassat, K. S. Brentner, and M. H. Dunn. A study of supersonic surface sources - the Ffowcs Williams Hawkings equation and the Kirchhoff formula. *AIAA Paper 98-2375 (1998)*, 5(6), 1998.
- [32] Richard William Farebrother. *Linear least squares computations*. Marcel Dekker, Inc., 1988.
- [33] John GF Francis. The qr transformation a unitary analogue to the lr transformationpart 1. *The Computer Journal*, 4(3):265–271, 1961.

- [34] John GF Francis. The qr transformationpart 2. *The Computer Journal*, 4(4): 332–345, 1962.
- [35] M. Gennaretti, C. Testa, and G. Bernadini. Frequency-domain method for discrete frequency noise prediction of rotors in arbitrary steady motion. *Journal of sound and vibration*, 331(25):5502–5517, 2012.
- [36] G. Ghorbaniasl and C. Hirsch. Validation of a time domain formulation for propeller noise prediction. *International Journal of Aeroacoustics*, 5(4):295–310, 2006.
- [37] B. A. Goldman and K. S. Brentner. New algorithms for reduced memory and real-time noise prediction. *18th AIAA/CEAS Aeroacoustics Conference (33rd AIAA Aeroacoustics Conference)*, 2012.
- [38] M. E. Goldstein. Aeroacoustics. *New York, McGraw-Hill International Book Co., 1976. 305 p.*, 1, 1976.
- [39] Marvin E Goldstein. An exact form of lilley’s equation with a velocity quadrupole/temperature dipole source term. *Journal of Fluid Mechanics*, 443: 231–236, 2001.
- [40] ME Goldstein. A generalized acoustic analogy. *Journal of Fluid Mechanics*, 488: 315–333, 2003.
- [41] Gene Golub and William Kahan. Calculating the singular values and pseudo-inverse of a matrix. *Journal of the Society for Industrial & Applied Mathematics, Series B: Numerical Analysis*, 2(2):205–224, 1965.
- [42] L. Gutin. On the sound field of a rotating propeller. *NACA TM-1195*, 1948.

- [43] P. Hammerton and C. J. Knighton. Preliminary appraisal of the rig-140 crp noise test results. *Rolls Royce Technical Report INR 90275*, 1990.
- [44] D. B. Hanson. Noise of counter-rotation propellers. *Journal of Aircraft*, 22(7): 609–617, 1985.
- [45] A. S. Householder. Unitary triangularization of a nonsymmetric matrix. *Journal of the ACM*, 5(4):339–342, 1958.
- [46] MS Howe. Contributions to the theory of aerodynamic sound, with application to excess jet noise and the theory of the flute. *Journal of Fluid Mechanics*, 71 (04):625–673, 1975.
- [47] R. J. Jeracki, D. C. Mikkelson, and B. J. Blaha. Wind tunnel performance of four energy efficient propellers designed for mach 0.8 cruise. Technical report, 1979.
- [48] M. J. Kingan and P. Sureshkumar. Open rotor centrebody scattering. *Journal of Sound and Vibration*, 333(2):418–433, 2014.
- [49] G. R. Kirchhoff. Towards a theory of light rays. *Annalen der Physik und Chemie*, 18:663–695, 1883.
- [50] T. J. Kirker. Procurement and testing of a 1/5 scale advanced counter rotating propfan model. *13th AIAA Aeroacoustics Conference*, 1990.
- [51] T. W. Körner. *Fourier analysis*. Cambridge University Press, 1989.
- [52] M. J. Lighthill. On sound generated aerodynamically - I. General theory. *Proceedings of the Royal Society of London. Series A. Mathematical and Physical Sciences*, 211(1107):564–587, 1952.

- [53] M. J. Lighthill. *An introduction to Fourier analysis and generalised functions*. Cambridge University Press, 1958.
- [54] GM Lilley. The radiated noise from isotropic turbulence with applications to the theory of jet noise. *Journal of sound and vibration*, 190(3):463–476, 1996.
- [55] M. V. Lowson. The sound field for singularities in motion. *Proceedings of the Royal Society of London. Series A. Mathematical and Physical Sciences*, 286 (1407):559–572, 1965.
- [56] E. J. Lynam and H. A. Webb. The emission of sound by airscrews. R. & M. No. 624. *British Aeronautical Research Committee*, 1919.
- [57] B. Magliozzi, D. B. Hanson, and R. K. Amiet. Propeller and propfan noise. In *Aeroacoustics of Flight Vehicles: Theory and Practice, Vol. 1*. NASA RP-1258, 1991.
- [58] CL Morfey. Amplification of aerodynamic noise by convected flow inhomogeneities. *Journal of Sound and Vibration*, 31(4):391–397, 1973.
- [59] CL Morfey and MCM Wright. Extensions of lighthill’s acoustic analogy with application to computational aeroacoustics. In *Proceedings of the Royal Society of London A: Mathematical, Physical and Engineering Sciences*, volume 463, pages 2101–2127. The Royal Society, 2007.
- [60] A. S. Morgans. *Transonic helicopter noise*. PhD thesis, University of Cambridge, 2004.
- [61] W. R. Morgans. Xiv. the Kirchhoff formula extended to a moving surface. *The London, Edinburgh, and Dublin Philosophical Magazine and Journal of Science*, 9(55):141–161, 1930.

- [62] A. Najafi-Yazdi, G. A. Brès, and L. Mongeau. An acoustic analogy formulation for moving sources in uniformly moving media. *Proceedings of the Royal Society A: Mathematical, Physical and Engineering Science*, 467(2125):144–165, 2011.
- [63] D. A. Newman. Proposals for performance and noise measurements on rig-140. *Rolls Royce Technical Report INM 90221*, 1989.
- [64] C. Paquet, E. Julliard, N. Genoulaz, J. Ricouard, and P. Spiegel. Z08: low-speed aero-acoustic experimental characterization of open rotor installation on aircraft. In *Proceedings of the 20th AIAA/CEAS Aeroacoustics Conference*, pages 16–20, 2014.
- [65] A. B. Parry and D. G. Crighton. Prediction of counter-rotation propeller noise. In *American Institute of Aeronautics and Astronautics Conference*, volume 1, 1989.
- [66] A. B. Parry, M. Kingan, and B. J. Tester. Relative importance of open rotor tone and broadband noise sources. 2011.
- [67] G. G. Podboy and M. J. Krupar. Laser velocimeter measurements of the flowfield generated by an advanced counterrotating propeller. *NASA TM-101437*, 1989.
- [68] J. Ricouard, E. Julliard, M. Omais, V. Regnier, A. B. Parry, and S. Baralon. Installation effects on contra-rotating open rotor noise. *16th AIAA/CEAS Aeroacoustics Conference*, 2010.
- [69] C. Rohrbach, F. B. Metzger, D. M. Black, and R. M. Ladden. Evaluation of wind tunnel performance testings of an advanced 45° swept eight-bladed propeller at Mach numbers from 0.45 to 0.85. *NASA CR-3505*, 1982.

- [70] Airbus S.A.S. *Global Market Forecast 2015-2034*. Art & Caractre, 2015.
- [71] W. R. Sears. Some aspects of non-stationary airfoil theory and its practical application. *Journal of Aeronautical Sciences*, 1941.
- [72] A. Sharma and H. Chen. Prediction of aerodynamic tonal noise from open rotors. *Journal of Sound and Vibration*, 2013.
- [73] Hyoun-Woo Shin, Charlotte E Whitfield, and David C Wisler. Rotor-rotor interaction for counter-rotating fans. i-three-dimensional flowfield measurements. *AIAA journal*, 32(11):2224–2233, 1994.
- [74] M. L. Shur, P. R. Spalart, M. K. Strelets, and A. K. Travin. Towards the prediction of noise from jet engines. *International journal of heat and fluid flow*, 24(4):551–561, 2003.
- [75] M. L. Shur, P. R. Spalart, and M. K. Strelets. Noise prediction for increasingly complex jets - Part I: Methods and tests. *International Journal of Aeroacoustics*, 4(3):213–246, 2005.
- [76] N Sohoni. Personal communication.
- [77] NG Sohoni, CA Hall, T Brandvik, and AB Parry. Prediction and measurement of unsteady blade surface pressures on an open rotor. In *ASME Turbo Expo 2015: Turbine Technical Conference and Exposition*, pages V001T01A007–V001T01A007. American Society of Mechanical Engineers, 2015.
- [78] P Spalart and M Shur. Variants of the fflowcs williams-hawkings equation and their coupling with simulations of hot jets. *International journal of aeroacoustics*, 8(5):477–491, 2009.

- [79] MATLAB Version 7.10.0.499 (R2010a Student). The MathWorks Inc., <http://www.mathworks.co.uk>.
- [80] Arne Stuermer and Jianping Yin. The case for counter-rotation of installed contra-rotating open rotor propulsion systems. *30th AIAA Applied Aerodynamics Conference*, 2012.
- [81] H. Tang, D. Qi, and Y. Mao. Analysis on the frequency-domain numerical method to compute the noise radiated from rotating sources. *Journal of Sound and Vibration*, 332(23):6093–6103, 2013.
- [82] P. H. Thomas, C. H. Hall, and A. S. Morgans. Analytical solutions for acoustic integral solvers. *18th AIAA/CEAS Aeroacoustics Conference*, 2012.
- [83] P. Vaníček. Approximate spectral analysis by least-squares fit. *Astrophysics and Space Science*, 4(4):387–391, 1969.
- [84] J. E. F. Williams and D. L. Hawkings. Sound generation by turbulence and surfaces in arbitrary motion. *Philosophical Transactions of the Royal Society of London. Series A, Mathematical and Physical Sciences*, 264(1151):321–342, 1969.
- [85] JE Ffowcs Williams. Hydrodynamic noise. *Annual Review of Fluid Mechanics*, 1(1):197–222, 1969.
- [86] R. P. Woodward. Noise of a model high speed counterrotation propeller at simulated takeoff/approach conditions. *NASA TM-100206*, 1987.
- [87] A. Zachariadis. *Open rotor design for low noise*. PhD thesis, University of Cambridge, 2010.